

# **Clean Integration of Single-Walled Carbon Nanotubes for Electromechanical Systems**

Dissertation submitted to  
ETH Zurich

for the degree of  
Doctor of Sciences

presented by  
Matthias Muoth  
MSc ETH ME, ETH Zurich

born January 15, 1982  
citizen of Basel and Breil/Brigels

accepted on the recommendation of  
Prof. Dr. Christofer Hierold, examiner  
Prof. Dr. John Robertson, co-examiner

2013



On the front cover (from left to right):

Array of silicon tips for tensile loading of carbon nanotubes. Own figure. See Figure 3.13. (bottom) Suspended carbon nanotube. See Figure 3.4. Adapted from [1]. © Wiley, 2010.

On-chip shadow mask for contamination-free metal patterning. Adapted from [2]. © IEEE, 2011.

Piezoresistive response of a carbon nanotube transistor device axially strained by a micro actuator. (inset) Corresponding electron diffraction pattern used for chirality assignment. See Figure 5.9. Adapted from [3]. © IEEE, 2013.

On the back cover (from left to right):

Electrically heated thermo-mechanical actuator fabricated by the multi project wafer service PolyMUMPs [4]. Own figure. (bottom) Raman spectra of a single-walled carbon nanotube with and without tensile strain. Conference contribution IWEPNM 2011 [5]. See Figure 5.2.

On-chip shadow mask slider for precise lateral alignment and small mask-to-nanotube gap. Own figure.

Transmission electron diffraction patterns of a single-walled and a double-walled carbon nanotube. Own figures. Transmission electron microscopy image of an  $\text{Al}_2\text{O}_3$ -encapsulated palladium contact to a carbon nanotube. See Figure 3.20. Adapted from [1]. © Wiley, 2010. (bottom) Single-walled carbon nanotube anchored to  $\text{Al}_2\text{O}_3$ . Own figure.

Document typeset by the author using the  $\text{\LaTeX}2_\epsilon$  system and the KOMA-Script document class scrbook. The text is set in 10/12pt Palatino. Figures and cover were produced by a combination of CorelDraw, Adobe Photoshop, and Matlab.

Copyright © 2013 Matthias Muoth, Zurich



## Quotation

**Love the Lord your God with all your heart,  
with all your soul,  
and with all your mind.  
Love your neighbour as you love yourself.**

*Jesus Christ according to Matthew 22, 37-39*

to my beloved Noémie



# Abstract

Carbon nanotubes are the tubular form of carbon. Their exceptional properties make them interesting for a wide range of applications. However, in order to exploit the properties of an individual single-walled carbon nanotube (SWNT) in an electromechanical or electronic device, contacts from the macro to the nanoscale must be established. Processes for integration of SWNTs into microfabricated systems shall maintain the low defect density of electronic-grade, as-grown carbon nanotubes.

Nanotubes  
Aim

Standard microfabrication approaches rely on resist-based lithography that may contaminate SWNTs, leading to device instabilities such as gate hysteresis. Although nanotubes are inert against most solvents, aggressive cleaning can still cause defects in the carbon nanomaterial. On the other hand, cleaning is not required for nanotubes directly grown on pre-patterned conductive electrodes. However, the contact materials must endure the high-temperature conditions required for high-quality SWNT synthesis. This greatly limits the choice of materials for contacting SWNTs.

Challenge

Here, the integration of individual single-walled carbon nanotubes for electromechanical applications is achieved in a clean manner while maintaining broad material compatibility. Hysteresis-free, chirality-assigned carbon nanotube transistors were integrated onto microactuator structures that are compatible with transmission electron microscopy (TEM), electron diffraction (ED), and confocal Raman spectroscopy.

Integration of  
SWNTs

In a modified metallisation approach, stencil lithography is implemented by on-chip shadow masks to enable resist-free patterning of metal electrodes. The shadow mask shields the mid-section of the nanotube. By physical vapour deposition, the contact material is directly deposited onto the suspended end sections of the as-grown SWNT and yields self-aligned, cone-shaped contacts. Guided on-chip sliders enable accurate mask alignment with sub-100 nm precision.

On-Chip  
Shadow  
Masking

In a second approach, nanotubes are transferred onto palladium electrodes on a substrate remaining at room temperature. The nanotubes are synthesised on a separate substrate featuring fork-like supports that can sustain the high-temperature nanotube synthesis conditions. The manipulation is performed under light microscopy observation to avoid electron-beam-induced carbonaceous contaminations of the SWNTs. Current monitoring is utilised to detect successful nanotube placement on the target electrodes. Transfer enables improved control over nanotube position, orientation, and number. Additionally, it opens up the possibility to select a specific nanotube.

Transfer

Hysteresis-free CNFETs	Both fabrication approaches for carbon nanotube field-effect transistors (CNFETs) eliminate gate hysteresis even when operated at ambient conditions. The absence of hysteresis and the improved stability of threshold voltage are attributed to the absence of oxides and contaminations in the vicinity of the suspended, nearly defect-free nanotube transistor channel. Despite the large gate separation of 3 $\mu\text{m}$ , subthreshold swings down to 110 mV/dec were achieved.
Strain	Mechanical tensile tests have also been performed. For this purpose, nanotubes were grown across sharp tip pairs and stretched by driving micro actuators inside a TEM. Metal markers on the suspended single and double-walled carbon nanotubes allowed observation of strain, rotation, slippage, vibration, and rupture. Phonon frequency downshifts upon strain were measured by Raman spectroscopy and quantitative shift rates were extracted by optical image analysis.
Piezoresistivity	Electromechanical responses of chirality-assigned, suspended CNFETs to uniaxial strain were recorded. As expected from theory, the strain-induced change in conductivity depends on chirality.
Encapsulation	A clean encapsulation process for the contacts was also developed in order to provide passivation for oxidation-prone contacts and to distinguish gas-sensing mechanisms acting at the contacts from those at the nanotube channel. Instead of patterning by means of resist-based lithography and etching, surface-selective nucleation of the passivation film during deposition was used to ensure cleanliness. Atomic-layer-deposited alumina (ALD $\text{Al}_2\text{O}_3$ ) nucleates on the contacts but not on the clean and defect-free surface of suspended individual SWNTs. Nearly hysteresis-free transistor operation was obtained after $\text{Al}_2\text{O}_3$ deposition at 300 $^\circ\text{C}$ . In contrast, hysteretic effects were observed for non-selective deposition at reduced temperature.
Conclusion	The fabrication approaches of CNFETs by shadow masking or by transfer suppress hysteresis and reduce threshold voltage fluctuations, and hence demonstrate optimised device performance. The CNFETs can be integrated in micro-fabricated tensile actuators and allow characterisation by transmission beams required for high-resolution imaging and chirality assignment.
Achievement	The clean integration strategies in combination with the demonstrated structure assignment provide a solid platform for the evaluation of individual, high-quality SWNTs as electromechanical transducers.



# Zusammenfassung

Kohlenstoff-Nanoröhren sind die röhrenförmige Ausprägung von Kohlenstoff. Ihre aussergewöhnlichen Eigenschaften sind interessant für eine grosse Bandbreite von Anwendungen. Um ein einzelnes einwandiges Kohlenstoffnanoröhrchen (SWNT) als elektronisches Sensorelement verwenden zu können, braucht es Fabrikationsprozesse die elektrische Kontakte zwischen der Makro- und der Nanowelt herstellen. Die Integration von SWNTs in Mikrosysteme soll die mechanische und elektronische Qualität des Ausgangsmaterials nicht mindern.

Nanoröhren

Ziel

Etablierte Fabrikationsmethoden der Mikrosystemtechnik strukturieren mittels Fotolack und können winzige Verunreinigungen hinterlassen. Lackreste sind eine mögliche Ursache von elektrischen Instabilitäten wie Hysterese im Bezug auf die Steuerspannung. Obwohl Kohlenstoffnanoröhren gegen die meisten Lösungsmittel beständig sind, können aggressive Reinigungsprozesse dennoch Defekte hervorrufen. Reinigungsschritte werden hingegen nicht benötigt, wenn die Nanoröhren direkt auf vorgängig strukturierte leitfähige Elektroden aufgewachsen werden. Jedoch muss das Elektrodenmaterial der Hochtemperatursynthese standhalten können, welche für qualitativ hochwertige Nanoröhrchen benötigt wird. Dies schränkt die Materialwahl für die Kontakte erheblich ein.

Herausforderung

In dieser Arbeit werden Integrationsprozesse untersucht die verunreinigungs-frei sind und gleichzeitig eine grosse Materialkompatibilität bieten. Hysterese-freie, freihängende Transistoren aus Kohlenstoffnanoröhren wurden auf Mikroaktuatoren aufgebracht, die kompatibel sind mit kombinierten Untersuchungen durch Transmissions-Elektronenmikroskopie (TEM), Elektronenbeugung (zur Chiralitätsbestimmung) und Raman Spektroskopie.

Integration von SWNTs

Ein Metallisierungs-Verfahren basierend auf Schablonen-Lithographie ermöglicht die Strukturierung von Metallelektroden ohne Fotolack verwenden zu müssen. Schattenmasken werden direkt auf dem Chip eingebaut und beschatten den mittleren Bereich der freihängenden Nanoröhre während das Kontaktmaterial als Dünnschicht aufgedampft wird (PVD). Das Kontaktmaterial legt sich direkt auf den freistehenden Endbereichen des Nanoröhrchens ab. Genau dort entstehen kegelförmige Kontakte. Mechanisch geführte Mikroschlitten ermöglichen die Positionierung der Maske mit einer Präzision von unter 100 nm.

Integrierte Schattenmaske

In einem zweiten Ansatz werden die Nanoröhren bei Raumtemperatur auf ein Substrat übertragen welches mit Palladium-Elektroden bestückt ist. Die Nanoröhren wurden zuvor auf einem separaten Substrat hergestellt welches gabelähnliche, hochtemperaturbeständige Stützen aufweist. Unter Vermeidung prozessbedingter Kontamination werden die Nanoröhren unmittelbar nach der Synthese transferiert. Die Positionierung erfolgt unter Beobachtung im Lichtmikroskop.

Transfer

Dadurch werden kohlenstoffhaltige Ablagerungen vermieden welche typischerweise im Elektronenmikroskop verursacht werden. Die erfolgreiche Platzierung von Nanoröhren auf den Ziel-Elektroden wird durch Stromüberwachung detektiert. Die Transfermethode ermöglicht eine verbesserte Kontrolle über die Ausrichtung, Position und Anzahl der Nanoröhren. Zudem eröffnet sie die Möglichkeit spezifische Nanoröhren auszuwählen.

Hysteresefreie CNFETs      Beide Herstellungsansätze für Kohlenstoffnanoröhren Feldeffekt-Transistoren (CNFETs) eliminieren Hysteresis im Bezug auf die Steuerspannung – sogar unter Raumbedingungen. Die Unterdrückung der Hysteresis und die verbesserte Stabilität der Schwellenspannung wird der Abwesenheit von Oxiden und Verschmutzungen in der näheren Umgebung des freistehenden, fast fehlerfreien Nanoröhren-Transistorkanals zugeschrieben. Trotz des grossen Abstands zum Gatter von 3  $\mu\text{m}$ , entfaltete die Steuerspannung gute Wirkung ( $S = 110 \text{ mV/Dek}$ ).

Dehnung      Nanoröhren wurden auf Zug belastet. Hierfür wurden sie über Mikrospitzen gewachsen welche mittels Mikroaktuatoren betätigt werden. Letztere sind ausreichend klein um in Transmissions-Elektronenmikroskope eingeführt zu werden. Metallische Markierungen auf den freistehenden ein- und doppelwandigen Kohlenstoffnanoröhren ermöglichen die Beobachtung von Dehnung, Rotation, Gleiten, Vibration und Bruch. Änderungen der Phononenfrequenzen aufgrund von mechanischer Dehnung wurden mittels Raman Spektroskopie gemessen und quantitative Änderungsraten durch optische Bildanalyse ermittelt.

Piezoresistivität      Elektromechanische Messungen an CNFETs zeigen dehnungsabhängige Widerstandsänderungen, in Abhängigkeit der Chiralität.

Verkapselung      Passivierung von Metallkontakten kann Langzeitstabilität ermöglichen und ist erwünscht für die Erforschung von Gassensoren. Die Verkapselung der Kontakte wird oberflächenselektiv aufgebracht – ohne lack-basierte Verfahren, um Kontamination zu vermeiden.  $\text{Al}_2\text{O}_3$  wird durch Atomlagenabscheidung (ALD) auf die Kontakte aufgewachsen, jedoch nicht auf die saubere, defektfreie Oberfläche der freihängenden Nanoröhre. Abscheidung bei 300 °C ermöglichte nahezu hysteresis-freie Transistoren mit eingekapselten Kontakten. Hysteresis wurde hingegen nach unselektiver Abscheidung bei tieferen Temperaturen beobachtet.

Schlussfolgerung      Beide Fabrikationsmethoden, Schattenmasken-Lithographie und Transfer, unterdrücken Hysteresis. Die CNFETs können in mikrofabrizierte Zugaktoren eingebaut werden und lassen sich durch hochauflösende Bildgebung und Chiralitätsmessung mittels TEM charakterisieren.

Erreichtes      Die rückstandsfreien Kontaktherstellungsverfahren in Kombination mit der gezeigten Strukturbestimmung liefern die Grundlage für die Evaluation von einzelnen, hochwertigen SWNTs als elektromechanische Messfühler.

# Acknowledgements

Foremost, I want to express my gratitude to Professor Christofer Hierold, who offered me the great opportunity to conduct exciting scientific work in his group.

I thank Prof. John Robertson, University of Cambridge, for accepting the examination of my thesis and I am thankful for the discussions with Martin Fouquet.

I am grateful for the cordial discussions with Shih-Wei Lee, for sharing success and happiness with him and for many encouraging talks. I am indebted to all colleagues of our Nanotube Team: Kiran Chikkadi, Tobias Süss, Valentin Döring, Wei Liu, Dr. Cosmin Roman, Dr. Miroslav Haluska, Dr. Emine Cagin, Dr. Stuart Truax, Yu Liu, and Maria Politou. Special thanks go to Dr. Lukas Durrer, Dr. Moritz Mattmann, and Dr. Thomas Helbling for their great advice and help. I thank the whole Micro and Nanosystems group for the cordial working environment, for the merry times at hut preparations, retreats, and Christmas parties.

I want to thank Stephan-Alexis Pohl, Alexander Intlekofer, Jérôme Grimm and Kathrin Truckses who conducted their theses in our group. Alexis Pohl prepared silicon grids equipped with through wafer holes and was characterising SWNTs grown across the grids by AFM and Raman. Alexander optimised material stacks for high-temperature durable electrodes and investigated oriented CNT growth by gas flow alignment. Jérôme measured Raman downshifts on strained SWNTs. Kathrin explored electrophoretically mediated adsorption of catalyst precursors. I thank Eeva Köpilä and Rebekka Hugger for all the administrative efforts which they conducted with a great friendliness.

Donat Scheiwiller and Stefan Blunier from the operational team of the FIRST-CLA cleanroom are acknowledged. Thanks go to all members of the FIRST Center for Micro- and Nanoscience of ETH. Especially Sandro Bellini, Dr. Emilio Gini and Dr. Otte Homan are acknowledged who helped with great devotion.

Dr. Roger Wepf from the Electron Microscopy Facility of ETH Zurich (EMEZ) and his team is acknowledged. Cordially, I want to thank Fabian Gramm for his teaching at the electron microscope and for the introduction to the good old imaging plates. I thank Elisabeth Müller-Gubler for the careful training at the dedicated STEM. Peter Tittmann and Philippe Gasser owe thanks for maintenance work on the FIB and TEM. Koji Asaka, Assistant Prof. at the Department of Quantum Engineering, Nagoya University, is cordially acknowledged for sharing expertise in TEM. Dr. Manish Tiwari and Prof. Dimos Poulikakos from LTNT at ETH Zurich are acknowledged for allowing access to the TEM sample holder initiated by Nicole Bieri and custom made by Mr. Dörfler.

Dannik Briand, Simone Schürle, Ji Cao and many others are acknowledged for idea exchanges within CabTuRes, Nano-Tera.ch, a program of the Swiss Confederation, evaluated by SNSF. I owe my gratitude to Brian Burg who integrated our nanotube material by dielectrophoresis. I thank Niklas Schirmer and Timo Schwamb for helpful collaboration. Joe Brown and Gabriel Puebla-Hellmann are kindly acknowledged for inspiring collaboration. I would like to show my gratitude to the group members of Prof. Ensslin, especially to Françoise Molitor, Johannes Güttinger, Susanne Dröscher, Arnhild Jacobsen and Dominik Bischoff for inspiring discussions. Furthermore, I thank Prof. Jun Lou from Rice University for the discussions about MEMS tensile tests.

Prof. Ph. Lambin, Les Facultés Universitaires Notre-Dame de la Paix, Belgium, is acknowledged for providing the FORTRAN code for diffraction simulation and Cosmin Roman for its implementation in Matlab. Andrea Kasper is acknowledged for help concerning image colouring, Yu Liu for code related to electrical measurements, Stefan Stoll for code related to Raman intensity attenuation, and Adrian Bachofner for inspiring discussions.

It is my pleasure to thank all alumni members of the MNS group, especially Dr. Alain Jungen, Prof. Christoph Stampfer, Dr. Debyoti Sarangi and Dr. Jochen Hötzel for the heritage of nanotube-related achievements.

It is an honor for me to have had the possibility to meet many fascinating personalities in our field including M. S. Dresselhaus, S. Ijima, B. Bhushan, J. Hanein, J. Meyer, U. Kaiser, R. Erni, S. Hofmann, S. Doorn, A. Vijayaraghavan, J. Brugger, G. Steel, A. Bushmaker, J. Maultzsch, V. Popov, and H. Kataura.

I thank my beloved ♥ fiancée Noémie who supported me wonderfully during my PhD studies. Cordially, I thank my friends and relatives for their interest in my nano-tiny scientific world. Especially, I express my gratitude to my parents Margrit and Daniel, and to my siblings Pascale and Dominik for their support and for sharing my enthusiasm about nanotubes. Special thanks go to all my relatives and dear friends including those from Basic, Huus-Chreis and Xapes.

I thank Jesus Christ who is my shelter, peace, joy and strength, especially during times when challenging burdens had to be faced.

I would like to thank the Swiss Government for our Constitution declaring „Im Namen Gottes des Allmächtigen! [...] in der Verantwortung gegenüber der Schöpfung, [und] gegenüber den künftigen Generationen, [...] dass die Stärke des Volkes sich misst am Wohl der Schwachen“ which is for me a commitment of our country to serve all people.

Financial support by the Swiss National Science Foundation (SNSF, 200021-108059/1, 200020-121831) is gratefully acknowledged. STEM, TEM and FIB work was carried out at EMEZ, which receives partial support by the SNSF through the R'Equip program. Swiss and EU COST Action MP0901 are acknowledged for knowledge exchange possibilities.

# Contents

<b>Abstract</b>	<b>vii</b>
<b>Zusammenfassung</b>	<b>ix</b>
<b>Acknowledgements</b>	<b>xi</b>
<b>1 Introduction</b>	<b>1</b>
1.1 Carbon materials: Overview and motivation . . . . .	2
1.2 Challenges in the electrical integration of SWNTs . . . . .	5
1.3 Objectives of this Thesis . . . . .	9
1.4 Contents of the Chapters . . . . .	10
<b>2 State-of-the-art</b>	<b>15</b>
2.0.1 Carbon history . . . . .	15
2.1 Carbon nanotube synthesis . . . . .	16
2.2 Fabrication of nanotubes device . . . . .	17
2.3 Carbon nanotube electronic devices . . . . .	21
2.3.1 Carbon nanotube field-effect transistors . . . . .	22
2.3.2 Gate hysteresis in CNFETs . . . . .	24
2.3.3 Integration of CNTs into macro-scale tensile stages . . . . .	26
2.3.4 Integration of CNTs into MEMS-based tensile stages . . . . .	26
2.4 Nanotube integration for electromechanical transducers . . . . .	26
2.4.1 External probes . . . . .	26
2.4.2 Electrical contacts to CNTs embedded in MEMS actuators . . . . .	27
2.5 Accessibility by TEM . . . . .	28
<b>3 Fabrication: Ultraclean, TEM-compatible CNFETs integrated into MEMS</b>	<b>31</b>
3.1 Electrical integration of ultraclean suspended SWNTs . . . . .	31
3.2 Integration of suspended SWNTs by shadow masking . . . . .	32
3.2.1 General concept of stencil lithography . . . . .	33
3.2.2 Adapted stencil lithography for integration of SWNTs . . . . .	37
3.2.3 Fabrication of ultraclean CNFETs by shadow masking . . . . .	38
3.2.4 Conclusions on the process flow of shadow masking . . . . .	46
3.3 Room-temperature integration of suspended SWNTs by transfer . . . . .	49
3.3.1 Fabrication of ultraclean CNFETs by transfer . . . . .	51
3.3.2 Conclusions on the process flow of direct transfer . . . . .	55

3.4	Integration of SWNTs strainable by micro actuators . . . . .	58
3.4.1	Electrically heated thermomechanical actuators . . . . .	60
3.4.2	Electrostatic actuators . . . . .	61
3.4.3	Electrical decoupling from actuator driving voltages . . . . .	62
3.5	TEM-accessibility of suspended SWNTs devices . . . . .	63
3.5.1	Options for TEM-accessibility . . . . .	67
3.5.2	Tilted-view transmission electron microscopy . . . . .	68
3.6	Passivation of electrical contacts . . . . .	73
3.7	Conclusions on Fabrication . . . . .	74
<b>4</b>	<b>Characterisation: Ultraclean, suspended CNFETs</b>	<b>77</b>
4.1	TEM imaging of integrated nanotubes . . . . .	77
4.2	Chirality assignment by electron diffraction . . . . .	78
4.3	Raman spectroscopy of suspended nanotubes . . . . .	84
4.4	Correlation of diameter determined by RBM and electron diffraction	84
4.5	Hysteresis-free transistor characteristics of ultraclean CNTs . . . . .	87
4.5.1	Contact formation by shadow masking . . . . .	88
4.5.2	CNFETs by shadow masking . . . . .	89
4.5.3	Simulation of electric potential for tapered electrodes . . . . .	92
4.5.4	Chirality-assigned CNFET fabricated by shadow masking . . . . .	95
4.5.5	CNFETs by direct transfer . . . . .	97
4.5.6	Influence of e-beam induced carbonaceous deposition . . . . .	100
4.5.7	Chirality assignment to CNFET fabricated by transfer . . . . .	100
4.5.8	Transistor output characteristics . . . . .	101
4.5.9	Shrinkage of gate separation . . . . .	102
4.6	STEM imaging of metal contacts . . . . .	105
4.7	Stability of threshold voltages . . . . .	105
4.7.1	Stability of threshold voltages in CNFETs . . . . .	107
4.8	Encapsulation by atomic-layer-deposited $\text{Al}_2\text{O}_3$ . . . . .	110
4.8.1	Hysteresis-induction by non-selective ALD $\text{Al}_2\text{O}_3$ . . . . .	112
4.8.2	Transistor polarity . . . . .	115
4.8.3	Effect of heating during passivation process . . . . .	115
<b>5</b>	<b>Mechanical loading of suspended CNTs</b>	<b>117</b>
5.1	Motivation . . . . .	117
5.2	Phonon shifts at defined strain in TEM-characterised SWNTs . . . . .	117
5.3	Uniaxial loading of SWNTs inside a TEM . . . . .	122
5.3.1	TEM imaging of mechanical contacts . . . . .	122
5.4	Electromechanical response of MEMS-embedded CNFETs . . . . .	125
5.4.1	Piezoresistive response of CNFET fabricated by transfer . . . . .	125
5.4.2	Piezoresistive response of CNFET encapsulated by $\text{Al}_2\text{O}_3$ . . . . .	126
5.4.3	Piezoresistive response of CNFET with top-metallisation . . . . .	126

<b>6 Conclusion and Outlook</b>	<b>129</b>
6.1 Summary and Conclusions . . . . .	129
6.2 Outlook . . . . .	131
<b>A Appendix</b>	<b>133</b>
A.1 Safety considerations . . . . .	133
A.2 Experimental procedure for electron diffraction at FEI CM12 . . . .	133
A.3 Run sheets - shadow masking, transfer from fork . . . . .	135
<b>B Theory and methods: Carbon nanotube properties and characterisation</b>	<b>139</b>
B.1 Carbon nanotube properties . . . . .	139
B.1.1 Structural description . . . . .	139
B.1.2 Mechanical properties . . . . .	143
B.1.3 Electronic properties . . . . .	144
B.1.4 Electrical transport . . . . .	149
B.1.5 Carbon nanotube field-effect transistors . . . . .	151
B.1.6 Electromechanical properties . . . . .	152
B.2 Characterisation techniques for carbon nanotubes . . . . .	158
B.2.1 Transmission electron microscopy (TEM) . . . . .	158
B.2.2 Electron diffraction . . . . .	160
B.2.3 Scanning electron microscopy (SEM) . . . . .	167
B.2.4 Scanning transmission electron microscopy (STEM) . . . .	167
B.2.5 Raman spectroscopy and related optical techniques . . . .	168
B.2.6 Scanning tunnelling microscopy (STM) and spectroscopy . .	170
B.2.7 Atomic force microscopy (AFM) . . . . .	170
B.2.8 Electrical transport measurements . . . . .	171
<b>C Towards chirality control during synthesis</b>	<b>172</b>
C.1 State-of-the-art in chirality control for SWNTs . . . . .	172
C.1.1 Catalyst control . . . . .	172
C.1.2 Chirality amplification by regrowth . . . . .	174
C.2 Opening ends of CNTs at defined lengths . . . . .	174
C.3 Electrophoretically mediated ferritin adsorption . . . . .	175
C.4 Chirality control for graphene nanoribbons . . . . .	175
C.4.1 Characterisation of atomically precise graphene nanoribbons	177
<b>D Symbols and abbreviations</b>	<b>182</b>
<b>Bibliography</b>	<b>187</b>
<b>Publications</b>	<b>206</b>
<b>Curriculum Vitae</b>	<b>211</b>





# 1 Introduction

## Context

Materials substantially influence our way of living. Names of archaeological periods often refer to novel materials applied – Stone Age, Bronze Age, Iron Age. Improved or new products enabled by the properties of advanced materials can disburden and protect life – it may be a clay pot for food storage, a plough on the field, an arrowhead for hunting or an anti-lock brake system at your bicycle. The ability to fabricate high quality raw materials and convenient goods has been, and still is, the basis of wealth and power. As indicated in many heroic stories and modern movies, sound principles has the one who devotes himself to support those in need, protects the endangered and offers others the possibility to join the campaign for the well-being of many. The effectiveness of action is based on courage and on the equipment – technology, excellence of manufacture, and availability. Many ideas in engineering are hindered by a lack of adequate fabrication capabilities and/or insufficient spread of knowledge about processing.

Material

Products

Action

Modern computing with its dramatic impact on daily life in our society has been enabled by the development of a novel material: doped silicon used as semiconductor in electronic chips and in image sensors for digital photography. The age of silicon – of course going in parallel with a multitude of other high-impact materials – not only enabled an extension of the calculation power demanded by research and engineering. It heavily influences the information exchange revolutionised by the World Wide Web, and by availability thereof via mobile devices. Considering the recent overthrows in Egypt, Libya and Syria, social networks powered by silicon-based technology played a crucial role in mobilising people and alerting international organisations. The use of technology gave once more proof of its impact on the everlasting (?) struggle of mankind. Courage cannot be fabricated – although wisely applied technology may open plenty of room and time for intensive thinking, and may finally lead to courageous ideas. In contrast to courage, equipment can be fabricated. But advanced equipment can only become part of the action if fabrication meets the required quality at costs which can be afforded.

Impact of  
Technology

One of the major challenges in the well-being of many is the growing energy demand. Promoted by cheap and hence widely affordable electronics, the number of electronic devices is growing. On the other hand, the energy efficiency of computing has been improved over the years.

Energy

### Subject: Carbon nanomaterials

Low Power	The quest for improved energy efficiency for computation (smart phones, ultra-books) and for distributed sensor systems demands novel materials. Carbon nanotubes (CNTs) [6] and graphene [7] are nanomaterials with potential to reduce the energy demand for information processing in electronics and signal acquisition in sensors. Carbon nanomaterials can exhibit superior mobility [8] of the charge carriers which represent information, can exhibit quasi-ballistic transport [9, 10] and high current densities. Improved carrier mobility promises reduced losses and lesser energy demand. In the future, your mobile phone may need to be recharged less often – despite its compact design.
Mobility	
Size	The tiny dimensions of carbon nanomaterials are appealing for continuing miniaturisation of electronic systems with small currents and high device density. Furthermore, fundamentally novel properties related to quantum confinement may enable the implementation of new concepts, such as spin-based electronics (spintronics). The extended spin relaxation times observed in carbon nanotubes might be exploited for computing [11, 12].
Quantum Effects	
Electro-Mechanical	Another interesting feature of carbon nanomaterials is their mechanical strength at light weight, rendering them promising candidates for resonant electromechanical devices and for structural composites – surpassing the mechanical properties of carbon fibres. Other anticipated application fields are conductive electrodes for touchscreens and catalytic material for chemical industry.
Fabrication	Whether carbon materials will reach the market in the diverse application areas or not, is crucially depending on the fabrication capabilities of the raw material and on the ability to integrate the material into complex systems.
Integration	

### 1.1 Carbon materials: Overview and motivation

SWNTs	Single-walled carbon nanotubes (SWNTs) are tubular nanostructures [6, 13]. The diameter of these macromolecules ranges from $\sim 0.4$ nm [14] to about 5 nm [15]. The tube wall consists of a single layer of carbon atoms. The length of nanotubes can reach centimetres [16], resulting in a huge aspect ratio.
Carbon	Carbon is the lightest chemical element that can form four covalent bonds. Carbon builds a large diversity of organic and inorganic molecular compounds. It is a major element in polymers, natural gas and proteins. In the human body, carbon is the second most abundant element. Pure, elemental carbon (C) can be arranged in different structural modifications, so called allotropes.
Diamond	The three-dimensionally linked tetrahedral lattice structure is known as diamond, the material of highest hardness due to the strong covalent C–C bonds (bond length = 0.154 nm).
Graphite	In graphite, the C atoms are covalently bonded together in a hexagonal arrangement and form planar sheets. These sheets are stacked with a spacing of 0.335 nm and are held together by weak interaction forces. The bonding within the sheets is very strong (bond length = 0.142 nm).
Carbon Fibres	Carbon fibres are cylindrical structures of partially folded graphitic sheets.

An individual sheet of graphite is called graphene. With a thickness of a single atomic layer, the honeycomb-like graphene lattice is a quasi-two-dimensional material. The low dimensionality gives rise to exciting electronic properties due to electron confinement. Additional lateral confinement can be induced in narrow ribbons of graphene, so called graphene nanoribbons (GNRs). Depending on the relative orientation between the ribbon edge and the hexagons of the graphene lattice, different patterns can be obtained (chirality). The electrical behaviour of graphene is semi-metallic [7]. Narrow GNRs and double-layer graphene [17] can exhibit semiconducting behaviour.

Graphene  
Nanoribbons  
Chirality

A single-walled carbon nanotube can be pictured as a rolled-up graphene ribbon seamlessly welded into a tube. Nanotubes can differ in diameter. Additionally, the hexagonal lattice of the rolled-up sheet can have different orientations with respect to the tube axis. Both diameter and lattice orientation are described by the term chirality. The variety in chirality influences the electronic properties. Nanotubes can exhibit semiconducting or metallic properties. The occurrence and the size of the bandgaps depend on the chirality. The electromechanical behaviour is governed by the chirality as well. In contrast to graphene nanoribbons – for which precise definition of edges is difficult with recent top-down patterning technologies – carbon nanotubes represent quasi-one-dimensional structures with atomically-smooth surfaces.

Single-walled  
Carbon  
Nanotubes

Nanotubes can feature multiple walls with regularly increasing diameters. A tube consisting of concentrically stacked carbon tubules is called multi-walled carbon nanotube (MWNT). A carbon nanotube whose wall incorporates exactly two sheets is called double-walled carbon nanotube (DWNT).

Multi-walled

### Application areas of single-walled carbon nanotubes

Carbon nanotubes are molecular tubes and have an exceptionally high elastic modulus (Young's modulus  $E$  of  $\sim 1000$  GPa) [18, 19]. Nanotubes can sustain high mechanical stress (99 GPa) and withstand large elastic deformations up to 13% [20]. The high resistance against tensile deformation combined with the ability to sustain large deformation renders nanotubes appealing for structural composites.

Stiffness  
Mechanical  
Strength

SWNTs are semiconducting or metallic – depending on chirality (see Appendix B.1.3). Electrical current can flow through an individual nanotube connected by metal contacts. The nanometre-scale diameters renders them extraordinary quantum wires. The high crystallinity of nanotubes and their atomically-smooth surfaces reduce scattering in electronic transport.

Electrical  
Properties  
Wire-like

A transistor is an electronic building block capable of switching or amplifying signals. A semiconducting nanotube can act as channel material of a field-effect transistor (FET). Semiconducting nanotubes are appealing material for electronics. Their width is very small which promises high integration density and offers quantum confinement useful for single-electron devices. Dense aligned arrays of nanotubes are appealing for analogue radiofrequency devices [21]. SWNTs in FET configuration offer high sensitivity and low power consumption when used

Sensors and  
Electronics

in nanosensors [22, 23].

Chemical	In the small-sized SWNTs, all atoms are on the surface of the tube. This geometrical property can enable high sensitivity for gas sensing [23].
Electro-mechanical Devices	Electrical transport in nanotubes can be strongly affected by mechanical deformations. The high sensitivity of certain chiralities to tensile or torsional strain [24] is appealing for nano-scale, low-power strain sensors. Although nanotubes have a high Young's modulus $E$ , an <i>individual</i> nanotube requires only a very weak force $F$ to induce tensile strain because of the small diameter $d$ and a comparatively large length $\ell$ (stiffness $k = E \cdot A/\ell$ , where $A$ is the cross-sectional area $\pi \cdot d^2/4$ ; displacement $u = F/k$ ).
Piezoresistivity	Piezoresistivity is the effect of change in electrical resistance upon mechanical strain. This can be exploited in membrane-based pressure sensors [25, 26] or possibly in small-size accelerometers and in strain gauges for integrated readout of scanning probe microscopy cantilevers. Piezoresistive readout schemes do not suffer from parasitic capacitances as capacitive readout. Moreover, nano-scale strain gauges can have much smaller sizes than capacitors. But due to the current, which is needed to measure the resistance of the strain gauge, heat is emitted. Power demand is often a crucial factor for portable or self-sustainable systems. Additionally, certain applications, such as deflection readout for scanning gate microscopy probes [27] to be operated at cryogenic temperatures, do not tolerate substantial heat emission. Nanotube-based strain gauges promise low power consumption and hence reduced thermal interference.
Suspended	When suspending a nanotube across a trench or between two pillars, the individual molecule is arranged similar to an overhead power line. Sensors in which the nanotube channel of an FET is freely suspended between two contacts have a number of advantages over those in which the nanotube adheres to a substrate. A suspended midsection of a nanotube is not mechanically deformed by interactions with the support. On a substrate, mechanical deformation can occur. Moreover, electrical charges at humid oxide surfaces of the support [28] and at resist residues [29, 30], or charges injected into the oxide [31], can distort the intrinsic electronic characteristics of carbon nanomaterials. Reducing the number of charge-traps in close proximity to the nanotube is crucial to reduce gate hysteresis [32], which is typically observed in carbon nanotube field-effect transistors (CNFETs). In suspended nanotube devices, gate hysteresis is reduced [33, 34]. Furthermore, avoiding contact between the nanotube and the substrate attenuates low-frequency noise [33, 35–37]. In addition, larger active sensing areas are obtained.
Large Strain	Nanotubes integrated between actuated electrodes can be stretched by retracting the electrodes. Suspended nanotubes allow large tensile strain – unlike if attached to a stiff and brittle membrane.
Resonators	The suspended arrangement allows vibrational motion of the doubly-clamped nanotube [38–40], which can be exploited in resonators acting as filters or as mass sensors [41]. The nanometre-sized diameter, high mechanical strength and low

mass density of SWNTs renders them promising candidates for high-frequency resonators [42–44].

The resonance frequency of the guitar-string-like mode of a suspended nanotube can be tuned by applying tensile strain [45]. Strain can be applied electrostatically by a gate bias [38] or possibly more rigorously by mechanical actuators based on micro-electromechanical systems (MEMS).

Nanotubes are also an interesting material for optoelectronic applications [46]. In a process called electroluminescence, an electrical current leads to light emission. Vice-versa, photoconductivity is the induction of an electronic current by light [47] pp.201, which can be exploited in solar cells [48].

Efficient water desalination is anticipated based on fast mass transport inside nanotubes while ions are rejected by charged entrances of nanotube pores [49].

Tunability

Optoelectronic  
Devices

Water  
Purification

## 1.2 Challenges in the electrical integration of SWNTs

For nanotube devices and sensors based on electronic, electromechanical or optoelectronic effects, the nanotube must be electrically interfaced.

To date, two main fabrication approaches have been used to incorporate electrically contacted SWNTs in a suspended configuration. The crucial difference is whether the electrical contacts are fabricated *before* or *after* nanotube synthesis.

Electrical  
Integration

Approaches

### (i) Post-growth metallisation

In the post-growth approach, the nanotubes are grown (or deposited) on a substrate. Afterwards, the nanotubes are clamped by metal electrodes patterned on top of the nanotubes by using resist-based lithography, metal deposition and lift-off. A final etching step can release the nanotube and results in suspended device configurations [43, 50–54].

CNT First

The resist contaminates the nanotubes, and the complete removal of resist residues is challenging [55]. Although carbon nanomaterials are inert against most solvents and acids, standard microfabrication cleaning procedures for resist-stripping such as oxygen plasma or ozone treatment can cause structural defects in carbon nanostructures<sup>1</sup>. Remaining contaminations on the nanotubes impede observations by transmission electron microscopy [56] and alter the electrical behaviour [29].

Cleanliness

Resist residues can be reduced by spacer layers, which prevent intimate contact of resists with the nanomaterials [57, 58]. Harsh oxidising cleaning steps can then be applied as the carbon nanomaterial is protected.

Separation  
Layer

Nevertheless, for suspended structures, nanotubes and contacts are exposed to etchants needed for release. Wet etching requires subsequent supercritical point drying to prevent mechanical damage of long, individual SWNTs [22, 59]. Both are possible sources of contamination.

Etching

<sup>1</sup> The term ‘electronic-grade’ denotes a material purity of 99.999999% (9N) or better. An ‘electronic-grade’ nanotube with a diameter of 2 nm (120 atoms per nm length) is requested to exhibit not more than one single-atom defect per cm length. Consequently, any cleaning step supposed to maintain the nanotube quality has to be extremely selective.

Palladium (Pd) is the preferred contact metal [9] for SWNTs. However, Pd can interfere with the commonly used release etching of silicon oxide ( $\text{SiO}_2$ ) by hydrofluoric acid (HF), as Pd catalyses etching of Si [60].

Another material related issue is that aluminium and titanium used for electrical contacts are not compatible with release etching by liquid HF [61].

Etching of  $\text{SiO}_2$  by hydrofluoric acid is isotropic. Hence the material underneath the contacts to the nanotube is removed partially during the release etch. This can affect mechanical stability. Moreover, adhesion layers such as chromium and titanium, used to more firmly attach Au, will oxidise and this is suspected to degrade the conductance of the electrical contacts.

Lithographic patterning of metal on as-grown nanotubes suspended across a trench was suggested [62, 63]. However, forces due to viscous flow and surface tension occur during spin-coating of resist [22]. Individual SWNTs of extended lengths ( $>0.5\text{ }\mu\text{m}$ ) can rupture [22, 59], which limits the application of resist-based lithography to short [64] or temporarily oxide-supported [42, 43] SWNTs.

Multi-walled carbon nanotubes were integrated onto MEMS tensile stages by micromanipulation and electron-beam-induced deposition (EBID) which enabled mechanical characterisation of individual CNTs [65]. Due to the spread of secondary electrons after impingement of the primary electron beam, care has to be taken about the deposition of material on the nanotube itself [66–68].

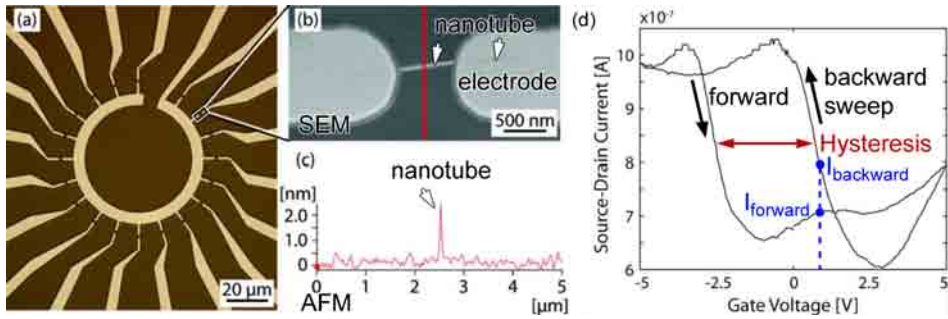
Fabrication steps after nanotube synthesis are prone to cause contamination [69, 70] or even mechanical damage in case of long suspended nanotubes. For nanotube-based resonators, contaminations from the integration process result in additional mass loading and possibly increased damping which both have to be minimised. For chemical or electromechanical sensors, residual material from fabrication is suspected to affect sensor stability.

## (ii) Pre-growth metallisation

In the pre-growth approach, a catalysed chemical vapour deposition (CCVD) process synthesizes the nanotubes on top of the pre-fabricated electrodes. Contaminations arising from post-growth processes and viscous forces during the nanotube integration are avoided. But the contact material must be able to withstand the high temperatures required for growing the nanotubes [22, 34, 40, 71–75] and may not inhibit nanotube growth, as it is the case for gold [76],[77] p.58. The direct integration can result in clean, suspended nanotubes FETs compatible with investigations by transmission electron microscopy (TEM) [78].

However, the synthesis of CNTs not only requires high temperatures (typically 700 to 950 °C) but also a hydrogen-containing atmosphere. Only few conductive thin-film materials can endure these conditions. This limits the choice of contact materials. The presence of  $\text{H}_2$  in the CVD process can lead to the formation of metal hydrides, prohibiting the use of palladium as it substantially swells upon  $\text{H}_2$  uptake [79]. Ti is removed [77] p.58 and Ta, Y, and Nb form hydrides.

Instead of direct growth of the nanotubes on the electrodes, assembly methods based on spin-coating or dielectrophoresis have given proof to be large-scale



**Figure 1.1:** Surface-bound nanotube transistors as piezoresistive strain gauges for membrane-based pressure sensing [85]. (a) Optical microscopy image of electrodes patterned by lithography and lift-off. (b) Scanning electron microscopy (SEM) image of a nanotube bridging across the electrodes after dielectrophoretic integration from solution. (c) Atomic force microscopy (AFM) height trace perpendicularly to the nanotube. (d) Nanotube transistor response. The current driven through the nanotube is modulated by the gate voltage  $V_g$ . As hysteresis occurs between forward and backward sweep directions of  $V_g$ , the magnitude of the source-drain current  $I_{ds}$  depends on the history of  $V_g$ . Small scan ranges around 0 V can reduce hysteresis, but the optimum readout location for strain measurements may be missed. The source-drain bias  $V_{ds}$  was 50 mV. Adapted and reproduced with permission from [85]. © American Institute of Physics, 2011.

compatible and to work at low temperatures [80, 81]. However, surfactants are needed and even a small amount of ultrasonication [82] required for dispersing might cause structural defects in the CNTs. To improve the mechanical and the electrical contact, annealing or electroless plating of a second metal [83] can be required. In addition, for suspended device configurations, drying is delicate and often large bundles are obtained rather than individual nanotubes [84].

Surfactants  
Sonication

### Effect of gate hysteresis on sensor readout

Figure 1.1 shows a membrane-based [26] pressure sensor [85]. The deflection of the membrane strains the nanotube integrated as a transistor channel. The current through the nanotube is taken as sensor signal. The readout has to consider that the current magnitude not only depends on pressure-induced strain but is also substantially affected by the history of the applied gate voltage. Gate hysteresis can hinder reliable sensor readout. Gate hysteresis of the order of several Volts (25% of full gate sweep range) is commonly observed for nanotubes on oxides [77, 86]. When operated in ambient conditions, FET devices fabricated by either the post- or the pre-growth approach typically exhibit gate hysteresis [28, 34, 54, 85] which makes device behaviour less reproducible and less time-stable for both sensors and electronics.

Hysteresis

Hysteresis is a „significant and persistent challenge“ in nanotube transistors [87]. Despite high-quality  $\text{SiO}_2$  surfaces, free of significant contamination and trapped charges at both interface and bulk defects [87], hysteresis occurs – at least for a large fraction of the devices [32]. Polar water molecules in the vicinity of the

nanotube can act as charge traps by alignment with the gate-induced electric field [28], [88] p.75.

**Passivation** Passivation by polymers [28, 29], methylsiloxane [87],  $\text{Al}_2\text{O}_3$  [89] or hydrophobic surface treatment [90] can reduce hysteresis. Organic contaminations, such as residues from resist-based lithography, appear to hamper the suppression of hysteresis by passivation [29].

**Device Function** For strain sensors in the large-strain regime, passivation layers need to be sufficiently elastic. For gas sensors, which require a direct access to the environment and for vibrating resonators, passivation layers must not cover the entire nanotube. Patterning of windows into the passivation layer is required and this post-growth processing is another possible source of contamination.

### Characterisation

**Chirality Assignment**

Detailed investigations of the device configuration are of fundamental interest for the design and evaluation of future nanotube-based nano-electromechanical devices, such as piezoresistive sensors and resonators. The atomic structure of SWNTs is uniquely determined by the chirality, which defines whether they are metallic or semiconducting (Appendix B.1.1). For physical or chemical sensors based on SWNTs, the chirality is expected to strongly influence the sensor response [23, 38, 91]. Experimentally, correlating chirality with sensor sensitivity is difficult to achieve within functional devices.

**Raman Spectroscopy**

In Raman spectroscopy (Appendix B.2.5), surface-bound nanotubes exhibit weak signals. For suspended nanotubes, the peaks of the radial breathing mode (RBM) are more intense [36]. Chirality assignment, however, is often ambiguous [92, 93]. In case of devices with many nanotubes, the signal can often not be attributed unambiguously to one of the nanotubes due to optically limited spatial resolution.

**TEM**

Transmission electron microscopy (Appendix B.2.1) offers high-resolution images which allow nanotube diameters to be measured. The number of nanotubes within a slim bundle can be determined and it is possible to discriminate between single, double and multi-walled carbon nanotubes. Observation of the contacts, however, can only be achieved if the contacted FET channel itself can be accessed by the transmission beam.

**Electron Diffraction**

Transmission electron diffraction [6, 94–98] is one of the most reliable chirality assignment methods. However, as it is based on TEM, it requires electron-transparent samples, which is often difficult to achieve. In atomic force microscopy, scanning electron microscopy, and micro-Raman spectroscopy, the sample surfaces are scanned and no special sample preparation is needed for CNTs. In contrast, as stated by Wong *et al.* TEM is the „most accurate method for measuring the diameter“ but it requires „somewhat complex sample preparation or processing“ [99].

**In situ Strain**

Micro-electromechanical systems offer small sample sizes and low-cost fabrication of actuation on the nano-metre scale [100]. Owing to their small feature sizes on the micron-scale, they are a versatile tool to impose mechanical stim-



uli to nano-scale objects. Integration of carbon nanotubes into micro-actuator-driven tensile stages enables in situ observations by TEM [2, 65]. Electrical measurements on clean, suspended carbon nanotubes accessible by TEM but without MEMS actuators have been demonstrated [78].

### 1.3 Objectives of this Thesis

This thesis focuses on the integration of suspended single-walled carbon nanotubes into electromechanical systems using clean process flows and enabling device characterisation by TEM. With the vision of employing carbon nanotubes in low-power sensors and in novel strain-based device concepts, fabrication methods for integration of suspended single-walled carbon nanotubes are developed and evaluated. Methods are sought to fabricate clean nanotube devices unperturbed by mechanical, chemical, and electrostatic disorder on the nano-scale. The integration approaches shall minimise geometrical disorder, originating from interaction with the substrate, by suspending the nanotube. Chemical disorder, arising from imperfections concerning contamination present in standard microfabrication processes, shall be minimised by banning resist-based lithography and wet chemistry after nanotube growth. Furthermore, oxides should be avoided to eliminate hysteresis in carbon nanotube field-effect transistors.

Structural characterisation of the individual macromolecule being the functional part of an electronic building block is to be achieved. Therefore, device designs are implemented which enable investigations based on transmission electron microscopy, including tensile loading inside the microscope. Electron diffraction is to be used in-house to assign the chirality of functional nanotube devices – paving the way for both device evaluation and verification of theoretical models.

#### Design of experiment

Evaluation of nanotube-based transducers for sensor applications is hindered by the lack of fabrication process for clean integration of individual, suspended SWNTs into small-sized test benches providing electrical interfaces and compatibility with TEM characterisation.

The design of experiment requests a suspended, individual, single-walled carbon nanotube strained by a microfabricated tensile actuator providing accessibility to TEM characterisation to measure electromechanical transistor response of chirality-assigned nanotubes.

The hypothesis is that cleaner fabrication processes for suspended electromechanical nanotube devices will enable more stable electron transport measurements, especially concerning suppression of gate hysteresis.

Table 1.1 lists the different samples and highlights the examined intermediate achievements.

The first set of samples demonstrate TEM imaging (Section 4.2) and chirality assignment (Section 4.1) by transmission electron diffraction for nanotubes integrated in microfabricated structures – for a sample with tensile actuator (sample #ed1), for improved accessibility by the transmission beam (#ed2), and combined

Objectives  
Suspended  
SWNTs  
Strain  
Clean  
Fabrication  
Suspended  
FET  
TEM  
Chirality  
Assignment

Challenge  
Micro  
Actuators &  
Chirality  
Assignment

Hypothesis

Samples

TEM

with diameter deduction by Raman spectroscopy (#ed3).

Hysteresis-free  
FET

A second set of samples (Section 4.5) demonstrates the resist-free electrical contact formation to suspended SWNTs for the demonstration of hysteresis-free field-effect transistors with needle-shaped contacts fabricated by shadow masking (#s1), including short channels (#s2), decreased gate distance (#s3), and sequentially modified contacts (#s4).

Orientation  
Control

A third set of samples shows room temperature integration of SWNTs by transfer (#t1). Transfer enables improved orientation control beneficial for reduced gate distances (#t2). Threshold voltage stability was monitored (#t4).

Encapsulation

A fourth set of samples targets zero-level encapsulation by atomic-layer-deposited Al<sub>2</sub>O<sub>3</sub> (#s5a: low deposition temperature of 150 °C and non-selective deposition causing hysteresis; #t3a, #t7a, and #t8a: 300 °C with surface-selective deposition enabling nearly hysteresis-free operation; #t9 indicating the influence of annealing at 300 °C without Al<sub>2</sub>O<sub>3</sub> deposition).

Mechanical  
Straining

A fifth set of samples allows investigation of mechanical clamping conditions using Raman spectroscopy of tensile-loaded nanotubes directly grown on SiO<sub>2</sub> (#m1, #m2) and using TEM of strained nanotubes which were metal-clamped by shadow masking (#m3s, #m4s).

Electro-  
Mechanical  
Response

A sixth set of samples is enabling electromechanical measurements of transistor operation under mechanical tensile strain for nanotubes placed onto Pd electrodes (#t11m), with additional encapsulation (#t12am), and with improved clamping by sandwiching the transferred nanotube by additional metal evaporation patterned by shadow masking (#t14sm).

## 1.4 Contents of the Chapters

Chapter 2

*State-of-the-art fabrication methods* for the integration of carbon nanotubes are reviewed in Chapter 2.

Chapter 3

The here employed contamination-free *fabrication approaches* are presented in Chapter 3. Stencil masks enable patterning of thin films, while avoiding resists and wet chemistry. The contact material is deposited directly onto suspended carbon nanotubes integrated in micro actuators [2, 101]. Sufficiently precise shadow mask alignment is provided by on-chip sliders. Nano-scale electrical contacts of tapered shapes are self-aligned on the suspended part of the nanotube. Any oxides in the vicinity of the nanotube are covered with metal. The choice of contact material is nearly unrestricted. As another approach, direct transfer [102] enables the placement of a nanotube onto predefined electrodes. The concept of tilted-view access for transmission electron microscopy implemented via etching of notches [103] is described and actuator designs are discussed.

Chapter 4

The *characterisation* of ultraclean suspended carbon nanotube devices is shown in Chapter 4. For both integration approaches (shadow masking and transfer), electrical transistor characteristics were free of gate hysteresis [101, 102]. Transmission electron microscopy images of the contact geometry were recorded and chirality was assigned to functional devices. The disturbing effects of oxides is

indicated by covering a previously hysteresis-free nanotube transistor by atomic-layer-deposited aluminium oxide [104]. Surface-selective deposition of  $\text{Al}_2\text{O}_3$  [1] enabled contact encapsulation while leaving the nanotube uncoated and maintaining the transistor operation nearly hysteresis-free.

Mechanical loading of the integrated CNTs by microfabricated actuators is presented in Chapter 5. The Raman frequency downshift of a chirality-assigned nanotube is shown. Electromechanical responses of ultraclean, chirality-assigned CNFETs is demonstrated.

Chapter 5

A summary of the *conclusions* and an *outlook* can be found in Chapter 6.

Chapter 6

*Safety* considerations, fabrication *run sheets*, and experimental details of *electron diffraction* are outlined in Appendix A.

Appendix A

The *theory* about carbon nanotubes and the basic principles of *characterisation techniques* are presented in Appendix B.

Appendix B

Attempts *towards chirality control* for carbon nanomaterials are commented in Appendix C. Raman measurements on atomically-precise, chirality-pure graphene nanoribbons are presented which confirmed the quality of the material produced by J. Cai *et al.* [105]. Transfer of the ribbons was demonstrated from the conductive synthesis substrate onto a non-conductive substrate suitable for potential device integration. For B. Burg [82, 85, 106], raw material for enriched deposition of metallic-type nanotubes was provided.

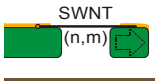
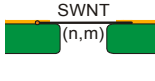
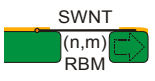
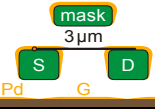
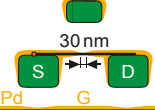
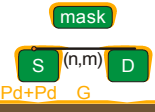



Appendix C

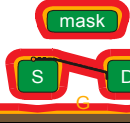



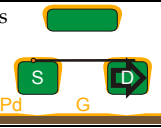
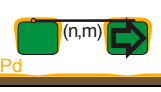
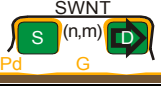


Lists of symbols and abbreviations are given in Appendix D.

Appendix D

## 1 Introduction

**Table 1.1:** Overview of samples. The design of experiment aims at TEM-characterised carbon nanotube field-effect transistors acting as strain transducers in micro-actuator-driven tensile stages. First, TEM-characterisation is demonstrated (Devices #ed1 to #ed3). Then, hysteresis-free transistor operation is demonstrated for devices fabricated by shadow mask evaporation (#s1 to #s4) and by direct transfer (#t1, #t2, #t4). Passivation is tackled by encapsulation using ALD alumina (#s5a, #t3, #t8, #t7). Tensile loading of nanotubes with micro actuators is evaluated using Raman spectroscopy (#m1, #m2) and in situ TEM imaging (#m3s, #m4s). Electromechanical transistor responses are investigated for as-transferred (#11m), encapsulated (#t12am) and for additionally metal-clamped (#t14sm) suspended carbon nanotube FETs.

Sample ID	Sketch	Aim	Fabrication Additional treatment	Channel length Gate geometry Gate distance Subthres. swing	System resistance On/Off ratio Threshold voltage No. of nanotubes	Chirality Actuation Hysteresis Reference
#ed1		<b>Chirality assignment to nanotube integrated into MEMS actuator</b>	Shadow mask, Cr/Au	- - - -	- - - 1 at tip + others	(17,17) el. not connected - Fig. 4.1a, Fig. 4.2
#ed2		<b>Chirality assignment at increased accessible tilt</b>	Shadow mask, Cr/Au	- - - -	- - - 1 at tip + others	(24,6) not available - Fig. 4.4
#ed3		<b>Chirality assignment and Raman</b>	RBM: 163.3 rel. cm <sup>-1</sup> Shadow mask, Cr/Au	- - - -	- - - 1 at tip + others	(14,7) el. not connected - Fig. 4.6, 3.18a
#s1		<b>FET operation hysteresis-free</b>	Shadow mask, Pd	3 µm nano-tapered S,D 3 µm 230 mV/dec	330 kΩ ~10 <sup>4</sup> 0.64 V 1	n.a. no actuator 0.008±0.005 V Fig. 4.10
#s2		<b>FET operation short channel</b>	Shadow mask, Pd	30 nm nano-tapered S,D 3 µm ~4900 mV/dec	89 kΩ 190 17 V 1	n.a. no actuator -0.039±0.188V Fig. 4.10
#s4		<b>chirality assigned FET sequential modification of contacts</b>	Shadow mask, Pd second evaporation	2.4 µm (→ 1.3 µm) nano-tapered S,D 3.6 µm 340 mV/dec	2.75 MΩ ~10 <sup>4</sup> 0.83 V 1, (2 at ends)	(28,11) no actuator -0.015±0.017 V Fig. 4.13
#t1		<b>FET operation room temperature integration hysteresis-free testing SEM contamination</b>	Fork transfer, Pd	2.6 µm blunt electrodes 5.5 µm 2200 mV/dec	1.7 MΩ ~10 <sup>3</sup> 11.2 V 1	(25,18) irreproducible 0.037±0.075 Fig. 4.16-19
#t2		<b>FET operation reduced gate distance</b>	Fork transfer, Pd	2.6 µm blunt electrodes 3.5 µm ~1600 mV/dec	640 kΩ ~8 1.3 V n.a.	n.a. irreproducible -0.007±0.081 V Fig. 4.19
#t4		<b>FET operation V<sub>th</sub> stability</b>	Fork transfer, Pd	3.1 µm blunt electrodes 3.5 µm 300 mV/dec	2.8 MΩ >10 <sup>4</sup> 0.37 V 1 SWNT	(35,9) no actuator 0.001±0.028 V Fig. 4.22

#s5		FET operation <b>ALD 150 °C</b> $V_{th}$ stability Hysteresis induction	Shadow mask, Pd encapsulation: 40 nm ALD $Al_2O_3$	3.2 $\mu m$ nano-tapered S,D ~3 $\mu m$ (inclined) 110 mV/dec	437 k $\Omega$ >3·10 <sup>4</sup> 0.16 V 1	- (ALD covered) no actuator -2±5 mV → >5 V Fig. 4.26
#t3		FET <b>ALD passivation</b> 300°C minute hysteresis	Fork transfer, Pd encapsulation: 40 nm ALD $Al_2O_3$	>2.7 $\mu m$ blunt electrodes 2.25 $\mu m$ ~12V/dec → ~1V/dec with ALD	2.6 M $\Omega$ → 120 k $\Omega$ (65 k $\Omega$ *) ~1.3 → ~3 (~6*) ~4 V; *n-branch n.a.	n.a. actuator, CNT lost 18±23 mV* w ALD Fig. 4.24a
#t8	same type as #t3	FET <b>ALD passivation</b>	Fork transfer, Pd 40 nm ALD $Al_2O_3$	>2.7 $\mu m$ blunt electrodes 2.25 $\mu m$ ~2400 mV/dec	440 k $\Omega$ w ALD >4 -2.7 V*; *n-branch n.a.	n.a. actuator, CNT lost 28±28 mV* w ALD Fig. 4.24b
#t7	similar type as #t3	<b>ALD passivation</b> demonstrating selectivity	Fork transfer, Pd 40 nm ALD $Al_2O_3$	2.6 $\mu m$ blunt electrodes 4.25 $\mu m$ 3500 mV/dec w/o	2.8 M $\Omega$ before ALD 10 ~2.4 V w/o ALD 1 CNT in SEM	n.a. actuator, CNT lost n.a. Fig. 4.25
#t9		<b>heating as in ALD</b>	Fork transfer, Pd	(>2.4 $\mu m$ ) nano-tapered 4.25 $\mu m$ ~1000 mV/dec	190 k $\Omega$ → 2.5 M $\Omega$ >20 (SGS) 1.18±0.011 V n.a.	n.a. no actuator 12±14 → -2±13 mV Fig. 4.27
#m1		<b>Raman under axial strain</b>	Direct growth on $SiO_2$	3.2 $\mu m$ G-peak shift rate: - -	mechanical only (13,11) -13.1±1.9 rel./cm/% strain -	- Figs. 5.2-5.4
#m2	same type as #m1	Raman under axial strain	Direct growth on $SiO_2$	3.6 $\mu m$ G-peak shift rate: - -	mechanical only - -15.8±0.6 rel./cm/% strain -	- p. 120
#m3s		<b>TEM in situ straining</b>	Shadow masking, Pd	2.1 $\mu m$ nano-tapered -	mechanical only - -	DWNT ~4% strain, slipping, rotation Fig. 5.5
#m4s		<b>TEM in situ straining</b> <b>strain to failure</b> <b>chirality assignment</b>	Shadow masking, Pd	2.2 $\mu m$ nano-tapered -	mechanical only - -	(24,0) break at ~+3% -
#t11m		<b>Electromechanical response of strained FET</b>	Fork transfer, Pd	~2.1 $\mu m$ blunt electrodes 5.5 $\mu m$ 1600→1300mV/dec	8.7 M $\Omega$ >10 <sup>4</sup> 5.4 → 4.8 V 2 SWNTs, same chir.	(24,20) p = 1 -19±74 mV Fig. 5.7
#t12am		<b>Electromechanical + encapsulation</b>	Fork transfer, Pd encapsulation by ALD	~2.5 $\mu m$ blunt electrodes 5.5 $\mu m$ n.a.	5.2 M $\Omega$ → 1.3 M $\Omega$ >4 (SGS) ~12 V wo ALD n.a.	- (storage test) p = 1 n.a. Fig. 5.8
#t14sm		<b>Electromechanical + improved clamping</b>	Fork transfer, Pd clamped by additional shadow masking	2.9 $\mu m$ blunt electrodes 2.25 $\mu m$ 1400→1100mV/dec	139 k $\Omega$ ~10 ... >3·10 <sup>3</sup> ~0.8 V 2 DWNTs, same chir.	(16,5)@(20,12) p = -1 1±30 mV Fig. 5.9

\* Subthreshold swings and threshold voltages are given for the p-branch unless marked with an asterisk



## 2 State-of-the-art

This chapter starts with the history of carbon and reviews the synthesis methods for carbon nanotubes. The requirements for wiring-up nanotubes are given and state-of-the-art methods for nanotube integration as electrically interfaced devices are highlighted. Approaches are given how to mechanically strain nanotubes. Finally, achievements are emphasised where mechanical and/or electrical stimulation of nanotubes are compatible with the size restrictions and the transparency requirement of transmission electron microscopy.

Content

### 2.0.1 Carbon history

Carbon has been used since early days. Carbon black served as paint. Diamond has ever been a precious gift and has found use as grinding material. Graphite is used in pencils since 1564. The material used was shown to consist of carbon in 1779. Nanotubes were formed during forging for the production of the legendary Damascus steel, based on macro-scale mechanical optimisation [107]. Carbon fibres were produced for light bulb filaments. A patent for a reactor for carbon fibre production was filed in 1889 which is basically very similar to today's chemical vapour deposition systems [99] p.4.

Carbon

With the introduction of the transmission electron microscope at the beginning of the 20<sup>th</sup> century, carbon structures were studied more detailed. In 1952, TEM images were presented showing carbon structures grown from carbon monoxide by decomposition on iron catalysts at 400 to 700 °C [108]. Nowadays, the images can be interpreted as multi-walled carbon nanotubes [99] p.6. Probably independently, worm-like carbon deposits from carbon monoxide at iron spots of the brickwork of furnaces were reported [109]. Obtained from heating n-heptane-saturated nitrogen, hollow carbon filaments were observed and the role of catalysts was discussed in 1958 [110].

TEM

In 1960, poly-crystalline carbon fibres were obtained from arc-discharge, which had an extremely high Young's modulus exceeding 700 GPa. In addition to extraordinary mechanical resistance against deformation, the fibres outperformed steel in terms of tensile strength by a factor of ten [99, 111]. The focus on mechanical properties of carbon initiated a wide exploitation of carbon fibres [99] p.7. Following the quest for low-cost, high-quality carbon fibres, Endo used sandpaper to remove carbon deposits from substrates, in order to reuse the cleaned substrates. Iron particles unintentionally deposited from the grinding paper led to the observation of hollow tubes, even with a single wall [99, 112]. Oberlin and Endo *et al.* also discussed amorphous deposition of carbon on the initially smooth nanotubes.

Carbon Fibres

SWNT Found  
Unintentionally

Fullerenes	In 1985, the discovery of C <sub>60</sub> fullerenes, a molecule made of 60 C atoms arranged in a soccer-ball shape, lead to tremendous interest in small-scale forms of carbon [113]. As published in 1991, Iijima observed multi-walled and double-walled microtubules [114], while investigating the growth mechanisms of fullerenes [99] p.10. Stimulated by the rediscovery of few-layer nanotubes by Iijima, theoretical studies evolved and predicted metallic or semiconducting electrical properties of single-walled nanotubes in dependence of diameter and chiral angle [115, 116]. Coalescence of fullerenes into larger cages at high temperatures was indicated by Chai and Smalley <i>et al.</i> [117]. In 1993, Iijima and Ichihashi as well as Bethune <i>et al.</i> published the observation of single-walled carbon nanotubes [6, 118]. Iijima and Ichihashi, who submitted one month earlier, cited the work by Oberlin and Endo <i>et al.</i> in the context of the role of catalysts. The single-walled carbon nanotubes were found by Iijima on a relatively old sample prepared before his focus turned to SWNTs.
MWNT Rediscovery	
Theory of SWNTs	
FET Suspended Graphene	The exploration of electrical properties of nanotubes as field-effect transistors started in 1998 [119, 120]. The demonstration of devices made of suspended graphene by Novoselov and Geim <i>et al.</i> [121] initiated broad excitement about the quasi-two-dimensional counterpart of quasi-one-dimensional nanotubes.

### 2.1 Carbon nanotube synthesis

Three major production methods are established for nanotube synthesis [122, 123],[77] pp.35. In general, a carbon source and energy is needed, often in conjunction with a catalyst.

#### Arc discharge and laser ablation

Arc Discharge In synthesis of nanotubes by arc discharge [6, 118], an electric voltage is applied across closely-spaced graphitic electrodes and leads to highly-energetic discharges. At temperatures reaching locally 3000 °C, the carbon plasma is attracted by the negative electrode and condensates. Stimulated by metal catalysts, nanotubes can be formed. The yield in nanotubes by weight is typically less than 40%. Subsequent purification is needed to remove fullerenes, amorphous carbon and carbon-coated catalysts [99] p.15.

Laser Ablation In synthesis of nanotubes by laser ablation [124], a laser is pointing on a hot graphitic target and vaporises its surface. The target typically contains metal catalysts for improved yield. The obtained SWNTs have relatively narrow diameter distributions, but occur generally as bundles rather than as individual nanotubes. Hence, solution-based debundling processes are required for fabrication of individual-nanotube devices.

#### Catalysed chemical vapour deposition

Thermal CCVD In synthesis of nanotubes by catalysed chemical vapour deposition (CCVD) [123, 125], a carbon-containing gas is feed into a reactor and is dissociated by catalytically active nanoparticles at high temperatures. Typical carbon source gases are methane, acetylene, ethylene, carbon monoxide or alcohol vapours. Most



often, the catalyst nanoparticles are metals, such as nickel, cobalt, iron, or molybdenum. The catalysts can be introduced into the gas phase as floating catalysts, or can be bound to a substrate. Metallic nanoparticles can oxidise at atmosphere, which renders a catalyst pre-treatment necessary. By heating in  $H_2$ , the oxidised catalysts are reduced into their metallic state. Increased hydrogen content during the growth phase decreases the self-pyrolysis of the carbon feedstock gas and hence can prevent amorphous carbon deposition [126]. The hydrogen/carbon-feedstock ratio is supposed to influence the diameter distribution by over or underfeeding the large or small nanoparticles respectively [127]. Typical growth temperatures of methane-based CCVD are in the range of 800 °C to 1100 °C. Synthesis temperatures for SWNTs can be reduced down to 350 °C by using acetylene [128]. Low growth temperatures tend to result in reduced crystallinity, as measured by relatively large defect-induced Raman D mode intensities [128–130]. Plasma assisted CVD [131, 132] can produce SWNTs at reduced growth temperatures (550 °C [133]). Small amounts of water preserve the activity of catalyst particles as amorphous carbon can be removed during the growth phase [134]. SWNTs longer than 18cm were grown by CCVD from ethanol, water vapour, and  $H_2$  [16].

Temperature

Plasma-Assisted  
Supergrowth

Concerning low defect density and purity with respect to suppression of amorphous carbon deposition, CCVD at high temperatures is considered to be the most suitable synthesis process for electronic grade nanotube material.

Conclusion

2.2 Fabrication of nanotubes device

Manifold approaches were developed to integrate nanotubes into electronic and electromechanical devices. An overview on fabrication methods is given in Table 2.1. The most important requirements and approaches to meet them are reviewed as follows.

For electrically interfaced devices, sufficient control has to be gained over the nanotube location, orientation, straightness, defect-density, length, number, and chirality (bandgap, piezoresistance).

Control

Fabrication of nanotube devices from raw material requires placement of the nanotubes on a suitable substrate. Post-growth assembly techniques include drop-casting, spin-coating, dielectrophoresis, or mechanical manipulation. Nanotubes grown by CCVD can be synthesised directly on the device substrate at the desired location [77, 135]. Rogers *et al.* stated that the electrical properties of nanotubes deposited from solution are typically „much worse than those of CVD tubes“ because of short lengths, structural defects and surfactant residues [88] p.230.

Location

Dielectrophoresis [80] and patterned surface treatment [136] can align the nanotubes during deposition from liquid dispersion. In direct growth by CCVD, the substrate geometry influences nanotube orientation [137, 138]. Nanotube alignment is also influenced by electrical fields [86, 139] and by directed gas flow [140, 141]. Parallel arrays of SWNT were synthesised on crystalline quartz sub-

Orientation

strates (and transferred by polymer stamps) [142]. At high area density, vertically aligned forests are obtained [143].

Quality	The straightness, defect-density, length, diameter and number of walls is depending on the synthesis conditions (gas composition, temperature, pressure, duration, additional stimuli (gas flow, plasma, external fields) and on the catalyst (material and morphology of catalyst and substrate, and their pre-treatment).
Number	For laser ablation and arc discharge, nanotubes are typically obtained as bundles. For CCVD, the number of nanotubes and the bundle-formation is governed by the area density of catalyst nanoparticles and the nanotube nucleation yield per catalyst [144].
Chirality	Strategies for chirality control during synthesis and post-synthesis chirality separation are discussed in Appendix C.
Conclusion	For device fabrication, nanotubes grown by the CCVD method are very interesting concerning purity, scalable synthesis conditions, and options for controlling density and orientation.
Contacts	As discussed in the Introduction 1.2, contacting nanotubes can be achieved by electrodes fabricated either before or after growth.

**Table 2.1:** Integration methods for fabrication of carbon nanotubes as electrically interfaced transducer elements.

Integration method	Advantage	Disadvantage	Cleanliness	Suspended <sup>a</sup>
Resist-based lithography [38, 50–54, 136]	top contacts (clamping)	resist residues	–	+
Spin-coating onto electrodes [119]	resist-free	bottom contacts	–	–
Dielectrophoresis [80–82, 85, 106]	orientation, location	surfactants, sonication	–	–
Manipulation [35, 68, 145–147]	orientation, location	time consumption	–	+
Transfer using mediator [148–150]	orientation	residues	–	–
Direct transfer [15, 151–155]	as-grown, (resist-free)	bottom contacts	++	++
Growth on electrodes [22, 34, 40, 71–74, 156]	as-grown, resist-free	electrode temperature	++	+
Shadow masking [19, 157–159]	as-grown, resist-free	alignment	++	+

<sup>a</sup> ease of obtaining individual, long SWNTs in suspended configurations

**(i) Post-growth metallisation: Nanotube integration by release etching**

Electrical contacts to suspended nanotubes were demonstrated by metal lift-off using electron-beam lithography (EBL) followed by a release etch removing the oxide underneath the nanotube [38, 50–54, 70] (Section 1.2).

Poly(methyl methacrylate), so-called PMMA, is used in EBL and is one of the favourite resists as it is comparatively easy to be removed [160]. The co-polymer PMMA/MAA has been used heavily in our group for contact patterning. D. Bischoff showed that PMMA 50K, with short polymer length, is more efficiently removed than the co-polymer [161].

Resist  
Residues

Contact resistance for graphene flakes decreased by an order of magnitude by changing from PMMA/MAA to PMMA 50K. This indicates the impact of contamination. However, fewer residues does not mean no residues [161].

Comment

In suspended graphene devices, annealing by electrical currents is required to clean up polymer residues. Before annealing, the devices were strongly p-doped. After annealing, the mobility increased by a factor larger than 10 and the Dirac neutrality point became clearly observable [162]. The annealing is done in repeated steps which are difficult to tune, time consuming and often cause disintegration of the device [158].

Current-  
induced  
Annealing

Annealing under H<sub>2</sub>-containing atmosphere can remove resist residues [30].

Annealing

In EBL, the contact areas are irradiated by electrons. High doses of electron irradiation at 30 kV on p-type CNFETs were suspected to cause tunnel barriers arising from accumulated charges in the oxide [163]. The noise amplitude at high frequencies increased by an order of magnitude after irradiation which was attributed to increased shot noise due to the induced tunnel barriers [163]. Electron irradiation of the oxide was even observed to switch nanotube transistors inside a TEM [70] p.119.

Electron Doses

Post-growth metallisation using resist-based lithography and release etching is prone to contaminate nanomaterials. Processing and cleaning steps can impair carbon nanomaterials and dielectrics. Annealing under H<sub>2</sub> is incompatible with some contact materials such as Pd which forms hydrides.

Conclusion

**Resist-free integration**

Soldering avoids the contamination issue faced in resist-based processing of carbon materials [164].

Soldering

Ion beam or electron beam induced deposition [66, 68, 146] enabled mask-less contact fabrication. However, material properties of the deposits [165] and deposition resolution [67, 68] are limited.

Beam-induced

Other approaches of lithography-free structuring of contacts are inkjet printing, ink writing, and stamping.

Printing

Blanket metal deposition and subsequent patterned metal removal can avoid direct contact of resists with nanotubes. But the nanotubes are exposed to etchants. Break junctions can provide clean electrode gaps. We demonstrated removal of metal from suspended nanotubes by stress-induced chipping and by melting via Joule heating [1].

Metal  
Removal

Shadow Mask Evaporation	Resist-free contacts were evaporated through shadow masks onto as-grown substrate-bound SWNTs on SiO <sub>2</sub> substrates [157]. The Au contacts did not need any adhesion layer because metal lift-off using solvents was avoided. A device resistance of 36 kΩ was obtained. The resist-free contacted nanotubes appeared to be more robust to Joule heating at high currents [157]. Devices fabricated by shadow mask evaporation showed „slightly higher or comparable performance“ in comparison to devices fabricated by EBL [166]. In 2010, shadow mask evaporation was used to contact graphene in a manner that „eliminates contaminants introduced by lithographical processes“ [158].
Suspended	Off-chip shadow masks were used to contact ultralong suspended nanotubes [167] providing an alignment for the 100-μm-sized pads within ~2 μm [19].
Conclusion	Resist residuals were shown to contribute to hysteresis [29]. Lithography-free patterning techniques avoid resist residuals. However, sub-micron alignment of the pattern is typically a challenge. Beam-induced deposition offers improved alignment, but suffers from pattern spread and poor material purity.
<b>Nanotube integration by manipulation</b>	
AFM Manipulation	MWNTs were placed onto electrodes by manipulation using the tip of an atomic force microscope (AFM) [35]. Electron-beam-induced carbonaceous deposition of residual gases [145], or ion or electron-beam-induced deposition of precursor gases [68, 146], can facilitate the manipulation of MWNTs under SEM observation. Individual suspended SWNTs were picked and placed using two scanning tunnelling microscopy (STM) probe tips [147].
SEM	
Conclusion	Manipulation under electron beam observation induces contaminations due to cracking of residual gases.
Transfer via Peeling	Using a PMMA thin film as a mediator, Raman-characterised SWNTs were transferred onto electrodes [148] and suspended graphene gates were aligned to CNFETs [150]. Oriented nanotube arrays grown on quartz were transferred by a gold coating and thermal tape onto a substrate with buried gates [149]. The Au served as separation layer [57, 58] to allow plasma cleaning of the tape residues by plasma without harming the nanotubes. The Au was wet-etched afterwards.
Direct Transfer	Nanotubes can be directly transferred from one to another substrate [15, 151–155]. The ends of ultralong suspended nanotubes on the growth substrate were rendered optically visible using Au evaporation through shadow masks. This enabled the direct transfer of chirality-assigned nanotubes onto thin-film electrodes on a planar substrate. Resist served as a temporary fixation [151]. Nanotubes grown across a mm-scale slit of a Si frame were directly transferred onto a gold-coated polyester sheet, suitable for strain sensors [155].
Dielectrophoresis	Manipulation of dispersed nanotubes by dielectrophoresis can place nanotube onto the target location in a parallel manner [85, 168, 169].
Conclusion	Except of direct transfer, solution-based manipulation or adhesion-layer-based transfer methods are prone to result in residual surfactants or contamination. Subsequent annealing can cause device failure.
Comment	The nanotubes available in our group are relatively short (<20 μm), which is

beneficial for integration into microsystems but prevents integration by macro-scale transfer and hinders gas flow alignment [141].

### (ii) Pre-growth patterning: Nanotube integration by direct growth on conductive electrodes

Direct growth of nanotubes on conductive electrodes establishes contacts to as-grown nanotubes and avoids mechanical damage during release etching. Direct Growth

Franklin *et al.* integrated nanotubes bridging between a molybdenum-coated poly-Si cantilever and a stationary electrode by direct growth using alumina-supported catalysts on top of Mo [22]. Mo

Cao *et al.* and others grew nanotubes from alumina-supported catalysts on top of Pt while ensuring diffusion-resistant substrates [34, 40, 71, 73, 75]. Pt

Despite the swelling of Pd during uptake of H<sub>2</sub> released from decomposition of the hydrocarbon feedstock gas during growth by CCVD, Kasumov *et al.* demonstrated Ta/Pd contacts by starting the growth on patterned alumina islands [156]. However, they reported that the metallisation „became very fragile and the sample degraded quickly“ [156]. Ta/Pd

Using conductive TiN, Karp *et al.* contacted SWNTs growing from patterned SiO<sub>2</sub> islands [72]. TiN

Multi-walled CNTs were grown across micromachined Si electrodes [74] but showed a large resistance of 54 MΩ. Si

Patterning of electrodes before CCVD growth avoids contamination issues, but the choice of electrode materials becomes severely restricted due to the harsh growth conditions. Conclusion

## 2.3 Carbon nanotube electronic devices

Dense vertically aligned nanotube forests are appealing for electrical interconnects and vias [143]. Owing to the large surface to volume ratio, nanotube-based electrode materials are employed to store electrical charges in supercapacitors [170]. The nanoscale radius of the ends of vertically standing nanotubes in combination with high aspect ratio was shown to be suitable for electron ejection by field emission [171]. As demonstrated by an atomic-resolution mass sensor based on a vibrating nanotube, field emission current can be used as readout signal for vibrational motion [172]. Again owing to the exceptional geometry, nanotubes were demonstrated to be useful for sharp tips in scanning probe microscopy [173]. Interconnects  
Capacitor  
Field-Emitter  
Scanning Probes

From carbon nanotubes, p-n junctions diodes were fabricated by chemical doping via covering one of the contacts [174]. Alternatively, electrostatic gating induced p-n junctions in suspended SWNTs fabricated by transfer [15]. Schottky barrier diodes were fabricated by crossing a semiconducting and a metallic nanotube [175]. Diode behaviour was observed for Schottky barriers within a single nanotube. Due to structural defects one segment of a nanotube was semiconducting and the other metallic which lead to strong rectification [176]. Rectifier

Electromechanical switches consisting of nanotubes grown across a 0.25-μm- Switch

narrow and shallow trench were demonstrated by using resist-based lithography [64]. Nanotube switches were also demonstrated by assembly via dielectrophoresis while additional resist layers served as sacrificial layers [177]. Horizontal forests of nanotubes directly grown at the sidewalls of Si beams served as wear-resistant contact material in micromechanical switches [178].

**Resonator** Doubly-clamped nanotube resonators were demonstrated to act as mass sensors [41]. Capacitive frequency-tuning of double-clamped SWNTs [38] was demonstrated for resonators fabricated by a transfer process [39] and by direct growth on Pt [40]. High quality factors  $Q > 10^4$  were obtained for frequencies as high as 39 GHz [40].

**High Q**

### 2.3.1 Carbon nanotube field-effect transistors

**Basic Principle** A transistor is an electronic building block whose conductance can be modulated by a gate voltage  $V_g$ . The voltage  $V_{ds}$  applied from the source electrode across the transistor channel to the drain electrode leads to a current  $I_{ds}$ . Depending on the gate voltage,  $I_{ds}$  can be turned on or off. An ideal device would have zero resistance in the on-state and infinite resistance in the off-state. Ideally, no current is flowing from the gate to the drain/source. Undesired gate leakage current  $I_g$  can be observed for non-ideal gate separation layers.

**FET History** The field-effect transistor was patented by Lilienfeld in 1925 and started its commercial break-through in 1960, after  $\text{SiO}_2$ -passivation of the silicon semiconductor surface was introduced [99] p.191. The electronic circuits enabled by miniaturised FETs have a tremendous impact on science and on daily life (computing, communication, automation).

**MOSFET** Latest metal-oxide-semiconductor FETs (MOSFETs) of the 22 nm generation [179] are featuring 8-nm-wide channel fins of 34 nm in height fabricated using 193 nm immersion lithography. The effective oxide thickness is 0.9 nm. The gate is covering three sides of the fin (tri-gate) enabling subthreshold slopes of  $\sim 70 \text{ mV/dec}$ . An  $I_{ON}/I_{OFF}$  ratio larger than  $10^5$  was obtained. Where needed, multiple fins are used per transistor in parallel to increase drive strength.

**Scaling** Motivated by the undesirable scaling phenomena faced at very small dimensions [180], work is undertaken to explore the use of carbon nanotubes as alternative channel material [8, 9, 119, 120].

**Array** Arrays of CNFETs fabricated on the same ultralong SWNT showed uniform electrical characteristics along the whole nanotube length [16]. An  $I_{ds}$  current on/off ratio of  $10^6$  was obtained [16].

**Contact Shape** Electrical contacts to carbon nanomaterials are typically made of metal processed by microfabrication. While traditional contacts are planar, contacts to nanotubes can have different geometries. Foremost, the contact area is small. Bottom contacts are created by deposition of a nanotube onto electrodes [119]. Top contacts are formed by deposition of the contact material onto the nanotube. Combination of bottom and top contacts is possible. Unusual end-bonded contacts can form at high temperatures resulting in SiC, or TiC [47].

A CNFET with a channel as short as 15 nm was operated at room temperat-

ure ( $I_{ON}/I_{OFF} > 10^5$ , conductance  $0.7 G_0$ ) while short-channel effects were absent [149]. Sub-10 nm channel lengths were demonstrated [181].

Thin and wide Schottky contacts for increased sensitivity of SWNT-network FETs were fabricated by evaporating metal contacts using a shadow mask at tilted angle evaporation [182].

The geometry of the source and drain contacts can significantly influence the gate coupling. Needle-like contacts were identified to reduce the shielding of the gate potential [183]. Clean suspended CNFETs with bottom gates were fabricated by direct growth on Pt [71, 73, 184].

Gate  
Geometry

Subthreshold swings of  $\sim 60$  mV/decade were achieved using few-nanometre-thin gate dielectrics [180, 185].

Subthreshold  
Slope

Pure p- or n-type CNFETs were demonstrated by chemical doping, or by electrostatic doping using dual-gate structures [180].

Polarity

Ohmic contacts to nanotubes were achieved by pure Au contacts or by annealing Cr/Au contacts at  $600^\circ\text{C}$  in Ar, which indicates that Au diffuses through the Cr used as adhesion layer. Pd contacts can also yield ohmic contacts [9, 10]. The absence of a Schottky barrier is indicated by increased conductance at lower temperatures [9].

Contact  
Material

Investigated by TEM imaging, Au and Pt deposited by evaporation showed relatively weak interaction with suspended SWNTs, while Ti, Pd and Rh showed good wetting resulting in continuous metal coatings [186]. Ti wets better than Pd and results in less deformation of the nanotube [187]. Adhesion layers of Ti improved the uniformity of Au deposits. These observations along with electrical measurements indicating more ohmic contacts for Pd and Rh than for Au or Pt suggest that the wettability is an crucial factor in addition to the metal work function [88] p. 69.

Wettability

Cr/Au contacts degraded over time if exposed to ambient conditions. Long-term stability was achieved by an  $\text{Al}_2\text{O}_3$  passivation layer [89]. Unpassivated Pd contacts exposed to ambient conditions were stable over months [188].

Contact  
Degradation

SWNTs show excellent transport of charge carriers. Their surface is atomically smooth which is assumed to suppress surface roughness scattering. Carrier mean free paths are of several hundreds of nanometres under low  $V_{ds}$  bias were extracted [88] p.115. High field-effect mobilities exceeding  $70\,000\text{ cm}^2/\text{Vs}$  at room temperature were observed for long CNFETs [8].

Mobility

High saturation currents of  $\sim 25\text{ }\mu\text{A}$  per SWNT were demonstrated [189]. The contact resistance was shown to depend on contact length. For 20-nm-short contacts, on-currents reached  $10\text{ }\mu\text{A}$  [149].

Saturation  
Current

In contrast to the semiconducting nanotubes, graphene lacks a bandgap and cannot directly be used as transistor material. Bilayer graphene or nanoribbons can open up bandgaps [17, 190]. Synthesis of 40-nm-wide ribbons defined in orientation and width by facets of a SiC substrate enabled the fabrication of 10 000 graphene transistors, but with a poor on/off ratio of 10 [191].

Graphene

Carbon nanotube FETs were shown to be competitive to MOSFETs with re-

Benchmarking  
MOSFET

gard to  $I_{ON}/I_{OFF}$  ratio while short-channel effects were absent [149]. Low sub-threshold swings of  $\sim 60$  mV/decade [180, 185] were achieved. Sub-10 nm CNFETs were demonstrated to outplay Si devices concerning normalised current density [181].

**Conclusion** Carbon nanotubes are superior material for FETs compared to graphene concerning performance in on-off ratio. The high field-effect mobilities obtained in CNFETs, the tiny dimensions and the high current carrying capabilities promise to outperform Si-based MOSFETs, but the technological maturity in integration precision and scalability of MOSFETs is currently far beyond what has been demonstrated for carbon nanomaterials.

### 2.3.2 Gate hysteresis in CNFETs

**Hysteresis** Gate hysteresis is an often observed non-ideal behaviour of CNFETs: A gate sweep from negative to positive gate voltages typically results in a different source-drain current response than a gate sweep the in opposite direction. The hysteresis width is the difference between the threshold voltages (see Section B.1.5) observed for the forward and the backward sweep ( $V_{th,forward} - V_{th,backward}$ ). The hysteresis depends on gate sweep range and on sweep rate [192] as well as on the source-drain bias  $V_{ds}$  [193].

**Origins of Hysteresis** Gate hysteresis can be caused by charges trapped at defects on the surface [28, 87, 193] close to the nanotube, and at defects in the bulk or at buried oxide-interfaces [32]. Water-adsorption on hydroxyl groups of oxide surfaces and on the nanotube are considered as a major source of hysteresis [28, 90]. Mobile ions were identified to contribute to hysteresis [194].

### Hysteresis Reduction

**Water** Prolonged storage under vacuum reduced the gate hysteresis in unpassivated CNFET on  $SiO_2$  [28]. Heating to 200 °C under dry conditions in order to desorb water diminished hysteresis.

**Suspended** For suspended nanotubes, the hysteresis present at ambient air diminished completely under vacuum conditions [28, 34]. Gate hysteresis is in general reduced in suspended nanotube FETs compared to surface-bound configurations [33].

**Conclusion** Direct suppression of hysteresis was achieved for suspended nanotubes but only under dry or vacuum conditions.

**Passivation** Encapsulation of the nanotube by a passivation layer can reduce hysteresis [28, 29, 87, 89, 193]. Application of a self-assembled-monolayer from liquid phase was observed to barely reduce the hysteresis while application of the same passivation material from gas-phase under vacuum conditions at elevated temperatures reduced hysteresis significantly [193].

**Surface Cleanliness** Tackling the reduction of hysteresis by passivation layers, Shimauchi *et al.* [29] confirmed that CNFETs on  $SiO_2$  substrates exhibit reduced hysteresis after baking in vacuum (from  $\sim 4$  V down to 2 V). If contact patterning by photoresist was omitted by using the catalyst areas themselves as electrodes, the hysteresis was reduced more pronouncedly (from  $\sim 4$  V down to approximately 0.5 V). Passiva-



tion of non-clean devices did not reduce hysteresis. Only if the passivation was applied after cleaning with piranha solution ( $\text{H}_2\text{SO}_4:\text{H}_2\text{O}_2$  4:1) hysteresis was reduced (from 6–10 V down to 0–6 V).

Passivation of surface-bound nanotubes can reduce hysteresis if the encapsulation material is sufficiently resistant against charge trapping/injection and if the material is applied on dry [193] and resist-free [29] surfaces. These results indicate that contamination induced during contact fabrication can increase hysteresis and corrupt hysteresis reduction measures such as passivation and vacuum annealing.

Conclusion

Careful treatment of the oxide during catalyst pre-treatment (annealing under argon) and encapsulation by methylsiloxane substantially reduced hysteresis by eliminating bulk and interface charge traps [87]. However, hysteresis occurred at high  $V_g$  [87], possibly due to charge injection at high fields. Annealing of atomic-layer-deposited oxides can reduce hysteresis [57].

Oxide Quality

Multi-layer gate dielectrics with interfaces close to the nanotube channel induce hysteresis – beneficial for memory application [32]. On the other hand, for short CNFETs on low-defect oxides, a fraction of the devices did not show hysteresis [32].

Interfaces

The oxide quality has substantial influence on hysteresis. Even on high-quality oxides, hysteresis on the order of Volts is observed for most of the devices.

Conclusion

Gating by polymer electrolytes suppressed hysteresis. Gating by electrolytes improves gate efficiency and reduces the required gate sweep range [195].

Electrolytes

Short pulsed gate measurements [196–198] reduce hysteresis and are especially effective if pulses of alternating sign are applied.

Pulsed  
Measurements

Pulsed gate measurements can reduce the hysteresis which otherwise corrupts sensor readout. However, gate voltage pulses are increasing the power consumption and require more complex readout implementation than static bias.

Conclusion

### Suspended Nanotubes

Suspended nanotubes show reduced hysteresis [28, 33]. In addition, they are not suffering from deformations induced by the substrate. Deformation of surface-bound SWNTs was predicted and indicated experimentally [199]. The strains resulting from surface features were suspected to be responsible for irregularities in electronic transport experiments [199].

Suspended vs.  
Non-  
Suspended

Suspending the nanotube by removing the underlaying substrate enables comparison of electrical performance before and after release. Suspending was found to lower the on-current and to deteriorate the subthreshold slope of the transistor [36]. The latter was attributed to the reduced gate control as air is a low- $k$  dielectric material. From 130 mV/dec before etching, the subthreshold swing degraded to ~600 mV/dec after the trench was etched.

Suspending the nanotube reduced the  $1/f$  noise amplitude by about one order of magnitude [36], consistent with trends observed in other work [33, 35, 37].

 $1/f$  Noise  
Reduction

Suspended nanotubes exhibit less hysteresis and noise. But as the gate oxide is replaced by air, larger gate voltages are required.

Conclusion

### 2.3.3 Integration of CNTs into macro-scale tensile stages

Piezo Actuator	SWNTs grown across a trench of a Si die were mechanically strained by a 7 mm large piezo actuator and measured by photoluminescence excitation (PLE) [200].
Translation Stages	Ultralong suspended nanotubes were grown across 40 to 200 $\mu\text{m}$ long trenches of a die with breakable connections. The die was mounted on a macro-scale translation stage before cleaving the connections. The nanotubes were tensile loaded and reversible changes in the Raman spectra ruled out slippage [20].
Thermal Expansion	Nanotubes suspended across trenches in a flexible polymer support were strained by a macroscale mechanical tensile stage enabling Raman measurements under strain [201]. Au was evaporated onto the nanotubes for improved clamping and annealing resulted in gold beads useful for displacement measurements. Changes in the band structure of ultralong SWNTs under axial strain were measured by Rayleigh spectroscopy. Ultralong SWNTs were grown across 100- $\mu\text{m}$ -wide slits in a Si die and Au was evaporated through a coarse shadow mask to clamp the nanotubes. The die was glued at both of its ends to a steel plate before being cleaved into two pieces with the help of breakable connections. Subsequently, axial strain was applied by heating the steel plate [167].
Conclusion	Tensile stages for axial loading of nanotubes were demonstrated, but they are too bulky to fit into the specimen chambers of transmission electron microscopes.

### 2.3.4 Integration of CNTs into MEMS-based tensile stages

Tensile Strain	Microelectromechanical systems (MEMS) are a versatile platform for tensile testing of nanostructures [65, 202–208].
SEM and probe	In a combined SEM/AFM system, individual MWNTs were „contamination welded“ onto a tip, manipulated and placed across the gap between an actuated and a stationary MEMS support [145]. An individual MWNT was welded onto a MEMS-based force sensor [209]. Espinosa <i>et al.</i> presented a MEMS-based tensile testing stage for multi-walled carbon nanotubes [65, 204, 205]. MWNTs were attached to a probe needle, cut by a focussed ion beam (FIB) and glued into place using electron-beam induced deposition (EBID) from Pt precursor gas.
Direct Growth	Strain-dependent Raman measurements on as-grown nanotubes bridging to a cantilever were achieved by deflecting the cantilever using an AFM tip [210] or by electrically heated thermomechanical micro actuators [211, 212].
Conclusion	Mechanical straining of CNTs by MEMS devices was demonstrated. However, clamping was often insufficient or contamination was induced during enhancement of the clamping conditions.

## 2.4 Nanotube integration for electromechanical transducers

### 2.4.1 External probes

AFM deflecting CNT	Sensitivity of electrically contacted MWNTs to mechanical deformations was demonstrated by actuation using an AFM probe tip [213].
	AFM tips also strained SWNTs on flat substrates, mechanically clamped by metal [214]. Down shifts in Raman G peak positions were observed.

AFM tips were used to strain suspended nanotubes while measuring the electrical transport properties by Tombler *et al.* [215] and by Minot *et al.* [91]. Tombler *et al.* [215] assumed band gap changes not only to happen because of pure tensile strain, but also due to strong local deformations induced by the tip. Maiti *et al.* suggested that the experimental data can entirely be explained by bandgap modulation induced exclusively by axial-strain [216].

Cao *et al.* used AFM tips to strain nanotubes integrated in microstructures [184]. SWNTs were grown across cantilevers coated with molybdenum enabling electromechanical experiments. Based on slack measured by SEM imaging, the conductance changed right after the nanotubes were fully straightened. Gauge factors of ~600 to ~1000 were extracted [184].

AFM  
deflecting  
Cantilever

Stampfer *et al.* presented high gauge factors for suspended nanotubes strained by cantilever structures actuated by an AFM tip [53].

Actuated by an AFM tip, a SWNT torsional pendulum was demonstrated to act as a transducer by changing its resistance upon torsion [217].

Pressure sensors were fabricated from CNFETs arranged as strain gauges on SiO<sub>2</sub> / Al<sub>2</sub>O<sub>3</sub> membranes [25, 26, 85, 218, 219].

Pressure

An electrical current was driven through an ultralong nanotube suspended across a 100 µm slit and contacted by coarse shadow masking. In an external magnetic field, the induced Lorentz force was used to strain the nanotubes while Rayleigh scattering was recorded. Gold evaporated onto the centre of the nanotube enabled optical detection of the nanotube position based on the displacement-calibrated intensity change of scattered light from a focused laser source [19].

Electromagnetic

Large-sized SWNT forests (500 µm · 500 µm · 4 µm) were manually manipulated and integrated as MEMS strain gauges (gauge factors of 3.75) actuated by a macro-scale four-point bending test [220]. Dense horizontal networks on SWNTs were employed as strain gauges (GF = 8.22 [221] and GF = 59.2 [222]).

Macro-Sized

Arrays of suspended, aligned CNTs showed GF of 248 [223].

Millimetre-long SWNTs were transferred onto a gold-coated polyester sheet and a strain sensitivity of 0.004% was extracted by piezoresistive detection [155].

A two-axis strain sensor was demonstrated for nanotubes grown across Pt electrodes (GF = 744) [224].

Strain sensors were fabricated based on macroscopically-large SWNT films tensile loaded perpendicularly to the orientation of the nanotubes. Fractural structures enabled straining of more than 200% with relatively consistent resistance changes for thousands of cycles [225]. Transparent, polymer supported CNT strain sensors were demonstrated by spray coating [226].

SWNT Films

Fabricated by spinning CNT yarns, strain sensors were demonstrated. The gauge factor of the CNT yarns was 0.5 [227].

Yarn

### 2.4.2 Electrical contacts to CNTs embedded in MEMS actuators

Lithographically patterned metal platelets attached to SWNTs were released by a wet sacrificial layer etch and afterwards electrostatically actuated by Meyer *et al.* [52]. Lee *et al.* integrated SWNTs as CNFETs into MEMS tensile actuators fab-

Post-Growth  
Metallisation

ricated from silicon-on-insulator (SOI) wafers. SiO<sub>2</sub> bridges provided temporary supports for SWNTs during resist-based patterning of metal contacts [42, 43].

Pre-Growth  
Metallisation

SWNTs were grown across TiN electrodes in MEMS structures [72]. Resistance changes of MEMS-embedded CNT were recorded [228]. However gate structures were missing and hence transistor operation was not shown.

SNR

The signal-to-noise ratio of small bandgap semiconducting CNFET piezoresistors is found to be maximal at the gate voltage for which the transistor current is minimal. To obtain highest strain resolution, operation at the device off-state is recommended [229].

Conclusion

Strain gauges with an individual nanotube of favourable chirality can exhibit larger gauge factors than gauges with many nanotubes of random chiralities [230]. Clean integration of SWNTs into complex MEMS devices including gates is a challenge.

### 2.5 Accessibility by TEM

Nanotubes can be characterised by transmission beams before integration into the device [147, 151, 231] or as functional nanotube device [52, 69, 70, 78, 232].

TEM before  
Transfer

Ultralong SWNTs were characterised by transmission electron diffraction and Rayleigh scattering and subsequently transferred [151] onto electrodes for electrical transport measurements [231].

TEM before  
Manipulation

SWNTs were characterised by TEM electron diffraction and subsequently picked up by multiple STM probe tips under SEM observation [147] to be placed onto Pd electrodes on a flat substrate [147]. Hence, electrical characterisation of a chirality-assigned, semiconducting nanotube was achieved, but the source-drain current showed only weak dependence on the gate voltage. Regular Coulomb blockade oscillations were missing in a large gate voltage range. This was suspected to be caused by defects in the nanotube, by substrate roughness or by residues from the fabrication process [147]. Carbonaceous contamination [147, 233] on the nanotube is known to occur during electron beam irradiation in TEM during imaging and electron diffraction as well as during manipulation under SEM observation.

Separate  
Observation  
Window

Ultralong DWNTs were electrically contacted as FETs on the substrate while spanning across a slit farer away enabling chirality assignment by electron diffraction [234].

Holder

Dedicated sample holders enable manipulation of nano-objects by AFM and STM inside a transmission electron microscope [235, 236].

In situ  
Manipulation

TEM-accessible nanotubes deposited by dielectrophoresis and clamped by metal pads were strained using an in situ manipulator [237]. Manipulation inside a TEM and using a mercury electrode enabled resistance measurement of chirality-assigned DWNTs [238].

MEMS inside  
TEM

MEMS-based in situ tensile stages provide high resolution in displacement and force measurements at small system sizes [65, 202–206].

Bundled FETs

Radial deformation in FETs consisting of small bundles was observed using

electron diffraction [232].

FETs compatible with TEM investigations were fabricated by direct growth on Mo electrodes [78].

Clean FET

Trenches in milled by a focused ion beam (FIB) and direct growth was used for imaging the mechanical resonances of doubly-clamped SWNTs. The vibration was excited by an AC electric field applied by an external piezo-positioned electrode [67].

Electrically  
Excited  
Mechanical  
Vibration

As carbon has a low atomic number, even very thin supports vanish nanotube contrast required for high-resolution imaging [84]. Electron beam transparency for nanostructures integrated in MEMS is commonly provided via through holes [204, 239, 240]. Substrate thinning was applied to facilitate wafer through etching [204]. TEM grids were fabricated by etching into the die from both sides. First, a large-area backside etch formed thinned membranes which were then etched fully through from the front side [241].

Transparency  
Through  
Holes

Backside lithography and etching can put constraints on the design of MEMS actuators because the arrangement of anchors is restricted by the size of the through-hole, including a tolerance for possible misalignment.

Comment

A method that avoids wafer through etching is accessing devices close to the edge of the die – enabled by a wet-etch of the substrate after cleaving [52, 69, 70]. Vertical pillars at the edge of the die enabled TEM observation in a direction nearly parallel to the substrate surface [137, 242].

At Edge

Meyer *et al.* achieved electrical measurements and TEM analysis of nanotube devices fabricated close to the die edge and released by etching the substrate to provide TEM-access [52, 70], including side-gated transistors [69] and nanotubes torsionally actuated by platelets [52].

Etching the substrate at its edge exposes the devices to wet chemistry and can cause contamination [69]. While cleaving works fine for large pillar arrays where the exact position of the cleaving edge does not matter, large suspended MEMS actuators could be destroyed during cleaving.

Comment

Transparency can be obtained by sliding large micromachined structures beyond the edge [211]. In addition to design constraints, establishing reliable electrical connections to the actuator after sliding is a challenge.

Beyond Edge  
Comment

### Summary and Comments

Ultralong aligned nanotubes have been successfully integrated into macroscale tensile stages [167] and suspended ultralong nanotubes were electrically contacted [19]. To overcome the size challenge (bulky tensile stage, permanent magnet, piezo) imposed by the limited space available in TEM, MEMS based-tensile stages were employed [65]. Resist-based fabrication provided samples for in situ electromechanical experiments by torsion induced by electrostatically actuated paddles [52]. Unlike for metal deposits acting as substitutional contact models [187], „unfortunately, the nanotube-metal interfaces can not be observed [...] in the present geometry“ [70] p. 119 for functional devices. Contaminations can impede observation [56, 69] and electrical behaviour [29, 199]. Characterisation of

Ultralong

MEMS

Lithography

Characterisation  
Before  
Integration

Lithography-  
free

as-grown nanotubes and subsequent integration into devices has been demonstrated [147, 167], however at the risk of contaminating the device before electrical characterisation. Lithography-free fabrication of TEM compatible transistors was shown [78] but integration of clean *and* electrically interfaced SWNTs into complex MEMS structures compatible with TEM inspection is still a challenge.

# 3 Fabrication: Ultraclean, TEM-compatible CNFETs integrated into MEMS

In this chapter, clean fabrication methods for suspended CNFETs integrated in micro actuators are presented. Standard processes used in microfabrication bear the risk of contaminating carbon nanotubes by traces of residual resist. Usual cleaning procedures cannot be applied, as they attack carbon nanomaterial.

Content  
Challenge

Resist-based lithography for electrical contact definition is excluded to avoid the risk of contamination. As a first fabrication method, on-chip stencil lithography is described. Electrical contacts are formed directly on the suspended end-sections of a suspended nanotube. The subsequent section presents a second approach based on transfer, which maintains the device die at room temperature. Then, the design of micro actuators for tensile loading is described. Afterwards, the so called 'tilted-view' approach is explained, which enables TEM investigations of functional nanotube devices without the need for through holes.

Solutions

Parts of this chapter have been published in Nature Nanotechnology<sup>1</sup> [101] and elsewhere [1, 2, 103, 104].

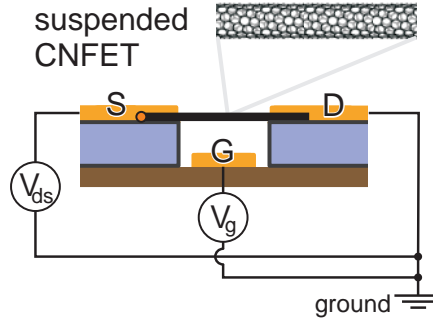
## 3.1 Electrical integration of ultraclean suspended SWNTs

Electrical connections to individual nanotubes are required to enable exploration of sensor concepts. The major focus of the presented integration processes is cleanliness at the nanoscale - hardly achievable if resists are employed for shaping the contacts [29]. The goal is to fabricate a suspended carbon nanotube transistor (CNFET). A SWNT bridges from the source electrode (S) to the drain electrode (D) as sketched in Figure 3.1. The source-drain voltage  $V_{ds}$  induces an electrical current  $I_{ds}$  through the SWNT. The electric field of the bias  $V_g$  applied on the gate electrode (G) modulates  $I_{ds}$ . As this current through the nanotube transistor channel is also influenced by other stimuli such as mechanical deformation or the presence of chemical analytes, the nanotube transistor configuration is a basis for sensor applications.

Objective

Configuration

<sup>1</sup> „Ownership of copyright in original research articles remains with the Authors, and provided that, when reproducing the contribution or extracts from it, the Authors acknowledge first and reference publication in the Journal, the Authors retain the [...] non-exclusive rights [...] to reproduce the contribution in whole or in part in any printed volume (book or thesis) of which they are the author(s) [...] and to reuse figures or tables created by them.“ Available at <http://www.nature.com/reprints/permission-requests.html>, October 5, 2011



**Figure 3.1:** Schematic representation of a suspended carbon nanotube field-effect transistor. The gate voltage  $V_g$  tunes the conductivity of the nanotube acting as channel between source (S) and drain (D).

**1<sup>st</sup> Method: Shadow Masking** The first fabrication approach for clean nanotube transistors is on-chip shadow masking. As described later in more detail, a SWNT is grown from the oxide-coated source electrode across a 3- $\mu\text{m}$ -long gap to the drain electrode. Subsequently, a solid shadow mask is moved at close proximity above the suspended mid-section of the SWNT. The mask patterns the metal contacts deposited by evaporation.

**Advantages** Direct growth followed by shadow masking allows resist-free fabrication of electrical contacts to as-grown CNTs. Contamination is excluded by avoiding resist-based lithography which would involve wet chemistry. Furthermore, shadow masking is compatible with a wide range of contact materials and the ends of the electrodes can be self-aligned to the nanotube.

**2<sup>nd</sup> Method: Transfer** As an alternative approach, SWNTs were grown on a fork structure, from which the nanotubes were transferred onto metal-coated electrodes of another die. The receiving die with metal-coated electrodes is not exposed to the high SWNT growth temperature of 850 °C. Thus, the process flow is in principle compatible with readout-circuitry fabricated by complementary metal oxide semiconductor (CMOS) technology, which would suffer from temperatures higher than 450 °C. Additionally, the assembly approach provides the option to select a certain nanotube to be integrated.

### 3.2 Integration of suspended SWNTs by shadow masking

**Overview** Stencil lithography is a contactless patterning method. It is applied here to deposit electrical contacts onto an as-grown nanotube, avoiding any wet chemistry after growth. Movable on-chip shadow masks outperform conventional off-chip stencil masks [19, 151, 158, 159, 166, 167] concerning alignment accuracy and minimise mask-to-substrate separation.



### 3.2.1 General concept of stencil lithography

Stencil lithography is a method to transfer a pattern defined as openings in a solid mask to the substrate placed underneath. A physical material flux is deposited through the openings of the mask onto the target substrate as depicted in Figure 3.2a. Wherever the mask is not perforated, the solid mask (stencil) blocks the material flux. The mask is separated from the substrate by a physical gap. Thin films can be structured by stencil masking without the need for resist. Manifold physical vapour deposition (PVD) techniques can be applied for shadow masking. They include thermal evaporation, electron beam evaporation, pulsed laser deposition (PLD), molecular beam epitaxy (MBE) and sputtering. In case of sputtering, non-zero gas pressure leads to a partially diffusive material flux. The material flux is less directional and consequently the pattern blurs. Moreover, sputtering includes (argon) plasma which can cause defects in CNTs. Therefore, plasma-free and highly directional e-beam evaporation is employed here. The material is put in a crucible and heated under vacuum by an electron beam. The material evaporates and is deposited through the mask openings onto the sample.

Shadow  
Masking

PVD

Stencil masks have been used for printing techniques since early days. A first demonstration for thin films was reported by S. Gray and P. K. Weimer in 1959 [243]. Wires close to a substrate surface served as stencil.

History

In general, stencil masks can be fabricated using milling, punching, laser cutting, arc erosion, and other methods. Typical stencil masks for microfabrication are made of Si nitride membranes on bulk-etched Si wafers.

Mask  
Fabrication

Stencil masks can not only be used to pattern the deposition of thin-film material. Stencil masks can also pattern ion implantation or dry etching.

Deposition,  
Implantation,  
Etching

A geometric limitation in resolution is inherent to stencil lithography. As illustrated in Figure 3.2b, geometric blurring of the deposited material arises as the material flux is not perfectly parallel. The flux is not fully directional because of the finite source-mask distance ( $h$ ) and owing to the broadness of the material source ( $s$ ). The extent of blur depends on the mask-to-substrate distance ( $g$ ).

Geometric  
Blur

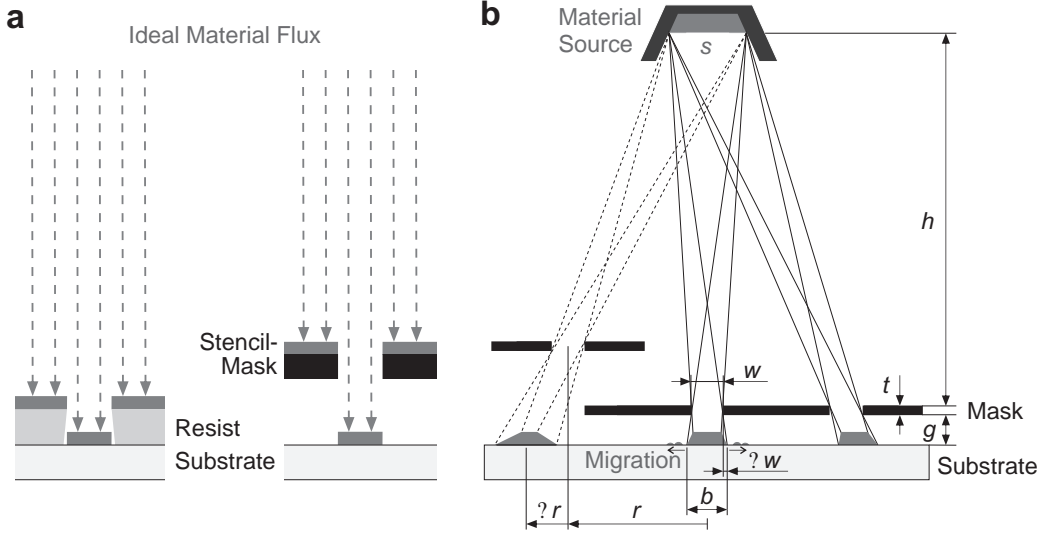
Following Arcamone *et al.* [244], the blurring extension  $\Delta w$  for thin masks can be approximated as:

$$\Delta w = \frac{b - w}{2} \approx \frac{s \cdot g}{2h} \quad (3.1)$$

Taking the values for a Plassys-II MEB550SL evaporator ( $h = 0.5$  m,  $s \approx 2$  cm), a typical mask-to-substrate gap of  $10 \mu\text{m}$  leads to an expected geometrical blur of  $0.2 \mu\text{m}$ . The blur depends linearly on  $g$ . A reduction of the gap to  $1 \mu\text{m}$  is expected to restrict the blur to approximately  $20$  nm.

Lateral shifts occur if the stencil aperture is off the centre axis of the slightly conical material flux. For a mask opening at a distance  $r$  from the centre of the substrate holder, the maximum lateral shift  $\Delta r$  due to inclined deposition is:

Lateral Shifts



**Figure 3.2:** Schematic illustration of patterned physical vapour deposition. (a) Ideally directional material flux patterned by resist-based lithography (left) and by stencil lithography (right). (b) Sketch illustrating the imperfections of the pattern transfer during stencil lithography (shadow masking): Blur due to non-zero source size ( $s$ ), shifts for off-axis areas, and surface migration. Clogging due to coverage at the mask and the sidewalls of the openings as well as mask distortions are neglected.

$$\Delta r = \frac{g+t}{h} \cdot r \quad (3.2)$$

where  $t$  is the thickness of the stencil mask.

Assuming an extreme sample position close to the border of the sample holder ( $r = 5 \text{ cm}$ ) and a mask thickness of  $t = 1.5 \mu\text{m}$  (corresponding to the Poly2 layer of the commercial poly-Si multi project wafer service PolyMUMPs), a lateral shift  $\Delta r$  of  $1.15 \mu\text{m}$  is expected for a gap  $g$  of  $10 \mu\text{m}$ , or  $\Delta r = 0.25 \mu\text{m}$  for  $g = 1 \mu\text{m}$  respectively.

Both the blurring extension and the lateral shifts are minimised by reducing the mask-to-substrate distance  $g$  and by maximising the source-to-mask distance  $h$ . Increased  $h$  comes along with the cost of higher material consumption (radial spread) and requires larger vacuum chambers. As a result of the non-zero source size and the thickness of the mask, the thickness of the deposited material is diminished for tiny mask openings  $w$  at comparatively large gaps  $g$ .

The blur occurring in stencil mask lithography is to be compared with blur occurring in metal lift-off using resist-based lithography. Lift-off is the commonly used technique in resist-based lithography for thin-film patterning, shown in the left part of Figure 3.2a. Lift-off is also a shadowing method and principally suffers from the same blurring effects. But resist-based masks with undercuts have

Mask-to-Substrate Gap

Comparison with Lift-Off

two major benefits. Firstly, thin mask layer thicknesses are achievable by resist spin-coating. Secondly, the mask-to-substrate distance is zero as the resist is in direct contact with the substrate surface. For resists, the blurring is dominated by the layer thickness. Resist thicknesses of micrometres are standard in photolithography and sub-100-nm thin resist layers are in use for high-resolution electron beam lithography (EBL). Undercuts are formed by appropriate exposure. Undercuts can also be formed by bi-layer resists where the lower layer is developed faster than the top one. For stencil lithography, the thickness of the mask is often large compared to resist thicknesses. More crucially, the mask-to-substrate distance is often even larger (depending on wafer curvature and fixation method). Commonly, silicon nitride membranes on bulk-micromachined Si wafers are used as masks. To minimise the mask-to-substrate gap, compliant membranes have been developed by Sidler *et al.* [245].

Another patterning technique is metal thin-film etching. Metal is deposited everywhere on the substrate. Using resist-based lithography, the metal is removed from the undesired locations by etching. The electrode edges are defined by the etch front. These edges might be sharper, but the nanotubes are exposed to etchants.

Comparison  
with Etching

During shadow masking, surface migration is an additional effect that contributes to reduced contrast in pattern transfer: Material deposited on the substrate can migrate along the surface by diffusion. Even for very short mask-to-substrate distances, which reduce the geometric blur, the vertically impinging material can diffuse laterally [246] leading to a halo. The extent of blur due to surface diffusion is governed by deposition temperature, kinetic energy of the material at impact, deposition rate, and material combination. In resist-based lithography, surface migration also appears towards the undercuts of the resist. Undercuts facilitate the lift-off of the deposited material from the unwanted areas. Small-sized undercuts can physically block surface migration, coming along with the risk of rim formation (pile-up of material at the resist boundary).

Surface  
Migration

Additional blur is induced by non-ideal vacuum conditions in evaporation systems. The directionality of the material flux can be affected by scattering owing to residual gases inside the evacuated deposition chamber.

Residual  
Gases

Atom diffraction at the openings (apertures) of the stencil mask is another factor which in principle affects the pattern transfer. Though, diffraction effects are usually negligible [247]. Reflection of material by the sidewalls of the openings can occur in principle as proposed by Gray *et al.* [243]

Scattering

In stencil lithography, the mask can be reused. In the course of many depositions, the openings of the mask can become smaller due to material deposited on the side walls of the openings [248] p27. To undo this so-called clogging, cleaning of the stencil by selective etching may be needed [249].

Clogging

Many thin films exhibit intrinsic stress after deposition. Hence, attention must be paid to the mechanical stiffness of shadow masks. The upwards-bending of cantilever-like mask structures can be especially pronounced in case of thick and

Stiffness

repeated depositions. Corrugated membranes [248, 250] can reduce the distortion of the stencil mask during material deposition.

Mask  
Alignment

Lateral alignment of the stencil to the substrate can be done using a bond aligner [251]. Arcamone *et al.* achieved an alignment accuracy of 1  $\mu\text{m}$  on wafer scale. For shadow masking in commercial services, such as SOIMUMPS [252], where physical contact of the shadow mask with freestanding structures must be avoided, alignment precision is low and tolerances larger than 30  $\mu\text{m}$  can be required.

Self-  
Alignment

Improved alignment was demonstrated by Brugger *et al.* [253]. A 3D shadow mask was self-aligned to a bulk-micromachined target wafer by making use of alignment slots fabricated along the  $\langle 111 \rangle$  crystal planes of the (100)-oriented mask wafer. Such micromechanical alignment guides were suggested by them [254] also to maintain alignment during deposition processes which induce temperature changes, and hence are prone to thermally induced mismatch.

Integrated  
Mask

Burger *et al.* [255] presented shadow masks integrated as a structural part of the substrate itself. Silicon nitride beams were released by a KOH etch and served as masks for the underlying bottom of the etch hole. Burger *et al.* emphasised that such integrated shadow masks no longer need to be aligned to the etched holes for which they themselves served as mask. In addition, on-chip integration can avoid thermally induced drift of the mask during evaporation [256]. However, the applicability of integrated masks for electrical contacts was considered to be limited [255] mainly due to restricted flexibility in pattern generation (mask deformation for elongated structures, no ring-like structures possible).

Geometric  
Obstacle

Here, as CNTs are to be grown on the substrate, the issue of geometric obstacles arises for integrated masks: The nanotube is aimed to bridge from the first electrode, where growth starts, to the second electrode. But if the mask is in place already before nanotube synthesis (or deposition) the nanotube may span to the mask rather than to the second electrode as intended. Keeping the same mask in position to define nanotube-support and contact metallisation would be preferable to reduce alignment mismatch. However, the mask would likely be an obstacle during growth.

Conclusions

Notwithstanding the drawbacks of limited pattern flexibility and being a potential obstacle during growth, stencil masks integrated on the chip provide significant advantages concerning alignment. A technique to circumvent geometrical obstacles during growth is described in the following subsection 3.2.2.

Few Process  
Steps

Compared with standard resist-based lithography, stencil masking has a low number of processing steps. Once the fabrication of the re-usable mask is completed, only three steps are to be taken: alignment, deposition, mask removal. In resist-based lithography, many steps are required: (dehydration bake), (adhesion promoter), resist application, (prebake), alignment, exposure, (postbake), development, drying, (plasma ashing), deposition, lift-off, (cleaning), drying.

The following lists summarise the strong and weak points of shadow masking:

Benefits of shadow masking:

- resistless and hence residual-free
- contactless (no mechanical loads as resist application is avoided)
- no wet chemical treatment of the substrate needed
- compatible with most materials
- reuse of shadow mask is possible
- low number of process steps
- parallel process

Challenges:

- high-resolution only for small mask-to-substrate gap
- surface migration
- alignment
- stencil deformation due to intrinsic stress in deposited material
- thermal expansion mismatch

#### 3.2.2 Adapted stencil lithography for integration of SWNTs

To benefit from resistless, contactless and highly material-compatible stencil lithography, the following main challenges must be addressed for integration of short individual SWNTs: lateral alignment precision and accuracy, mask-to-substrate gap minimisation without mechanically harming the nanotube, and surface migration of the deposited material.

Challenges

Here, a movable, guided shadow mask for the nanotube mid-section is integrated on the chip itself to ensure sufficiently precise alignment. The metal electrodes have to be aligned to the nanotube suspended between opposing tips  $3\text{ }\mu\text{m}$  apart. The die sizes are as small as  $1\text{ mm} \times 1\text{ mm}$  (needed for TEM-accessibility as described in Section 3.5) which renders off-chip mask alignment difficult. Instead, an on-chip shadow mask bar shields the nanotube from metal deposition. The mask bar is attached to a laterally movable slider. The slider is fabricated in parallel with the MEMS structures, into which the nanotube is to be integrated. The vertical play (clearance) of the slider is constricted. Vertical mask-to-nanotube gaps as small as  $700\text{ nm}$  were reached. Cone and matching bumper structures in addition to collateral guides enable sub- $100\text{ nm}$  lateral alignment precision.

On-Chip  
Shadow Mask

For bond pad areas and extended electrical leads, large features need to be patterned. Although movable on-chip shadow masks made of poly-Si membranes can structure multi- $100\text{-}\mu\text{m}$  large features, challenges were faced concerning uniformity of the mask-to-substrate distance. Moreover, the die exhibits topography with mechanically fragile structures: MEMS actuators and electrodes elevated above the substrate to suspend the nanotubes. These structures and especially the nanotubes themselves impose the need for careful placement of the shadow mask without mechanical collisions. To meet the need for large features, a second

Undercuts

shadow mask type is implemented: Leads and bond pads are vertically separated from the substrate by undercuts all around their borders. Anchors are placed in the centre area of leads and bond pads. The anchors mechanically connect these structures to the insulating silicon nitride which covers the Si substrate. The undercuts are sufficiently broad to ensure electrical separation during global metal evaporation. Therefore, the movable shadow mask needs to shield only the suspended part of the nanotube. The movable on-chip shadow mask becomes substantially smaller, which relaxes the stiffness requirements for the mask.

Related Work

The undercuts themselves are somewhat similar to the concept of Cao *et al.* [34] where isotropically etched trenches patterned the gates. In the work of Brugger *et al.* [254], nanodots were evaporated onto freestanding MEMS beams. As a side effect, the beams pattern the deposited material. Park *et al.* [257] used undercuts fabricated by stencil lithography to reverse a pattern.

Alternative to Undercuts

An alternative to on-chip undercuts would be the use of a conventional off-chip stencil wafer with large feature tolerances for the coarse features. However, alignment is difficult on the small die sizes required here for TEM accessibility. Most convincingly, the undercuts are fabricated in parallel with the MEMS process. A drawback of undercuts is the increased area consumption around the anchors. The bond pads have borders with undercuts. Therefore, the pad size must be sufficiently large to prevent mechanical damage during wire bonding.

Tilted Rotation

During direct growth, some of the nanotubes land on the sidewall instead of reaching the topside of the electrode. Covering the sidewalls of the oxidised polycrystalline silicon electrodes with evaporated metal allows to contact those nanotubes as well. Sidewall coverage can be achieved by tilted sample rotation during evaporation as illustrated in Figure 3.3. However, tilting the mask and the substrate with respect to the material flux results in a lateral shift of the deposited metal pattern [255]. Thanks to the small mask-to-substrate distances  $g$  achieved by the on-chip shadow masks employed here, the sidewalls can be metallised without significant widening of the pattern. A large mask-to-substrate distance would prohibit increased tilting angles as the additional geometric blur of the deposit would yield fully metallised CNTs.

After these general considerations, the detailed process flow for shadow masking is described.

#### 3.2.3 Fabrication of ultraclean CNFETs by shadow masking

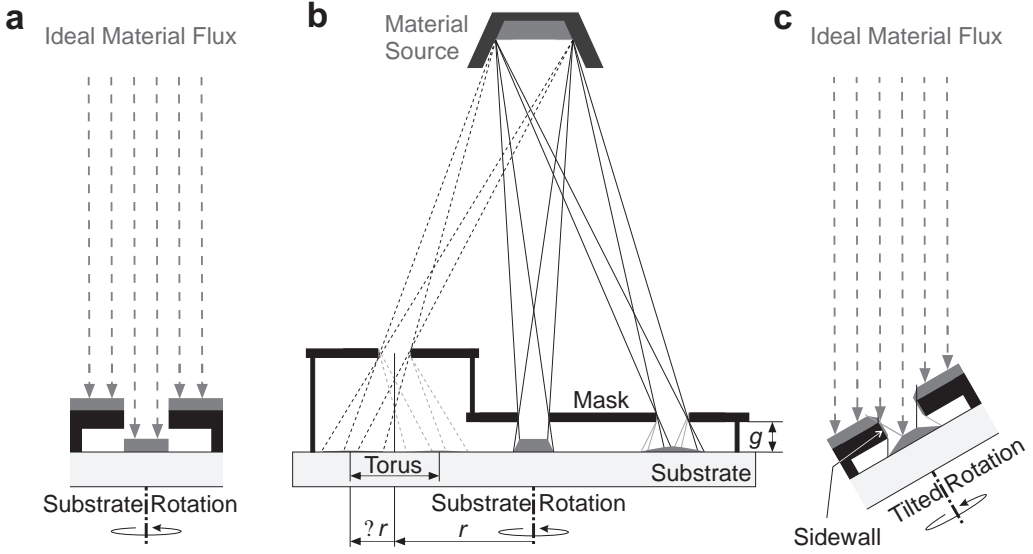
Overview

The ultraclean fabrication of suspended nanotube field-effect transistors by shadow masking is presented in the following subsections. The process run sheet can be found in Appendix A.2. Figure 3.4 illustrates the process flow comprising poly-Si surface micromachining with sacrificial layer etching, local deposition of catalyst nanoparticles followed by nanotube growth and palladium evaporation patterned by on-chip shadow masks.

##### (a) Surface micromachined poly-Si structures

Poly-Si

Support structures for direct growth of suspended SWNTs at high temperatures



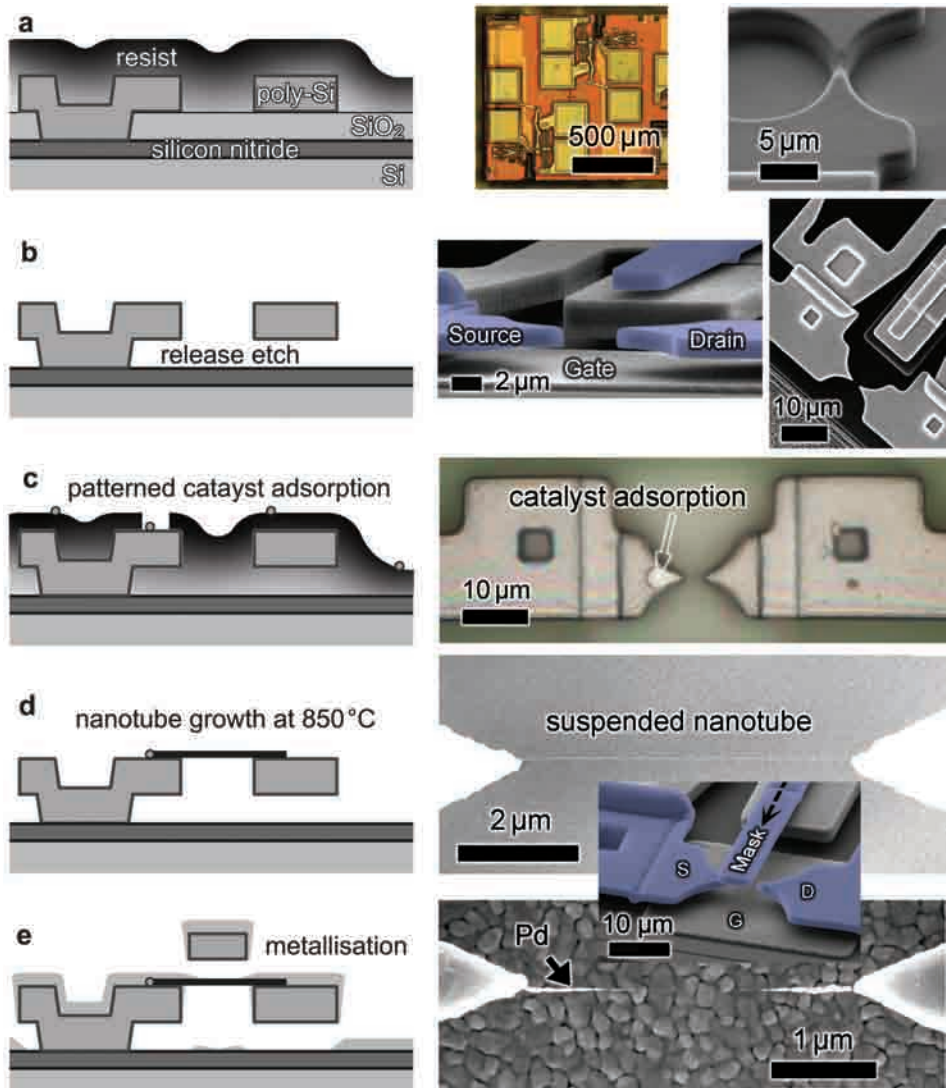
**Figure 3.3:** Schematic illustration of the influence of substrate rotation in stencil masking. (a) Ideal parallel material flux with substrate rotation – unchanged. (b) Real source with finite distance to substrate. The distance of the mask opening from the axis of rotation  $r$  and the mask-to-substrate distance  $g$  induce geometrical blur. For large values of  $r$  and  $g$ , small mask features form concentric deposits with radius  $\Delta r$ . (c) Tilted substrate rotation yields even under ideal assumptions deposits of decreasing thickness. Sidewalls of the mask – or vertical structures in general – are covered with material.

were fabricated from polycrystalline silicon (poly-Si) thin films. Similar to work by A. Jungen [211, 212], a commercially available multi-user MEMS process (PolyMUMPs, MEMSCAP inc.) [4] was employed for fabrication. This multi-project wafer-scale MEMS process incorporates deposition of three poly-Si layers and two  $\text{SiO}_2$  layers on a silicon nitride covered Si wafer. Each poly-Si layer is structured by dry etching at a minimum feature size of  $2\text{ }\mu\text{m}$ . The  $\text{SiO}_2$  sacrificial layers enable freestanding poly-Si structures. By three anchor/via etching steps, poly-Si layers can be anchored to the silicon nitride, or to the previous poly-Si layer respectively. Dimples are defined by a partial etch into the sacrificial  $\text{SiO}_2$ . The slots result in spikes at the bottom of the poly-Si layers and minimise stiction of released structures. A final metal layer (Cr/Au) is available<sup>1</sup>. After this eight-mask photolithography process, the wafer is protected by resist and diced before shipping to the customers.

### (b) Sacrificial layer etch

The protective resist was removed in acetone. The dies were dipped in isopro- HF

<sup>1</sup> Cr/Au metallisation is avoided on dies which undergo the high-temperature nanotube synthesis. Metal migration over hundreds of microns was observed and is suspected to corrupt nanotube growth.



**Figure 3.4:** Schematic illustration of the process flow for electrical integration of suspended SWNTs by resist-free on-chip shadow masking. SEM and light microscopy images are shown on the right. (a) Surface micromachined poly-Si layers penetrate through the SiO<sub>2</sub> sacrificial layer to be anchored on isolating silicon nitride. Resist serves as protection. (b) Release etch by HF to form undercuts and freestanding poly-Si structures. (c) To define the starting point of the nanotubes, adsorption windows are patterned by electron beam lithography. Iron-loaded ferritin proteins are adsorbed on the oxidised poly-Si surface. Catalyst islands are patterned by lift-off. (d) CNTs are synthesised by catalysed chemical vapour deposition (CCVD) at 850 °C in 128 mbar CH<sub>4</sub> plus 82 mbar H<sub>2</sub>. (e) Directly after growth, palladium (Pd) is evaporated onto the suspended end-sections of the nanotube. A movable on-chip shadow mask and undercuts around the leads are shaping the metal. Deposition at 30° tilted sample rotation coats side-walls and forms tapered, self-aligned contacts to the nanotube. Part of the images are adapted from Nature Nanotechnology [101] and from [104]. © Macmillan Publishers Limited, 2010 and © Wiley, 2011.



panol and deionized water (DI-water), and then dried by an N<sub>2</sub> stream. The sacrificial SiO<sub>2</sub> was etched in 40% hydrofluoric acid (HF) for 3 to 5 min. The dies were rinsed thoroughly in flowing DI-water and were put in subsequent baths of 1:1 isopropanol:DI-water and pure isopropanol. Finally, the dies were dried by a stream of N<sub>2</sub> and placed on a hotplate at 65 °C which was then heated to 120 °C.

### (c) Catalyst patterning

Nanotubes were grown by the direct synthesis method from carbon feedstock gas decomposed on catalytically active nanoparticles placed on a substrate. Local placement of iron catalyst nanoparticles on the poly-Si microstructures defined the starting position of the nanotubes.

SWNT  
Starting  
Position

### Diffusion barrier layer by thermal oxidation

At high growth temperatures of about 800 °C, Fe and Si can form silicides which are energetically more favourable than iron carbides. Iron silicide formation corrupts the catalytic activity of the Fe nanoparticles for SWNT synthesis [258]. To prevent silicide formation, a diffusion barrier layer of at least 4 nm thick SiO<sub>2</sub> is needed according to Simmons *et al.* [259]. As a simple and fast method to thicken the native oxide layer, the poly-Si growth supports were placed on a ceramic plate and heated above 600 °C in ambient air for 10 min using a Bunsen burner.

SiO<sub>2</sub>

### Growth island definition by electron beam lithography

The starting position of the nanotube was defined using electron beam lithography (EBL) for catalyst island patterning, similar to Kong *et al.* [135]. As resist for lift-off, copolymer methylmethacrylate/methylacrylic acid (P(MMA/MAA)) in ethyl lactate (MicroChem) was spin-coated without further dilution (pure). Three layers of P(MMA/MAA) were spun at 4000 rpm with three intermediate bakes at 150 °C for 90 s each. Moderate baking conditions and the triple-layer stack improved coverage of the highly topographic and sharp poly-Si features. Additionally, rounded corners of the structures facilitated full coverage with resist. At an electron dose of 420 μC/cm<sup>2</sup>, windows of 3 μm diameter were written using a Raith<sup>150TWO</sup> electron beam direct writer operated at 30 kV. The 30 μm aperture resulted in a current of typically 0.34 nA. The exposure time per growth site is theoretically about 0.1 s neglecting driving and waiting times. Alignment was performed with respect to markers (10 μm long crosses of 2 μm width) defined in the same poly-Si layer onto which the catalyst nanoparticles were to be placed. The exposed resist was removed by developing for 70 s in 1:3 methyl isobutyl ketone (MIBK):isopropanol. The die was immersed into isopropanol for 60 s and then dried under an N<sub>2</sub> stream. Optionally, an O<sub>2</sub> plasma was applied (3 min, 250 W) to clean the oxidised poly-Si surface on the bottom of the windows for adsorption of catalyst islands.

EBL

### Ferritin adsorption for catalyst formation

For deposition of catalyst nanoparticles, iron-loaded ferritin was adsorbed from aqueous solution [144, 260]. Ferritin is a spherical protein complex which can

Protein Shell

incorporate a core of iron hydroxide. The shell is composed of 24 subunits and can enclose up to ~4500 iron atoms [261]. Partial loading of the approximately 8 nm large hollow cage allows production of catalyst nanoparticle sizes suitable for SWNT synthesis [260]. As reported by Durrer *et al.* [144], the concentration of ferritin in the solution governs the ferritin density on the substrate surface. Hence, the final number of nanotubes growing per catalyst island can be tuned by adjusting the concentration in the solution. Charges on the surface of the protein hinder coagulation by electrostatic repulsion. As published by Chikkadi *et al.* [262], changes in the surface charge of the target substrate can massively increase the area density of adsorbed proteins. Lowering the pH value of the ferritin solution down to pH 4 allows more diluted ferritin solution to be used. The amount of ferritin stock solution needed to obtain a certain area density of catalysts is drastically reduced. This is especially important for ferritin treated by size-separation centrifugation, where the available amount of ferritin stock solution is limited. As introduced by Durrer *et al.* [263], ferritin size-separation can be achieved by centrifuging the proteins according to their loading-level dependent sedimentation velocity (twice at 30 000 rpm for 17 h in a density gradient using glycerol). For ferritin adsorption on the oxidised poly-Si through the windows in P(MMA/MAA), the dies were preconditioned by a dip into MES buffer solution (2-(N-morpholino)ethanesulfonic acid, 50 mM, pH 4) for 1 min, rinsed in DI-water and subsequently dried by an N<sub>2</sub> stream. Thereafter, the ferritin adsorption from stock solution diluted in MES buffer lasted for 3 min, followed again by a DI-water rinse and drying.

#### Catalyst lift-off

The P(MMA/MAA) was removed and the ferritin proteins outside of the growth islands were lifted-off in three consecutive baths of acetone at room temperature. Re-adsorption of ferritin proteins onto unwanted areas must be avoided during lift-off. To improve the lift-off, the dies were stirred well and moved quickly from bath to bath. Drying of the die was prevented using broad tweezers. After a final acetone bath at 50 °C for 10 min, the die was immersed into isopropanol for 5 min. The die was dried by an N<sub>2</sub> stream and was put on a hotplate. A bake in air on a ceramic plate above 600 °C for 1 min removed the protein shell by oxidation and calcinated the ferrihydrite particles.

#### Subdicing

As it will be discussed in Section 3.5, the final die size is 1 mm × 1 mm. A single die contains one to six devices. Spin-coating on such small chips leads to tremendous edge beads. These resist accumulations can be reduced to a certain extent by surrounding the die by additional dummy chips of the same height. The die and the dummy dies were assembled on an SEM carbon tape attached to a carrier die. As edge beads occur at the border and for reasons of throughput, multiple die sites were processed in parallel. Processing a die size of 2 mm × 10 mm reduced the time consumption during EBL preparation and alignment. Handling

was facilitated (up to 32 die sites are manipulated at once prior to final subdicing into  $1\text{ mm} \times 1\text{ mm}$  sizes). The final subdicing must be done before the nanotube growth as long individual SWNTs would hardly ever survive spin-coating [22]. Hence, after ferritin adsorption and lift-off, subdicing to  $1\text{ mm} \times 1\text{ mm}$  sizes was done – before growth. To protect the poly-Si structures during dicing, a double layer of pure P(MMA/MAA) was spun onto the die at a final rotational speed of 3000 rpm and baked each for 70 s at  $150^\circ\text{C}$ .

#### (d) Direct synthesis of CNTs by CCVD

Carbon nanotubes were grown from the catalyst island located on the first electrode of the device structure. The nanotubes shall bridge from the first electrode across the gap to the second electrode.

#### CNT Growth by catalysed chemical vapour deposition (CCVD)

CNTs were grown from methane by catalysed chemical vapour deposition in a hot-wall quartz reactor (PEO-603-PLC-300C, ATV Technologie GmbH) [126, 144]. After evacuation of the reactor below  $10^{-5}$  mbar, the  $\text{Fe}_2\text{O}_3$  nanoparticles were reduced in 310 mbar  $\text{H}_2$  at  $850^\circ\text{C}$  for 10 min (static conditions, approximately  $16\text{ dm}^3$  reaction volume). The reactor was evacuated again. Hydrogen was supplied into the reactor to avoid excessive self-pyrolysis of the carbon feedstock gas [126]. The pressure of  $\text{H}_2$  injected at 0.2 slm for 58 s reached 82 mbar. The partial pressure of  $\text{CH}_4$  supplied at 1 slm for 34 s was 128 mbar, which added up to a total pressure of 210 mbar. The growth time was set to 12–15 min. Thereafter, the reactor was evacuated, cooled to below  $400^\circ\text{C}$ , and purged with  $\text{N}_2$  three times before being vented. The dies were unloaded below  $250^\circ\text{C}$ .

#### (e) Resistless contact patterning by on-chip shadow masking

##### Placement of the mask

Directly after growth, the shadow mask was positioned closely above the mid-section of the suspended nanotube. As described in [101], the guided sliders of the on-chip shadow masks were moved by a micromanipulator. The slider was slid laterally by a worn-out atomic force microscopy (AFM) tip mounted on a probe stage equipped with manually controlled piezo actuators (Burleigh® PCS-5000-150). While operating the light microscope in differential interference contrast mode (DIC), colour changes of the AFM cantilever helped detect the touchdown of the AFM tip on the sample surface.

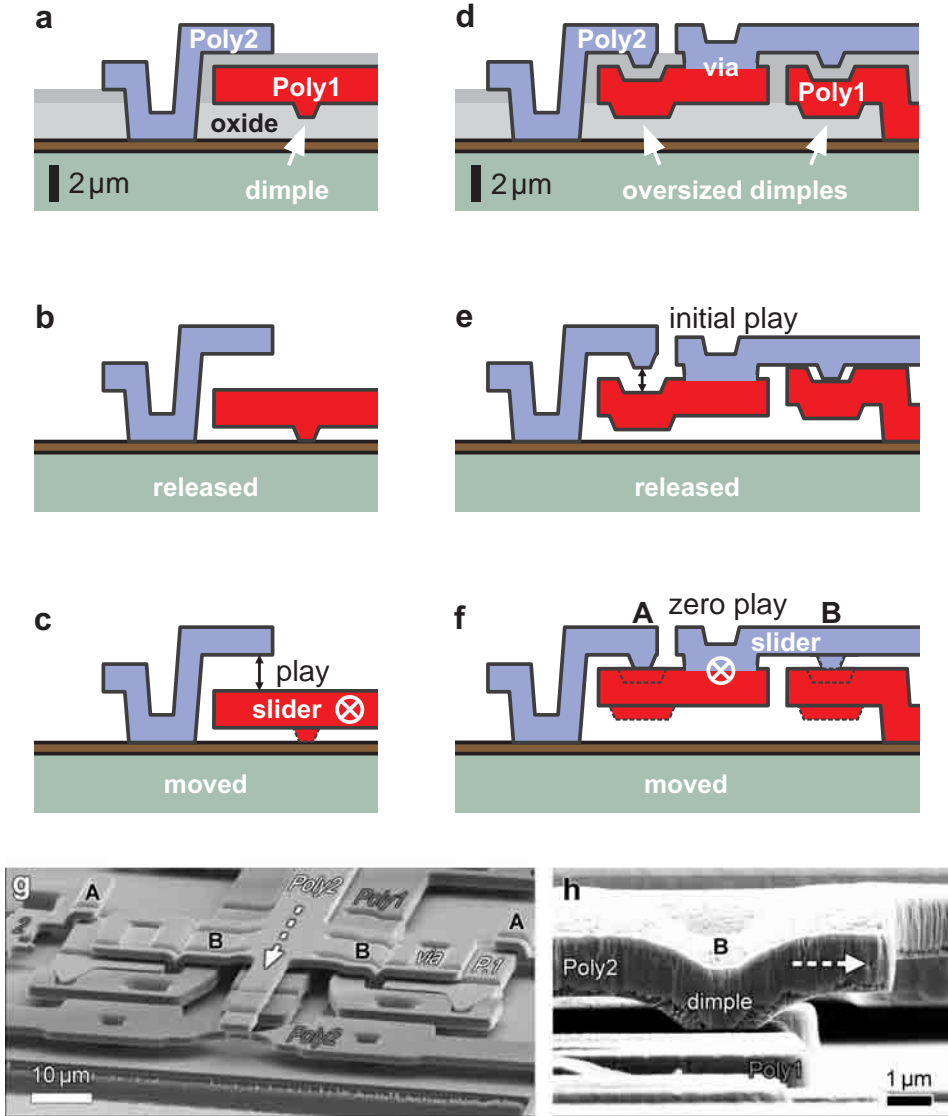
Micro  
Manipulation

Collateral guides are schematically illustrated in Figure 3.5a–c, as demonstrated by Jungen *et al.* [264]. The moving  $2\text{-}\mu\text{m}$ -thick Poly1 (PolyMUMPs) is guided by a  $1.5\text{-}\mu\text{m}$ -thick Poly2 layer. The Poly2 is separated by a  $0.75\text{-}\mu\text{m}$ -thick sacrificial  $\text{SiO}_2$  and is wrapping around the side and on top of Poly1.

On-Chip  
Guides

To keep the mask-to-substrate gap small without risking mechanical damage of the nanotube during mask placement, vertical play has to be minimised. The full vertical play of the movable Poly1 is  $2.75\text{ }\mu\text{m}$ , a sum of the thicknesses of the sacrificial layer between Poly1 and Poly2 and the sacrificial layer underneath Poly1. Dimple structures are available, and can constrict the vertical play. But in

Vertical Play



**Figure 3.5:** Reduced vertical play of the shadow mask slider. The mask-to-nanotube distance can be minimised if the vertical play is low. Former slider design (a-c) with a vertical play of 2 μm [264]. and novel slider design (d-h) with zero vertical play. (a) Former slider design before release with standard dimples. (b) Released slider with 2 μm vertical play. (c) Slider moved into direction of projection. (d) Novel slider design before release with oversized dimples and a Poly2 bar to become sliding on a Poly1 rail. (e) After release with initial play of 1.5 μm. (f) Upon movement of the slider, the dimple on the Poly1 rail is pushing the slider upwards while the dimple of the stationary guide (left, Poly2) is pushing the slider downwards. Vertical play is reduced to zero. (g) SEM image of slider (white labels, Poly2+P.1) where Poly2 moves on top of the anchored Poly1 (grey label). 'A' indicates the anchored downwards-pushing dimples, and 'B' indicates the moving up-lifted dimples. (h) SEM image of the up-lifted Poly2 dimple sliding on top of the Poly1 rail.

PolyMUMPS the dimples are only  $0.75\ \mu\text{m}$  in height.

A novel concept to decrease the vertical play is shown in Figure 3.5d-f. The movable Poly1 is connected to a piece of Poly2, which slides on top of an anchored Poly1 bar. The play at the initial slider position is reduced to twice  $0.75\ \mu\text{m}$ , as illustrated in Figure 3.5e. Although the dimple etch is originally intended for Poly1 and etches into the lowest sacrificial layer, adding dimple structures in Poly2 is feasible by over-sizing the dimple etch area. Upon movement of the mask slider (f), the Poly2 dimples of the slider finally reach a non-indented part of the Poly1 support bar. This lifts the slider by  $0.75\ \mu\text{m}$ . In addition, the Poly1 of the slider is constricted by the  $0.75\text{-}\mu\text{m}$ -deep Poly2 dimple of the stationary guide. Thus, the vertical play is reduced to virtually zero.

Zero Vertical  
Play

In addition to the in-plane collateral guides of the slider, cones and bumper structures were formed. The cones match into the bumpers and define the lateral position of the slider after movement. To ensure precise mechanical positioning of the shadow mask with respect to the tip pairs for nanotube integration, the alignment mismatch between Poly1 and Poly2 layers occurring in standard lithography has to be compensated.

Cone and  
Bumper

Compensate  
Lithography  
Misalignment

Approach 1 compensates the mismatch between the Poly2 mask and the Poly1 tips by fitting Poly2 cones into Poly1 bumpers. For some wafers, the lithographic mismatch between Poly2 and Poly1 was larger than  $1\ \mu\text{m}$ . The available  $\sim 0.75\ \mu\text{m}$  lateral play was not enough to compensate for the lithographic mismatch and the slider became blocked. Additional lateral play was implemented by cut-outs of the guiding structures of the slider.

Cone-Bumper  
Compensation

Approach 2 fabricates both the tip pair *and* the mask in the same Poly2 layer. As both belong to the same photolithography mask layer and are defined simultaneously in the same photolithographic step, lithographic mismatch between the tips and the shadow mask at its initial position cannot occur. However, the shadow mask must be moved atop the tips, fabricated from the same structural layer. The mask is formed on top of spacer layers (Poly0, Poly1). Additionally, the tips are placed at a lower elevation, implemented by thinning the sacrificial layers using the dimple etch. Therefore, the mask made of Poly2 can be slid over the tips made of the same Poly2.

Same  
Lithographic  
Layer

A small mask-to-nanotube separation of  $\sim 0.7\ \mu\text{m}$  was achieved.

Gap

Taking advantage of the cone-bumper fit, a lateral alignment of the shadow mask along the SWNT axis was routinely achieved with an accuracy better than  $50\ \text{nm}$ . After removing outliers where particles or incomplete movement caused obvious misalignments larger than  $0.5\ \mu\text{m}$ , a set of 23 mask placements was evaluated. An estimate for alignment accuracy of  $\sim 0.009\ \mu\text{m}$  and a  $1\text{-}\sigma$  alignment precision of  $\sim 0.077\ \mu\text{m}$  were extracted<sup>1</sup>.

Alignment

To keep the shadow mask slider in its final position, poly-Si springs clamped the slider while the pushing AFM tip was finally retracted.

Clamps

<sup>1</sup> Only designs with sliding direction perpendicular to the nanotube axis were considered. Sliding direction along the nanotube axis, or older designs without full compensation of lithography-mismatch can exhibit substantially larger misalignment.

### Metal evaporation

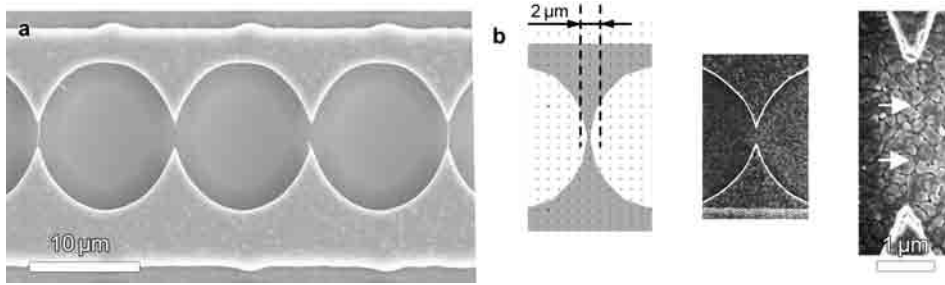
- PVD Electron-beam evaporation of palladium was carried out at a base pressure of  $9 \cdot 10^{-8}$  mbar (Univex 500, Leybold) and a source-to-substrate distance of 40 cm or at a base pressure of  $4 \cdot 10^{-8}$  mbar (Plassys-II MEB550SL, Plassys) and a distance of 50 cm. A nominal thickness of 120 to 170 nm of Pd was deposited while the axis of sample rotation (5 rpm) was tilted by  $30^\circ$  with respect to the direction of material flux. The metal deposition extends onto the suspended nanotube end-sections. The contacts were self-aligned to the nanotube itself as the nanotube acts as a template.
- Self-Alignment
- ESD As electrostatic discharges (ESD) can harm the electrically contacted nanotubes, the small samples were mounted on a carrier chip using silver paste, rather than carbon tape. An ionizing fan and soft-grounded wrist-straps were used during sample handling.

### Discussion on growth alignment

- Waving Growth SWNT were reported to bridge between microstructured pillars [137, 242, 265–267] as a result of thermal waving of the nanotube while growing in a flying mode: The nanotube is growing while being attached to the support only at the catalyst site [268]. Jungen *et al.* demonstrated orientation of SWNTs along opposing sharp tips according to nearest-boundary attachment [138, 269]. A similar nearest-neighbour alignment method is employed here. The catalysts are deposited locally to define the starting point of nanotube growth on the first electrode close to the opposing tip. Concerning the fabrication of sharp tips, opposing electrode tip pairs were made of poly-Si solely by photolithographic means, as described in Reference [103] and shown in Figure 3.6. The standard photolithography process has a specified minimum feature size of  $2 \mu\text{m}$ . Sharper structures were achieved by drawing patterns smaller than the specified minimum feature size. In the mask layer, two circles were subtracted from a bar. The circles had radii of  $7 \mu\text{m}$  and were separated from each other by  $0.25 \mu\text{m}$ . As the standard lithography is not capable of reproducing this waisted bridge design completely, desired sharp poly-Si tips were formed. The gap between the tips was around  $3 \mu\text{m}$ . Tips were thinned down in lateral dimensions below 500 nm.
- Nearest-Neighbour Attachment
- Sharp Tip Pairs
- Earlier Work This process is simpler compared to the tip formation approach introduced by Jungen *et al.* [138], where sharp tips had to be fabricated by an HF etch of thermally oxidised poly-Si bridges. Here, any buckling of double-clamped beams due to compressive strain induced by oxidation is omitted. Moreover, the initial structural layer thickness can be maintained.

### 3.2.4 Conclusions on the process flow of shadow masking

- Sequence The process sequence is optimized to prevent any contaminations from wet chemistry and resist-based lithography. All process steps involving liquids, especially the release etch and dicing are carried out before nanotube growth. Metal contacts are patterned resist-free by on-chip shadow masking directly after growth. As the metal is deposited after growth, growth temperature incompatibilities of
- Clean Processes after Growth Material Compatibility



**Figure 3.6:** SEM images illustrating the nearest neighbour attachment of SWNTs during growth. (a) Sub-feature size definition of opposing tip pairs for nanotube growth at preferential alignment by nearest-neighbour attachment. Adapted from [103]. (b) Nanotubes grown from patterned growth island are bridging preferentially along the sharp tips defined solely by lithography [103]. 120 nm Pd was evaporated globally which enhances visibility. © Elsevier B.V., 2009.

the contact material and swelling of Pd in  $H_2$  is avoided. Pd is known to catalyse Si etching during etching in liquid HF [60], which was also observed during tests on poly-Si layers. Support structure degradation after metallisation is excluded here by completing the sacrificial etch before Pd deposition.

Crucial for contact formation to short nanotubes, the on-chip shadow mask concept enables improved accuracy of mask alignment along the nanotube axis (better than 50 nm) compared to standard off-chip wafer stencils. Perpendicular to the nanotube axis, the metal leads are efficiently self-aligned to the suspended nanotube without the need for the exact location-mapping of the nanotube, which would be necessary if electron beam lithography was used. The contacts protrude onto the nanotube and have a tapered shape.

The metal evaporation under tilted substrate rotation covers all side-walls and also the substrate directly underneath the nanotube. Thus, all  $SiO_2$  surfaces around the nanotube are metallised, which is beneficial for hysteresis-suppression as presented later.

Catalyst patterning using lift-off can be troublesome, especially if the die sizes are large [76]. Catalyst particles removed with the resist can re-adsorb on random positions. Multi-layer P(MMA/MAA) copolymer resist and rapid change of solvent baths improved lift-off efficiency.

The area occupied by the on-chip shadow mask is relatively large, which currently limits the device density. Following our discussion published in the Supplementary Information of [101], a reduction in area consumption is achievable by more compact designs and by single sliders providing shadow masks to multiple tip pairs. A decreased shadow mask slider size of 90 μm by 170 μm was obtained, consuming 48% of the area of the design of the first devices. In a later design, a size of 65 μm by 75 μm was demonstrated, as shown in Figure 3.7. This design corresponds to a device density of 20 500 devices/cm<sup>2</sup>, neglecting electrical routing and bond pads. An untested design anticipates a

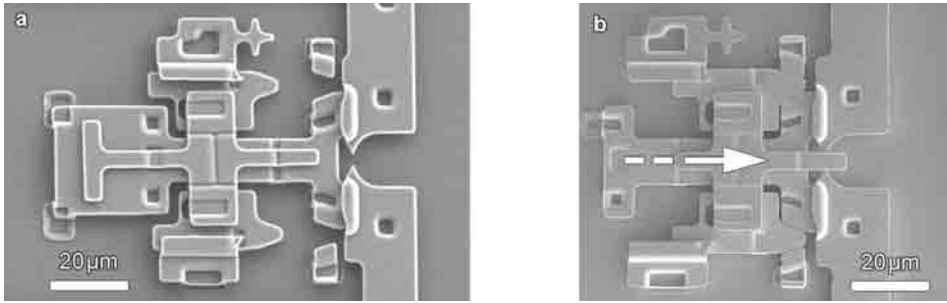
Alignment

Tapered  
Contacts

Covered  
Oxide

Catalyst  
Lift-Off

Scalability  
i: Area Density



**Figure 3.7:** SEM images of the 65-μm-wide shadow mask slider design. (a) Initial position and (b) after sliding the two alignment cones into the bumpers.

43 μm × 27 μm sized shadow mask slider. Unless advanced off-chip stencils allow for higher density, the achieved device density with the on-chip shadow mask method is at least suitable for sensor applications where moderate device densities are acceptable.

ii: EBL      Electron beam lithography, used for the catalyst island definition, is a serial process and could be replaced by deep ultraviolet (DUV) lithography to augment throughput. The reasons for having chosen EBL over parallel exposure lithography were: superior alignment capabilities, difficulties in applying standard photolithography due to the small die sizes (polyMUMPs), the relative ease of stripping P(MMA/MAA) compared to other resists, and flexibility (no need for Cr masks).

iii: Manipulation      The mechanical manipulation of the shadow masks is a serial process step too. Having the die ready for micromanipulation, the manually controlled sliding of the masks can take as short as 10 s per slider. Customised arrays of manipulator tips could possibly speed up the shadow mask positioning. Ultimately, advances in wafer-scale off-chip stencils are expected to substitute the presented on-chip shadow mask sliders.

Yield      The current bottle-neck is the control of growth. Exactly one SWNT is desired, as several-nanotube devices are more difficult to interpret. A suitable direction of the nanotube is required. A nanotube short-circuiting to the gate impedes transistor operation of another properly suspended nanotube. Improvement of the yield of individual SWNT devices can be achieved by tuning the number of catalyst particles at increased catalyst nucleation yield. SWNT orientation could be improved beyond the employed nearest-neighbour alignment by electrical fields [86, 139] or by directed gas flow [140, 141]. However, alignment by gas flow may require a minimum nanotube length [141]. Relying solely on the geometrical nearest-neighbour alignment, currently only ~1 out of 100 devices yielded in a single-nanotube transistor without gate leakage.



### Summary

Implementing on-chip shadow masking addresses the challenges in off-chip stencil masking by enabling small mask-to-substrate gaps. Superior lateral alignment is achieved by sliders with conical alignment structures and simultaneous definition of mask and nanotube support tips in the same lithographic step. Relatively compact dimensions reduce the effects of stencil deformation upon material deposition and minimise thermal expansion mismatch. Thus, the benefits of stencil lithography can be exploited. Resistless and hence residual-free patterned metal contacts are deposited self-aligned onto the as-grown nanotube. Compatibility with a wide range of contact materials is ensured as the contacts are deposited at moderate substrate temperatures after the SWNT growth. Avoiding any wet chemistry after growth enables electrical integration of as-grown, suspended nanotubes in an ultraclean manner.

### 3.3 Room-temperature integration of suspended SWNTs by transfer

The shadow mask approach, introduced in Section 3.2, comprises direct growth of the SWNTs, which exposes the die to high temperatures. Hence, the incorporation of readout electronics in a monolithic system design is hindered due to thermal budget limitations. To avoid the exposure of the die to the harsh SWNT synthesis conditions, an alternative process has been established.

Overview

Suspended SWNTs grown on a separate substrate are mechanically transferred onto predefined electrodes of a receiving device die [102]. Nanotube transfer from fork-like growth substrates enables compatibility with device substrates sensitive to high temperatures, allows bottom contact geometries, and opens possibilities to select a nanotube of desired chirality for integration into electromechanical devices.

Concept

#### Motivation: Enable monolithic chip design, simple contact geometry, and pre-selection of nanotubes

The shadow-mask concept is capable of providing electrical contacts to as-grown, suspended nanotubes without contaminating them as resist-based lithography is avoided. But there remains a system design limitation: Even though the metalisation is applied after nanotube growth and hence the metal is not exposed to high temperatures, the die itself still has to endure the growth conditions. The usual way to escape from the temperature challenge is to implement a hybrid system design. Nanotube devices and CMOS electronics are separated physically on two different dies. The dies are connected by external leads, e.g. wire bonds or flip-chip solder bumps optionally including through-silicon vias. In a monolithic approach, on the other hand, nanotube devices and readout electronics are integrated on the very same chip. Monolithically integrated readout circuitry can increase sensor performance due to mitigated parasitics as the length of wiring is reduced. In principle, the process flow for monolithic integration can be done either ‘electronics first’ or ‘MEMS with nanotubes first’ [270]. Often, the preferred

Thermal Budget

Hybrid Chip Design

approach is ‘circuitry first’ to prevent damages of suspended nanotubes and to be able to rely on standard foundry processes which usually exclude non-standard metals such as Pd or catalyst materials. Low-temperature metal interconnects of standard CMOS technology typically suffer from degradation above 450 °C. Post-CMOS annealing at 600 °C was considered to have insignificant influence on the transistor performance itself in 0.25 µm CMOS circuits, but interconnects degraded [271].

CMOS  
Degradation

Tseng *et al.* [272] achieved monolithic integration of carbon nanotubes in n-channel metal oxide semiconductor (NMOS) circuitry by implementing dedicated poly-Si and molybdenum (Mo) interconnects. However, Mo silicide formation and/or dopant diffusion were suspected to induce changes in material composition of the contacts to nanotubes, which changes the work function and hence the contact properties.

High-  
Temperature  
Interconnects

Despite progress in lowering the synthesis temperatures to allow for direct integration by using more reactive gases such as acetylene (C<sub>2</sub>H<sub>2</sub>) [128] and by plasma enhanced growth [131, 132], there is still no satisfying process available to synthesise highly crystalline SWNTs at temperatures compatible with standard-CMOS. The quality of nanotubes obtained at reduced temperatures is generally rather poor [128–130].

Low-  
Temperature  
Growth

Local heating of micro bridges [212] provides a path to restrict the thermal loading during CCVD to a small part of the die. However, local heating requires in situ electrical power supply, or optical feedthroughs for laser energy, limiting batch compatibility.

Micro Heaters

Deposition of nanotubes from solution by dielectrophoresis maintains low temperature on the device chip - as demonstrated by Burg *et al.* [85] using the same nanotube raw material as employed here. Dielectrophoresis is thermally compatible with standard CMOS. However, surface bound CNFETs typically exhibit severe gate hysteresis in the range of several volts [85] (see 1.2). Moreover, suspended geometries are difficult to obtain due to the risk of nanotube rupture during drying. Contamination is inevitable during wet processing and annealing is needed to desorb the surfactants [81].

Solution-based  
Deposition

#### Concept of direct transfer

Direct transfer [154] of suspended nanotubes from a growth substrate onto a receiving device substrate is a room-temperature process free of liquid media. Transferring the externally grown nanotube onto the device chip is compatible with low-temperature metallic interconnects, and hence opens up possibilities for monolithic integration of nanotube-based sensors.

Direct Transfer

Transfer [154, 155] and stamping [151–153] of nanotubes have been reported earlier. Predefined pillars [152–154] or a single slit [155] served as growth supports. For these concepts the nanotubes will be transferred to a predefined spot. An exception is the work by Huang *et al.* [151] where the location of placement can be chosen, but cleanliness suffers due to clamping by resist. Also for the direct synthesis of the nanotube on the device site (Section 3.2), the nanotubes

Related Work

belong to a certain, predefined location.

In contrast, the fork approach [102] presented in this work, opens the way for selecting a nanotube to be integrated. For example, a specific nanotube of desired chirality grown between one of multiple pairs of parallel arms of a fork can be chosen for transfer. Placement by pressing the nanotube between the selected arm pair onto the receiving electrodes by micromanipulation paves the way to select chiralities. Raman spectroscopy can be employed to pre-select specific nanotubes without exposing them to electron beams and thus avoiding any carbonaceous deposition during the selection sequence. The integrated nanotubes are still accessible by transmission electron beams in tilted-view, as discussed later in 3.5.2. This enables verification of the chirality and the number of nanotubes. Huang *et al.* employed Rayleigh scattering to select ultralong SWNTs and burned off undesired nanotubes by intense optical irradiation. However, cleanliness is sacrificed in their approach as the nanotube is kept fixed on the flat target substrate by adding a drop of photoresist [151].

Selection

Compared to shadow masking, the transfer approach allows modified device geometries. The tapered, needle-like contacts extending onto the suspended nanotube - unique for the shadow masking process - are excluded while the rest of the ultraclean configuration is basically maintained. Combining transfer and shadow masking will allow comparing blunt contacts obtained by transfer with needle-like contacts fabricated by shadow masking on the very same nanotube.

Contact  
Geometry

The technology for poly-Si MEMS fabrication employed here comes along with high-temperature steps. These steps will have to be substituted for monolithic CMOS integration by low-temperature MEMS technology, for instance based on polycrystalline silicon-germanium (poly-SiGe) or on polymers.

MEMS  
Fabrication

The solution-free, room-temperature direct transfer is a process able to integrate ultraclean, suspended nanotubes into surface micromachined devices. The nanotube is not exposed to any release etching step. Neither the as-deposited metal electrodes nor the device die itself must withstand the nanotube synthesis conditions. Clean selection of nanotubes becomes possible using optical spectroscopy. For demonstrator fabrication, a major benefit is the repeatability of the nanotube placement ensuring that the nanotubes are available - certainly and exclusively - at the predefined spot.

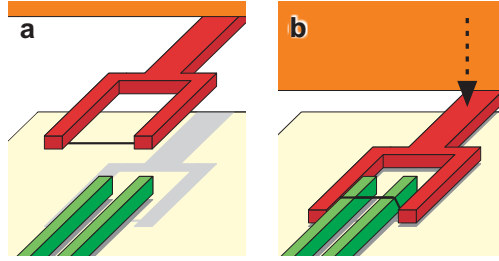
Benefits

After these general considerations, the fabrication of CNFETs by fork transfer [102] is described in detail.

#### 3.3.1 Fabrication of ultraclean CNFETs by transfer

Carbon nanotubes were grown on a separate die across the arms of a poly-Si fork. Those CNTs spanning across the fork arms were then transferred onto metallised electrodes of the receiving device die as sketched in Figure 3.8. The process run sheet can be found in the Appendix A.2.

Transfer from  
Fork



**Figure 3.8:** Schematic illustration of the nanotube integration by transfer. A nanotube is grown in-between the arms of a fork and transferred onto the electrodes on a second die, which remains at room temperature. (a) Fork with as-grown nanotube suspended in-between the arms. (b) Placement of the nanotube onto receiving metal electrodes. Reprinted from [102]. © IEEE, 2011.

#### (A + B) Surface micromachined poly-Si structures and release etch

As described in Section 3.2.3(a), surface micromachined poly-Si layers were fabricated and the sacrificial  $\text{SiO}_2$  was etched in HF. As illustrated in Figure 3.9a and b, two distinct dies were fabricated. One serves as SWNT growth substrate featuring a comb-like fork. The other die carries two parallel 2- $\mu\text{m}$ -wide poly-Si bars separated by a nominal distance of 2  $\mu\text{m}$ . The bars will act as electrodes and are elevated above the substrate<sup>1</sup>. The  $\text{SiO}_2$  sacrificial layer forms undercuts all around the receiving electrodes.

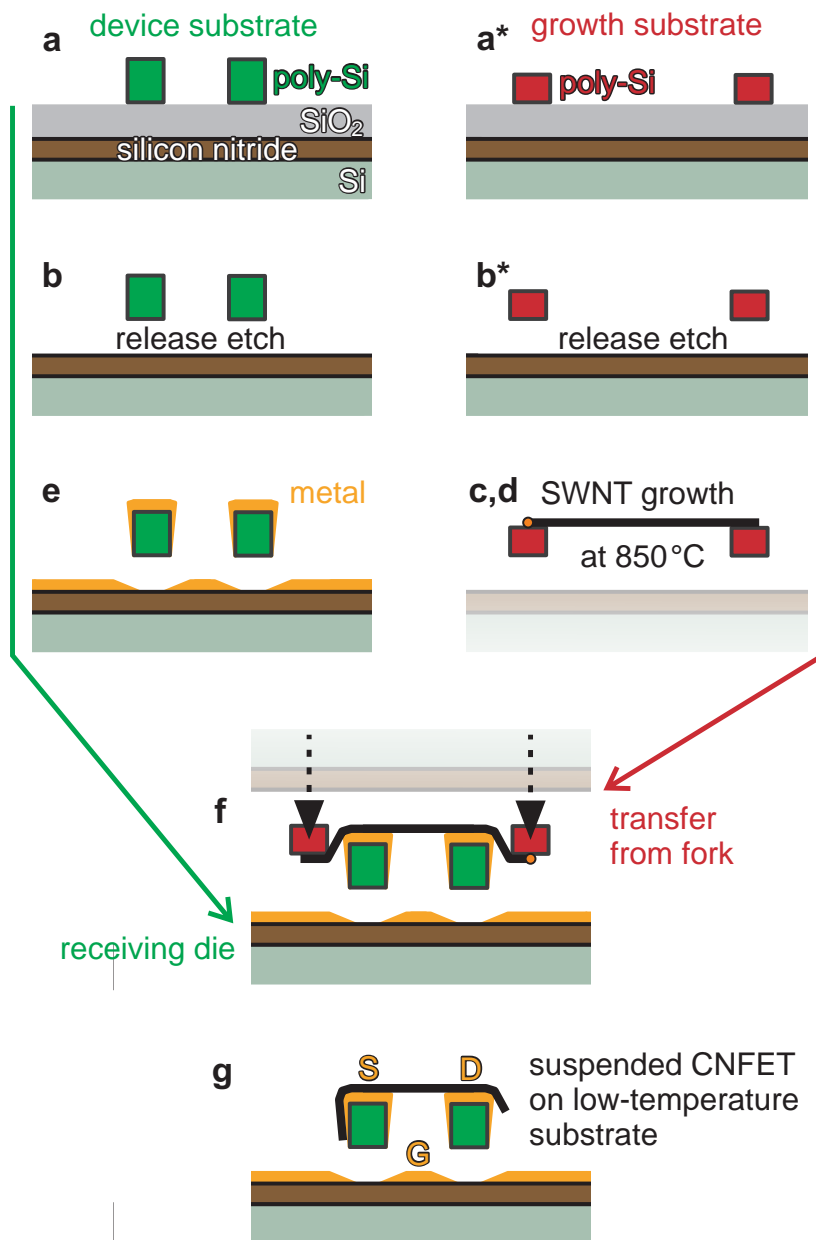
#### (C) Catalyst deposition

The die with the poly-Si fork serving as SWNT growth support was heated above 600 °C for 10 min to thicken the  $\text{SiO}_2$  surface layer acting as a diffusion barrier as discussed earlier in Section 3.2.3(c). Thereafter, without any patterning, iron-loaded ferritin proteins were adsorbed (see Section 3.2.3) on the oxidised poly-Si surface of the forks.

#### (D) Synthesis of CNTs by CCVD on separate growth substrate

The fork was slid beyond the edge of the die, based on the slider principle introduced by Jungen *et al.* [264]. The micromanipulation was done with manually controlled piezo-driven AFM tips (see 3.2.3(e)). Since the fork is protruding from the die, the nanotubes are prevented from attaching to the substrate during growth. The nearest-neighbour is the opposing arm and not the substrate. Thus, the 8  $\mu\text{m}$  wide gaps between the arms of the fork can be bridged by the nanotubes. SWNT were grown by CCVD at 850°C for 15 min, using the same recipe

<sup>1</sup> The gap between the substrate and the electrode bars is 2  $\mu\text{m}$  in height for Poly1 (stacked with Poly2), or 1.25  $\mu\text{m}$  if the oxide is dimple-etched, or 0.75  $\mu\text{m}$  for Poly2 using Poly1 as bottom gate.



**Figure 3.9:** Sketch of the transfer process for fabrication of suspended, ultraclean carbon nanotube transistors (CNFETs) on temperature-sensitive substrates. (a,a\*) Surface micromachined poly-Si structures with sacrificial SiO<sub>2</sub>. (b,b\*) Release etch in HF to form undercuts and movable structures. (c+d) Catalyst adsorption and SWNT synthesis at 850 °C across the arms of a fork moved beyond the edge of the growth substrate. (e) Pd evaporation onto the pre-structured – possibly temperature-sensitive – die where undercuts pattern the metal leads. (f) Transfer of the nanotube from the growth substrate (flipped by 180°) onto the Pd electrodes by micromanipulation. (g) Suspended transistor with gate, source and drain electrodes (G,S,D). Adapted and reprinted from [102]. © IEEE, 2011.

described in Section 3.2.3(d). The number of nanotubes between the arms of the fork can be influenced by the dilution of the ferritin solution. In contrast to the growth substrate, the device chip remains at room temperature.

#### (E) Contact pre-fabrication on receiving die

Metallisation

On the device chip, contact electrodes and gates were formed by blanket evaporation of Pd intrinsically patterned by shadowing at the undercuts resulting from sacrificial layer etching. In contrast to the transfer process by Wu et al. [154], with photolithography and Au etching for gate structuring done after electrode deposition, here the metal evaporation was performed as the last step before transfer, ensuring clean electrode surfaces. Individual gates can be structured using undercuts in the intermediate poly-Si layer (Poly1, not shown).

Die and Wire  
Bonding

A stack of two 500  $\mu\text{m}$  thick spacer chips were bonded into a ceramic package using epoxy glue (EPO-TEK<sup>®</sup> H20E, from Epoxy Technology). The receiving die was bonded onto the spacer chips by silver paste (detachable for subsequent TEM investigations). Aluminium bond wires connected the pads of the package (Ceramic Leadless Chip Carrier, CLCC32) with the bond pads of the device die. Bonding parameters can be found in the run sheet in Appendix A.2.

#### (F) SWNT transfer by electron-irradiation-free micromanipulation

Light  
Microscopy

The transfer of a nanotube, grown between the arms of a fork, onto electrodes of the device die is sketched in Figure 3.8, in Figure 3.9f, and is shown in the light microscopy images in Figure 3.10. The die with the fork carrying the as-grown nanotubes was flipped and attached to the bottom-side of a cantilever. The cantilever was manipulated by a piezo-driven micromanipulator<sup>1</sup>. The fork movement was observed by light microscopy<sup>2</sup>. The fork approached the receiving Pd-coated electrode pair of the device die from above. Upon lowering the fork, the suspended nanotube bridging between the fork arms touched the topside of the Pd electrodes and was bent around the edges of the electrodes. Monitoring the current resulting from a 0.2 V bias applied across the receiving electrodes [146] allowed the detection of successful placement of nanotubes. The source-drain bias was increased aiming at annealing the contacts between the nanotube and the Pd electrodes. An N<sub>2</sub> stream was intended to prevent nanotube burn-out. Thereafter, the fork was pushed all the way down to the substrate. This ruptured, or detached, the nanotube from the fork. In some cases, the nanotube was not broken off, or detached, from the fork but slid away from the receiving electrodes when the fork was retracted. Such events were detected by a sudden drop of  $I_{\text{ds}}$  to zero. Placement can be repeated, simply by using nanotubes from the next pair of fork arms. Typically, multiple growth dies with different ferritin dilutions were prepared. Consequently, forks with an adequate area density of nanotubes can be selected. In addition to tuning the nanotube density, the risk of placing multiple nanotubes at once was reduced as follows: The fork was lowered with an initially

Current  
Monitoring

Nanotube  
Density

<sup>1</sup> Burleigh<sup>®</sup> PCS-5000-150, 150  $\mu\text{m}$  travel (0.14  $\mu\text{m}$ /degree rotation of turnwheel)

<sup>2</sup> Olympus BX-series, LMPlan FI 50X long working distance objective with 10.6 mm working distance or LMPlan FI 100X with 3.4 mm working distance and 0.8 NA; 10X oculars

short overlap with the receiving electrodes. If no nanotube placement was detected, the fork was pulled upwards and the overlap was slightly increased for the next placement trial (saw-tooth-like movement)<sup>1</sup>.

After nanotube placement and withdrawal of the fork, changeover switches (see Figure 3.10a) disconnected source and drain electrodes from the BNC plugs which had been used to apply the bias. Instead, S and D were connected to ground via 2-M $\Omega$ -resistors in order to protect the nanotube device from electrostatic discharges during handling.

ESD

#### 3.3.2 Conclusions on the process flow of direct transfer

As SWNT growth takes place on an external substrate equipped with forks, the nanotube receiving die is not exposed to the harsh growth conditions. Hence, fork-based transfer in principle enables monolithic integration of carbon nanotubes on substrates incorporating CMOS circuitry.

Sequence

Advantages

Room-Temperature

Moreover, packaging and wire bonding can be finalised before the nanotube is integrated. Therefore, the risk of losing the nanotube during wire bonding is eliminated.

Wire Bonding

The assembly approach offers opportunities to select a certain nanotube for integration by Raman spectroscopy, photoluminescence, or Rayleigh scattering (or by electron diffraction if some carbonaceous depositions are acceptable).

Selection

Similar to the shadow mask approach, metal evaporation at tilted sample rotation allows coverage of all oxide surfaces in the vicinity of the nanotube.

Oxide Coverage

The nanotubes grow on a separate die. In this case, catalyst patterning is not needed and incomplete catalyst lift-off cannot result in excess nanotubes growing at unintended locations of the device die.

Catalyst Lift-Off

Additionally, nanotube orientation can be influenced by nearest-neighbour attachment [138] by geometrical structuring of the growth substrate. Oriented nanotubes can be transferred from forks with alignment tips onto blunt electrodes.

Orientation

During growth on the fork, insufficiently long nanotubes are discarded as they fall back on the arm from which they started to grow. Presumably, the rare case of single-clamped nanotubes can hardly be brought into firm contact with the receiving electrodes, and will not be annealed in any case. However, two nanotubes growing from adjacent arms can meet each other and form a bridge consisting of a bundle. This drawback may be suppressed by introducing patterned catalyst deposition on the fork and/or by directional control during growth.

Discard of Short CNTs

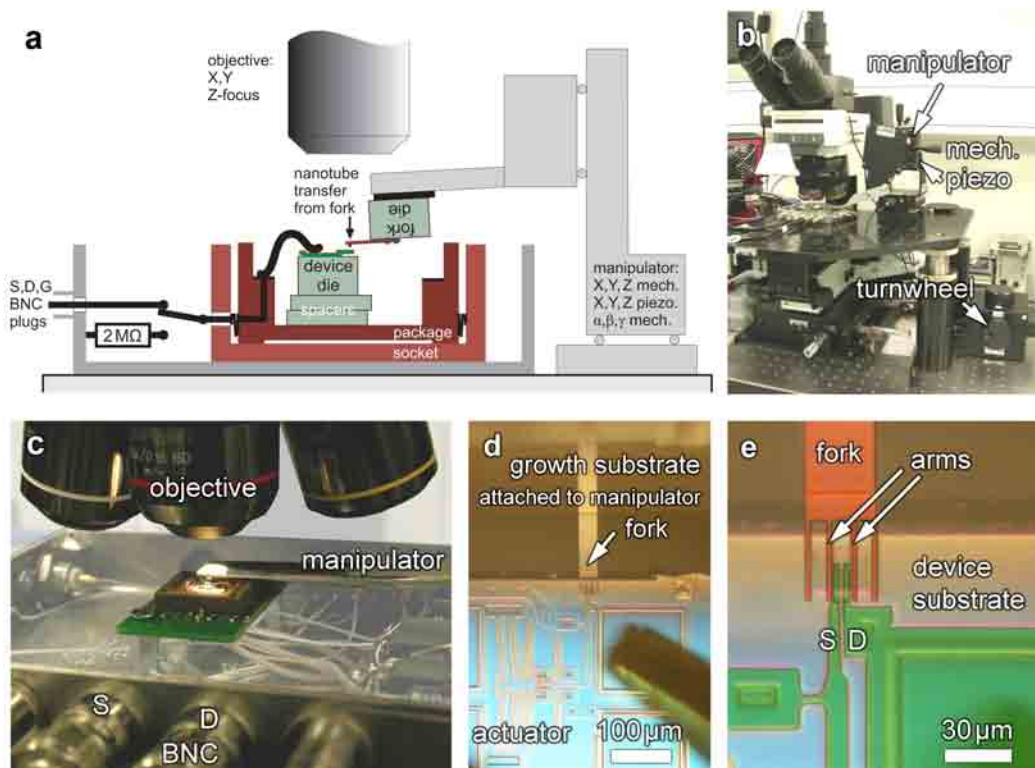
As the nanotubes to be transferred are attaching to the arms, most of them are straightened due to zipping-effects [273] either with the arms or with other nanotubes. Hence, nanotubes are pre-aligned and straightened. The amount of pre-straining is currently under evaluation [274].

Straightening

A small gate distance is important for efficient gate coupling. For the earlier presented direct growth however, a short vertical distance from growth spot to

Gate Distance

<sup>1</sup> An additional improvement could be achieved by rendering the nanotube ends optically visible as demonstrated by Huang *et al.* [151], or by spectroscopic mapping.



**Figure 3.10:** Transfer of SWNTs under light microscopy observation. (a) Sketch of the nanotube grown on the fork. The fork was slid beyond the edge of the chip. The chip is attached by SEM tape to the cantilever of the manipulator. (b) Picture of the micromanipulator. Three piezo-driven translation directions X,Y,Z (150  $\mu\text{m}$  each) in parallel with 28 mm mechanical hub, and three mechanical rotation axes  $\alpha, \beta, \gamma$  are available. (c) The growth substrate is attached to the micromanipulator cantilever by carbon tape. The packaged receiving die is connected to BNC plugs via the PLCC32 socket for in situ current monitoring. Image contrast is artificially increased. (d) and (e) Light microscopy images taken during manipulation of the nanotube-carrying fork (coloured for better visibility). Electrical current across the receiving source and drain electrodes [S and D, in (d), coloured] indicates successful nanotube placement. This device was contacted by probe needles instead of wire bonds. A part is reprinted from [102]. © IEEE, 2012.



bottom gate tends to result in electrical shorts: Nanotubes land on the bottom gate due to nearest-neighbour attachment. In contrast, transfer ensures that the nanotube is suspended across the whole gap length as insufficiently long nanotubes are discarded. Moreover, the transferred nanotubes are placed on the top surfaces of the electrodes and cannot unintentionally attach to the sidewalls. Owing to these reasons, smaller bottom gate distances become possible compared to direct growth.

Not every placement trial results in successful nanotube bridging (depending on nanotube area density) and not every electrically detected nanotube stays in place upon retraction of the fork. But placement can be repeated. Moreover, the nanotube density can be adjusted on several fork dies (re-usable) without wasting receiving MEMS dies. The final success rate in fabrication of devices increases and was larger than ~80%. The reasons for failed devices were mainly failures related to wire bonding, handling mistakes, or in rare cases broken receiving electrodes due to manipulation mishaps.

Yield

In the transfer approach, the nanotube placement can be repeated (and nanotubes can be re-grown on the forks). In the shadow mask approach in contrast, growth can not be easily repeated because post-growth metal evaporation has to be conducted before electrical evaluation becomes available. Before electrical characterization, all processing steps of catalyst patterning and adsorption, growth, mask placement and metallisation must be completed and cannot be redone without considerable efforts. Stringently, before growth, the chip had to be sub-diced into small die sizes which hardly allow repeated spin coating required for catalyst patterning. For the fork transfer in contrast, the nanotube integration step can be repeated, until in situ current monitoring indicates successful bridging of nanotubes.

Comparison to  
Shadow  
Masking

The assembly by micromanipulation is a serial process. However, future automation can be anticipated, in analogy to robots employed nowadays for assembly in automotive industry.

Scaleability

The following lists summarise the strong and weak points of direct transfer:

Benefits of fork-based transfer:

- ultraclean, as neither liquids, nor resists, nor electron beams are involved after growth
- compatible with most contact materials

additional benefits compared to shadow masking:

- receiving substrate remains at room temperature (CMOS-compatible)
- nanotubes are on desired location exclusively (no risk of incomplete catalyst lift-off)
- blanket catalyst deposition on fork replaces the costly electron beam lithography for catalyst patterning
- nanotubes oriented along the arms are discarded
- insufficiently long nanotubes are discarded

- smaller gate distances become possible
- structures for nearest-neighbour-orientation can be outsourced to the fork
- nanotube integration step is repeatable
- in situ current monitoring enables high final yield per MEMS device
- simpler contact geometry possible (blunt contacts, simpler for simulation)
- possibility to select a certain nanotube
- nanotube density series possible using multiple growth substrates (instead of single ferritin dilution per MEMS die)
- wire bonding is finalised before nanotube placement
- ease of ESD protection by changeover switches

Challenges compared to shadow masking:

- mechanical clamping is weaker
- nano-tapered contacts are missing
- transfer is a serial assembly step in contrast to direct growth

### Summary

Transfer of nanotubes from a fork structure enables the use of temperature-sensitive substrates, such as CMOS chips, because the device die bypasses the high SWNT growth temperatures. In contrast to other assembly methods, the fork approach avoids contamination often caused by wet chemistry or electron beam observation. High yield per device site is enabled by repeated placement until a current is detected. As wire bonding is finalised before nanotube placement, ESD and/or ultrasonic power during bonding cannot cause harm to the nanotube. As the nanotube growth on the forks is separated from the receiving electrode pair, the possibility is enabled to select a specific nanotube for placement. Short or wrongly oriented nanotubes are discarded as they do not bridge the fork arms. The gate-to-nanotube distance can be reduced and simpler contact geometries are enabled. Issues related to catalyst lift-off are avoided and nanotubes at undesired locations are efficiently excluded. However, industrial exploitation of transfer from arrays of forks for sensor fabrication will need substantial progress in micro-automation and high-speed Raman/Rayleigh screening. Despite the current lack of automation, nanotube transfer provides suspended, straight, and ultraclean electrically integrated nanotubes at a desired location and with some orientation control for demonstrator devices.

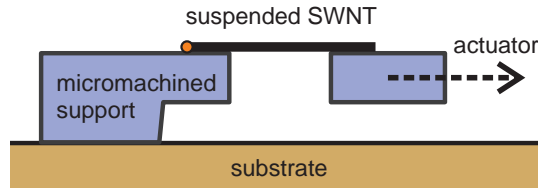
### 3.4 Integration of SWNTs strainable by micro actuators

Motivation

The application of mechanical loads to integrated SWNTs is not only of fundamental interest for the investigation of mechanical properties of nanotubes. Straining nanotubes is also the key to exploit their piezoresistive behaviour in electromechanical transducers and opens possibilities for frequency-tunable mechanical resonators.

Figure 3.11 illustrates straining of an individual nanotube. The drain electrode, one of the two supports of the suspended nanotube, is mechanically connected to a pulling micro actuator.

Overview



**Figure 3.11:** Schematic illustration of a nanotube suspended between a stationary support and a movable shuttle displaced by a microfabricated actuator. A nanotube is uniaxially strained if well aligned to the direction of displacement.

Nanotubes can experience several different kinds of deformation. Tensile strain along the nanotube axis is called uniaxial tensile strain. Off-axis deformations can lead to shear-strain or torsional strain.

Deformations

Earliest deformation experiments of suspended nanotubes [91] made use of probe tips pushing the suspended nanotube perpendicular to its axis. In addition to tensile strain, bending, radial compression, kinking, and possibly torsion were induced simultaneously. To keep the system as simple as possible for comparison with theoretical predictions, less complex deformations are preferred.

Torsional deformation by electrostatically actuated paddles attached to suspended nanotubes was demonstrated [52]. Several electrodes and well defined geometry would be required to apply pure torsional loading without additional tensile contribution.

Torsional Loading

Compared to pure torsion, pure axial strain can be imposed more easily. Linear actuators can axially load a nanotube bridging from a fixed anchor to a shuttle as already shown in Figure 3.11. Alignment of the nanotube axis with respect to the direction of displacement is crucial to avoid rotation around the anchor points of the nanotube. Rotation would imply bending or even non-linear buckling. For calculation of strain levels based on actuator displacement, angular deviation from the displacement direction has to be taken into account. The sharp opposing tips (Figure 3.6) improve alignment of nanotubes in direction of displacement during growth [138, 269]. In case of nanotube transfer from a fork (Section 3.3), the nearest-neighbour attachment aligns nanotubes preferentially perpendicular to the arms.

Axial Loading

Nanotube Alignment

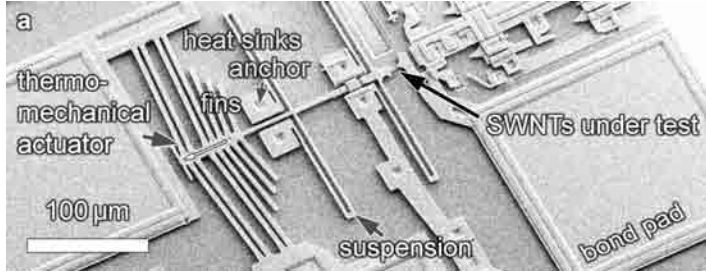
Support Design

Microfabricated actuators are appealing for tensile loading of carbon nanotubes for the following reasons: integration into small-sized systems, compatibility with size-restrictions of measurement chambers (TEM), reduced thermal drift issues compared to external actuators such as AFM probes.

MEMS

Electrically heated thermomechanical actuation and electrostatic actuation were chosen as displacement mechanisms. Piezoelectric materials would be difficult to be integrated in direct growth approaches. Three-/or four-point bending

Actuation Principles



**Figure 3.12:** SEM image of an electrically heated thermomechanical MEMS actuator for integration of SWNTs. Reprinted from [2]. © IEEE, 2011.

devices would be highly accurate due to the immense mechanical reduction ratio and are an appealing option on the macro scale. For the intended use for experiments inside a TEM, however, bending the whole substrate typically requires relatively large forces and much space.

### 3.4.1 Electrically heated thermomechanical actuators

Electrically heated thermomechanical actuators were designed similar to those of Jungen [212, 275] and Espinosa [204]. Figure 3.12 shows an actuator fabricated by poly-Si surface micromachining (PolyMUMPs). A V-shaped array of beams is arranged in a double-clamped manner. This chevron arrangement acts as displacement amplification of the thermal expansion of the electrically heated beams. The centre of the beams is connected to a common backbone, which is coupled to the electrode to be displaced. Compliant springs serve as heat sinks, as additional guidance and as electrical signal paths.

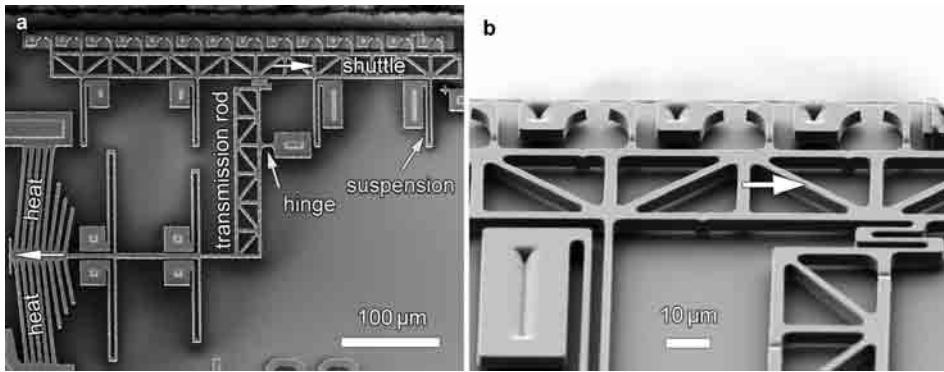
Compared to designs of A. Jungen [212, 275], the thickness of the beams was increased by stacking Poly1 and Poly2. The increased aspect ratio enhances the vertical stiffness. To optimize the design of springs and actuator beams, the ratio of the section moduli  $Z_z$  out of plane and  $Z_y$  in plane has to be maximised.

$$\frac{Z_z}{Z_y} = \frac{\frac{b \cdot h^2}{6}}{\frac{h \cdot b^2}{6}} = \frac{h}{b} \quad (3.3)$$

Using the stack of poly layers instead of a single layer,  $h$  was increased from  $1.5 \mu\text{m}$  to  $3.5 \mu\text{m}$ . The width of each actuator beam was  $3 \mu\text{m}$ .

Actuators based on thermal expansion via Joule heating can induce substantial amounts of heat. To minimise interference with the nanotube under test, the distance to the actuator should be large. Heat sinks via springs anchored to the substrate and fins were added to reduce parasitic temperature increase.

To facilitate TEM investigations in tilted view, to be described in more detail in Section 3.5, the structures under investigation have to be placed close to the edge of the chip. The symmetry axis of an actuator cannot be placed closer to the edge than half of the actuator width. To locate the region of interest closer to the



**Figure 3.13:** Movable shuttle with array of tips close to edge of the chip. (a) SEM image of electrically heated thermomechanical actuator with mechanism. Mechanical motion is translated via a transmission rod from the actuator to the shuttle. (b) Close-up of the tip pairs tilted by  $54^\circ$ .

edge, mechanical transmission rods were used to translate the displacement generated by the actuator onto a shuttle close at the edge. Figure 3.13 shows an array of displaceable tip pairs located at the chip border. A framework construction increased the stiffness of the translation structure. The openings of the framework enabled short release etching times. Dimples reduced the risk of stiction during drying. The array of tips allows mechanical loading of several individual nanotubes per actuator.

### 3.4.2 Electrostatic actuators

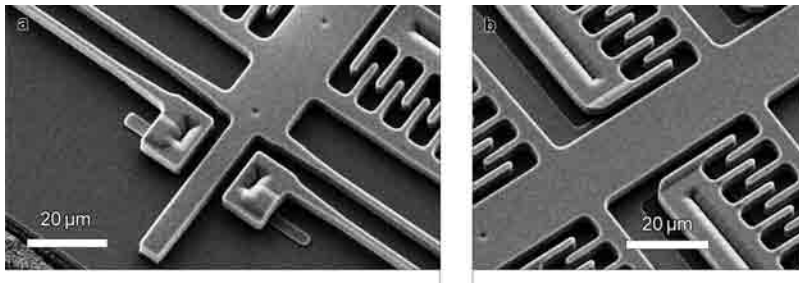
Electrostatic actuators were implemented as an alternative to electrically heated thermomechanical actuators. Charges of opposite sign sitting on opposing surfaces induce attractive forces. Charged parallel plates allow relatively large forces, although thermomechanical actuators can supply higher forces per chip area. The force output per area is weaker for interdigitated electrodes arranged as opposing combs than for parallel plate configurations. But the displacement is more linear with respect to driving voltage. The feature size of  $2\text{ }\mu\text{m}$  limited the number of comb fingers to one finger per  $8\text{ }\mu\text{m}$  comb length. Tree-like structures with several branches of combs were used to increase the number of fingers. The force contribution which is linear with driving voltage arises from the energy minimisation by increasing the overlap between opposing fingers. Dimensions along the actuator axis should be kept short to maintain the required bending stiffness of the moving actuator backbone. Therefore, the distance between the finger ends and the opposing comb plate is finite. Consequently, a force is contributed by the segments at the finger ends (parallel plate) and the fringing fields which are non-linear with driving voltage. Bumper structures and dimples limit the maximum displacement to prevent stiction in-plane and out-of-plane during release etching and during operation (pull-in).

Electrostatic  
Actuation

Comb Drive

Electrostatic actuation avoids temperature issues caused by Joule heating in

Advantages



**Figure 3.14:** SEM image of an electrostatic comb-drive for tensile loading of CNTs.

thermomechanical actuation. This renders the temperature the nanotube more predictable. Besides the small capacitive currents flowing only during displacement changes, there is no static power consumption in principle. Therefore, electrostatic actuation is compatible with cryostatic temperatures where the heat input of Joule heating would corrupt low-temperature measurements. Drawbacks of electrostatic drives are the typically high voltages needed. The designs presented here were operated in a range up to 190 V, while the electrothermal actuators achieve comparable displacements in the single digit Volt regime – but at mA-currents. The high voltages for electrostatic actuation can cause unpleasant image shifts during in situ experiments in electron microscopes.

Catalyst island definition by e-beam lithography and catalyst adsorption require the MEMS structures to be immersed in viscous media. While the electrothermal actuators are robust, sufficient mechanical stiffness was more difficult to obtain for electrostatic comb drives. A compromise between acceptable actuation voltage and mechanical robustness had to be found.

### 3.4.3 Electrical decoupling from actuator driving voltages

Electrical insulation is needed to avoid cross-talk from the actuator driving voltage to the electrodes of the nanotube. For electrothermal actuators, the driving voltage  $V_{\text{act}}$  was applied as  $+\frac{1}{2} V_{\text{act}}$  and  $-\frac{1}{2} V_{\text{act}}$  (anti-symmetric) [212, 275] which kept the actuator backbone at virtual ground<sup>1</sup>. Fabrication asymmetries may slightly shift the potential at the actuator backbone from ideal ground. To a minor extent, the Thomson effect [212] pp.67 also causes asymmetry.

Figure 3.15 shows an approach used to electrically isolate the actuator from the nanotube support electrode. The schematic cross section of the electrical decoupler illustrates the sandwich structure. Two plates of poly-Si were mechanically connected by insulating  $\text{SiO}_2$ . The  $\text{SiO}_2$  stems from the sacrificial oxide. Its etching was retarded by sandwiching the  $0.75 \mu\text{m}$  thin oxide layer between extended plates. The lower plate was spaced from the substrate by a thicker  $\text{SiO}_2$  of  $2 \mu\text{m}$  thickness. A time-dependant etch of 3 min in 40% HF fully removed the thicker oxide, while the thinner oxide remained at the centre part between the

<sup>1</sup> For the practical reason of measuring the full  $V_{\text{act}}$  at a single Keithley SourceMeter 2400, the reference potential of the SourceMeter was set to  $-\frac{1}{2} V_{\text{act}}$  using a second voltage source.

plates. The etching path for the thinner oxide at the step onto Poly1 (highlighted by an arrow in Figure 3.15a) was prolonged vertically and was even slightly thinner than 0.75  $\mu\text{m}$ . The 2  $\mu\text{m}$  additional vertical oxide of reduced thickness helped to maintain the mechanical  $\text{SiO}_2$  link during the release of the thick  $\text{SiO}_2$  layer. Test structures of different sizes placed next to the device structure enabled verification of release timing<sup>1</sup>. The undercuts ensured electrical isolation to be maintained during blanket metal evaporation at tilted sample rotation.

A second approach to decouple the actuator driving voltages from the nanotube drain is shown in Figure 3.16. The mechanically connected actuator and the drain electrode were electrically separated by a discontinuity in the metallisation. A poly-Si bridge spanning across the mechanical connection between actuator and drain electrode patterned the evaporated metal by its shadow. The rough surface of the poly-Si is supposed to cause the observed electrical connection of the bond wires with the underlying poly-Si, even if the native oxide was thickened by heating above 600 °C in air for 15 min and using 100 nm thick metallisation. To suppress any DC cross-talk from  $V_{\text{act}}$  to the drain electrode via the poly-Si, the poly-Si lead to the drain was interrupted by a gap. The electrical path to the drain is given across the gap solely via the metallisation. In addition to the thin  $\text{SiO}_2$ , an insulating oxide layer (40 nm  $\text{Al}_2\text{O}_3$  by ALD at 300 °C) prevented shorts from the metal to the poly-Si.

Approach 2:  
Poly-Si Gap

Compared with the isolation approach by non-conductive glue [203], the here presented decoupling requires only standard processing steps.

Discussion

Micro actuators apply tensile strain on the integrated nanotubes. Electro-thermal actuators and electrostatic actuators featuring appropriate displacement ranges were designed to withstand the wet processing steps during release etch, and during catalyst patterning in case of shadow masking. The driving voltage is electrically decoupled from the nanotube drain. Mechanical transmission rods enable placement of actuated tip pair arrays close to the edge of the die.

Summary

### 3.5 TEM-accessibility of suspended SWNTs devices

Transmission electron microscopy (TEM) (Appendix B.2.1) can provide information about individual nanotube devices not obtainable by SEM or Raman spectroscopy. The main difficulty in sample preparation for TEM is the requirement for electron beam transparency. The thinness and the low atomic number of SWNTs demand a very thin support or even better a suspended configuration without any obscuring support at the region of interest. Even background contribution of thin supports can severely deteriorate contrast of single-walled nanotubes.

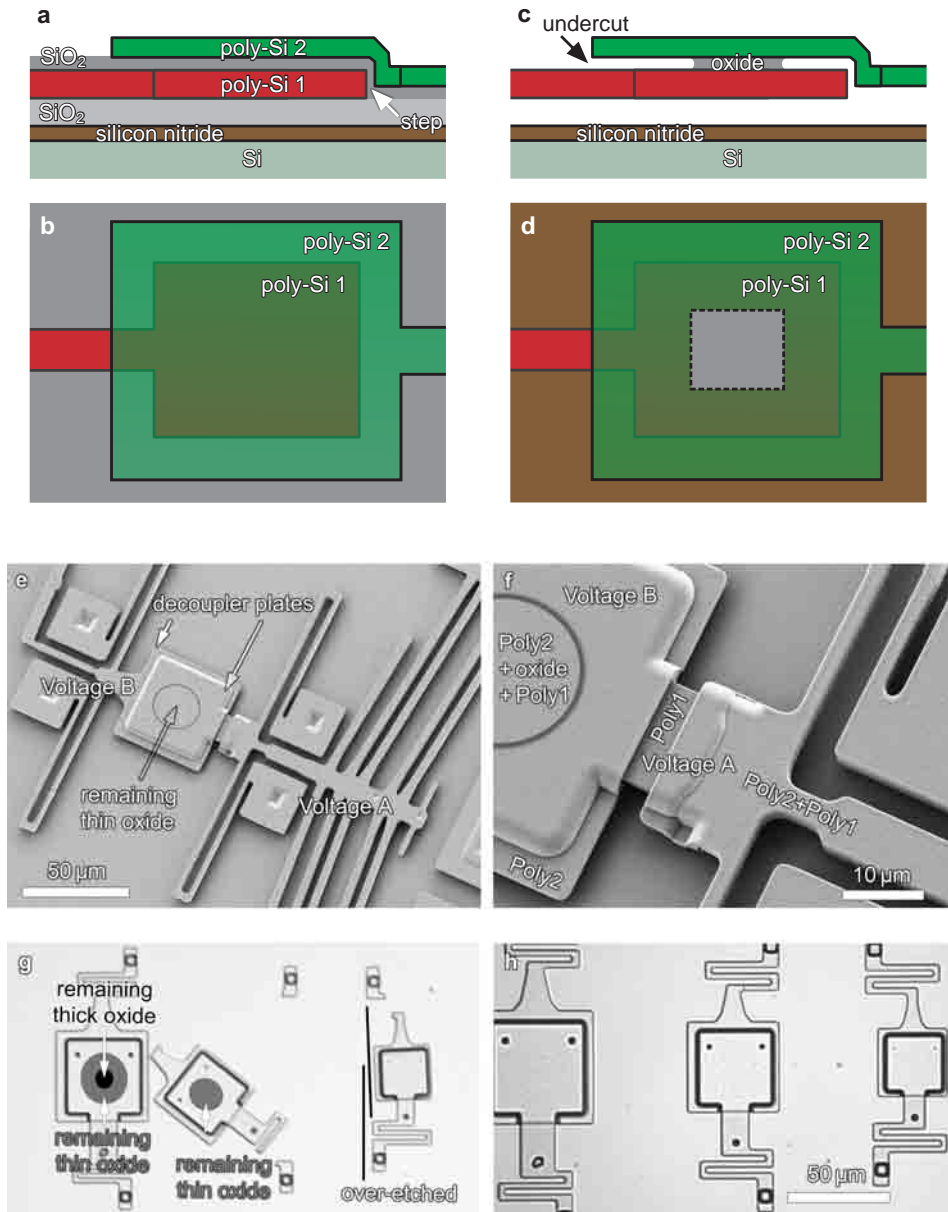
Motivation

Challenge

Notches were etched from the front side within the standard PolyMUMPs mi-

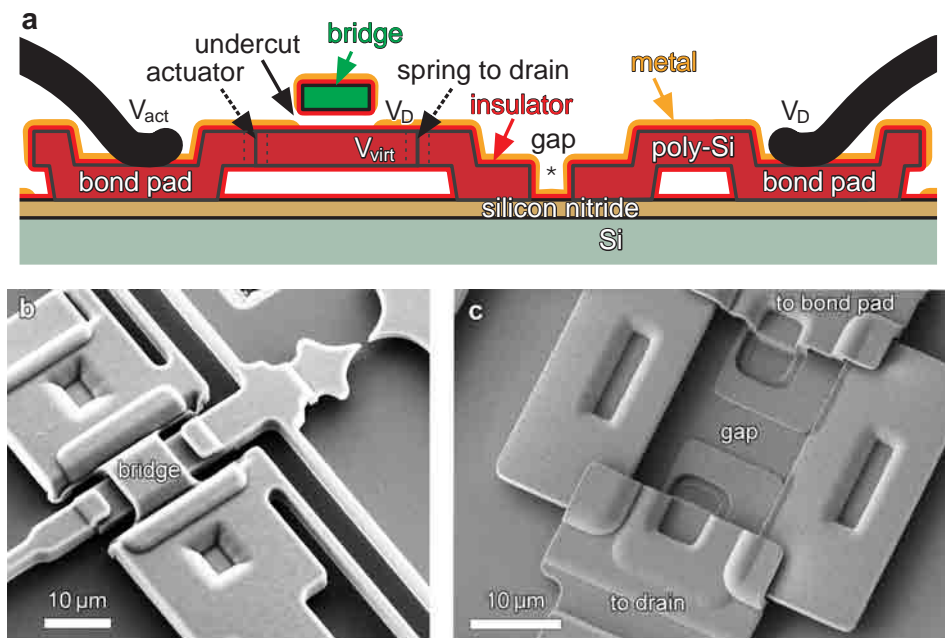
Solution

<sup>1</sup> Proper release of the thick oxide is indicated if the suspended dummy decoupler moves upon lateral pushing by a probe needle or by a manually controlled AFM tip. Hard pushing elastically deforms the plates in the periphery where they are not connected by the thin  $\text{SiO}_2$ . Thus, the size of the remaining  $\text{SiO}_2$  joint can be visualised in light microscopy as a planar centre area of the plate stack under heavy deformation. Over-etching of the thin oxide is observable as rotation of the two plates towards each other or as non-joint movement of the plates.



**Figure 3.15:** Concept A of an electrical decoupler. The actuator side is electrically disconnected by the remaining thinner layer of sacrificial oxide. (a) Cross-sectional sketch before release etch. (b) Top view. (c) After timed release etch in concentrated HF, cross section. (d) Top view. (e) SEM image of decoupler in inclined view. (f) Close-up of decoupler plates. (g) Optical image of test structures for mechanical verification of full release of thicker oxide layer and remaining thinner layer (middle). For the larger plate (left), thick oxide still remained, as schematically illustrated by the black dot. The smaller plate (right) was over-etched as indicated by the slight rotation. (h) Close-up of the test structures for release etching before pushing.





**Figure 3.16:** Concept B of an electrical decoupler. (a) Cross-sectional sketch. The actuator side is electrically disconnected by a gap in the metallisation created by a bridge with undercuts.  $\text{Al}_2\text{O}_3$  from ALD ensures electrical isolation to the poly-Si. Probably due to the rough surface of the poly-Si bond pads, wire bonds can penetrate the oxide and connect to the poly-Si. Therefore a gap in the poly-Si (highlighted by an asterisk) is needed to prevent cross talk from the actuator to the drain. The actuator and the flexible spring to the drain electrode of the pulled nanotube are not shown in detail for simplicity. (b) SEM image in inclined view of the bridge which interrupts the metallisation. (c) Additionally, a gap is interrupting the poly-Si for electrical separation of the metal layer from the poly-Si. This is needed because the wire bonds connect to the poly-Si. Across the gap, the current is carried by the metallisation on the insulating silicon nitride.

crofabrication. Electron beams slightly tilted from being parallel to the chip surface can interact with the integrated nanotube. The notches lead into the dicing path and allow the electron beam to be transmitted un-attenuated.

In the following, SEM (Appendix B.2.3) and Raman spectroscopy (Appendix B.2.5) are briefly revisited as characterization methods complementary to TEM. Options for transmission beam access are discussed and the fabrication scheme for the tilted-view access is described.

Confocal Raman spectroscopy is a powerful characterization method for nanotubes, especially if the nanotubes are free-standing as in the configurations here. As the trenches (or gap between the electrodes respectively) are at least  $2.25\text{ }\mu\text{m}$  deep, the confocality at a depth of focus of about  $1.5\text{ }\mu\text{m}$  can efficiently exclude signals from the underlying substrate. Valuable information about de-

Content

TEM vs.  
Raman

fects and amorphous carbon can be gathered from the D-mode intensity. Raman spectroscopy can reveal the diameter of integrated nanotubes if they are close enough to resonance conditions to allow RBM detection. In some cases chiralities can be assigned. Metallic and semiconducting nanotubes can be distinguished by the line shape of the G-mode. Bundles can be detected if different RBMs are recorded. However, bundles cannot be excluded using a single laser line as the RBM resonance conditions may be missed. Although interactions between the walls of double-walled nanotubes alter their spectroscopic signature in principle, the inner or the outer wall can be excited and can contribute to a single RBM peak. Interpretation concerning the number of nanotubes and the number of walls is difficult. The position of the nanotube can only be coarsely estimated, due to the diffraction limited spatial resolution (spot size 400 nm).

TEM vs. SEM

Scanning electron microscopy (SEM) enables precise visualisation of the location of the nanotube. Inclined views (stage tilt, and/or pre-tilted sample mounting) allow an estimation of the horizontal position. For instance, a nanotube can be identified to span from the top surface electrode down to the sidewall of the opposing electrode.

To highlight the benefits from fabricating samples accessible by transmission beams, the information which can be provided using TEM and scanning transmission electron microscopy (STEM) beyond the capabilities of SEM is listed.

TEM imaging mode:

- number of nanotubes in a bundle
- diameter from electron-optical image
- distinction between single and multi-walled tubes
- grain sizes of metal contacts
- deformation of nanotubes at contacts
- more precise visualisation of contamination
- imaging of nanotube ends: open or capped; kinks; catalyst shape

TEM in diffraction mode:

- chiral angle from layer line spacing
- diameter from equatorial line
- unambiguous chirality assignment for straight, aligned SWNTs of small diameters ( $< \sim 3$  nm) (tentative for larger diameters as differences in  $d$  and  $\theta$  shrink with larger  $d$ )
- verification of continuity of chirality along nanotube (100 nm nanotube length is enough for a diffraction pattern)

A sample compatible with TEM can also be investigated by  $C_s$ -corrected STEM (Appendix B.2.4), which enables following options:

- enhanced spatial resolution
- chemical analysis by electron energy loss spectroscopy (EELS) and energy-dispersive X-ray spectroscopy (EDX) of contacts (oxidation) and catalysts

- (SE detector facilitates finding of region of interest)
- 3D tomography

In summary, the higher resolution achievable by TEM and STEM compared to SEM provides information about diameter, number of nanotubes and contact geometry. TEM electron diffraction is one of the most reliable chirality assignment methods. Electron diffraction unambiguously discriminates between single- and double-walled CNTs. STEM opens possibilities for enhanced spatial resolution and chemical mapping at the nanoscale. For those reasons, it is very valuable to enable electron beam transparency of functional devices.

Conclusion

### 3.5.1 Options for TEM-accessibility

As presented in Section 2.5, there are different options to allow transmission beam investigations of nanomaterials in microfabricated devices. The most common one is by wafer through holes. A mask is aligned on the back side and holes penetrate the wafer by etching from the back side. The 650  $\mu\text{m}$  thickness of the PolyMUMPs die prohibits infrared back side alignment. As the standard die size of PolyMUMPs is only 2 mm  $\times$  2 mm, at a maximum die size of 10 mm  $\times$  10 mm, alignment by a back side camera is not feasible using our current chuck of the mask aligner. Moreover, the 600 nm silicon nitride (front and back side) would need to be removed during the PolyMUMPs process itself as done by Espinosa *et al.* [204]. This special request would impose high costs as front side Si nitride etching is not available in the standard process flow. We demonstrated removal of the nitride by focussed ion beam (FIB) milling from the front side. However, this is a time-intensive serial process. Large area etches are needed at the back side (as the upper limit of aspect ratio during inductively coupled plasma (ICP) etching of 650  $\mu\text{m}$  Si and the back side misalignment impose a lower limit to the hole size). Instead, a hard mask for etching on the back side could be patterned by electron beam lithography. In general, the size of through wafer holes has to be sufficiently large to account for limited aspect ratio during etching and for potential misalignment. Large hole sizes can impose design restrictions as anchors to the substrate can not be placed in the area occupied by the hole. Combined coarse etching from the back side and fine etching from the front side [241] was applied by A. Pohl [276] using the buried SiO<sub>2</sub> layer of an SOI wafer as etch stop. Micron-scale trenches in membranes of crystalline material were fabricated, enabling combined investigations of as-grown nanotubes by AFM, Raman and TEM [276]. In any case, a many-step process involving back side alignment and through wafer etching is needed for through holes.

Through  
Holes

J. Meyer *et al.* clamped nanotubes by metal leads patterned by electron-beam lithography and lift-off. To enable TEM investigations, the die was cleaved close to the device and bulk etching removed the substrate underneath the device [52, 69, 70]. Using this method, Meyer demonstrated an electrostatically driven torsional nanotube pendulum [52]. This concept might be adapted to incorporate MEMS actuators for tensile loading too. For instance by a wide, mechanically

Wet Etch at  
Edge

rigid beam that is electrostatically deflecting a narrow, parallel beam attached to a nanotube under test. However, the nanotube and its electrical contacts have to be exposed to KOH etchant for several hours and careful drying is needed – both are potential causes of contamination.

### 3.5.2 Tilted-view transmission electron microscopy

Tilted-View	The method used here to integrate SWNTs into poly-Si micro actuators accessible for transmission beam investigations is as follows, and was published in [103].
Closeness to Edge	As depicted in the cross-sectional sketches of Figure 3.17b and c, the electron beam must penetrate the nanotube without being absorbed by the substrate. To achieve TEM-accessibility without the need for wafer through holes or bulk wet etching, the nanotube is located close to the edge of the die (25–200 $\mu\text{m}$ from the edge). The nanotube is suspended between support structures slightly elevated above the substrate level (3.5–6.75 $\mu\text{m}$ ). The nanotube can be reached by the transmission electron beam by irradiating the die nearly parallel to the substrate surface. As shown in Figure 3.17b, the vertically mounted substrate is slightly tilted off the coplanar orientation to the beam. Hence, electrons can interact with the nanotube without being stopped by the substrate. Here, this inclined observation configuration is called tilted-view TEM.
Elevation	
Notch	To allow for larger tilting angles without blocking the electron beam by the edge of the die, the substrate was etched from the front side. Also shown in Figure 3.17a and d, the notch starts near the position of the nanotube. The notch continuous towards the edge of the chip and reaches the dicing path. The notch was etched by several front side etching steps already available in the PolyMUMPs process. The overlay of the two anchor etches, the via etch, and the dimple etch dug through the 600 nm silicon nitride into the Si handle. The depth of the resulting notch was $\sim 4.5 \mu\text{m}$ . Neglecting the original purpose of all these etching masks, the notch was formed in parallel to the MEMS fabrication without any additional processing effort. Standard manual dicing with a 30- $\mu\text{m}$ -wide, diamond-coated blade reliably achieved the $\pm 25 \mu\text{m}$ precision needed to avoid damage of the structures close to the edge of the die.
Tilt Range	The tilt angle $\alpha$ of the TEM sample holder has to be adjusted carefully, or else the nanotube becomes hidden either by the closer edge or by the far edge of the die. If the tilt is inappropriate, clipping can occur in electron diffraction pattern, as shown in Section 4.4. At a distance from the edge of 165 $\mu\text{m}$ and at an elevation of 4.25 $\mu\text{m}$ above the substrate level, the notch increases the angular range of accessibility from $\alpha = 1.5^\circ$ to $3.0^\circ$ , provided the nanotube is lying on top of the support structures. For other designs as close as 25 $\mu\text{m}$ from the edge and at 6.75 $\mu\text{m}$ elevation, the accessible range is increased from $15^\circ$ to $24^\circ$ by the notch. In the other tilt direction ( $\beta$ -tilt), the sharp opposing tips allow for widely unrestricted access.
Focal Plane	Alignment of the SWNTs to the TEM focal plane is facilitated by nearest neighbour alignment (3.2.3) occurring at the sharp opposing tips. The opposing tips are aligned parallel to the close edge of the die. However, the growing nano-

tubes were preferentially aligned in the focal plane by nearest neighbour attachment. Thus, the nanotubes were often aligned nearly perpendicularly to the beam, which is important for electron diffraction (B.2.2). Moreover, the sharp tips can be partially penetrated by electrons at the thin apex, which enables imaging nanotubes in contact with the poly-Si. The tips also simplify coarse focusing and the adjustment of the eucentric height. The tilted-view TEM images are nearly 90° rotated with respect to top-view SEM images. Hence, this TEM side-view can reveal relevant geometrical information about the nanotube not seen in SEM images taken in top-view only.

Side-View

### Related work

J. Meyer introduced an approach called „Isotropic underetching near the corner“ [70] p.29, which is very similar to what is called tilted-view TEM here. Wet etching releases clamped nanotubes, and those nanotubes very close to the edge of the substrate can be observed in TEM. However, only nanotubes as close as 1–2 µm to the edge were accessible. Etching after the integration of the nanotubes exposes the nanostructures to etchants and requires critical point drying to prevent damage. Here, accessibility is ensured by raising the nanotubes higher above substrate level and by etching a notch towards the well defined location of the dicing edge.

At Edge

In 1999, A. Cassell *et al.* [137] showed TEM images of SWNTs grown between arrays of microfabricated towers. Similarly, Takagi and Homma *et al.* [242, 277] imaged SWNTs grown on large arrays of 360 nm-high pillars. The substrates were cleaved and mounted nearly vertically (tilted by a few degrees) into a TEM. SWNTs suspended between the pillar rows in the vicinity of the cleaved edge were accessed by the transmitted electron beam. However, to enable characterization of functional SWNT integrated in MEMS devices, control over the position of the edge is needed, which is difficult to be achieved by cleaving Si substrates. Unless using mechanical transmission rods (3.4.1), the restriction in accessing only the outermost edge of the chip must be overcome to provide enough area for actuators or inertial masses.

Pillar Arrays

In previous work by A. Jungen, electron transparency was obtained by sliding large micromachined grids [264] and actuator structures [211] beyond the edge of the chip. This imposes limitations on MEMS design as mechanical anchoring of actuators is difficult under the constraint that the structures must be moved. Moreover, the reliability of electrical connections to the relocated actuator tends to be poor at larger currents.

Sliding

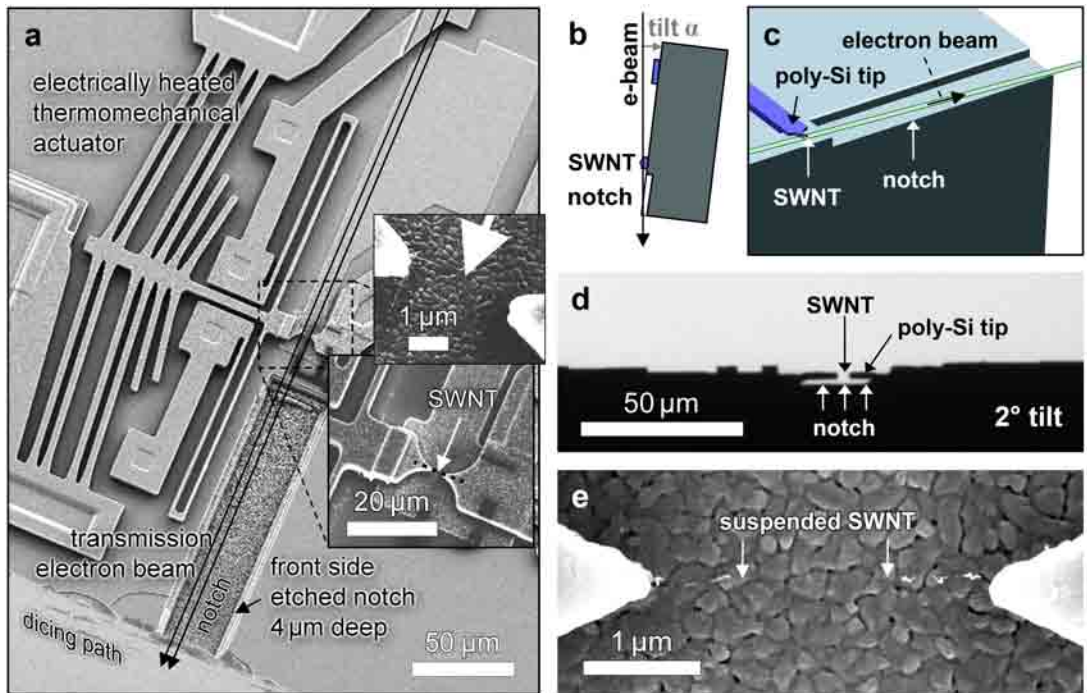
Inclined observation by SEM enabled observation of the deflection of suspended nanotubes upon gating, as demonstrated by Weng *et al.* [278].

Tilted SEM

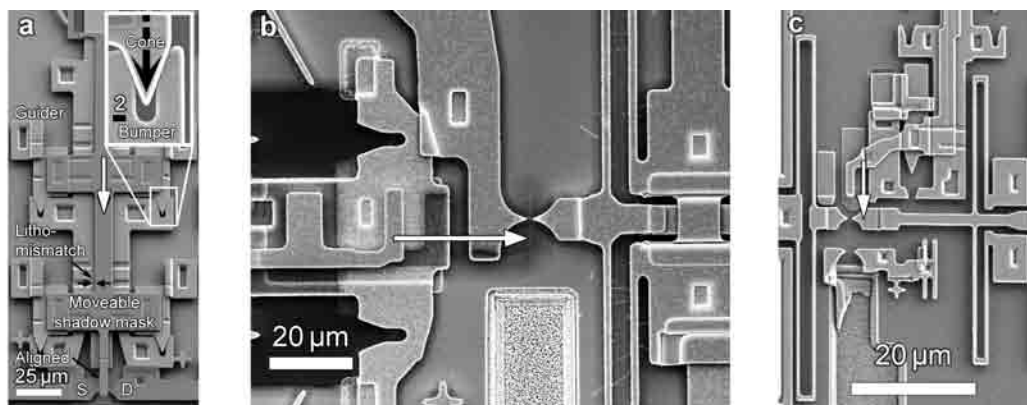
### Compatibility of the shadow mask with tilted-view TEM

Important for TEM accessibility of samples with on-chip shadow masks (3.2), the mask must not hide the nanotube from the electron beam. For nanotube locations close to the edge of the die, retracting the mask is sufficient to allow electron beam

Mask



**Figure 3.17:** Access to functional nanotube devices by TEM in tilted-view. (a) SEM image with a sketch of a SWNT on a MEMS actuator. The TEM beam is represented by two parallel arrows passing through the nanotube close to the surface of the chip. The notch is fabricated by overlaying front side etching steps which penetrate the substrate for more than 4  $\mu\text{m}$ . The insets show the two polysilicon tips facing each other. A nanotube (schematically represented by the dashed line in the lower inset) bridges between the poly-Si tips and is elevated above the substrate. (b) Cross-sectional sketch of the vertically mounted die allowing for electron beam access to nanostructures located on centre area of a MEMS chip. The notch towards the edge of the chip enlarges the accessible angular tilting range. (c) Cross section of the die in perspective representation. (d) Low-magnification TEM image in tilted-view. At the tilt angle of 2°, the opposing poly-Si tips become visible (side-view). Direction of view corresponds to the black arrow in b. (e) Top-view SEM image of a SWNT spanning across the sharp poly-Si support tips. The metal clusters on the nanotube originate from shadow masked metallisation (2 nm Cr/60 nm Au). More detailed TEM images of this nanotube are given in Figure 4.1a. The nearest neighbour alignment preferentially orients the nanotubes in the TEM focal plane. Reprinted from [103]. © Elsevier B.V., 2009.

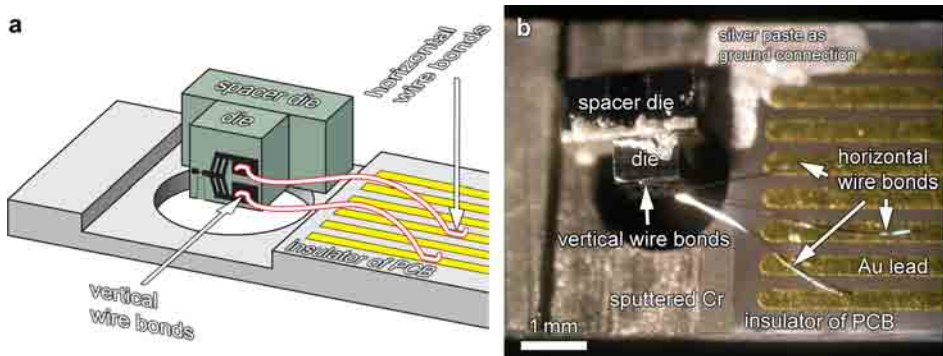


**Figure 3.18:** SEM images of shadow masks compatible with TEM observation in tilted-view. (a) Vertically moved shadow mask slider with extended retraction range to enlarge the angular accessibility for the transmissive beam. (b) Horizontal movement of the shadow mask slider. White arrow indicated sliding direction. The slider does not need to be retracted for TEM accessibility. (c) Parallel oriented slider with horizontal off-set. Parts are reprinted from [101]. © Macmillan Publishers Limited, 2010.

access. For positions far from the edge, and in general to enlarge the angle of observation, the movable range of the shadow mask slider was extended, as shown as comparison in Figure 3.18 a and b. Larger retraction distances are needed if the shadow mask bends upwards due to the bimorph-like effect of thick metal layers featuring intrinsic stress on top of the poly-Si shadow mask finger. Alternatively, to extended retraction ranges, the slider can be placed laterally beside the beam path, as shown in Figure 3.18c and d for two variants. The mask is short enough in direction of the beam not to block the electron path while resting above the nanotube. The design shown in 3.18d is slid perpendicularly to the nanotube axis and offers more precise alignment compared to c.

For tilted-view TEM observation, the die has to be mounted vertically into the sample holder. Standard Cu platelets (3.05 mm in diameter and 50  $\mu\text{m}$  thick, from Gilder) with rectangular openings (2 mm  $\times$  0.75 mm) were used as support. A drop of electrically conductive silver-epoxy glue (EPO-TEK<sup>®</sup> H20E, from Epoxy Technology) was placed next to the opening of the Cu platelet using a thin Cu wire. The chip was gripped by tweezers and rotated by 90° into vertical position, as sketched in Figure 3.17b. The down-facing sidewall was pressed onto the epoxy glue, while centring the edge of the die to the middle of the opening in the Cu platelet. The epoxy glue provides secure mechanical fixation and electrical conductivity. Electrical conductivity is required to dissipate charges which accumulate during electron microscopy. A heat treatment on a hotplate at 125° for 20 min cured the epoxy glue. A dummy droplet served as a reference to monitor the hardening. To prevent the die and the copper support from being glued inadvertently to the microscope slide used as a carrier, the Cu support was placed on

Vertical  
Mounting



**Figure 3.19:** (a) Sketch of a vertically mounted die wirebonded to the PCB for in situ TEM experiments. (b) Optical image of a vertically mounted die wirebonded for the CM12 TEM holder with electrical feedthroughs (nearly top view).

a cleanroom tissue. Two additional microscope slides weighed the tissue down to counteract buckling of the tissue during heating.

Wire Bonding  
TEM-  
compatible

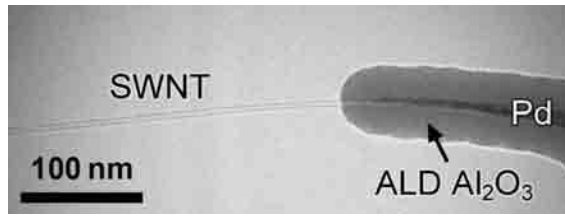
Wire bonds connected the micro actuators for mechanically straining the nanotubes inside the electron microscopes. The driving voltage of the actuator was supplied via the electrical feedthroughs of dedicated TEM sample holders, as described in Appendix B.2.1. In situ actuation allowed investigation of clamping conditions (5.3.1) and straightening of nanotubes required for electron diffraction (5.3.1). The vertical mounting of the chips for tilted-view TEM requires the wire bonding to be adapted. The bond wire must connect the horizontal Au leads of the PCB with the vertical bond pads of the die. First, the die was glued temporarily in horizontal orientation onto a dummy PCB using silver paste. The wire was bonded to the dummy PCB, but the bonding parameters were detuned towards too high bonding weight at the first bond. Thus, the wire was ruptured off the PCB after loop formation while moving the bond head backwards at search-height. The freestanding wire was attached only at the head and was bonded onto the bond pad of the die. Using tweezers, the die with the single-clamped wires was detached from the dummy PCB, was rotated by 90°, and glued in vertical orientation onto the target PCB. Figure 3.19 shows a spacer die, secured with epoxy glue in advance, which facilitated placement of the die surface near the centre of the hole. The PCBs had been sputter-coated with 120 nm chromium (Cr) from both sides to reduce image distortions otherwise appearing due to charging of the insulating material. Kapton® tape shielded the Au leads of the PCB from Cr deposition.

### Conclusions on tilted-view TEM access

Summary

Integrated, as-grown SWNTs become accessible by transmitted electrons without the need for wafer through holes. Exploiting the standard MEMS fabrication process steps (PolyMUMPs), the nanotube support structures are raised above substrate level and a notch is etched on the front side towards the edge of the die.





**Figure 3.20:** SEM image of an encapsulated Pd contact to a SWNT. Surface-selective atomic layer deposition (ALD) of  $\text{Al}_2\text{O}_3$  nucleates conformally on the contacts but not on individual, clean, and defect-free SWNTs. Reprinted from [1]. © Wiley, 2010.

Compared to cleaving, the location of the dicing edge is well defined. Accessibility to functional devices farther from the edge is ensured.

### 3.6 Passivation of electrical contacts

In this section, a process to encapsulate the contacts of suspended nanotubes is described. Depending on contact materials, passivation of electrical contacts can be needed to prevent contact degradation. T. Helbling *et al.* achieved long-term electrical stability of Au/Cr contacts via an encapsulation made of  $\text{Al}_2\text{O}_3$  from atomic layer deposition (ALD) [89]. Importantly for understanding chemical sensing, passivation can separate sensing mechanisms related to metal contact regions from those related to the SWNT channels [54, 279].

Encapsulating the metallic contacts is challenging for suspended SWNTs. For surface-bound devices, selective encapsulation of contacts was achieved by an  $\text{Al}_2\text{O}_3$  passivation layer into which windows were etched patterned by EBL [54, 279]. But such resist-based shaping can hardly be applied for suspended SWNTs, as individual freestanding SWNTs are prone to rupture during spin coating of resists. The risk of mechanical damage is especially pronounced if the nanotubes are several micrometres long [22]. Moreover, the cleanliness of the nanotubes maintained so far would suffer from wet chemical treatments during lithography and etching.

Figure 3.20 shows selective nucleation of an  $\text{Al}_2\text{O}_3$  passivation layer applied here to enable encapsulation of the Pd contacts to a suspended SWNTs only, while leaving the suspended part of the nanotube open to the environment [1].

The surface-selective ALD approach does not expose the SWNTs to wet-chemistry and eliminates the need for resist-based patterning. Therefore, resist contaminations during passivation are avoided.

Atomic layer deposition is a method where two precursor gases are alternately adsorbed on the substrate. Each cycle will result in a chemical transformation of exactly one adsorbed layer. Controlling the cycle number is effective in controlling the thickness of the deposited material. ALD provides conformal, pinhole-free [280] layers deposited at low temperatures [281]. Conformity and tightness are considered to be important to prevent the oxidation of contacts. For

Encapsulation  
Objectives

Challenge

Solution

Surface-  
Selective  
ALD  
Advantage

ALD

metallic contacts, it is beneficial that the deposition temperature for the encapsulation process is low (here, down to 110 °C). ALD can be free of any exposure to plasma, which otherwise would be harmful for the carbon nanomaterial. ALD layers are known not to grow on clean and defect-free SWNTs [185, 189, 282, 283], while growth nucleates on substrates, on functionalised SWNTs and on multi-walled carbon nanotubes (see references in [1]). On SiO<sub>2</sub> and on metal surfaces, ALD is initiated by chemisorption of precursor gas molecules. Because defect-free SWNTs are chemically inert and dangling bonds are absent, nucleation of ALD layers is inhibited on the surface of carbon nanotubes [282, 283]. The growth starts on the substrate or on the contact. The layer grows onto the SWNT, but the interaction between SWNTs and the dielectric encapsulation is rather of van der Waals type than covalent bonding. Scattering due to interface states and structural deformation is probably low for atomic-layer deposited materials such as Al<sub>2</sub>O<sub>3</sub>, HfO<sub>2</sub> [283, 284] and ZrO<sub>2</sub> [284].

Equipment	ALD of Al <sub>2</sub> O <sub>3</sub> was carried out in a Picosun Sunale R-150B system by sequentially pulsing trimethyl aluminium Al(CH <sub>3</sub> ) <sub>3</sub> and H <sub>2</sub> O as precursor gases. N <sub>2</sub> served as carrier gas. Deposition temperatures ranged from 110 °C to 300 °C.
Summary	Encapsulation of electrical contacts to suspended SWNTs is patterned resist-free by surface-selective nucleation of atomic-layer-deposited Al <sub>2</sub> O <sub>3</sub> . The suspended, individual, clean and defect-free SWNTs remain non-encapsulated, which is required for chemical and strain sensing as well as for resonator applications.

### 3.7 Conclusions on Fabrication

Contacting As-Grown CNTs Stencil Lithography	The process flows presented in this chapter for integration of suspended SWNTs prevent mechanical damage and contamination by residual resists.  Shadow masking allows the electrical integration of clean, suspended nanotubes into micromachined actuators. Nearly any material can be chosen for the contacts as the metallisation is applied after nanotube synthesis. The needle-like apexes of the contacts are self-aligned to the nanotube.
Transfer	As an alternative approach, transfer of nanotubes from a fork structure improves three major issues. (i) Pre-aligned nanotubes can be placed at the target location, without the need of precise control over the number, position, and direction of nanotubes during growth. The nanotube area density can be tuned on separate growth substrates without wasting MEMS devices. Insufficiently long nanotubes are discarded as well as those growing in wrong directions. The gate distance can be reduced as only long nanotubes are placed: The risk, present in direct growth, that downwards growing nanotubes short circuit to the gate is excluded. (ii) The device die can be kept at low temperatures as only the growth die with the fork needs to endure the nanotube synthesis conditions. This opens a way for monolithic integration of readout circuitry or the use of polymer substrates. (iii) Selection of a specific nanotube out of an ensemble is enabled.
Actuators	MEMS actuators can provide mechanical loading of clean, suspended nanotubes. The design is stiff enough to prevent stiction during the wet processing

steps of catalyst patterning. For mechanical tests, arrays of opposing tip pairs can be driven by a single actuator.

Vertically mounted samples allow TEM investigations on nanotubes integrated in MEMS supports, which can be actuated in situ. Electron beam access is provided via a notch reaching into the dicing edge. Notch formation by existing front side etching steps of the MEMS fabrication process replaces back side mask alignment and back side patterning. Sharp poly-Si tips can guide the alignment of nanotubes during their waving growth. Thus, the nanotubes preferentially lie in the focal plane of the microscope – and are aligned to the direction of displacement. The nanotubes are sufficiently elevated above the substrate to allow for confocal Raman spectroscopy with low background contribution.

TEM  
Accessibility

A dry process aiming at passivation of the contacts is demonstrated to cover the contacts while leaving the suspended, clean and defect-free nanotube section unaffected. This resist-free patterning relies on the surface-selective nucleation of atomic-layer-deposited  $\text{Al}_2\text{O}_3$ , and it is conducted at moderate temperatures.

Encapsulation

SWNTs are integrated in a suspended transistor configuration into devices equipped with microfabricated tensile stages. The complete process flow is optimized for cleanliness: Electrical contacts and their passivation are patterned without contamination-prone resist-based lithography. Two alternative nanotube integration processes are utilized: (1) On-chip shadow masking forms self-aligned, nano-tapered contacts to the as-grown nanotube, without exposing the metallisation to the harsh growth conditions. (2) Contamination-free transfer from a fork opens possibilities for nanotube selection and ensures nanotube placement exclusively at the predefined location. The device die is kept permanently at moderate temperatures which paves the way for monolithic integration. The functional nanotubes are accessible by TEM, which enables counting of the number of nanotubes, and of their walls, and allows chirality measurements by electron diffraction. The actuators can be driven inside the TEM to investigate the nanotube clamping conditions.

Summary



# 4 Characterisation: Ultraclean, suspended CNFETs

In this chapter, TEM imaging of integrated nanotube devices and chirality assignment by electron diffraction is presented. Hysteresis-free operation of ultraclean, suspended nanotube field-effect transistors is shown for both fabrication methods – on-chip shadow masking and direct transfer from a poly-Si fork. Electrical influences of passivation are investigated. Table 1.1 (Section 1.4) lists the different samples and highlights the achievements. Parts of this chapter were published in *Nature Nanotechnology*<sup>1</sup> [101, 285] and elsewhere [1, 2, 102–104, 286].

Content

## 4.1 TEM imaging of integrated nanotubes

Nanotubes were directly grown on poly-silicon MEMS structures (Section 3.2.3). As described in Section 3.5, accessibility by transmissive electron beams is provided via tilted-view. The beam passes along the slightly inclined chip surface, interacts with the nanotube which is suspended few micrometres above the substrate, and reaches the detector via a notch towards the nearby dicing edge of the die. Figure 4.1a, published in *Sensors and Actuators B* [103], shows a TEM image of an integrated nanotube spanning the gap between sharp micromachined poly-Si tips of a micro actuator (Sample #ed1). The actuator design is the same as the one shown in Figure 3.17a. The nanotube was grown by ferritin-based Fe-catalysed chemical vapour deposition and a top-view SEM image was shown in Figure 3.17e. Although the SWNT spanning the tips is located 165  $\mu\text{m}$  away from the edge of the die, the notch enabled TEM imaging at an accessible tilt range of 2.5°. Thus, the geometry of metal contacts to nanotubes can be investigated and the absence of SWNT bundles can be confirmed. The diameter  $d$  was measured from the bright field image to be  $2.27 \pm 0.1$  nm.

Imaging  
Integrated  
SWNTs

As shown in Figure 4.1a and more pronounced in Figure 4.1b, the sharp tail of the polysilicon tip becomes thin towards its apex – sufficiently thin to be penetrated by electron beams at 100 keV. This way, TEM images can be collected of SWNTs in interaction with the substrate. For the SWNT of Figure 4.1c, a diameter of  $\sim 2.6$  nm was derived in the freely suspended section whereas the imaged diameter increased to  $\sim 2.7$  nm in the polysilicon-supported section.

Substrate  
Interactions

Widening of the apparent diameter indicates radial deformation of the nanotube by interactions with the substrate. Hertel *et al.* [199] predict 13% radial compression of a 2.71-nm SWNT due to van der Waals forces. The increase in lateral

Discussion

<sup>1</sup> see footnote at Section 3 for details about ownership of copyright

dimensions by 7% ( $\sim 2.9$  nm) is of the same order as the here estimated  $\sim 4\%$ . Imaging the thinned side face of the tips (Figure 3.6) by tilted-view is not only an enabling platform to investigate growth catalyst nanoparticles but it may also be a beneficial approach to prepare thin or pre-thinned samples for TEM in general. Cumbersome ion milling by focused ion beam and demanding lift-out of TEM lamellae might be bypassed. Most importantly, the nanotube device can be investigated without the risk of artefacts originating from sample preparation.

## 4.2 Chirality assignment by electron diffraction

TEM electron diffraction [6, 95, 97] (Appendix B.2.2) was applied to assign the atomic structure of integrated SWNTs. As for imaging, the suspended nanotubes were accessible for transmissive beam investigations using the tilted-view approach (Section 3.5) [103, 286].

### Chirality assignment to nanotube integrated onto microactuator

Electron  
Diffraction

Electron diffraction of the same individual SWNT shown in Figure 4.1 was performed [103] (see theory and instrumentation B.2.2 and experimental A.2). The diffraction pattern is shown in Figure 4.2a. Figure 4.2b shows the comparison to a simulated diffraction pattern [95] of a (17,17) nanotube. The chiral indices (17,17) were unambiguously assigned to the integrated nanotube as summarised in Table 4.1. The indices (17,17) correspond to an armchair-type nanotube with a calculated diameter of 2.305 nm. The armchair nanotube is expected to exhibit metallic electronic properties in absence of torsional deformation.

Unambiguity

The chiral angle  $\theta$  was measured from layer line spacings of the diffraction pattern to be  $30.0^\circ + 0^\circ / -0.2^\circ$  (Appendix B.2.2, Equation B.22). Alternatively to (17,17), a (17,16) or an (18,17) nanotube would be closest with respect to chiral angle ( $29.00^\circ$  and  $29.06^\circ$ ) for a similar diameter. The  $1^\circ$  deviation from  $30^\circ$  would result in a rotation of both hexagons of diffraction spots in opposite directions. The splitting of the layer lines of a (17,16) nanotube is shown in the simulation of Figure 4.2c. Intensity profiles lines perpendicular to the layer line (averaged over a width of 70 pixels) are shown as insets in Figure 4.2c. The experimental intensity shows a single peak only. This confirms the chiral angle of  $30^\circ$ <sup>1</sup>.

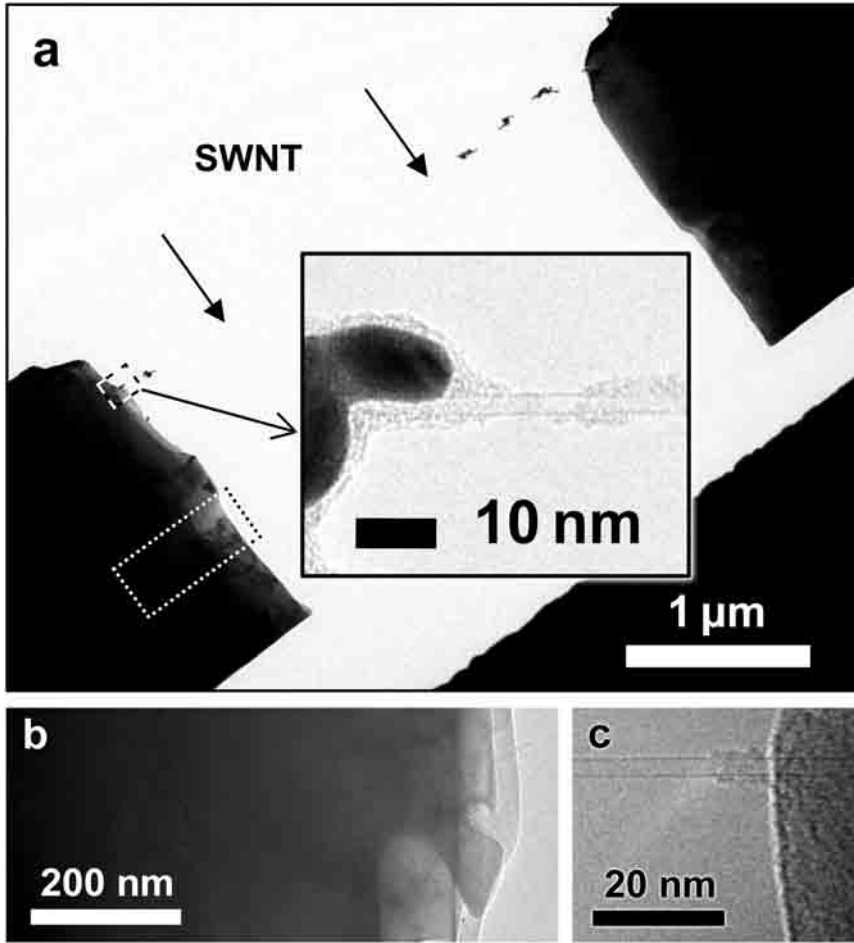
Diameter

The closest alternative chiralities with  $\theta = 30^\circ$  would be (16,16) and (18,18) with diameters of 2.170 nm and 2.441 nm respectively. Figure 4.3a shows the measured intensity profile of the equatorial line in comparison to the simulated intensity profile for (17,17). Figure 4.3b shows the same experimental data compared with simulations for (16,16) and (18,18) nanotubes. The simulated equatorial line for (17,17) matches best<sup>2</sup>. The diameter of  $2.27 \pm \sim 0.1$  nm measured in bright field

$d$  from TEM  
image

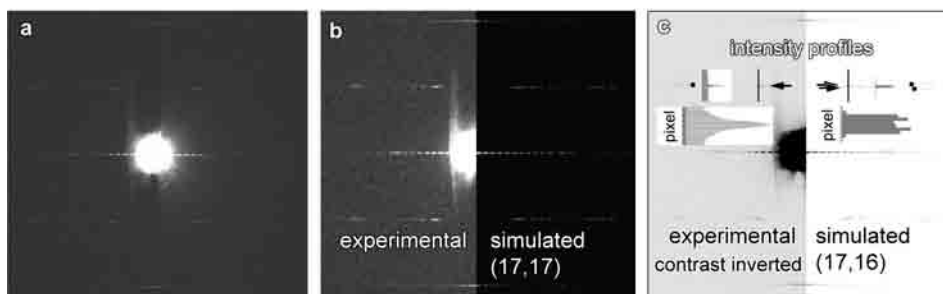
<sup>1</sup> The splitting due to  $+1^\circ$  and  $-1^\circ$  rotation would correspond to  $\sim 2\%$  ( $\sim 15$  pixel) of the layer line spacing from the equatorial line (736 pixel on the image plate) which would be observable (the intensity profile had a full width at half maximum of 11 pixel). Compared to these  $\langle 1100 \rangle$  diffraction spots, the splitting would be more pronounced for the higher diffraction spots  $\langle 2110 \rangle$ , as indicated by black dots in Figure 4.1c.

<sup>2</sup> Diffraction aberration and nanotube inclination can impair the assignment and must be corrected carefully.



**Figure 4.1:** Bright field TEM image showing a (17,17) SWNT integrated on polysilicon supports (Sample #ed1). The arrows point to the nanotube. The metal deposits originate from Cr/Au evaporation. The inset shows a close-up of the SWNT and the Cr/Au contact (dark). The amorphous carbon contamination around the nanotube and the metal deposit was mainly induced during observation. The dotted rectangle indicates exemplarily a region similar to the one given in (b) showing a TEM image of the side face of the poly-Si tip which thins down towards the right. It becomes sufficiently thin to allow imaging SWNTs and catalyst nanoparticles in interaction with the substrate. Solely standard photolithography-based processing was applied for tip structuring. All lithography and etching steps were completed before nanotube growth. (c) TEM image of a freestanding SWNT reaching the polysilicon support at the right hand side. Adapted from [103]. © Elsevier B.V, 2009.

TEM imaging matches reasonably well to the theoretical diameter  $d = 2.305$  nm of a (17,17) nanotube. The TEM images support the assignment of (17,17) based on electron diffraction.



**Figure 4.2:** Electron diffraction of the integrated SWNT shown in Figure 4.1. (a) Experimental electron diffraction pattern recorded at 100 kV, 30  $\mu\text{m}$  condenser aperture, 300 s exposure time on imaging plate. (b) Comparison of experimental diffraction pattern (left, increased contrast) with simulated diffraction pattern of a (17,17) nanotube ( $\theta = 30^\circ$ ,  $d = 2.305 \text{ nm}$ ). (c) Comparison of experimental diffraction pattern (left, inverted contrast) with simulated diffraction pattern of a (17,16) nanotube. Intensity profiles perpendicular to the layer lines are shown as insets. The chiral angle of  $29^\circ$  for the simulated (17,16) nanotube results in a splitting of the layer lines, which would correspond to 15 pixels on the image plate. Black dots indicate the more pronounced splitting for the counter-clockwise rotated diffraction spot and its clockwise rotated counterpart. Code for diffraction simulation was provided by Ph. Lambin [95] and implemented for MATLAB<sup>®</sup> by C. Roman. Adapted from [103]. © Elsevier B.V, 2009.

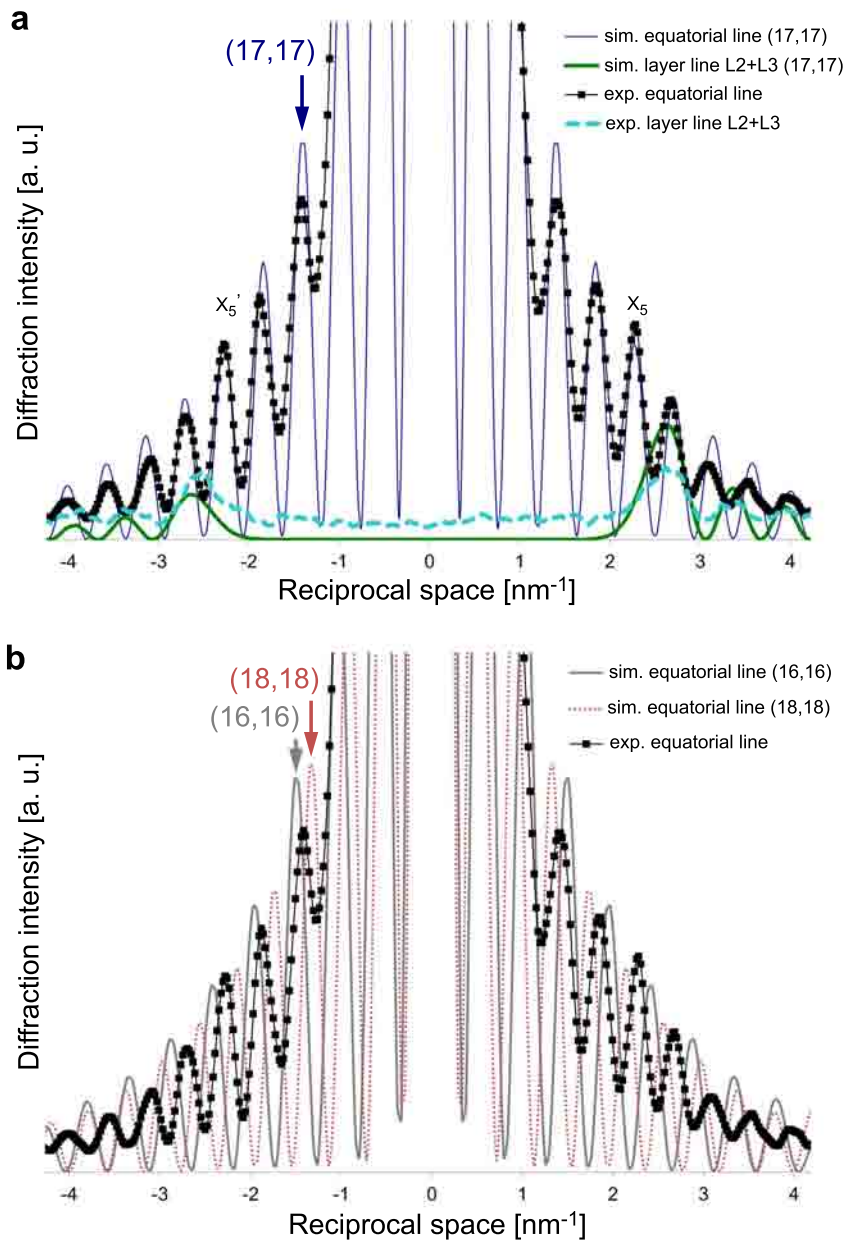
**Table 4.1:** Comparison of experimental data with theoretical chirality candidates for Sample #ed1. The nanotube diameter was measured from TEM images and from the equatorial line of the electron diffraction pattern (Appendix B.2.2, Equation B.21). The chiral angle was deduced from the layer line spacings of the ED pattern (Equation B.22, Figure B.13). Values which exclude a chirality candidate are typeset in *italics*.

Experimental			Theoretical		
Diameter	Diameter	Chiral angle $\theta$	Chirality	Diameter	Chiral
TEM image	ED eq. line	ED layer line sp.	( $n,m$ )		angle $\theta$
$2.27 \pm 0.1 \text{ nm}$	$2.34 \pm 0.1 \text{ nm}$	$30.0^\circ + 0^\circ / - 0.2^\circ$	(16,16)	2.170 nm	30.00°
			(17,16)	2.238 nm	29.00°
			<b>(17,17)</b>	2.305 nm	30.00°
			(18,17)	2.373 nm	29.06°
			(18,18)	2.441 nm	30.00°

Layer Line  
Intensity  
Profile

The peak separation ratio  $X1/X2$  between the first and the second intensity peak positions along the layer lines [287] (Appendix B.2.2, Figure B.14) is estimated to be  $\sim 1.29$ . A comparison with the computed values obtained from Bessel functions of order  $n$  and  $m$ , indicates the chiral indices  $n$  and  $m$  to be in the range of 15 to 18 which is in agreement with the chirality assignment of (17,17).





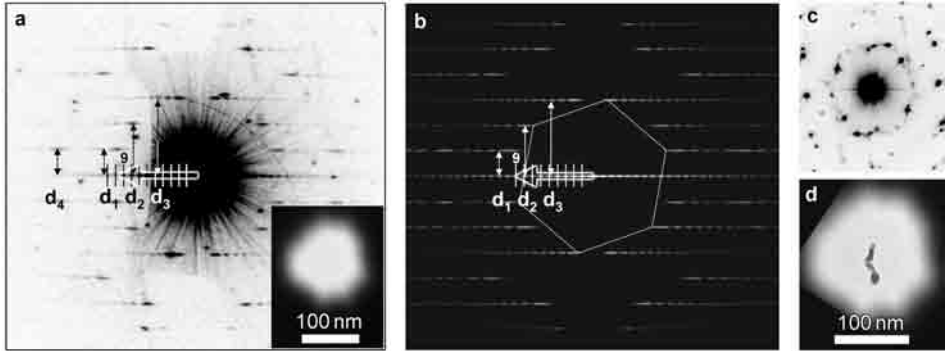
**Figure 4.3:** Electron diffraction intensity profile lines. (a) Simulated equatorial line (thin line) and layer line profiles (thick line) of a (17,17) nanotube in comparison with experimental equatorial line intensity (squares) and the layer line (dashed line). (b) Comparison of the experimental equatorial line intensity with simulation for (16,16) and (18,18), the closest chirality alternatives with a chiral angle of  $30^\circ$ . Code was provided by Ph. Lambin [95] and implemented for MATLAB<sup>®</sup> by C. Roman.

## Conclusion

While chirality assignment could also be derived within some limitations from other techniques such as Rayleigh scattering or Raman spectroscopy without sample transparency, the detailed imaging capabilities of TEM require electron beam transmissibility.

### Same chirality deduced for different diffraction patterns on same nanotube

Figure 4.4a shows electron diffraction patterns of a SWNT bridging between sharp poly-Si tips (Sample #ed2). The inset shows the TEM bright field image of the section of the nanotube illuminated for pattern recording. The nanotube is located 25  $\mu\text{m}$  far from the edge of the die. The beam of transmitted electrons can reach the nanotube within an  $\alpha$  tilting range of  $11^\circ$ . A chiral angle  $\theta$  of  $10.9^\circ$  and a diameter of 2.14 nm were extracted from the diffraction pattern. A (24,6) nanotube matches best and has theoretical values of  $\theta = 10.89^\circ$  and  $d = 2.153$  nm. For an unambiguous chirality assignment, all other close-by chiralities need to be excluded. First, chiralities with similar diameter but slightly different  $\theta$  were considered as summarised in Table 4.2. The chirality (23,5) [ $2.025$  nm,  $9.64^\circ$ ] was ruled out due to the discrepancy between the layer line spacings  $d_1$  and  $d_4$  predicted by simulation but not observed in the experimental data. Detectable discrepancies would be expected also for (23,6) [ $2.076$  nm,  $11.30^\circ$ ], (25,6) [ $2.230$  nm,  $10.51^\circ$ ], (24,5) [ $2.102$  nm,  $9.28^\circ$ ] nanotubes. Even for larger diameters with very similar  $\theta$ , a mismatch in  $d_1 = d_4$  would be observable, e.g. for (31,8) [ $2.793$  nm,  $11.20^\circ$ ], and (33,8) [ $2.947$  nm,  $10.61^\circ$ ]. The relative size of  $d_1$  and  $d_4$  is independent of nanotube inclination  $\tau$  with respect to perpendicular incidence of the beam.



**Figure 4.4:** Electron diffraction on integrated nanotube (Sample #ed2). (a) Experimental electron diffraction pattern of a SWNT located 25  $\mu\text{m}$  away from the chip edge resulting in an accessible tilting range of  $11^\circ$ . Adapted from [103]. The inset shows the corresponding  $\sim 150$  nm long section of the straight nanotube illuminated at 100 kV. The camera length was set to 770 mm. Contrast is inverted. (b) Simulated electron diffraction pattern of a (24,6) nanotube. Code was provided by Ph. Lambin [95] and implemented for MATLAB<sup>®</sup> by C. Roman. (c) Diffraction pattern of the same nanotube, but at a different position intentionally including a metal cluster as shown in (d) for comparison of intensities. Contrast is inverted. The cluster originates from metal evaporation of Cr/Au patterned by shadow masking. From both ED pattern, a chirality of (24,6) is assigned to the SWNT. Adapted from [103]. © Elsevier B.V, 2009.

**Table 4.2:** Comparison of experimental data with theoretical chirality candidates for Sample #ed2.

Experimental			Theoretical		
Diameter	Diameter	Chiral angle $\theta$	Chirality	Diameter	Chiral
ED pattern	ED eq. line	ED layer line sp.	( $n,m$ )		angle $\theta$
4.4a	$2.14 \pm \sim 0.1$ nm	$10.9^\circ \pm 0.1^\circ$	<b>(24,6)</b>	2.153 nm	$10.89^\circ$
4.4c	$2.14 \pm \sim 0.1$ nm	$11.0^\circ \pm 0.15^\circ$	(23,5)	2.025 nm	$9.64^\circ$ <sup>a</sup>
			(23,6)	2.076 nm	$11.30^\circ$ <sup>a</sup>
intrinsic			(25,6)	2.230 nm	$10.51^\circ$ <sup>a</sup>
layer lines:			(24,5)	2.102 nm	$9.28^\circ$ <sup>a</sup>
$m/n$ ratio			(31,8)	2.793 nm	$11.20^\circ$ <sup>a</sup>
= 0.250			(33,8)	2.947 nm	$10.61^\circ$ <sup>a</sup>
$m = 6.065$			(20,5)	1.794 nm	$10.89^\circ$
$n = 23.97$			(28,7)	2.551 nm	$10.89^\circ$

<sup>a</sup> The simulated mismatch between layer line spacings  $d_1$  and  $d_4$  is not occurring in the experimental ED pattern.

The closest candidates with the very same  $\theta$  but different  $d$  are (20,5) and (28,7). Their diameters are 1.794 nm and 2.511 nm. Both are safely far from the extracted  $d = 2.14$  nm with a readout precision of  $\sim 0.05$  nm for repeated pattern analysis. The diameter is represented graphically by the intensity peak interval along the equatorial line. Within the radius of the innermost hexagon ( $4.69 \text{ nm}^{-1}$ ), the experimental diffraction pattern counts nine intensity peaks, plus a part of an intensity decay. This matches well with the simulation for a (24,6) nanotube featuring nine intensity peaks, as shown in Figure 4.4b. For a (20,5) nanotube only eight intensity peaks, and for a (28,7) nanotube 11 peaks plus a part would be expected. The assignment of (24,6) is corroborated by the  $m/n$  ratio (Equation B.23) and the intrinsic layer line spacings (Equations B.28).

Figure 4.4c shows another diffraction pattern of the same nanotube, but recorded on a different part of the nanotube. A metal cluster was included in the exposed area as shown in Figure 4.4d. The cluster originated from evaporation of Cr/Au patterned by shadow masking. The intense diffraction spots for the metal indicate the weak intensity of the carbon-related spots. The metal could also be used to calibrate the diffraction pattern and to correct for diffraction astigmatism. Despite the intense spots of the metal cluster, the nanotube diffraction pattern was analysed based on the intrinsic layer line spacings. The chirality of (24,6) is assigned as well to this other section of the same nanotube. The intermediate value for  $m$  before truncation was 6.065. The extracted  $m/n$  ratio of 0.250 indicates  $n = 24$ . The intermediate value for  $n$  was 23.97 according to the intrinsic layer line spacing (indicating readout imperfection as value was  $< 24$ ). A diameter of 2.14 nm and  $\theta = 11.0^\circ \pm 0.15^\circ$  were deduced for this second diffraction pattern.

### Conclusions on electron diffraction

By electron diffraction chiralities were unambiguously assigned to SWNTs integ-

$\Delta d, = \theta$

2<sup>nd</sup> Pattern

Again (24,6)

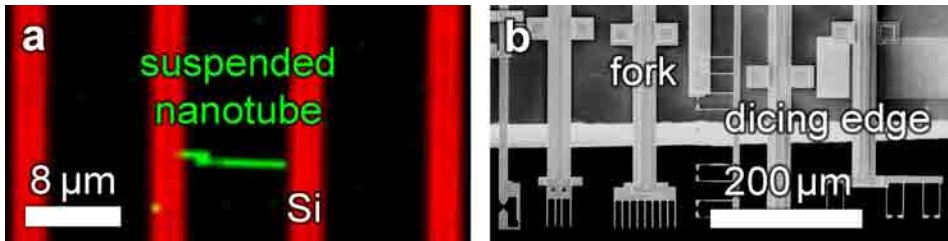
Conclusions

rated in MEMS structures. For unambiguous assignment of chiral indices, it is important to exclude all other chiralities with similar chiral angle and diameter. Simulated diffraction patterns are compared to the experimental data, considering the misorientation of the nanotube with respect to normal beam incidence ( $\tau$ ). For nanotubes of large diameters, the differences in  $d$  and  $\theta$  become smaller, and for very large diameters the candidates cannot be distinguished [70] p.59. Assignment can be provided for the target diameter range of  $\sim 2$  nm which is expected to yield ohmic contacts as proposed by L. Durrer [77, 263] pp.17. Alignment and tautening of the nanotubes occurring during growth according to nearest-neighbour alignment is beneficial. First, the tilt angle  $\tau$  is typically small as the opposing tips are aligned with the focal plane. Second, nanotubes are straightened due to zipping with the tips [273]. Straightness is a prerequisite for obtaining a diffraction pattern (periodicity).

### 4.3 Raman spectroscopy of suspended nanotubes

Figure 4.5b shows an SEM image of different designs of forks used for transfer of nanotubes. The Raman intensity map shown in Figure 4.5a is intensity-filtered for Si and for the G-mode. A nanotube bridges across the arms of the fork. A radial breathing mode (RBM) peak is located at  $150 \text{ rel. cm}^{-1}$ . For the 532 nm excitation wavelength, a (16,8) nanotube with  $d = 1.66$  nm (and  $\theta = 19.1^\circ$ ) or a (17,6) nanotube with 1.62 nm ( $14.6^\circ$ ) are the candidates of highest probability [288] (Appendix B.2.5). Both possible chiralities are semiconducting and are of class  $p = -1$  (Appendix B.1.6, Equation B.14).

Raman spectroscopy provides diameter measurements. In contrast to electron diffraction, chirality assignment based on RBM position can be ambiguous [92].



**Figure 4.5:** (a) Confocal Raman image of an as-grown nanotube suspended between poly-Si arms (filtered for G-mode and for Si intensity). Laser wavelength was 532 nm. (b) SEM image of forks with arrays of arm pairs. Adapted from [102]. © IEEE, 2012.

### 4.4 Correlation of diameter determined by RBM and electron diffraction

The diameter measurement and (tentative) chirality assignment based on the RBM position in Raman spectroscopy is cross-checked by combined investigations on the same nanotube. Figures 4.6a,b show the Raman spectrum and the

electron diffraction pattern of the very same nanotube device #ed3. TEM images of the nanotubes are shown in Figure 4.6c.

The radial breathing mode (RBM) frequency was  $\omega_{RBM} = 163.3 \text{ rel. cm}^{-1}$  with  $\pm 1 \text{ rel. cm}^{-1}$  calibration precision. Inserting the parameters of Bachilo *et al.* [289] into relation B.33, the diameter is deduced to be  $d = 223.5/(\omega_{RBM} - 12.5) \text{ [nm]} = 1.49 \text{ nm}$ . For other parameter sets, the diameter is calculated to be 1.50 nm [290] or 1.40 nm [15], as listed in Table 4.3.

RBM  $\Rightarrow d$ 

**Table 4.3:** Possible chirality candidates deduced from Raman spectroscopy and electron diffraction on Device #ed3. Different experimental parameter sets for the relation between  $\omega_{RBM}$  and  $d$  are listed (Appendix B.2.5). Values which exclude a chirality candidate are typeset in italic.

Experimental Raman & electron diffraction	Theoretical Chirality ( $n,m$ )	RBM expected?	Diameter	Chiral angle $\theta$
Raman: $d$	(13,7)	<i>no</i>	1.376 nm	20.17°
$d$ from RBM at 163.3 rel. $\text{cm}^{-1}$ :	<b>(14,7)</b>	yes	1.450 nm	19.11°
$d_{RBM \text{ Meyer}} = 1.50 \text{ nm}$ [290]	(15,7)	yes	1.524 nm	18.14°
$d_{RBM \text{ Bachilo}} = 1.49 \text{ nm}$ [289]	(15,8)	(yes)	1.583 nm	20.03°
$d_{RBM \text{ Liu}} = 1.40 \text{ nm}$ [15]	(19,0)	yes	1.491 nm	0.00°
	(11,10)	(yes)	1.427 nm	28.43°
Electron diffraction: $d$ & $\theta$	(18,2)	yes	1.496 nm	5.21°
$d_{ED} = 1.47 \text{ nm}; 1.44 \text{ nm}$ <sup>a</sup>	(15,5)	yes	1.415 nm	13.90°
$\theta = 19.5^\circ$	(16,3)	yes	1.388 nm	8.44°

<sup>a</sup> Diameter extracted from the equatorial line (Equation B.21); or including intrinsic calibration (Equation B.32).

Considering RBM intensities according to Jungen *et al.* [288] for the excitation at 2.33 eV ( $\lambda = 532 \text{ nm}$ ), the chiralities (14,7) [1.450 nm], and (19,0) [1.491 nm] are the most probable candidates. The next closest candidates are (11,10) (relatively strongly attenuated intensity) and (18,2), followed by (15,5), and (16,3).

RBM Intensity

The diffraction pattern was recorded (4.6b) and the chiral indices (14,7) were assigned. The measured values were  $d = 1.47 \text{ nm}$  (or 1.44 nm for intrinsic layer lines, Appendix B.2.2) and  $\theta = 19.5^\circ$ . The  $m/n$  ratio was 0.513. (15,8) and (13,7) are the closest alternative candidates.

Electron  
Diffraction

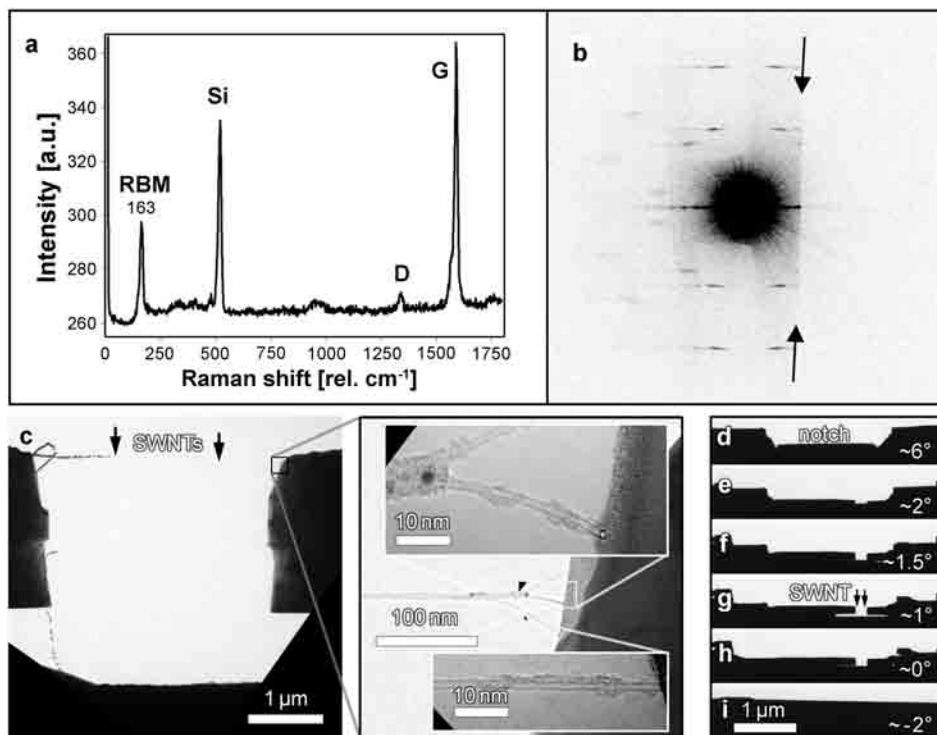
Many of the potential candidates based on the  $d$ -RBM relations can be ruled out owing to the chiral angle obtained from TEM electron diffraction.

 $\theta$ 

Clipping was observed owing to inappropriate tilting conditions. This underlines the importance of setting the  $\alpha$  tilt properly.

The theoretical diameter for a (14,7) nanotube is 1.450 nm which matches reasonably well to the values of  $d$  obtained from the RBM position. More convincing, the RBM of (14,7) is expected to be in resonance for the employed excitation laser line whereas (15,8), (13,7), and others are not anticipated to exhibit an RBM peak at the excitation energy of 2.33 eV [288].

Resonance  
Conditions



**Figure 4.6:** (a) Confocal Raman spectrum of an integrated nanotube device #ed3 with a radial breathing mode peak at  $163.3 \text{ rel. cm}^{-1}$ . Integration time was 12 s at a laser intensity of 1.5 mW and excitation at  $\lambda = 532 \text{ nm}$ . (b) Electron diffraction pattern of the same SWNT. A chirality of (14,7) is assigned based on the diffraction pattern. Image contrast is inverted for better visibility. Suboptimal tilting conditions lead to clipping, as indicated by arrows. The accessible  $\alpha$  tilt range was  $2.5^\circ$ . Adapted and reprinted with author rights from [103]. (c) TEM images of the nanotubes suspended between the poly-Si tips. SEM images of the same device were given in Figure 3.17a. The shadow masked contact is strongly misaligned owing to an out-dated slider design with movement direction along the nanotube axis. (d-i) Low magnification TEM image series in tilted-view for decreasing tilt angle  $\alpha$ . The opposing tip pair is (d) obscured by the close edge, (f) seen at  $\sim 1.5^\circ$  owing to the notch, (i) obscured by the far edge of the chip for negative  $\alpha$ -tilt. Reprinted from © Elsevier B.V., 2009.

D-mode

Probably due to the previous ED pattern recording, the feature of the defect mode (D) is pronounced. As the G/D ratio of our pristine SWNTs is usually above 100, the decrease of G/D to 15 seems to support the foreseen necessity to perform electrical sensor measurements prior to chirality assignment. Although the SWNTs endured routinely long electron beam exposures at 100 keV, which is above the knock-on damage threshold of 87 keV [291] for carbon nanotubes, degradation cannot be excluded [292]. Furthermore, carbonaceous deposition is likely, which can originate from residual hydrocarbons polymerised under electron irradiation [233]. Another reason for the exceptional high D peak may arise

from the metal deposition for electrical integration.

The diameter deduced from the experimental RBM peak position in Raman spectroscopy is in agreement with the chirality assigned by electron diffraction.

Conclusion

For a small diameter the commonly used theoretical parameters to relate  $\omega_{RBM}$  to  $d$  were confirmed by electron diffraction. The relation  $d = 223.5/(\omega_{RBM} - 12.5)$  [nm] [289] appears to over-estimate the diameter (1.49 nm instead of 1.45 nm), while  $d = 228/\omega_{RBM}$  [nm] [15] under-estimates  $d$  (1.40 nm).

A detailed verification of the RBM-diameter relation by the combined analysis of Raman and electron diffraction was achieved by Meyer *et al.* for nanotubes suspended via a resist-based process including wet etching ( $C_1 = 204 \text{ rel. cm}^{-1} \cdot \text{nm}$  and  $C_2 = 27 \text{ rel. cm}^{-1}$ ).

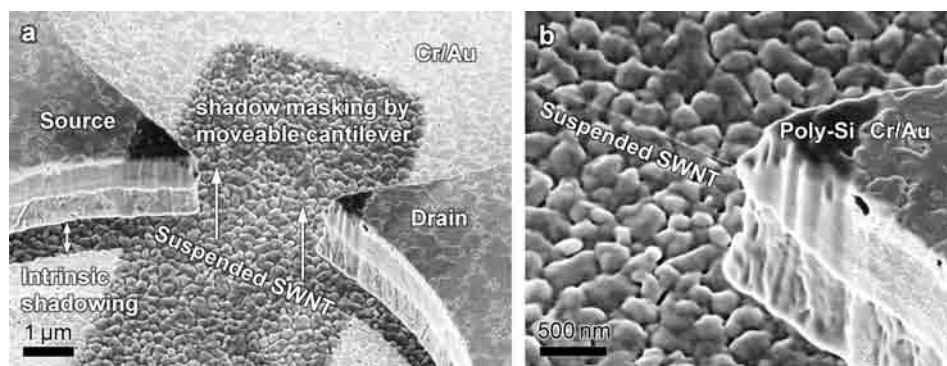
Related Work

Liu *et al.* measured intrinsic RBMs of clean and long suspended nanotubes without perturbations from the environment [15] ( $C_1 = 228 \pm 1 \text{ rel. cm}^{-1} \cdot \text{nm}$  and  $C_2 = 0 \text{ rel. cm}^{-1}$ ) They determined  $C_2$  equals zero which matches the theoretical prediction for pristine SWNTs.

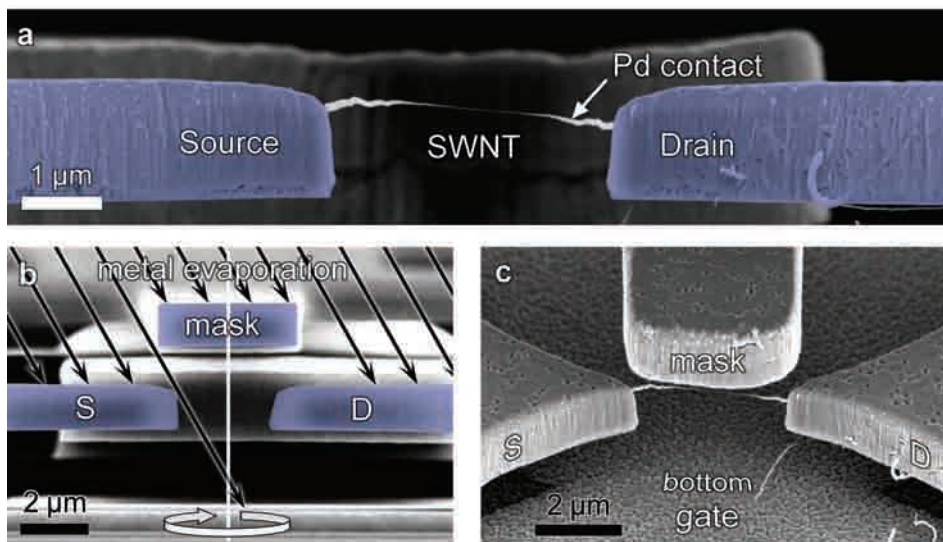
## 4.5 Hysteresis-free transistor characteristics of ultraclean CNTs

After the demonstration of device characterisation by electron diffraction and Raman spectroscopy, the fabrication results of electrical contacts by shadow masking (Section 3.2) are presented and hysteresis-free transistor operation is shown.

Overview



**Figure 4.7:** On-chip shadow masks - intrinsic mask plus moveable cantilever - for high material contrast by short mask-to-substrate gaps. SEM image of a tip pair for SWNT integration. Undercuts at the partially suspended poly-Si tips act as intrinsic shadow mask. The tips are bridged by a SWNT. The SWNT is shielded from metal deposition by a shadow mask cantilever attached to an on-chip slider (retracted again). A stack of 2 nm Cr + 40 nm Au was evaporated without sample rotation at zero tilt. Misalignment is due to first-generation alignment guidance without alignment cones. (b) SEM close-up of the suspended SWNT showing the high material contrast owing to the small separation between shadow mask and tip-shaped poly-Si electrodes. The SWNT image is blurred towards the middle-section due to vibrations. Adapted and reprinted from Nature Nanotechnology, supplementary information [101]. © Macmillan Publishers Limited, 2010.



**Figure 4.8:** Nano-tapered metallisation of suspended SWNTs by on-chip shadow masking. (a) On-chip shadow-masked evaporation of 170 nm palladium at 30°-tilted sample rotation provides gradually thinned contacts with the suspended SWNT. The contactless patterning also covers the sidewalls. (b) Front side view (SEM) of the opposing tips and shadow mask, including a schematic of tilted metal evaporation with sample rotation around the white axis. The mask shields the middle section of the suspended nanotube from metal deposition. Undercuts act as intrinsic shadow masks and isolate the electrodes (S and D) from the substrate. (c) Same device as shown in (a) in perspective view. Owing to tilted sample rotation, the oxidised poly-Si of the bottom gate becomes metallised, in contrast to non-tilted deposition shown in Figure 4.7. Adapted and reprinted from Nature Nanotechnology, supplementary information [101]. © Macmillan Publishers Limited, 2010.

#### 4.5.1 Contact formation by shadow masking

Material  
Contrast

Inherent to shadow masking, material contrast limitations evolve from geometric blurring. The mask-to-substrate gap influences the blurring (Section 3.2.1). Here, the small gaps achievable with the on-chip masks reduce the blurring. High material contrast was achieved by the cantilever-like shadow stencils attached to the moveable slider as shown in Figure 4.7. Sample rotation was disabled and sample tilt was set to zero degrees during evaporation of 2 nm Cr and 40 nm Au. Tests with larger gap distances and/or weaker vacuum conditions ( $\sim 8 \cdot 10^{-6}$  mbar, Edwards coating system E306) resulted in degraded contrast as expected (see Section 3.2.1 topics Mask-to-Substrate Gap and Residual Gases). This indicates the importance of small mask-to-substrate gaps achieved by the on-chip masks.

Tapered  
Contacts

Sample rotation about an axis with 30° tilt with respect to the material flux during evaporation (Section 3.3 and Figure 4.8b) reduces the electrode material thickness gradually towards the shadowed area. Consequently, tapered needle-type metal electrodes were fabricated in a self-aligned manner (Figure 4.8a).



The shadow mask can be as close as 700 nm from the suspended nanotube and despite tilted evaporation, only the endsections were metallised. As the mask was more than 3  $\mu\text{m}$  further apart from the substrate than from the nanotube, the substrate became metallised during evaporation even right underneath the shadow mask, as shown in Figures 4.8b,c. Thus, the substrate surface consisting of oxidised poly-Si (or silicon nitride on doped Si) was covered with highly conductive metal. Consequently, the substrate surface acting as bottom gate can be assumed to be free of charge traps.

Metallised  
Bottom Gate

### Surface migration

Surface diffusion is migration of evaporated material after impingement on a substrate (Section 3.2.1 topic Surface Migration). The partially shielded, suspended SWNTs acted as substrate for the self-aligned contacts. For 2 nm Cr + 60 nm Au evaporation, nanometre-sized clusters were observed at Y-junctions of bundles of suspended SWNTs relatively far underneath the shadow masks [285].

Migration

Palladium is reported to exhibit better wetting to SWNTs than Au [186, 187]. In the case of Pd, the surface migration on SWNTs seemed to be less pronounced than for Au on SWNTs. This observation is also in agreement with findings from density functional theory which claim that nanotube-metal interaction is stronger for Pd than for Au [293], which leads to higher diffusion barriers.

Discussion

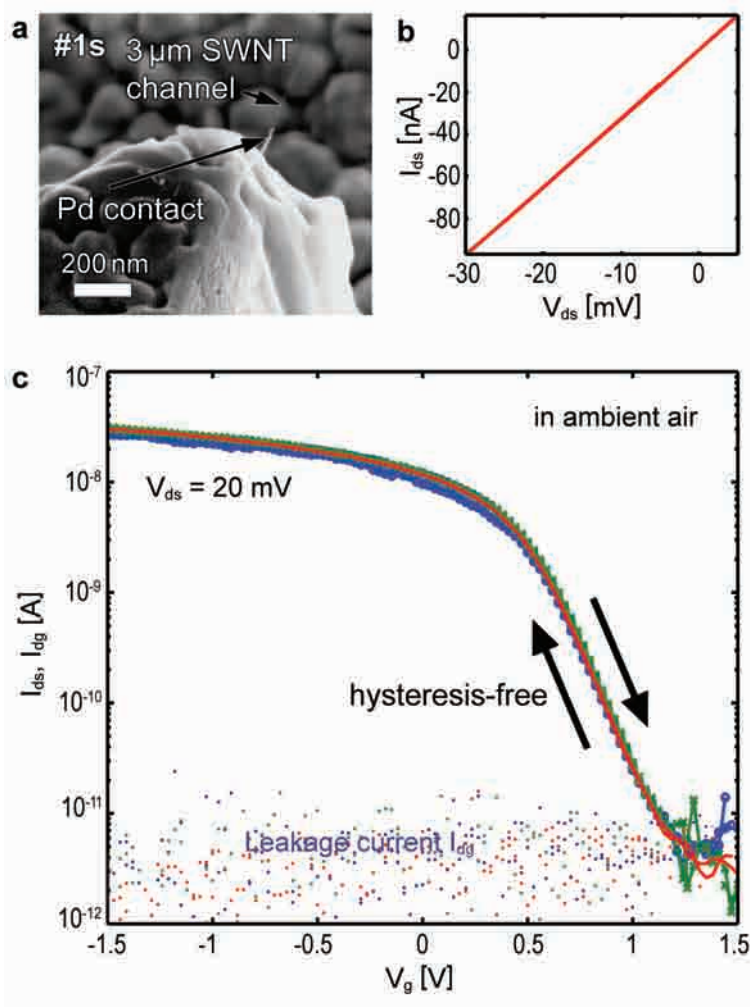
### 4.5.2 CNFETs by shadow masking

Figure 4.9 shows the transistor operation of a suspended nanotube. The Pd contacts were evaporated onto the as-grown nanotube by shadow masking. The SEM image of Figure 4.9a shows a long channel device (Device #s1) with a channel length of 3  $\mu\text{m}$ , suitable for strain or chemical sensing. The CNFET was fabricated with a small gap of 1  $\mu\text{m}$  between the shadow mask and the SWNT. Electrical device characterisation was carried out at room temperature in ambient air. The linear source-drain current ( $I_{\text{ds}}$ ) versus source-drain voltage ( $V_{\text{ds}}$ ) characteristic of Device #s1 at a gate voltage  $V_{\text{g}} = 0 \text{ V}$  is shown in Figure 4.9b.  $I_{\text{ds}}/V_{\text{g}}$  curves for several  $V_{\text{g}}$  sweeps at 4 mV/s are plotted in Figure 4.9c, showing repeatable FET behaviour.  $V_{\text{g}}$  was applied at the metallised bottom gate, 3  $\mu\text{m}$  from the channel. The following device performance figures were determined: subthreshold swing  $S = 230 \text{ mV/dec}$ , threshold voltage  $V_{\text{th}} = 1 \text{ V}$ , on-state system resistance  $R_{\text{ON}} = 330 \text{ k}\Omega$  and current on/off ratio  $I_{\text{ON}}/I_{\text{OFF}} = 1 \cdot 10^4$  at  $V_{\text{ds}} = 20 \text{ mV}$ . The hysteresis in gate voltage was as low as  $8 \pm 5 \text{ mV}$  and the hysteresis expressed in current was  $0.09 \pm 0.06 \text{ nA}$ , which corresponds to 0.3% of  $I_{\text{ON}}$ .

CNFET #s1  
3  $\mu\text{m}$  Channel

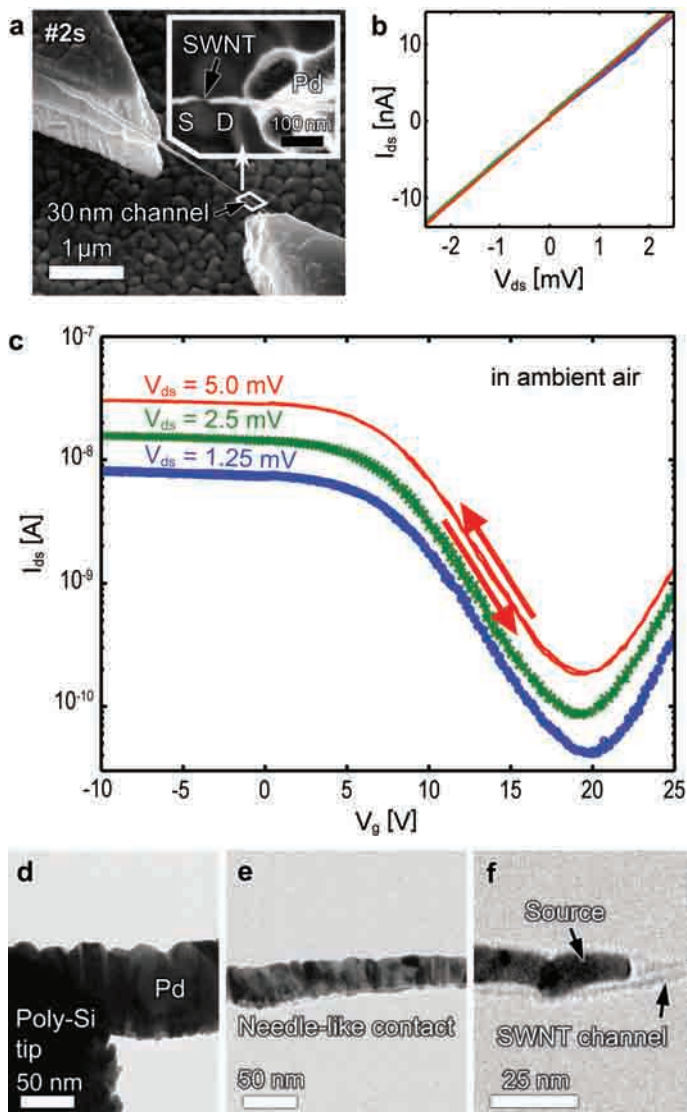
For Device #s2, tilted sample rotation during palladium evaporation and the relatively large separation between the SWNT and the shadow mask allowed obtaining a very short non-metallised part of the SWNT. Short channel lengths as narrow as 30 nm could therefore be obtained as shown in the SEM image of Figure 4.10a. The metal deposition on the long shadow masking bar of the design of Device #s2 caused upwards-bending and caused finally a large mask-to-nanotube gap. The width of the shadow mask, the separation between the

CNFET #s2  
30 nm channel



**Figure 4.9:** Suspended, pristine SWNT arranged as a long-channel field effect transistor with minute hysteresis (Device #s1, with a channel length of 3 μm). (a) SEM micrograph of a SWNT contacted by on-chip shadow-masking with tilted-axis sample rotation during evaporation of 170 nm palladium. (b) Source-drain current ( $I_{ds}$ ) versus source-drain voltage ( $V_{ds}$ ) curve for a gate voltage  $V_g$  of 0 V. (c)  $I_{ds}$  versus  $V_g$ . Three dual sweeps (4 mV/s) are plotted for  $V_{ds} = 20$  mV. The distance between the SWNT and bottom gate is 3 μm. Leakage current  $I_g$  is at the noise level. Note the negligibly small hysteresis of  $8 \pm 5$  mV. Adapted and reprinted from Nature Nanotechnology [101]. © Macmillan Publishers Limited, 2010.

SWNT and mask, the evaporation tilt angle, and the cantilever length and material thickness may be used as tuning parameters for the channel length and mechanical anchoring. The linear  $I_{ds}$ - $V_{ds}$  characteristic of #s2 is shown in Figure 4.10b, and was found to withstand the FET measurements unchanged.  $I_{ds}$ - $V_g$  curves are plotted in Figure 4.10c.



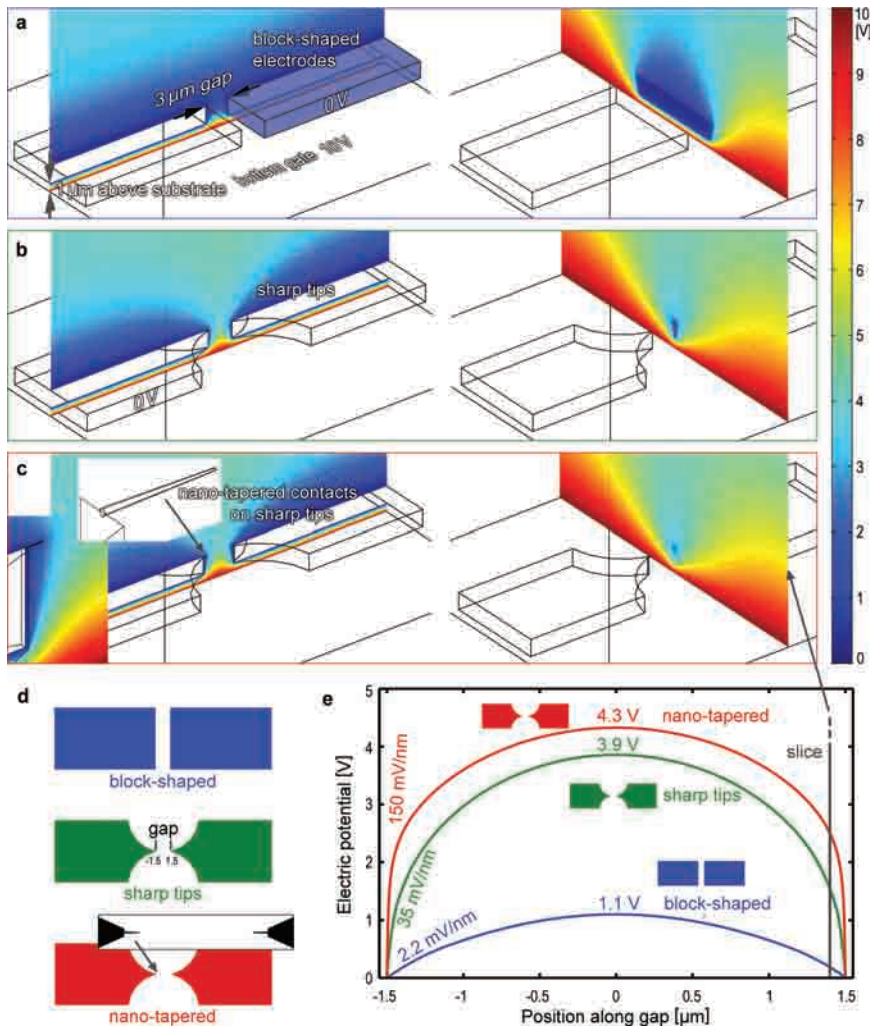
**Figure 4.10:** Suspended short-channel field-effect transistor without hysteresis operated in ambient air (Device #s2). (a) SEM image of a SWNT formed with an enlarged SWNT-shadow-mask gap, leading to a 30-nm-short SWNT channel. Inset: enlargement of the channel in top view. (b)  $I_{ds}$ - $V_{ds}$  curves at  $V_g = 0$  V before and after FET measurements. (c)  $I_{ds}$  measurements for the suspended directly contacted SWNT for continuous gate sweeps (0.3125 V/s) applied to the backgate (3  $\mu$ m below the SWNT). Dual sweeps are shown for  $V_{ds} = 1.25$ , 2.5 and 5.0 mV. Note the absence of hysteresis. (d) TEM images of the needle-like contact of Device #s2 fabricated by on-chip shadow masking. (e) The thickness of the evaporated palladium contact reduces gradually along the suspended SWNT. (f) Close-up of the carbon nanotube FET channel, showing a nanoscale needle-like contact. Vibrations have caused image blurring. Adapted and reprinted from Nature Nanotechnology [101]. © Macmillan Publishers Limited, 2010.

Hysteresis-free	Even in an ambient cleanroom environment with 45% relative humidity, hysteresis was absent. For Device #s2, the following performance data were extracted: $S \approx 4900 \text{ mV/dec}$ , $V_{th} = 17 \text{ V}$ with the bottom gate located $3 \mu\text{m}$ below the channel, $R_{ON} = 89 \text{ k}\Omega$ and $I_{ON}/I_{OFF} = 190$ at $V_{ds} = 1.25 \text{ mV}$ . Gate leakage current was below $2 \cdot 10^{-11} \text{ A}$ at $I_{OFF}$ . The ambipolar FET behaviour can be attributed to ohmic palladium-SWNT contacts to a small-bandgap nanotube or to a large-diameter nanotube with moderate bandgap.
TEM Images of Contact	Figures 4.10d-f show the nano-tapered contact of Device #s2, recorded using TEM under tilted-view conditions [103] (Section 3.5.2), allowing the combination of electrical and structural characterisation that is necessary for fundamental investigations and model validation. To avoid beam-induced defects or contamination, electron microscopy was conducted following electrical measurements. A bandgap of $\sim 0.2 \text{ eV}$ (Equation B.7) would be expected for the observed diameter of $\sim 4 \text{ nm}$ . The outermost metal contact diameter of #s2 is $\sim 7 \text{ nm}$ .
Discussion	Although difficult to compare directly due to its dependence on gate voltage range and scan rate, hysteresis in ambient air is usually on the order of volts [28, 54, 85]. Hysteresis is commonly observed for unpassivated channels exposed to humid air, at least in approximately 50% of devices [32] unless the supporting surface is rendered hydrophobic [90] or passivated [87, 193].
Conclusion	The observed suppression of hysteresis even at humid ambient conditions by ultraclean CNFETs is an important feature for nanotube sensors. Especially for gas sensors, which require interfaces to the environment, the hysteresis-free operation in humid atmosphere is beneficial for sensor readout. Suppression of hysteresis is attributed to (i) excluding charge traps by maintaining clean, defect-free nanotube surfaces during processing and to (ii) shielding any oxide-related charge traps by metal-covering of the gate. By simulation, needle-like contacts have been identified to be the optimal contact geometry [183]. Here, needle-like, nano-tapered contacts were fabricated and good gate coupling was achieved.

#### 4.5.3 Simulation of electric potential for tapered electrodes

The relatively steep subthreshold slopes observed for the  $3 \mu\text{m}$  large air gap of devices #s1 and #s2, indicate a good gate coupling considering this large gate-to-nanotube distance. Transistor geometry and especially the shape of source and drain electrodes have a strong impact on gate coupling [183]. In order to estimate the enhancement of the gate coupling by the nano-tapered contacts on sharp micro tips, 3D simulations of the electrostatics based on finite element method (FEM) were carried out (Comsol Multiphysics® version 3.4).

As shown in Figure 4.11, three geometries were compared: Standard block-shaped electrodes; micro-sharp electrode tips (representing the poly-Si supports); and similar micro-sharp tips additionally equipped with nano-tapered contacts (representing Pd protruding onto the nanotube). For all configurations, the gap between the electrodes was kept at a length of  $3 \mu\text{m}$ . The SWNT itself was neglected. Although this simplification alters the electric potential, the model allows for qualitative comparisons.



**Figure 4.11:** Finite element simulations of the electric potential for different electrode geometries with a bottom gate potential set to 10 V and having the source and drain electrodes at ground potential were carried out using Comsol®. The nanotube spanning the electrodes is neglected. A slice along the symmetry plane and a perpendicular slice 100 nm in front of the electrode are plotted for three different geometries having a source-drain gap of 3  $\mu\text{m}$  each: (a) Block-shaped electrodes (2  $\mu\text{m}$  thick, 12  $\mu\text{m}$  wide, 1  $\mu\text{m}$  elevated above the substrate which acts as bottom gate). The black arrows are pointing at the location where the suspended SWNT would be. (b) Sharp tip pair. (c) In addition to the sharp tips, the source and drain are extended with nano-tapered contacts (400 nm in length, 30 nm diameter at the base and 10 nm diameter at apex). (d) Sketch of the three different electrode geometries in top view. (e) The electric potentials along the fictitious nanotube are plotted for the block-shaped electrodes (bottom), micro-sharp tips (middle), and micro-sharp tips with nano-tapered contacts (top). Reprinted from Nature Nanotechnology [101], supplementary information. © Macmillan Publishers Limited, 2010.

Boundary Conditions	The substrate, acting as bottom gate, was set to a potential of 10 V. Both, source and drain electrodes were assumed to be perfect conductors and were set to a potential of 0 V. The boundary setting „symmetry/zero charge“ was chosen for the sidewalls of the air-filled simulation domain. This boundary conditions correspond to a periodic array of electrode-pairs. To allow the iterative adaptive mesh refinement to run efficiently, infinite elements for the boundary at the top boundary were replaced by a ground plane at an altitude of 100 $\mu\text{m}$ .
Block-shaped	Figure 4.11a shows the simulated electric potential for the block-shaped electrodes (2 $\mu\text{m}$ thick, 12 $\mu\text{m}$ wide, 1 $\mu\text{m}$ separated from the substrate acting as bottom gate). On the left hand side in 4.11c, a slice along the axis of the nanotube shows how the electrostatic potential extends into the 3 $\mu\text{m}$ long gap. The nanotube position would be at the upper edge of the electrodes (black arrows) but was neglected. The right hand side of Figure 4.11c depicts a slice of the electric potential perpendicular to the nanotube axis 100 nm in front of the onset of the electrode.
Micro-sharp	Figure 4.11b shows the electric potential for micro-sharp tips (radius of curvature is 7 $\mu\text{m}$ , 10 nm width at apex, 2 $\mu\text{m}$ height at apex).
Nano-tapered	Figure 4.11c shows the electric potential for micro-sharp tips with added nano-tapered contacts (400 nm in length, 30 nm diameter at the base and 10 nm diameter at apex, planar tip). The electric potential at the upper end of the electrode gap where the nanotube would be located is increasing due to reduced shielding by the electrodes. This confirms qualitatively the effectiveness of the reported nano-tapered geometry. As mentioned, the nanotube itself is neglected and therefore with the additional screening because of the nanotube is not taken into account.
Electric Potential	In Figure 4.11e, the modelled electric potentials along the fictitious nanotube are plotted for the three different geometries. Two characteristics are relevant: The bulk potential reached in the middle of the gap and the potential in the contact region. The latter is especially relevant for barrier-dominated transistors. Nano-tapered contacts are simulated to enhance the electrical field by a factor of 67 compared to block-shaped electrodes.
Devices	Regarding the real devices presented in Figures 4.9 and 4.10, the subthreshold swings vary significantly (long-channel Device #s1: $S = 230 \text{ mV/dec}$ and short-channel Device #s2: $S = \sim 4900 \text{ mV/dec}$ ). One factor that contributes to the poorer subthreshold swing observed for Device #s2 is the asymmetry of the contacts: The drain contact is shorter than the source contact. The geometrical shift of the channel position close to the drain electrode is due to first-generation shadow masks, where the mismatch in photolithography was not compensated <sup>1</sup> . As the channel and therewith the nanotube-metal interfaces are close to the metallised poly-Si drain electrode, the backgate is shielded more than for the symmetric Device #s1. Therefore, the enhancement by nano-tapered contacts is expected to be smaller for Device #s2 than for #s1.

<sup>1</sup> Opposing tips and shadow mask were fabricated in different lithographic steps and cantilevers were bending upwards upon metal deposition

#### 4.5.4 Chirality-assigned CNFET fabricated by shadow masking

Chirality is assigned by electron diffraction to nanotubes acting as transistor channels. This enables correlation of structural properties with electron transport measurements.

Overview

Suspended SWNTs integrated as field effect transistor channels are shown in top view of Figure 4.12a in an SEM image. For the same Device #s4, Figure 4.12b shows the source-drain current for a forward and a backward sweep of the bottom gate. The subthreshold swing is 340 mV/dec and the current on/off ratio is  $\sim 10^4$ . The corresponding electron diffraction pattern (4.12c) allows the chirality (28,11) to be unambiguously assigned to the individual nanotube in the middle part<sup>1</sup>. TEM images shown in Figure 4.12d – in tilted-view – reveal that both end segments of the transistor consist of bundles of two nanotubes each, as schematically illustrated by thick lines. By electron diffraction, the second SWNT #2 on the end section of the right hand side is identified as armchair-type nanotube and therefore expected to behave metallic.

Device #s4

The (28,11) nanotube which completely bridges between the source and drain electrodes is predicted to have a bandgap of 0.28 eV. The semiconducting electronic properties (Figure 4.12b) are consistent with the structure determination predicting a semiconducting behaviour.

Discussion

#### Contact modification of functional device

Shadow masking can be used iteratively to alter contact geometry. The slider can move the mask again closely spaced atop of the suspended nanotube. A second metallisation was patterned as shown in the SEM and TEM images of Figure 4.12g of Device #s4. The electrical response after modifying the suspended electrical contacts by a second evaporation is shown in Figure 4.12e.

The transition from semiconducting to metallic conduction can be explained by the metal coverage of the previous (28,11) transistor channel. The dominant section after the second metallisation is the (28,11) nanotube bundled to the armchair-type nanotube. This demonstration of sequential modification of contacts to long, suspended nanotubes is a unique feature of shadow mask evaporation and could not be achieved by resist-based lithography.

Discussion

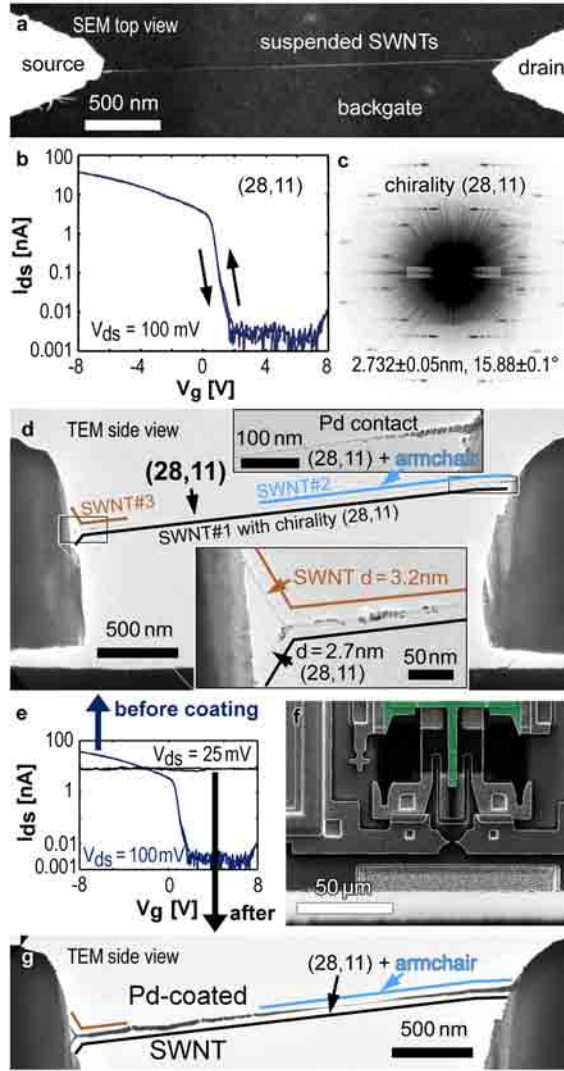
#### Conclusion on CNFETs fabricated by shadow masking

On-chip shadow masking enabled the operation of nanotube transistors in a humid atmosphere without hysteresis. Suspended, individual, and ultraclean nanotubes were grown directly between unmetallised device contacts, onto which palladium was then evaporated through self-aligned on-chip shadow masks. This yielded pairs of needle-shaped contacts that have been theoretically shown to allow high nanotube-gate coupling and low gate voltages [183]. On-chip shadow

Hysteresis-free

<sup>1</sup> A diameter of  $2.732 \pm 0.05$  nm and a chiral angle of  $15.88 \pm 0.1^\circ$  were extracted. The diameter was measured from the TEM image to be  $2.75 \pm 0.2$  nm. The theoretical values for a (28,11) nanotube are 2.727 nm and  $15.874^\circ$ . The closest alternative candidates would be (29,11) and (27,11). The deviation from the theoretical values of these closest alternative candidates are  $+0.075$  nm,  $-0.44^\circ$  and  $-0.075$  nm,  $+0.46^\circ$ .





**Figure 4.12:** Hysteresis-free SWNT field-effect transistor #s4 with assigned chirality and demonstration of metal contact modification. (a) SEM top view image of a suspended CNFET. (b) Hysteresis-free  $I_{ds}$  for a gate dual-sweep after electrical burn-out of short-circuiting nanotubes. Subthreshold swing  $S$  was 340 mV/dec at a nanotube-to-gate distance of  $\sim 3.6$   $\mu$ m. On resistance  $R_{ON}$  was 2.75 M $\Omega$  at  $V_g = -8$  V. (c) The electron diffraction pattern recorded at the middle section revealed that exactly one individual SWNT with chirality (28,11) spans the whole distance between the tips. (d) TEM images of the same CNFET in side view. The diameter of the lower nanotube (left inset) was measured from an image to be  $2.75 \pm 0.2$  nm, matching to (28,11). The second nanotube on the right end section is a metallic, armchair-type nanotube. (e)  $I_{ds}$  before and after additional Pd-coating of the same device. (f) SEM top view image with shadow mask slider in retracted position. (g) TEM image after additional Pd coverage by reuse of the shadow mask. Adapted and reprinted from [2]. © IEEE, 2011.



masking demonstrated the electrical interfacing of suspended ultraclean nanotube FETs in prefabricated MEMS structures. This process paves the way for creating ultrasensitive nanosensors based on pristine suspended nanotubes.

Stencil lithography allows a wide range of metals to be used as contacts, without the need for any post-metallisation treatment such as lift-off, nanotube growth, or release etching.

For fundamental investigations, the contact geometry was changed successively even for the suspended nanotube configuration. Tilted angle evaporation (without sample rotation) [159] will be useful to fabricate distinct contacts of unequal materials for the two nanotube ends, and to pattern multiple gates.

Tilted-view TEM observation enables discrimination between devices with an individual nanotube and devices with multiple nanotubes or bundles. Chirality assignment to functional devices was demonstrated by electron diffraction.

Material  
CompatibilityReuse  
OutlookChirality  
Assignment

#### 4.5.5 CNFETs by direct transfer

The dry transfer of nanotubes from a fork to a device die was described in Section 3.3. Electronic characteristics and electron beam investigations are presented in the following.

Overview

##### Current detection and voltage sweep response

A bias  $V_{ds}$  of typically 0.2 V was applied across the Pd-coated receiving electrodes. During lowering the nanotube-carrying fork the  $I_{ds}$  current was triggering the placement of nanotubes. The  $I_{ds}$ - $V_{ds}$  characteristics of several devices are shown in Figure 4.13. For some devices, as plotted for Device #t2 ( $\times$ ), the conductivity increased stepwise after setting  $V_{ds}$  to values larger than 1 V. This indicates that contacts can be permanently improved after high bias was applied. The resistances – at zero gate voltage, which can be far from the on-state – were in the order of  $M\Omega$ : 1, 1, 2, 4, 15, 23, 55  $M\Omega$ .

Current  
Monitoring

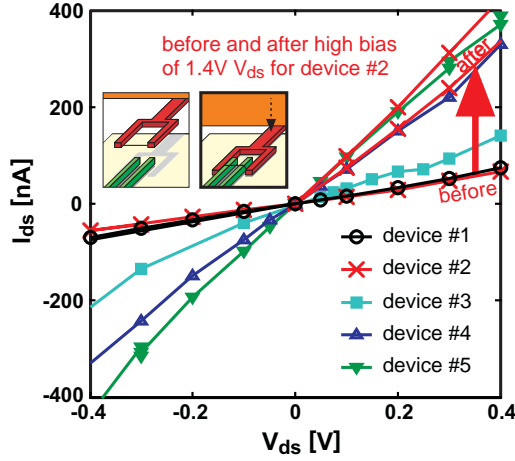
Understanding the exact mechanisms of the observed contact improvements, which might be related to tempering by self-heating or to charge injection, requires more detailed studies. Jones *et al.* reported sudden increase in current at high bias larger than  $\sim 2.5$  V for Pd electrodes previously exposed to  $O_2$  plasma [294]. They attributed the current increase to the breakdown of a 2-nm-thin palladium oxide layer. Dong *et al.* attributed the current increase observed for Pt electrodes to desorption of adsorbates and to thermally enhanced bonding [295].

Discussion

##### Transistor measurements

A transistor fabricated by the transfer method is shown in Figure 4.14. The nanotube is suspended in between the electrodes. The inset reveals the end of the nanotube which was previously in contact with the fork. SEM imaging was conducted after electrical measurements were completed to avoid contamination. The transistor characteristics are plotted as  $I_{ds}$ - $V_g$  curves in Figure 4.15. Although measured in humid ambient air, the transfer characteristics are hysteresis-free: forward and backward traces are plotted both and match each other. A full continuous dual gate sweep took 70 s ( $V_{g \text{ extremal}} = \pm 20$  V) corresponding to a sweep

CNFET #t1



**Figure 4.13:**  $I_{ds}$ - $V_{ds}$  response of five devices fabricated by transfer onto Pd electrodes. The conductivity of Device #t2 (crosses) increased after raising  $V_{ds}$  to 1.4 V (bold arrow). Device #t1 (circles) is shown in Figures 4.14, 4.15, and 4.16.  $V_g$  was zero. Adapted and reprinted from [102]. © IEEE, 2012.

Hysteresis-free

rate of 1.14 V/s. In earlier work by Sangwan *et al.* [33], hysteresis was still observed although the transferred nanotubes were suspended. Here, the devices do not show hysteresis even at relatively slow  $V_g$  sweep rates. Recently, Wu *et al.* used a similar transfer method and obtained negligibly small hysteresis [154].

Gate Coupling

The  $I_{ON}/I_{OFF}$  ratio exceeded  $10^3$ . The gate coupling with a subthreshold swing of  $\sim 2200$  mV/dec is relatively weak as expected for the configuration without extending needle-like contacts. Note that the gate-to-nanotube distance is as large as  $5.5 \mu\text{m}$ ,  $3.5 \mu\text{m}$  is the thickness of the poly-Si receiving electrodes being spaced by  $2 \mu\text{m}$ , as depicted for Device #t1 in Figure 4.20.

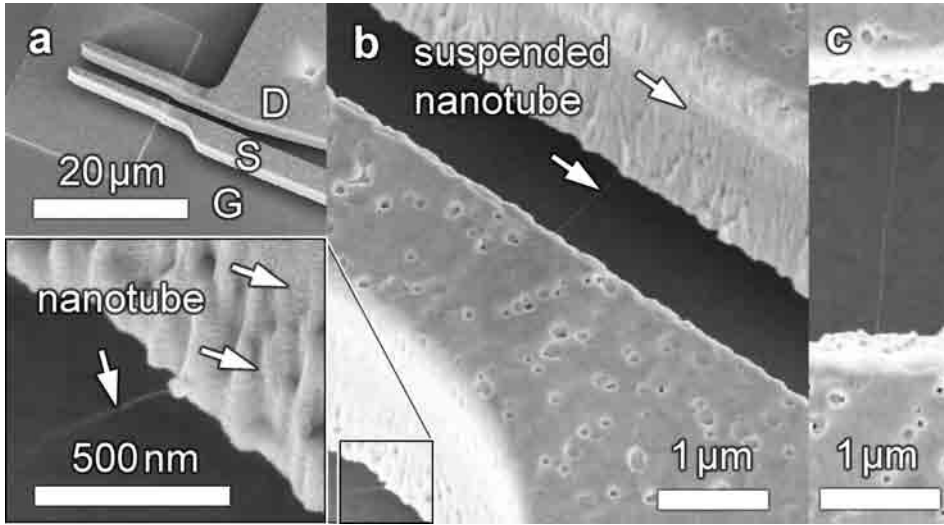
Storage

In Figure 4.15b, the  $I_{ds}$ - $V_g$  characteristics recorded directly after transfer and 5 days later after storage in cleanroom environment are compared. An increase in  $I_{ds}$  was observed. On day 6, the threshold voltage  $V_{th}$ , extracted by fitting a linear curve in the point of steepest slope and extrapolating to zero  $I_{ds}$ , was found to be 11 V.  $V_{ds}$  as high as 300 mV was sustained by Device #t1. Despite the relatively high  $V_{ds}$  bias [193], hysteresis was negligible. The minimum system resistance for this individual nanotube device was  $1.7 \text{ M}\Omega$ .

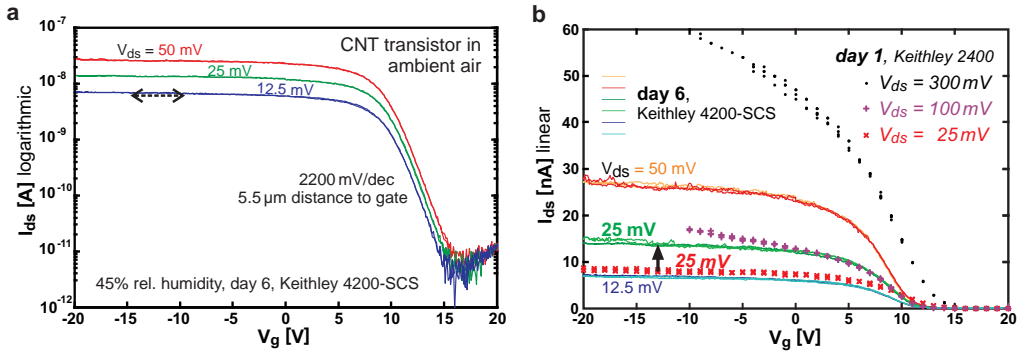
### Thermal annealing

RTA

Annealing is reported to be not necessary for freshly evaporated metal surfaces [154]. Nevertheless, it was tested whether rapid thermal annealing (RTA) can improve the contact resistance. Figure 4.16 shows the gate response which deteriorated after RTA at  $450^\circ\text{C}$  for 1 min.



**Figure 4.14:** SEM images of the CNFET Device #t1 fabricated by transfer. (a) Parallel source (S) and drain (D) electrodes covered by 120 nm Pd deposited at tilted sample rotation. (b) Close-up view of the nanotube suspended across the receiving electrodes after direct transfer. Zoom: End of the nanotube separated from the fork. (c) Top-view of the transistor. Images were recorded after electrical characterisation. Adapted and reprinted from [102]. © IEEE, 2012.



**Figure 4.15:**  $I_{ds}$ - $V_g$  transistor response of the nanotube Device #t1 shown in Figure 4.14 fabricated by direct transfer using the fork approach. (a) Transfer characteristics recorded in humid air at the 4200-SCS on day 6 after transfer, plotted in semi-log scale. Forward and backwards sweeps are plotted. (b) Same data plotted in linear scale and additional data points recorded on day 1 by a Keithley 2400. The increase in on-current for  $V_{ds} = 25$  mV is emphasised by an arrow. For the computerised Semiconductor Characterisation System (SCS) - on day 6 - two forward and backward sweeps are plotted each per source-drain voltage. Adapted and reprinted from [102]. © IEEE, 2012.

#### 4.5.6 Influence of e-beam induced carbonaceous deposition

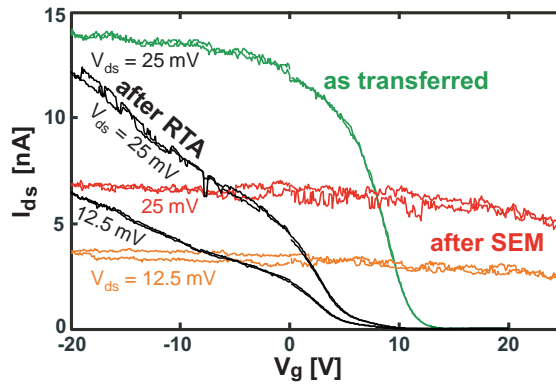
SEM After SEM imaging and electron beam induced carbonaceous depositions the same device was electrically measured again.  $I_{ds}$  started to fluctuate more and the gate coupling was weakened as seen in Figure 4.16. Typically, nanotubes are manipulated under SEM observation [35, 68, 145–147]. The deteriorated electrical properties after SEM imaging shown here, indicates the importance of performing the transfer under the absence of electron beams.

Deteriorated  
Coupling

The reduced gate coupling can be interpreted as enhanced shielding of the gate potential by the amorphous, conductive carbonaceous deposits being biased by the source or drain respectively. In addition, the carbonaceous film itself may contribute to  $I_{ds}$  and corrupt the OFF-state. An amorphous carbon layer of roughly 2 nm (estimated from TEM images) wrap the nanotube which could give rise to an additional current path. Assuming a resistivity of  $3.5 \cdot 10^{-5} \Omega m$ , a 2 nm coaxial shell would correspond to a parallel 7 M $\Omega$  resistor, which would be expected to contribute significantly to the device current at large  $V_g$  where the nanotube channel should turn off.

Conclusion

The observed degradation of the CNFET after SEM imaging corroborates the importance of avoiding electron beams during manipulation. For fork transfer, nanotubes are placed under light microscopy observation instead of SEM.



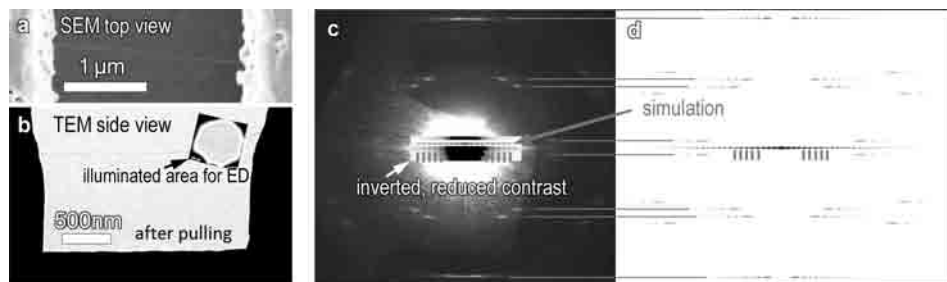
**Figure 4.16:**  $I_{ds}$ - $V_g$  transistor response of Device #t1 as-transferred, after rapid thermal annealing to 450 °C and after electron beam induced carbonaceous deposition during prolonged SEM imaging at 5 kV at a pressure of  $3 \cdot 10^{-6}$  mbar. Adapted and reprinted from [102]. © IEEE, 2012.

#### 4.5.7 Chirality assignment to CNFET fabricated by transfer

(25,18) CNFET

Electron diffraction patterns were recorded and a chirality of (25,18) was deduced for the CNFET Device #t1 fabricated by fork-transfer, shown in Figures 4.14, 4.15, and 4.16. In Figure 4.17a and b, the SEM image and the TEM overview image show an individual structure bridging the electrodes. The inset represents the area which was illuminated to record the diffraction pattern shown in Figure 4.17c. The non-modulated equatorial line of the diffraction pattern confirms that

the nanotube is indeed single-walled. Figure 4.17 shows the simulated pattern of a (25,18) nanotube which matches the experimental data best<sup>1</sup>. Theoretically, (25,18) corresponds to 2.93 nm and 24.63°. As the diameter is large, there are many other chiralities laying close to the measured values of 3.01 nm and 24.68°.



**Figure 4.17:** Electron diffraction on Device #t1. (a) SEM top view image of the nanotube integrated by transfer from a fork. (b) TEM overview image in tilted-view. The inset is the area illuminated for recording the diffraction pattern. (c) Experimental diffraction pattern recorded at 100 kV for 300 s. The part of the equatorial line is given with inverted and adjusted contrast for better visibility. A simulated equatorial line is placed next to the experimental data (grey arrow). Grey lines are guides to the eyes. (d) Simulated diffraction pattern of a (25,18) nanotube. Code was provided by Ph. Lambin [95] and implemented for MATLAB® by C. Roman. Reprinted from [102]. © IEEE, 2012.

#### 4.5.8 Transistor output characteristics

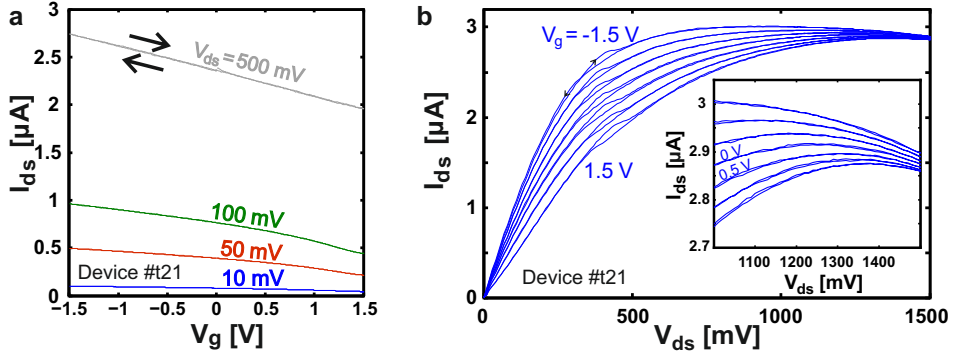
Output characteristics ( $I_{ds}$  versus  $V_{ds}$  for different values of  $V_g$ ) of transistors fabricated by transfer are shown in Figures 4.18 and 4.19.  $V_g$  was varied by steps of 0.5 V for Device #t21 (Figure 4.18) exhibiting small-bandgap semiconducting behaviour, and by 1 V for Device #t22 (Figure 4.19) exhibiting semiconducting behaviour. For source-drain bias voltages increasing to high levels, the current  $I_{ds}$  started to decrease in a repeatable manner. This negative differential conductance may be attributed to self-heating of the suspended nanotube(s) [297].

Franklin *et al.* reported that the magnitude of hysteresis can increase for larger  $V_{ds}$  [193]. Here, even the gate sweep at a large  $V_{ds}$  bias of 2000 mV (Figure 4.19a,b) did not exhibit hysteresis.

$I_{ds}$  vs.  $V_{ds}$

high  $V_{ds}$

<sup>1</sup> The closest alternative assignment would be (26,19) with 3.06 nm and 24.87°. Concerning  $\theta$ , (22,16) with 2.59 nm and 24.79° could be another option, but is unlikely due to the deviation in diameter. Moreover, it would be an  $(n-m)=3 \cdot q$  nanotube and hence would be expected to show metallic properties. The intrinsic layer line spacing including  $L_2$  to  $L_6$  [296] (Equations B.28), indicates  $n=25$  and  $m=18$ . The average  $m/n$  ratio of 0.723 matches best for (25,18) with 0.720. If assuming (25,17) the calculated tilt angle  $\tau$  would be 16°, which is much larger than the tilt angle of 6.5° measured by SEM top-view. Additional tilt may be introduced due to  $\beta$  tilt of the chip, but is estimated from TEM images to be less than 2°. As 16° > 6.5° ± 2°, (25,17) appears unlikely. For (25,18),  $\tau$  is calculated to be 8° – close to 6.5° ± 2°. The diameter is calculated using Equation B.32 to be 2.97 nm. This is closer to the theoretical diameter of 2.93 nm for (25,18), than the initial extraction of  $d=3.01$  nm conducted without including  $\tau$  for calibration.



**Figure 4.18:** Output characteristics of Device #t21 fabricated by transfer onto Pd electrodes. (a)  $I_{ds}$ - $V_g$  characteristics and (b)  $I_{ds}$ - $V_{ds}$  output characteristics for steps of 0.5 V in  $V_g$ .

#### 4.5.9 Shrinkage of gate separation

Gate  
Geometry

By implementation of the receiving electrodes in the thinnest poly-Si layer available in polyMUMPs and by reducing the height of the undercut, the gate distance to the nanotube can be reduced. Figure 4.20 illustrates the gate separation reduction from 5.5  $\mu\text{m}$  for Device #t1 to 3.5  $\mu\text{m}$  for Device #t2. The gate voltages needed to turn the transistor fully on, respectively off become smaller<sup>1</sup> when the gate is closer and the lever arm of the gate is larger. Smaller gate voltage ranges are not only important for low-power applications, but keeping the involved voltages low can also be important to avoid gate leakage currents.

Device #t2  
3.5  $\mu\text{m}$

On the right hand side of Figure 4.20, the transfer characteristics of the CNFET Device #t2 is shown. The current is modulated from the p-branch ON state to the n-branch ON state within a  $V_g$  range of  $\pm 7$  V. As the current does not turn off completely, an SGS-nanotube can be assumed.

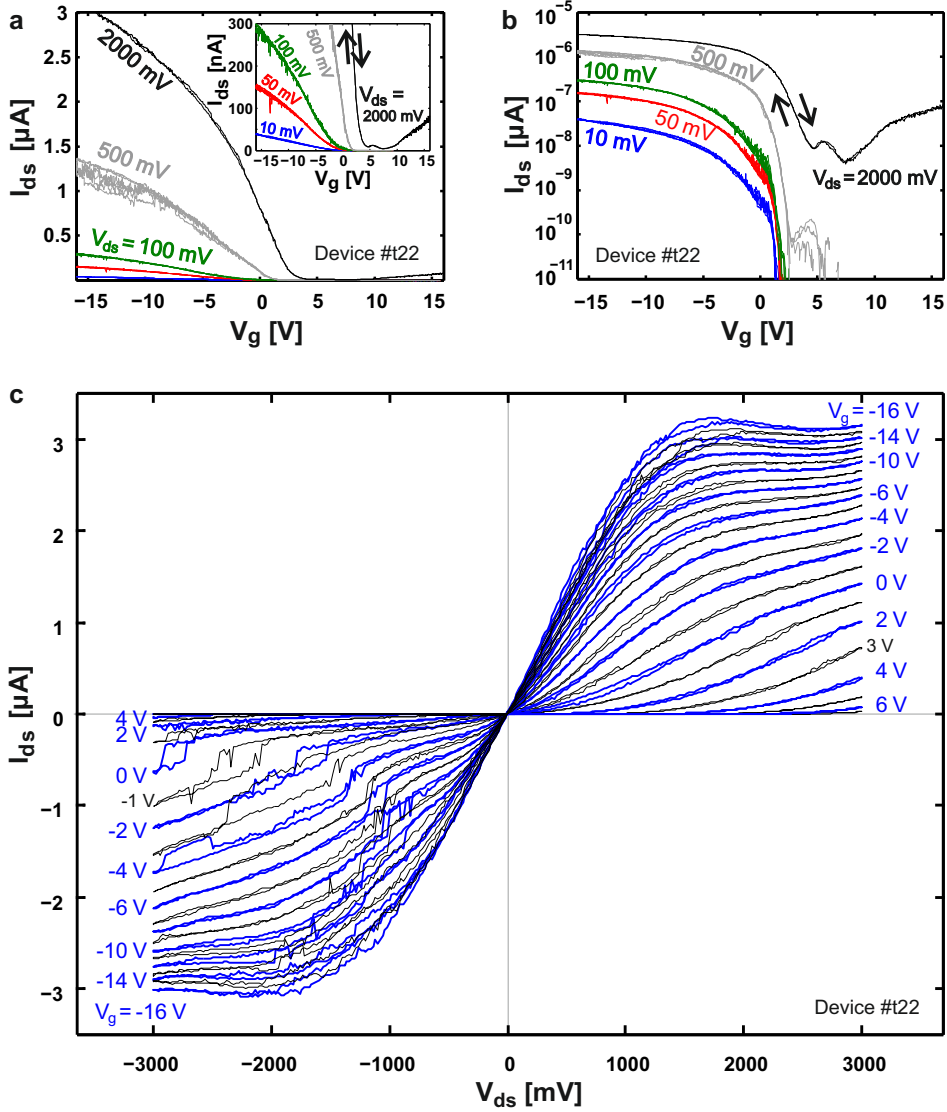
Discussion

The horizontal alignment obtained by the fork transfer is improved compared to alignment obtained by direct growth. In direct growth across released structures, only the starting point is defined while the nanotube may end on sidewalls. Nanotubes landing on the sidewall (see Figure 4.27f) are closer to the gate which is beneficial for good gate coupling, but reproducibility is difficult to achieve. Moreover, mechanical clamping is suboptimal. Nanotubes may also fall down onto the gate during direct growth and cause electrical shorts. In contrast, the placement by the fork approach avoids electrical shorts as the nanotube is placed on top of both electrodes. For the transfer approach, the air gap can be reduced to improve gate coupling without increased risk of electrical shorts.

Outlook: Gate  
Distance

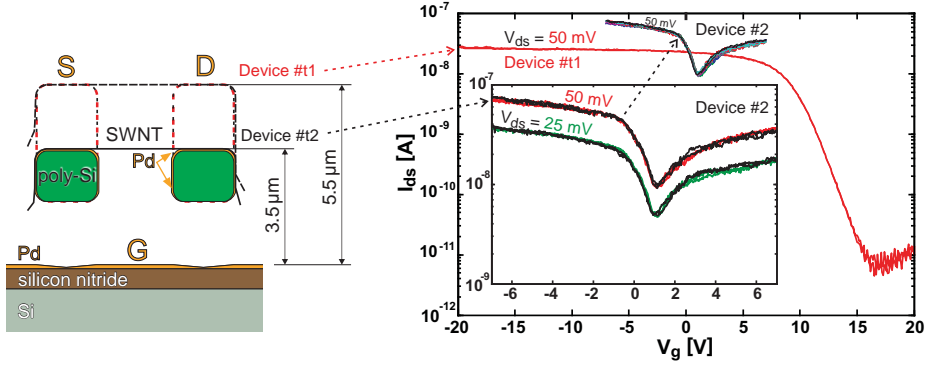
Further shrinkage of the size of the air gap is difficult to achieve within the polyMUMPS framework: The thinnest poly-Si layer which can possess undercuts is 1.5  $\mu\text{m}$  thick. The height of the undercut can be reduced down to 2  $\mu\text{m}$  by

<sup>1</sup> A practical aspect is, that the gas measurement setup of M. Mattmann [298] has a gate voltage range limited to  $\pm 7.5$  V. For the in-house gas measurement setup by K. Chikkadi [299] and for the setup at the vacuum chamber the limits are with  $\pm 10$  V more relaxed.



**Figure 4.19:** Output characteristics of the semiconducting Device #t22 fabricated by transfer onto Pd electrodes. (a) Linear plot and (b) logarithmic plot of the  $I_{ds}$ - $V_g$  transfer characteristics for large  $V_{ds}$  of up to 2000 mV. (c)  $I_{ds}$ - $V_{ds}$  output characteristics for steps of 1 V in  $V_g$ . In contrast to the branches of negative values of  $V_{ds}$  where single dual-sweeps are plotted for each  $V_g$  value, the branches of positive values of  $V_{ds}$  are averaged over three series of  $V_g$  steps. Alternating line colours are a guide to the eye.

the dimple etch, or down to  $0.75 \mu m$  by excluding the thicker oxide layer (Poly1 as gate or non-standard use of Anchor1). Although thinning of the poly-Si as an additional post-polyMUMPs etching step is possible, the upcoming limitation might be the geometrical height needed to bend the nanotube to be transferred



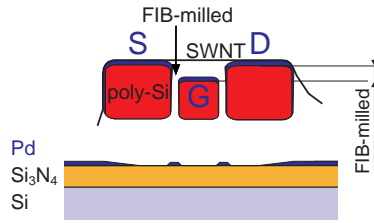
**Figure 4.20:** Illustration of the cross-section of Device #t2 fabricated by transfer, to scale. Device #t2 was fabricated by transfer onto the design with reduced gate separation of 3.5  $\mu\text{m}$ . The reduced gate-to-nanotube distance compared to the design of Device #t1 with a gate separation of 5.5  $\mu\text{m}$  is expected to reduced the required  $V_g$  magnitude to modulate the transistor.

properly around the edges of the receiving electrodes. Moreover, nanotubes can be attached on the bottom of the arms of the fork rather than on the top. As a consequence, depending on the vertical orientation of the nanotube, the fork has to be lowered below the receiving electrodes to bring the nanotube in contact with the receiving electrodes. A proposed alternative allowing for small gate-to-nanotube distances while providing enough vertical height for fork lowering is as follows. The bottom gate could be replaced by a poly-Si bar, very similar to the receiving electrodes, as sketched in Figure 4.21. The height reduction needed to separate the gate from the nanotube can be fabricated by lithographically masked etching, by thick depositions on the electrodes, or by FIB milling. The latter also allows cutting the three electrodes out of a single bar of poly-Si. Hence, shortening the suspended length of the nanotube below typical feature sizes in photolithography are possible. In contrast to direct growth, the risk is eliminated that nanotubes attach inadvertently on the gate during the waving growth: The nanotube on the fork has already spanned a distance corresponding to the separation between source and drain electrodes. The nanotube is constricted by the height of both S and D electrode upon lowering the fork. Thus, the suspended nanotube can be placed very close to the gate while stiction to the gate is not to be expected.

Moreover, out-of plane actuators, for instance electrostatic rocker actuators, might be used to mechanically tune the gate-to-nanotube distance.

Inspired by a concept presented by E. Cagin, the poly-Si electrodes themselves could be employed as gates. The source and drain contacts could be provided by pre-fabricated leads (lift-off) which are to be decoupled by an oxide and a poly-Si gap (Section 3.4.3).





**Figure 4.21:** Illustration of the cross-section of a concept for reduced gate distance by a FIB-milled gate implemented on a poly-Si bar instead of using the Pd-coated  $\text{Si}_3\text{N}_4$  as bottom gate. Milling/etching is to be completed before nanotube transfer.

## 4.6 STEM imaging of metal contacts

A sample holder was purchased from Gatan to accommodate a wire-bonded MEMS die inside the latest Cs-corrected STEM at EMEZ (Appendix B.2.4). Figure 4.22a,b shows the comparison of finding a region of interest in the TEM CM12 and in the STEM HD-2700Cs. STEM-mode with secondary electron detector facilitates finding of the region of interest compared to conventional TEM.

Region of Interest

STEM images of Pd metal clusters on a suspended bundle of nanotubes suspended across MEMS supports were recorded at 200 kV as shown in Figure 4.22d-f. The high-magnification STEM image shown in Figure 4.22h, and the corresponding intensity profile of Figure 4.22g, demonstrate atomic resolution of crystal lattices of a Pd cluster on a poly-Si MEMS support.

Pd

Figure 4.22c shows a nanotube segment between two supports consisting of ALD  $\text{Al}_2\text{O}_3$ . A rapid build-up of carbonaceous contamination was observed. Operation at 80 kV increased contrast.

Contamination

The HD-2700Cs offers possibilities for future chemical analysis, like probing oxidation of electrical contacts. However, the HD-2700Cs is a dedicated STEM and not capable of switching to TEM mode. Electrical feedthroughs will enable investigation of electromigration and straining of SWNTs at increased resolution.

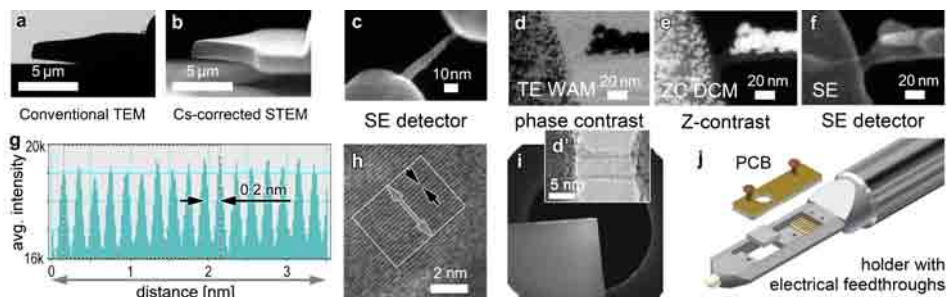
Outlook

## 4.7 Stability of threshold voltages

The threshold voltage  $V_{\text{th}}$  (Appendix B.1.5) is one of the possible measurands to be used as sensor output signal. For the gas sensors with surface-bound CNTs investigated by M. Mattmann [298],  $V_{\text{th}}$  was found to fluctuate in a range of  $\Delta V_{\text{th}} \approx \pm 1 \text{ V}$  in synthetic dry air for a  $V_g$  range of  $\pm 7.5 \text{ V}$  ([298] Chapter 7, Figure 7.2.). A surface-bound CNFET fully passivated by ALD  $\text{Al}_2\text{O}_3$  ([298] Figure 7.5.) showed reduced fluctuations of about  $\Delta V_{\text{th}} \approx \pm 0.55 \text{ V}$ , in a 64 h long measurement (neglecting the initial 8 h), respectively  $\pm 0.25 \text{ V}$  in 2 h – which indicates an improvement compared to the CNFET with the channel exposed to dry air. However, for gas sensing, the channel has to be exposed to the environment which also renders questionable whether the intrinsic fluctuations attributed to charge traps could be permanently reduced by annealing strategies. Some improvement can be achieved by long-time averaging and by defining more stable signal

Gas Sensors

$V_{\text{th}}$   
Fluctuations



**Figure 4.22:** Scanning transmission electron microscopy. Comparison of finding region of interest (a) in standard TEM and (b) in STEM HD-2700Cs using the SE detector. (c) SE image of carbon nanotube bridging between MEMS structures and clamped by  $\text{Al}_2\text{O}_3$ . Carbonaceous deposition was observed. (d') A SWNT clamped by  $\text{Al}_2\text{O}_3$  imaged in phase contrast mode. (d-f) Pd metal clusters deposited on suspended carbon nanotubes imaged in phase contrast, ZC and SE mode. (g) Intensity profile line of a Pd contact metal cluster shown in the STEM image of (h) demonstrating atomic resolution of crystal lattices. (i) MEMS die accommodated by the dedicated Gatan MEMS sample holder in vertical orientation. (j) The printed circuit board features 8 leads and is assembled using screws.

output calculation schemes, such as computing the area enclosed by  $I_{ds}$  and the  $V_g$  axis in a certain  $V_g$  range [298]. However, to massively improve the signal-to-noise ratio (SNR), a reduction in fluctuations is unavoidable.

Suspended and non-suspended nanotube devices were compared by Lin *et al.* [36] with respect to noise. The suspended section of the same nanotube exhibited an approximately 10-fold reduced noise amplitude. Mattmann suggests that this indicates that charge traps typically occurring in and on the gate oxide may be responsible to a large extent for the observed fluctuations. A reduction of these fluctuations is essential for  $\text{NO}_2$  sensors and probably for individual-nanotube-based gas sensors in general. Mattmann stated in his outlook: „The most important issue to be addressed next [...] is the high level of intrinsic fluctuations.“ [298].

The suspended CNFET fabricated by shadow masking or transfer showed to be free of hysteresis, which means  $V_{th,forward}$  and  $V_{th,backward}$  are identical. A dual-sweep measurement, recorded typically within a minute, hence approves threshold voltage stability within mid-term time scales. The stability of  $V_{th}$  over extended time scales is of importance for sensing applications. This section evaluates the stability of  $I_{ds}$  and the  $V_{th}$ -stability on longer time scales for suspended nanotubes that are integrated using the resist-free and oxide-covering approaches.

#### 4.7.1 Stability of threshold voltages in CNFETs

The threshold voltage  $V_{th}$  is extracted by fitting a linear curve at the steepest slope and extrapolating to zero  $I_{ds}$ . The number of  $I_{ds}$  data points used for curve fitting has to be selected carefully as explained in the following. A p-branch is considered, where  $I_{ds}$  is decreasing for more positive  $V_g$ . If the range of measurement points is extended over a too far  $V_g$  range, the linear fit will yield a too flat slope. Consequently,  $V_{th}$  is extracted to be more positive than it actually is. In case of too few data points, the fit of the slope may be less reliable. A MATLAB<sup>®</sup> routine was programmed to define the range of measurement points. The highest current,  $I_{dsfit\ max}$ , and the lowest current,  $I_{dsfit\ min}$ , were optimized iteratively by minimising the average  $V_{th}$  for the ensemble of gate voltage sweeps.

$V_{th}$  Extraction

#### Threshold voltage stability of CNFET fabricated by shadow masking

Figure 4.27b, presented later in the context of encapsulation, shows  $I_{ds}$ - $V_g$  curves of Device #s5 fabricated by shadow masking (before encapsulation). The measurements were taken on day 1, day 6 and day 12 after Pd evaporation. Table 4.4 shows the forward and backward threshold voltages for the p-branch.

Several Days

Compared to the threshold voltage fluctuations reported by Mattmann on the order of volts, the  $V_{th}$  was more stable here, represented by an average forward (and reverse) threshold voltage of 0.162 V (0.163 V) with a standard deviation of  $\pm 0.030$  V ( $\pm 0.032$  V) for the seven scans at a gate voltage range of  $-20$  V to  $20$  V. The standard deviation of  $V_{th}$  for forward and reverse gate sweeps was 0.074% of the full gate range. Despite the fact that the on-current decreased over the days, the maximum difference in  $V_{th}$  was 0.08 V.

$V_{th}$

Although these measurements are sparsely distributed over 12 days, the observed  $\Delta V_{th} \approx \pm 0.08$  V appears to be relatively small. Continuous  $V_{th}$  measurements are presented later for Device #t4.

Conclusion

The hysteresis,  $V_{th,forward} - V_{th,backward}$ , was  $-2 \pm 5$  mV. Hysteresis is typically either advancing or retarding. The negligibly small hysteresis width of 0.002 V is within the uncertainty not enough to determine whether the hysteresis is advancing or retarding. This justifies the attribution of the term hysteresis-free. The mismatch in current at the off-state for the forward and reverse gate sweep in the first scan of day 6 cannot be attributed to hysteresis as the position of the swing is unchanged. It is rather an incomplete off-switching of the transistor channel of unknown reason.

Hysteresis  
Discussion

**Table 4.4:** Threshold voltage of CNFET #s5 fabricated by shadow masking of Pd.  $V_{th}$  is extracted by linear fit in the region of steepest slope of the transfer characteristics.

		Day 1			Day 2		Day 12	
$V_{th,forward}$	[mV]	168	203	199	132	152	135	142
$V_{th,backward}$	[mV]	168	213	200	134	146	138	144

$V_{ds}$	mean	max.	min.	No. of	time	$I_{ds,fit,max}$	$I_{ds,fit,min}$	mean
	$V_{th} \pm stdev.$	$V_{th}$	$V_{th}$	sweeps	span <sup>a</sup>			$R^2_{fit}$
[mV]	[V]	[V]	[V]	[-]	[d]	[nA]	[nA]	[-]
25	$0.162 \pm 0.031$	0.213	0.132	7	12	$\sim 10^b$	$\sim 1^b$	0.991

<sup>a</sup> distributed as sets of 3 or 2 dual gate sweeps on day 1, day 6 and day 12

<sup>b</sup> 3 data points around 0  $V_g$  at steepest slope

### Threshold voltage stability of CNFET fabricated by transfer

Figure 4.23a shows the  $I_{ds}$ - $V_g$  characteristics for Device #t4 fabricated by transfer. The chirality was assigned by electron diffraction to be (35,9). The semiconducting behaviour matches the structure assignment.

Figure 4.23b shows the threshold voltage extracted from 246 gate sweeps recorded arbitrarily over a period of 5 h.  $V_{ds}$  was 50 mV. The average threshold voltage  $V_{th}$  was 0.366 V with a standard deviation of 0.013 V. The minimum  $V_{th}$  was 0.346 V, the maximum  $V_{th}$  was 0.407 V. The values for  $V_{ds}$  of 25 mV and 12.5 mV are summarised in Table 4.23.

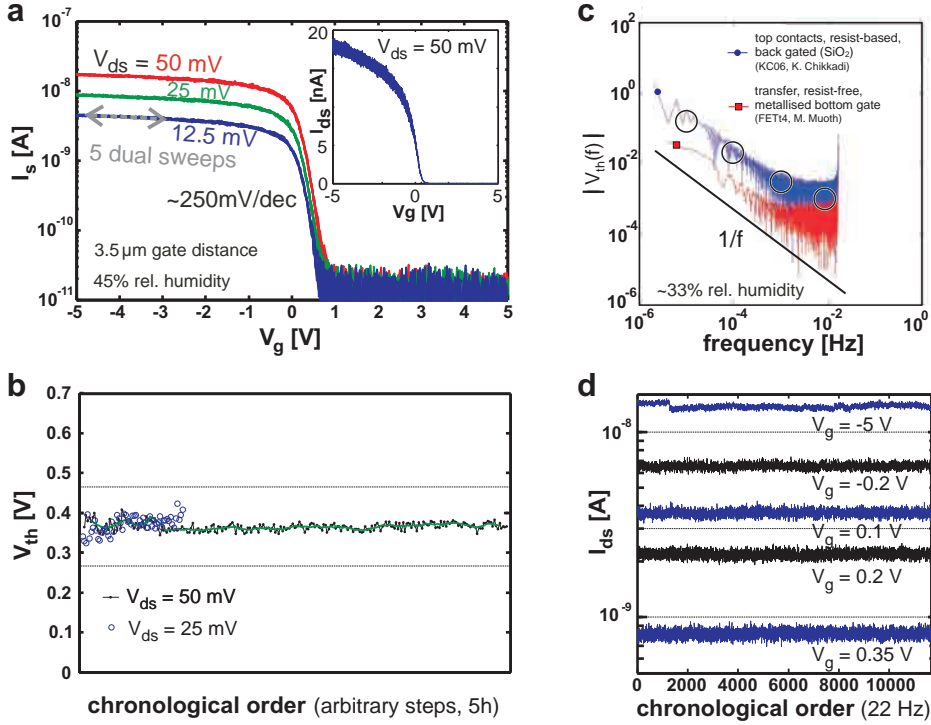
The frequency spectrum of  $V_{th}$  recorded over a time span of 62 h is shown in Figure 4.23c. As comparison, a frequency spectrum is given for a surface-bound CNFET fabricated by K. Chikkadi using resist-based lithography.

$I_{ds}$  values for constant  $V_g$  are shown in Figure 4.23d using a logarithmic scale. Three data sets, consisting each of 4000 data points recorded in 3 min, were recorded subsequently. The variation in  $I_{ds}$  was generally observed to be larger in the on-state than in the threshold region or in the off-state.

After maximising the slope of the linear fits by optimizing  $I_{ds,fit,max}$  and  $I_{ds,fit,min}$ , 19 to 22 data points were included for  $V_{ds} = 50$  mV for the full set of 246 sweeps, and 8 to 10 data points for the subset of 40 sweeps. 7 to 12 points were included for 25 mV and 6 to 10 points for 12.5 mV.

The CNFET #t4 fabricated by transfer exhibited a difference of 0.06 V between the minimum and the maximum  $V_{th}$  measured within 5 h.  $\Delta V_{th} \approx \pm 0.03$  V is much less than the  $V_{th}$  fluctuations observed in surface-bound devices [298].

Operation at static  $V_g$  values unequal 0 V is possible without substantial drift.



**Figure 4.23:**  $V_{th}$ -stability of Device #t4 fabricated by transfer. The transistor channel is an individual, 3.1- $\mu\text{m}$ -long SWNT of chirality (35,9). (a)  $I_{ds}$ - $V_g$  characteristics for  $V_{ds}$  of 50 mV, 25 mV and 12.5 mV. 5 dual gate sweeps are plotted for each  $V_{ds}$ . Inset is in linear scale. (b)  $V_{th}$  values of 246 gate sweeps in chronological order (arbitrary time steps). Overall time span was 5 h. Dots are for  $V_{th}$  extracted at  $V_{ds} = 50$  mV. Open circles correspond to  $V_{ds} = 25$  mV. The thick line is the 9-point moving average. (c) The frequency spectrum of  $V_{th}$  recorded over a time span of 62 h. The measurement was a collaboration with K. Chikkadi. Data for Device #t4 is labelled by a square. Data for a surface-bound, lithographically top contacted CNFET on  $\text{SiO}_2$  is shown as comparison by courtesy of K. Chikkadi. The approximated values for the gas sensor device of M. Mattmann [298] p.101 is indicated by open circles. (d)  $I_{ds}$  measurement at constant  $V_g$ . Three consecutive data sets of 4000 data points each were recorded within 9 min.

**Table 4.5:** Threshold voltage of CNFET #t4 fabricated by direct transfer onto Pd electrodes.  $V_{th}$  is extracted by linear fit in the region of steepest slope of the transfer characteristics.

$V_{ds}$ [mV]	mean $V_{th} \pm \text{stdev.}$ [V]	max. $V_{th}$ [V]	min. $V_{th}$ [V]	No. of sweeps	time span <sup>a</sup> [h]	$I_{ds \text{ fit max}}$ [nA]	$I_{ds \text{ fit min}}$ [nA]	mean $R_{fit}^2$ [-]
50	$0.366 \pm 0.013$	0.407	0.346	246	5	6.38	2.02	0.929
50	$0.372 \pm 0.014$	0.420	0.348	40 <sup>b</sup>	$\sim 2$	4.92	2.32	0.986
25	$0.371 \pm 0.021$	0.423	0.323	60	4	2.21	1.12	0.975
12.5	$0.388 \pm 0.031$	0.447	0.287	40	4	1.18	0.66	0.977

<sup>a</sup> sparsely distributed as sets of 5 successive dual gate sweeps

<sup>b</sup> subset of the 246 sweeps

Low drift is important for gauge factor tuning [26]. Reduced noise is indicated by comparison with surface-bound devices. The CNFET #s5 fabricated by shadow masking showed a maximum difference of 0.08 V in  $V_{th}$ . For a conclusive comparison between transfer and shadow masking more data would be needed. However, both fabrication methods result in devices with strongly reduced  $V_{th}$  fluctuations compared to earlier presented devices ( $\sim \pm 0.5$  V) [298].

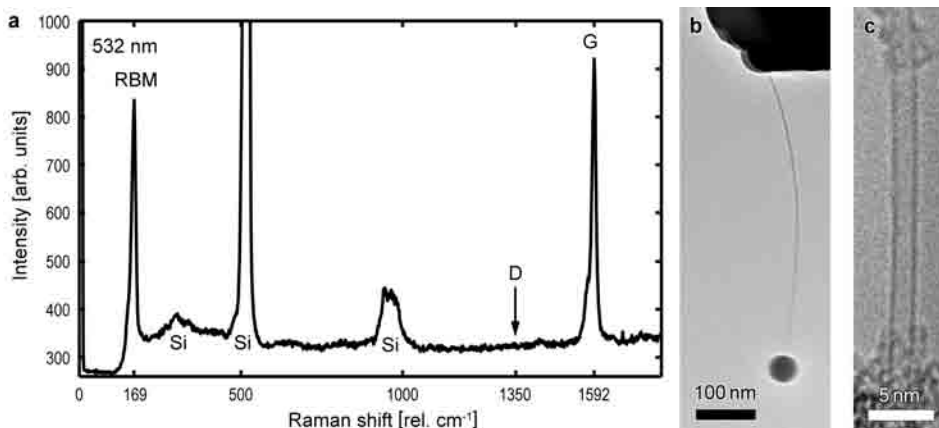
#### 4.8 Encapsulation by atomic-layer-deposited $\text{Al}_2\text{O}_3$

Overview

Passivation of contacts by encapsulation is of interest for gas sensing applications. A dry process flow for zero-level passivation was described in Section 3.6. The surface-selective  $\text{Al}_2\text{O}_3$  deposition requires clean and defect-free nanotubes.

CNT Quality

Following Jungen *et al.*, the D-mode in Raman spectroscopy indicates amorphous carbon deposition and/or defect density and was used to tune the  $\text{H}_2/\text{CH}_4$  ratio during SWNT growth [126]. Figure 4.24a shows a typical spectrum of the SWNT material grown by CCVD. The intensity peak for the defect mode (D) at  $1350 \text{ rel. cm}^{-1}$  is buried in the noise which is an indication of good SWNT quality. Figure 4.24c shows a TEM image of a suspended SWNT protruding from a poly-Si support tip. The nanotube has a constant diameter which corroborates the high crystallinity found by electron diffraction (Section 4.2). Figure 4.24b shows a single nucleation site of  $\text{Al}_2\text{O}_3$  from atomic layer deposition on a suspended SWNT. The low density of nucleation sites on individual SWNTs is an indication of low defect density and low amorphous carbon deposits.



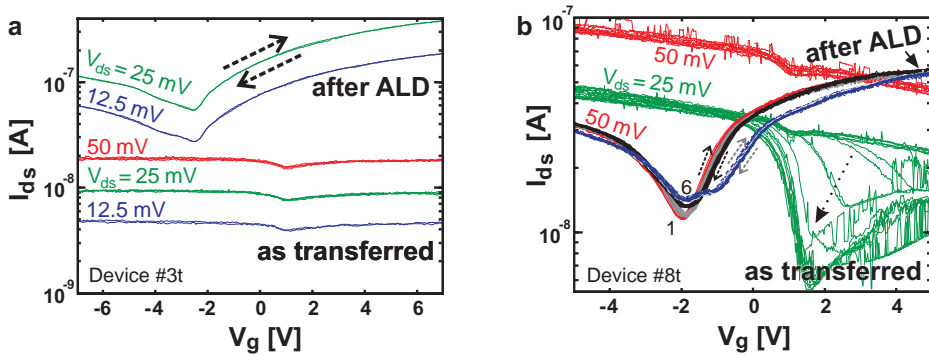
**Figure 4.24:** (a) The high ratio between tangential mode (G) and defect mode (D) intensity in the Raman spectrum is an indication for high-quality SWNTs. (b) SWNT and a single  $\text{Al}_2\text{O}_3$  bead formed by atomic layer deposition indicating a low defect density. (c) TEM image of a straight SWNT. Part of the carbonaceous deposits were deposited during imaging. Adapted and reprinted from Nature Nanotechnology, supplementary information [285]. © Macmillan Publishers Limited, 2010.

In Figure 4.25a,b, the electrical transfer characteristics of Device #t3 and Device #t8 are shown before and after encapsulation by ALD  $\text{Al}_2\text{O}_3$ . The thickness of  $\text{Al}_2\text{O}_3$  was 40 nm and the deposition temperature was 300 °C.

For both devices, the n-type branch became pronounced and the off-state was shifted towards more negative gate potentials.

The n-branch of Device #t3 showed a minute hysteresis of  $18 \pm 23$  mV based on the evaluation of  $V_{\text{th}}$  (extrapolated line at steepest slope). When evaluating the hysteresis at an  $I_{\text{ds}}$  level of 65 nA (to suppress the influence of the weak on/off ratio causing relatively large  $V_{\text{th}}$  readout uncertainty) the hysteresis was  $5 \pm 10$  mV after ALD deposition at 300 °C. The gate sweeps remained basically hysteresis-free after ALD. For Device #t8 a discrepancy between the successive gate sweeps was observed. Within 5 successive sweeps a difference in  $V_{\text{th}}$  of  $\sim 0.1$  V was observed. However, as indicated by later sweeps (labelled in Figure 4.25b by the numbers 1 and 6), the mismatch between  $I_{\text{ds}}-V_{\text{g}}$  traces has to be attributed to a general drift, rather than to typical hysteresis. The hysteresis between forward and backward sweeps was  $28 \pm 28$  mV after  $\text{Al}_2\text{O}_3$  deposition.

Before encapsulation,  $I_{\text{ds}}$  of Device #t8 was fluctuating at  $V_{\text{ds}} = 50$  mV and especially pronounced for the sweeps at  $V_{\text{ds}} = 25$  mV which exhibited even switching-like behaviour. The reason for this is currently unknown, however, it might also contribute to the drift observed after ALD.



**Figure 4.25:** (a) Device #t3 before and after atomic layer deposition of 40 nm  $\text{Al}_2\text{O}_3$  at 300 °C. The gate sweeps remained hysteresis-free after ALD. The n-type branch became pronounced. (b) Device #t8 before and after atomic layer deposition of 40 nm  $\text{Al}_2\text{O}_3$  at 300 °C. Switching-like drift in  $I_{\text{ds}}$  before ALD is highlighted by the dotted arrow. After ALD, a series of gate sweeps was recorded at 50 mV (black dashed arrows). 30 min later, a second series of gate sweeps was recorded (grey dashed arrows). The single sweeps show negligible hysteresis, but a general drift is occurring (indicated by number 1 and 6).

Figure 4.26 shows SEM images of Device #t7 which suffered (ESD?) damage during ALD encapsulation. The close-ups in 4.26a,b show not any ALD  $\text{Al}_2\text{O}_3$  bead on the suspended part of the nanotube. The absence of beads indicates that the deposition of the passivation was indeed surface-selective.

ALD

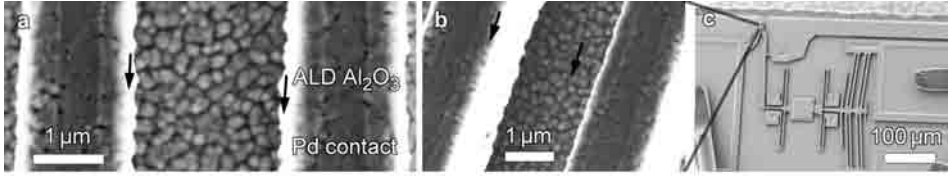
Towards  
n-TypeNearly  
Hysteresis-free

Drift

Switching

Surface  
Selectivity

Compatibility with MEMS	Device #t8 was integrated on a MEMS tensile stage 5.4. The electromechanical response of the encapsulated Device #t12am will be shown in Figure 5.8a.
Long-Term	After storage for two months, $I_{ds}$ of Device #t12am was found to have slightly increased. To prove enhancement of long-term stability by passivation, contacts know to be prone to degradation such as Cr/Au should be investigated.
Conclusion	Surface-selective nucleation of atomic-layer-deposited $Al_2O_3$ is compatible with MEMS-embedded CNFETs. Single dual sweeps show negligible hysteresis even after contact passivation by 40 nm $Al_2O_3$ grown at 300 °C, but a general drift was occurring for Device #t8.

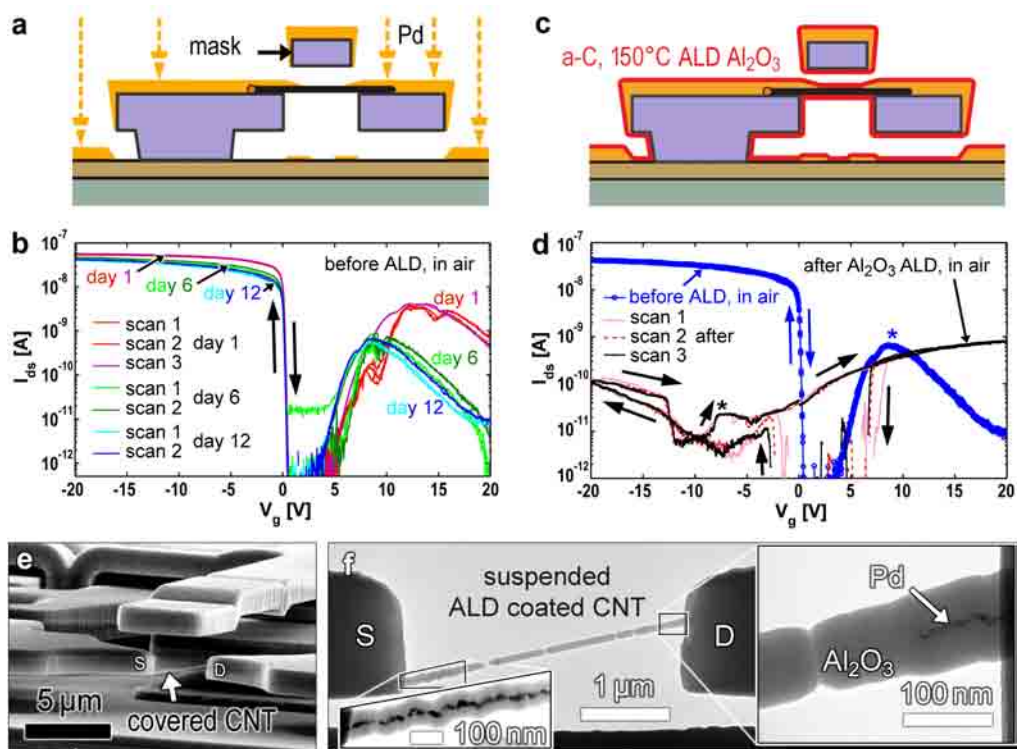


**Figure 4.26:** (a) Device #t7 after atomic layer deposition of 40 nm  $Al_2O_3$  at 300 °C. The encapsulation was not nucleating on the suspended nanotube section between the Pd contact electrodes. The device was fabricated by transfer.

#### 4.8.1 Hysteresis-induction by non-selective ALD $Al_2O_3$

CNFET #s5	Figure 4.27 shows Device #s5 electrically measured before and after atomic-layer deposition of $Al_2O_3$ at a reduced temperature of 150 °C on a sample with exceptionally much amorphous carbon. As published in Physica Status Solidi B [104], before the deposition of $Al_2O_3$ , no hysteresis was observed in the suspended CNFET fabricated by shadow masking. Figure 4.27b shows the $I_{ds}$ response to continuous $V_g$ sweeps at 0.9 V/s on different days: on day 1 shortly after Pd evaporation, later on day 6, and on day 12. On day 1, the three current plots nearly coincided for the p-type range. The weak currents at positive $V_g$ shifted slightly.
Storage	After storage in $N_2$ , the characteristics were similar on day 6. However, the maximum on-current was reduced. After storage in vacuum until day 12 and 2 h exposure to ambient air directly before the measurement, the $I_{ds}$ - $V_g$ curves were still free of hysteresis. The maximum on-current was decreased a little more. Every 2 <sup>nd</sup> scan on each day achieved slightly higher on-currents than the first scan of a measurement session. Stability of $V_{th}$ was discussed in Section 4.7.1.
Encapsulation	Figure 4.27d shows a comparison of the $I_{ds}$ - $V_g$ curves before and after coverage of the CNFET channel by 40 nm $Al_2O_3$ deposited at 150 °C. Large hysteretic effects were observed. The three consecutive scans starting at $V_g = 0$ featured a threshold voltage in forward sweep direction ( $V_g$ moving towards positive bias, arrows above the graph) at around -12 V. The current did not turn off completely for the forward scan. For reverse sweeps, a threshold voltage of approximately -3 V was observed. For gate sweeps to $\pm 20$ V, hysteresis on the order of volts occurred. The change from p-type towards n-type is consistent with the observations for devices #t3 and #t8 (Figure 4.25).





**Figure 4.27:** Effect of low-temperature atomic-layer-deposited  $\text{Al}_2\text{O}_3$  on gate hysteresis. (a) Schematic of a suspended nanotube transistor fabricated by shadow masking. (b) Hysteresis-free  $I_{\text{ds}}-V_{\text{g}}$  characteristics of Device #s5, measured over several days in ambient conditions. Forward and reverse sweeps are plotted. The subthreshold swing was 110 mV/dec.  $R_{\text{on, day 1}} = 437 \text{ k}\Omega$ .  $R_{\text{on, day 6}} = 536 \text{ k}\Omega$ .  $R_{\text{on, day 12}} = 591 \text{ k}\Omega$ .  $V_{\text{ds}}$  was 25 mV. The  $V_{\text{g}}$  sweep rate was 0.9 V/s. (c) Schematic of the same suspended CNFET after additional deposition of  $\text{Al}_2\text{O}_3$ . ALD at a low deposition temperature of 110 °C was non-selective on a sample with exceptionally much amorphous carbon deposition during CCVD. (d) Hysteresis and threshold voltage shifts were observed after the non-selective deposition of  $\text{Al}_2\text{O}_3$ . For comparison, the hysteresis-free scan 2 on day 12 before ALD is plotted (circles).  $V_{\text{ds}}$  was 25 mV. (e) Inclined SEM image of Device #s5. (f) TEM images recorded after the electrical characterisation. At the source (S), the nanotube is attached to the bottom of the electrode and consequently the deposited Pd is discontinuous. ALD  $\text{Al}_2\text{O}_3$  wrapped around the CNT. The gap between nanotube and backgate was 3  $\mu\text{m}$ . The edge of the die is visible and appears to be closer to the nanotube due to tilted-view observation (3.5.2). Adapted and reprinted from *Physica Status Solidi B* [104]. © Wiley-VCH 2011.

Figure 4.27e shows an inclined SEM image of Device #s5. Figure 4.27f shows the corresponding TEM images. The entire length of the CNFET channel was covered with ALD  $\text{Al}_2\text{O}_3$  except of a short gap. The gap did not contain a nanotube and is attributed to a rupturing event observed as sudden current drop during a slow  $V_{\text{g}}$  sweep (Quiet mode) to  $-30 \text{ V}$ .

Electron  
Imaging

Discussion	The suspended CNFET proved to stay hysteresis-free over several days and exhibited stable p-branch threshold voltages when measured in ambient air. Circumventing any resist- or wet chemistry-based processes after nanotube synthesis allows integration of suspended CNTs as transistor channels free of residual resist. The exclusion of defect-prone oxides in the vicinity of the CNT is regarded as essential to omit hysteresis.
Induced Hysteresis	Inducing hysteresis in a previously hysteresis-free device by adding an oxide layer demonstrated that the deposition of oxide can contribute to hysteretic effects. Comparing the hysteresis-free $I_{ds}$ - $V_g$ characteristics directly before and after ALD $Al_2O_3$ coverage allows attributing the observed hysteresis to the presence of the additionally deposited $Al_2O_3$ and/or its interfaces. Pronounced hysteresis was observed, which could possibly be related also to electrochemical effects in addition to charge trapping. However, it cannot be rule out that also the Pd contacts changed during the ALD process at a temperature of 150 °C. As to be shown in Section 4.8.3, no hysteresis is induced if the sample is heated in the $N_2$ -purged ALD chamber to even higher temperatures but without deposition. Hence, the hysteretic effects are suspected to be caused by trap states and possibly due to water adsorption on the $Al_2O_3$ surface. $H_2O$ adsorption is known as one cause for hysteresis with $SiO_2$ [28] and may be enhanced by the large hydrophilic [300] surface of $Al_2O_3$ .
Charge Injection	Charges directly injected from nanotubes into dielectrics [31] have been modelled to shift the forward threshold voltage of the p-branch towards more negative gate potentials [301], which is in agreement with our observations. The part of $Al_2O_3$ wrapped around the CNT channel is more prone to charge injection than the $Al_2O_3$ on the gate due to larger electric field strengths at the nano-scale curvature of the CNT surface. Following Fuhrer <i>et al.</i> [302], V. Döring calculated the electric field at the nanotube/ $Al_2O_3$ interface to be as high as 4 MV/cm at $V_g = 20$ V for our geometry. This is close to typical breakdown voltages of ALD alumina which are between 5 and 10 MV/cm [303]. Substantial charge injection is suspected to have caused device damage at $-30$ V. Charge injection alone, however, is not able to account for the complex changes in transconductance. It may be speculated that mobile ions present in the water layer may contribute to dynamic effects too.
Layer Quality	ALD at higher temperatures is known to provide higher quality layers with less (hydrogen) impurities [303, 304] and reduces hysteresis in previously hysteretic non-suspended devices [89]. Additionally, post-deposition annealing can diminish hysteresis [57].
n-Branch	The dips in conductance in the n-branch, and the shifted dips after ALD, are not expected for an ideal SWNT. While not being able to properly explain the cause, it might be speculated that disconnected Pd metal segments on the nanotube at the source electrode induced disorder and/or even confinement.
Non-selective	In contrast to the surface-selective ALD (3.6), the $Al_2O_3$ deposition is here rendered non-selective, covering the whole CNT, which is attributed to enhanced

amorphous carbon deposition during nanotube growth and a pronounced D-band (the intensity ratio of G-mode to D-mode was  $\sim 10$ ). A higher deposition temperature of  $300^\circ\text{C}$  indicated reduced nucleation on less ideal nanotubes, while here deposition took place at  $150^\circ\text{C}$ .

Passivation by ALD  $\text{Al}_2\text{O}_3$  deposited at  $150^\circ\text{C}$  was observed to introduce hysteresis into a previously hysteresis-free suspended nanotube field-effect transistor. The extraction of electrical device properties before and after an individual processing step provides an insight into the fundamental issue of hysteresis, which is of particular relevance for nanoscale devices with electrical field-strength enhancement due to nanoscale dimensions. The  $\text{Al}_2\text{O}_3$  deposition at higher temperature ( $300^\circ\text{C}$ , 4.8) resulting in negligible hysteresis indicates the influence of layer quality.

Conclusion

Measurements in vacuum may clarify the amount of hysteresis to be attributed to water adsorption on fully covered transistor channels.

Outlook

#### 4.8.2 Transistor polarity

Transistors with contacts formed of high work function metals are typically unipolar p-type because of Schottky barriers at the contacts. Conversion to n-type behaviour, or towards ambipolar behaviour, can be induced by annealing and operation in vacuum [88, 305] p.226, p.68. The change from p-type to n-type conduction is attributed to the desorption of  $\text{O}_2$  from the metal surface [183]. During ALD oxygen can be crowded out by the  $\text{N}_2$  carrier gas.

Polarity

For Device #s5, shown in Figure 4.27, a change from p- towards n-type characteristics was observed. The non-selective ALD deposition included a flushing step at  $110^\circ\text{C}$  at low-pressure in  $\text{N}_2$ . Also for selective deposition on the contacts at  $300^\circ\text{C}$ , devices #t3 and #t8 (Figure 4.25), a change towards n-type conduction was observed. The influence of heating during ALD is tested as follows.

Towards  
n-type

#### 4.8.3 Effect of heating during passivation process

The deposition of the passivation layer by ALD includes loading of the sample onto a hot wafer carrier (chamber temperature  $110^\circ\text{C}$ ) and unloading at typically even higher temperatures. While the unloading is regarded to be non-critical as the contacts are passivated at that stage, the loading and also the storage before passivation (exposure to oxygen) can possibly influence the device characteristics. For the semiconducting CNFET Devices #s5 (Figure 4.27) and #t4 (4.23), storage of the Pd contacts resulted in small changes of the  $I_{\text{ds}}$  magnitude while  $V_{\text{th}}$  was quite stable. RTA tested on Device #t1 (4.5.5) left-shifted  $V_{\text{th}}$ .

Aim

To indicate the effect of storage and heating during ALD the SGS-nanotube Device #t9 was stored and exposed to the loading/heating/unloading sequence of the ALD process, but without deposition of a passivation layer (0 nm  $\text{Al}_2\text{O}_3$ ).

Experiment

Figure 4.28 shows  $I_{\text{ds}}-V_{\text{g}}$  curves for the CNFET Device #t9 fabricated by transfer. The first series was recorded on day 1 after transfer. For 50 mV, 15 dual gate sweeps distributed over a time span larger than 30 min are plotted. After storage for 5 days in ambient cleanroom environment, the measurement was repeated.

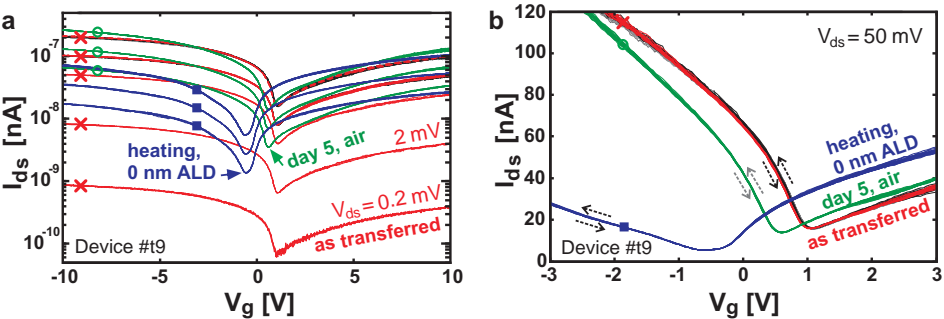
Device #t9

The values of  $V_{th}$  and the hysteresis width are listed in Table 4.6. The maximum current  $I_{max}$  increased slightly for both the p-branch and the n-branch.

Heating After loading the sample into the ALD chamber at 110 °C, pump-down, heating in N<sub>2</sub> to 300 °C, and unloading at 200 °C, the measurement was repeated.

**Table 4.6:** Threshold voltage  $V_{th}$  and hysteresis for the p-branch of Device #t9 shown in Figure 4.28.

Condition	Threshold voltage [V]	Hysteresis [V]
As-transferred	$1.18 \pm 0.011$ V	$0.012 \pm 0.014$
After storage in air for 5 days	$0.70 \pm 0.004$ V	$0.003 \pm 0.004$
After templated ALD (0 nm)	$-0.20 \pm 0.014$ V	$-0.002 \pm 0.013$



**Figure 4.28:** Influence of storage in air and heat cycle during ALD reactor conditioning in N<sub>2</sub> at 300 °C. Device #t9 was fabricated by transfer. (a)  $I_{ds}$ - $V_{ds}$  characteristics after transfer onto the Pd electrodes (crosses), after storage for 5 days in ambient cleanroom environment (circles), and after heating (squares) in N<sub>2</sub> to 300 °C (loading into the ALD chamber at 110 °C, unloading at 200 °C).  $V_{ds}$  was set to 50 mV, 25 mV, and 12.5 mV unless labelled differently. Several dual gate sweeps are plotted, for the as-transferred condition with  $V_{ds} = 50$  mV 15 gate sweeps are plotted that were recorded within a time span larger than 30 min. The gate sweep rate was 0.6 V/s. (b) Zoom to the same data but for  $V_{ds} = 50$  mV exclusively and in linear scale.

Discussion The  $I_{ds}$ - $V_{ds}$  characteristics remained hysteresis-free after loading/heating/unloading. A slight change in transistor polarity towards n-type was observed. For the SGS-nanotube device, a substantial shift in  $V_{th}$  occurred during storage in air and after unloading from the templated ALD run. In contrast to temporary  $V_{th}$  left-shifts for N<sub>2</sub> flushing at room temperature, the shift after heating does not disappear within minutes. Prolonged measurement are needed to evaluate whether the  $V_{th}$  will right-shift after long exposure to ambient conditions.

Conclusion The shift in threshold voltage had the same direction as for devices where Al<sub>2</sub>O<sub>3</sub> was deposited. The absence of hysteresis after 0 nm ALD Al<sub>2</sub>O<sub>3</sub> indicates that the hysteresis observed for Device #s5 (Figure 4.27) is not related to possible oxidation of the contacts during loading into the ALD chamber.

# 5 Mechanical loading of suspended CNTs

## 5.1 Motivation

Nanotubes were mechanically strained by MEMS actuators and characterised by combining TEM, Raman and displacement measurements to enable evaluation of nanotubes as strain gauges and as tunable resonators. Piezoresistive responses of ultraclean nanotube transistors to uniaxial strain were recorded and nanotube chirality was measured to pave the way for model validation.

Electro-mechanical Transducers

Parts of this chapter were presented at the IEEE MEMS12 [2], IWEPNM11 [5], and at IEEE MEMS13 [306].

## 5.2 Phonon shifts at defined strain in TEM-characterised SWNTs

As-grown, strained SWNTs were characterised by Raman spectroscopy and transmission electron microscopy. Tensile load was applied by micro actuators with characterised displacement output. Based on the quantitatively characterised displacement, chirality-dependent shift rates of the G-mode phonon frequency were deduced. Part of this section was presented at the IWEPNM 2011 [5] and includes contributions of J. Grimm [307].

Overview

Figure 5.1a shows a tip pair for nanotube straining. While one tip is anchored, the other one is linked to a shuttle driven by the actuator (Section 3.4.1). SWNTs were grown by CCVD and bridged between oxidised poly-Si tips as shown in the SEM image of Figure 5.1b. Tip pairs with properly oriented nanotubes were identified by confocal Raman mapping (Figure 5.1c) (14 tip pairs per actuator). Raman spectra were obtained while operating the electrically heated thermomechanical actuators in ambient air [307]. TEM imaging was employed to estimate the orientation of the nanotubes and to elucidate whether a bundle or an individual nanotube had been measured by Raman. Chirality was determined by TEM electron diffraction. To relate the actuator driving voltage to the strain value of the nanotube, the actuators were characterised in ambient air by optical image correlation using a planar motion analyzer (PMA). Voltage/displacement characterisation was performed as last step of the experimental sequence because the large displacement ranges applied can rupture or detach the nanotubes.

Experiment

Raman

Actuator

TEM

PMA

### Raman spectroscopy on strained, TEM-accessible nanotubes

The Raman spectroscopy map of a suspended single-walled carbon nanotube grown between a pair of actuated poly-Si tips is shown in the inset of 5.2b.

Device #m1

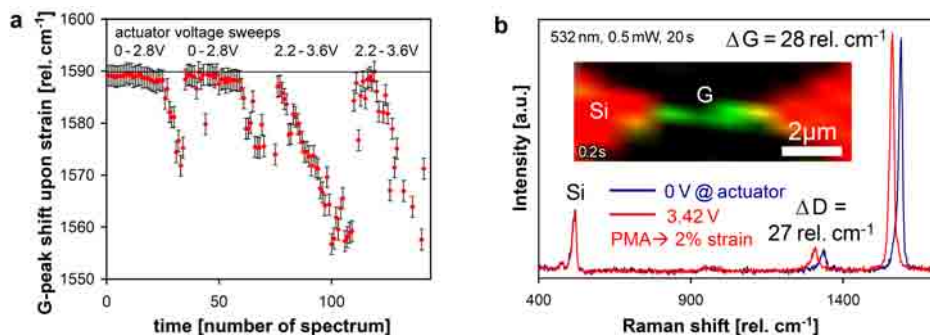


**Figure 5.1:** (a) SEM image of a poly-Si tip pair. One tip is anchored, the other is connected to a movable shuttle (dashed arrow) driven by an electrically heated thermomechanical actuator (see Figure 3.13). (b) Inclined SEM image of a nanotube suspended between a tip pair. (c) Raman intensity map of another tip pair, filtered for Si (tips) and for G-mode (nanotube). Presented at IWEPNM 2011 [5].

By driving the thermo-electromechanical micro actuator, the tip array (see Figure 3.13) was retracted and the pristine nanotubes were strained. Figure 5.2a shows the down-shifting of the G-peak position with increasing actuator driving voltage. Figure 5.2b shows two spectra of the same device for actuation voltages of  $V_{\text{act}} = 0$  V, and  $V_{\text{act}} = 3.42$  V. Both, G peak and D peak were down-shifted upon strain. The weak Si peak position remained unchanged.

Discussion

Four repetitive sweeps in  $V_{\text{act}}$  resulted in repeated down-shifting. The values of the fitted peak positions for the last  $V_{\text{act}}$  sweep are scattered more because the peak intensity decreased. Probably, the intensity decreased since the device drifted out of focus. Repeating the actuation is important to monitor possible slippage [20, 211]. The Si peak originates from the tips and not from the background. Its position stability indicates that the parasitic temperature effect of the actuator heating is small [212] p.70.



**Figure 5.2:** Raman spectroscopy on a SWNT integrated in a micro actuator. (a) Shift of G-peak position upon strain for Device #m1. The phonon frequencies of the axially strained SWNT are plotted for two actuator voltage sweeps from 0 V to 2.8 V and then for two voltage sweeps from 2.2 V to 3.6 V. (b) A spectrum in the unstrained state (0 V) is compared with a spectrum at 3.42 V actuator driving voltage. This voltage corresponding to 2% strain as deduced by the planar motion analyzer (see Figure 5.4 and the TEM images in Figure 5.3). The inset shows the corresponding Raman map in the unstrained state. Presented at IWEPNM 2011 [5].

### TEM imaging and chirality assignment by electron diffraction

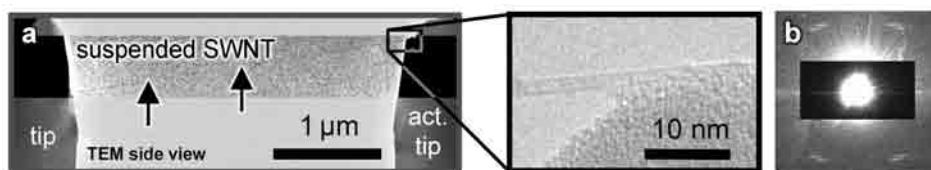
Figure 5.3a shows the TEM image of the tip pair corresponding to the Raman measurements of Figure 5.2 (Device #m1). In TEM, a nanotube was found at the top of the tips. The nanotube is an individual one, as shown in the close-up.

TEM

The corresponding electron diffraction is shown in Figure 5.3b. The nanotube is single-walled. A chiral angle  $\theta$  of  $27.3 \pm 0.2^\circ$  was determined according to the layer line spacings. The diameter was extracted to be 1.65 nm based on the equatorial line intensity interval including intrinsic layer line spacing correction [296]. The intrinsic layer line spacings result in  $n_{exp} = 13.32$  and  $m_{exp} = 11.03$  (Equations B.29 and B.28). The  $m/n$  ratio is 0.85 (Equation B.23). The chirality (13,11) with [1.629 nm,  $27.26^\circ$ ] and  $m/n = 0.846$  matches best to the extracted values. The closest alternative is (14,12) [1.7645 nm,  $27.46^\circ$ ]. The simulated pattern [95] for (13,11) nanotubes fits better than the one for (14,12).

Electron  
Diffraction

The nanotube signal disappeared during Raman measurements at large actuator displacements. In the subsequent TEM investigations, a nanotube was found which had slack and was out of focus apart from the anchoring points at the tips. Upon irradiation, the nanotube zipped closer to the tips and was straightened as shown in Figure 5.3a. This nanotube is expected to be the one giving rise to the Raman signals, as it is the only nanotube found within the focal depth of the Raman measurement.



**Figure 5.3:** TEM investigation of the individual SWNT found between the tip pairs where the Raman measurements shown in Figure 5.2 were taken (Device #m1). (a) TEM image of the tip pair of Device #m1 showing a suspended nanotube. The inset reveals an individual nanotube. (b) Electron diffraction verified that the nanotube is single-walled. The chirality of (13,11) was assigned. Presented at IWEPNM 2011 [5].

### Nanoscale displacement calibration at ambient conditions

Nanoscale displacement would be readily measurable by electron microscopy. But the displacement output under vacuum conditions during electron microscopy differs from the displacement output under ambient conditions during Raman measurements. To overcome the discrepancy in displacement output due to reduced thermal dissipation under vacuum conditions, displacement was recorded under ambient air by a planar motion analyzer (PMA, POLYTEC GmbH) relying on correlation of light microscopy images. As shown in Figure 5.4a, two areas were identified, one on the moving shuttle and the other on a fixed anchor. Measuring the relative displacement between the two areas rejects lateral drift

Non-vacuum  
Displacement

PMA

and reduces the effect of vibrations. The displacement was measured at nine different actuation voltages  $V_{act}$ .

**Averaging** For each value of  $V_{act}$ , ten voltage steps from 0 V to  $V_{act}$  and back to 0 V were applied with a hold time of 20 s each. Three data points before and after the transition were neglected. The remaining  $\sim 40$  data points per voltage level  $i$  were averaged to the position  $x_{avg,i}$ . To suppress the offset, induced by drift occurring between area definition and measurement start, the displacement at each of the ten repeated levels of  $V_{act}$  was determined as:  $u_{avg,i}(V_{act}) = x_{avg,i}(V_{act}) - [x_{avg,i}(0\text{ V}) + x_{avg,i+1}(0\text{ V})]/2$ . The standard deviation of  $u_{avg,i}(V_{act})$  for all  $i$  was  $\leq 10.1\text{ nm}$  for all  $V_{act}$ , 5.8 nm on average. The final displacement value attributed to  $V_{act}$  was the average of all  $u_{avg,i}(V_{act})$  for  $i \in \{1 \dots 10\}$ .

**Test** As a simple validation, the displacement was extracted for  $V_{act} = 0\text{ V}$ . The final displacement value attributed to zero displacement was  $0.07 \pm 2.66\text{ nm}$ , measured by light microscopically means utilising image correlation.

**Displacement** The displacement-voltage data for the actuated tip of Device #m1 are plotted in Figure 5.4a. The displacement relation  $u(V_{act}) = 9.437 \cdot V_{act}^2 - 7.262 \cdot V_{act} [\text{nm}]$  was fitted as second-order polynomial. The resulting coefficient of determination is  $R^2 = 0.9978$ .

**Length** The length of the suspended nanotube segment was  $3.15 \pm 0.2\text{ }\mu\text{m}$ , based on  
**G-Mode Shift** TEM side view images. A shift rate of  $-13.1 \pm 1.9\text{ rel. cm}^{-1}/(\%\text{ strain})$  was ex-  
**Rate** tracted while initial slack (or slippage) was detected and taken into account by defining 0% strain at the displacement value where the G-peaks started to shift.

**Orientation** Misalignment with respect to the direction of motion influences the effective strain of the nano-object under test [208]. A nanotube inclination of  $11^\circ$  was observed on the TEM side view images. A displacement  $\delta u_{tip}$  of the actuated tip (gap enlargement) results in an attenuated displacement  $\delta u_{CNT}$  along the inclined nanotube. The attenuation factor for the slightly rotating nanotube is 0.982 for small displacements (0.984 at 500 nm displacement). The inclination of the nanotube in top view is smaller than  $8^\circ$  which corresponds itself to a displacement attenuation of 0.990. The strain in the nanotube is overestimated when using  $\delta u_{tip}$  instead of  $\delta u_{CNT}$ . Consequently, the shift rate of  $-13.1 \pm 1.9\text{ rel. cm}^{-1}/(\%\text{ strain})$  has to be taken as lower limit.

**Motion** The suspensions of the shuttle ensure in-plane motion and out-of-plane motion was negligible for the actuator designs with transmission rods (Figure 3.13).

**Device #m2** Another nanotube device fabricated by direct growth on  $\text{SiO}_2/\text{poly-Si}$  was measured (not shown). For Device #m2, a lower limit for the G-peak shift rate with strain of  $-15.8 \pm 0.6\text{ rel. cm}^{-1}/\%$  was extracted, after correcting the effects of initial slack and/or slippage. The distance between the tips at the initial positions was  $3.6 \pm 0.1\text{ }\mu\text{m}$ . The tip displacement relation  $u(V_{act}) = 8.837 \cdot V_{act}^2 - 3.949 \cdot V_{act} [\text{nm}]$  was fitted ( $R^2 = 0.9969$ ). According to the second order polynomial fit, the onset of displacement is expected at 0.45 V. This is lower than for the first actuator with a displacement onset at 0.77 V. The interpolation of the displacement fit predicts that displacement requires a minimum



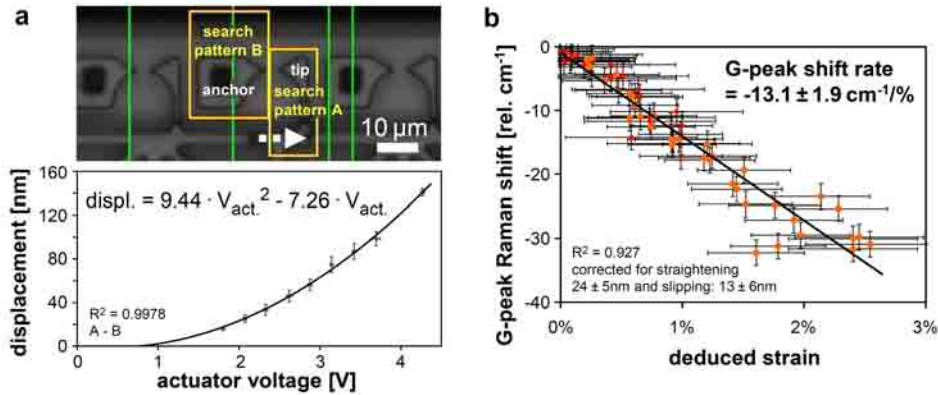
actuation voltage. This was confirmed by in situ TEM observations. Also under vacuum conditions, no displacement was observed for small voltages. The reasons might be related to the stiffness of the hinges of the transmission rod and/or to initial stress in the actuator beams.

At a  $V_{\text{act}}$  of 3 V, which can be considered to be the working point for large strain, the two different actuators displace the tips by  $u(V_{\text{act}}) = 63.2$  nm and 67.7 nm respectively according to the fit. This corresponds to a relatively small discrepancy of 3% in  $V_{\text{act}}$  to reach the same displacement for both actuators.

The same actuator type was operated under vacuum conditions inside a TEM. The relation  $u(V_{\text{act}}) = 35.25 \cdot V_{\text{act}}^2 - 19.22 \cdot V_{\text{act}}$  was fitted ( $R^2 = 0.9944$ ). A calculated displacement of 63.2 nm would be obtained a  $V_{\text{act}} = 1.637$  V. The displacement output was roughly 4 times larger under vacuum conditions than in ambient air. The displacement is strongly changed due to the lack of heat dissipation via convection of air. This underlines the importance of calibrating the actuators for Raman experiments by the PMA in air.

Actuator  
Comparison

Vacuum/Air



**Figure 5.4:** The actuator displacement was calibrated by optical image correlation at the same ambient conditions as present during Raman experiments. (a) Optical image recorded by the planar motion analyzer (PMA, Polytec) where two areas were identified for differential displacement measurements. Area A is the search pattern for the moving tip. Area B is the search pattern for the static anchor. The displacement  $A-B$  is plotted in dependence of the actuator voltage. 160 nm displacement corresponds to a 6% enlargement of the gap between the poly-Si tips. (b) A G-peak shift rate of  $-13.1 \pm 1.9 \text{ rel. cm}^{-1}/(\% \text{ strain})$  was extracted based on the displacement measurements by PMA. Device geometry was deduced from TEM images. Initial slack and slippage was detected and taken into account by defining 0% strain at the displacement value where the G-peaks started to shift. Presented at IWEPM 2011 [5].

By Raman mapping, 45 nanotubes were found to be suitably located between tips. The nanotubes were grown directly on the oxidised poly-Si and were not clamped by any metal or encapsulation. Only in two cases a G-peak shift was observed [307]. Initial slack as well as slippage of SWNTs was often observed by TEM (Section 5.3).

Slippage

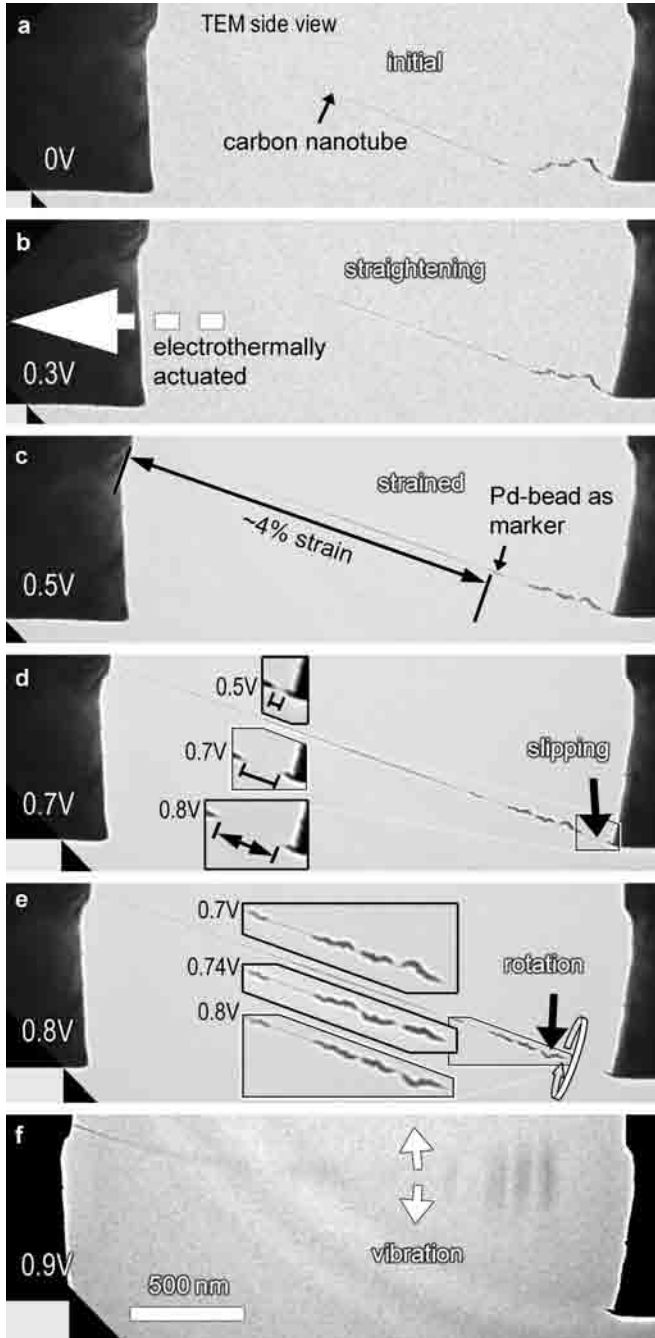
- Discussion** Down shift of phonon frequencies in carbon nanotubes due to tension has been predicted [308] and was measured by AFM manipulation of nanotubes on substrates [214] and chirality dependence was shown for suspended nanotubes [201]. Compared with these works our shift rate values are in a similar range. Slipping was observed to occur for long nanotubes on flat substrates over a length of several microns [309]. The nanotube orientation and its bending around corners of the microstructure may dictate whether the nanotube will slip or not. As demonstrated for long nanotubes, reliable clamping can be achieved by evaporated metal contacts [167, 201].
- Conclusion** Repeated shifts in the G-mode and D-mode of a SWNT were demonstrated. Compared to earlier work by Jungen [211], quantitative displacement calibration for operation in air was obtained and strain was deduced. Optical image analysis (PMA) characterised actuator displacement up to large displacements. Moreover, the proposed actuation inside a TEM was demonstrated [2]. TEM enabled discrimination between bundled and individual SWNTs. Chirality assignment of nanotubes between actuator tips was shown which is of interest as the shift rate is chirality dependent and  $(n,m)$ -assignment is desired for validation of theoretical models [308]. The sharp tips promote small inclination angles, important to translate the tip displacement in nanotube displacement with little rotational contribution. Adhesion forces on oxidised poly-Si were only in few cases sufficient to substantially strain SWNTs with overlap lengths of few microns.

### 5.3 Uniaxial loading of SWNTs inside a TEM

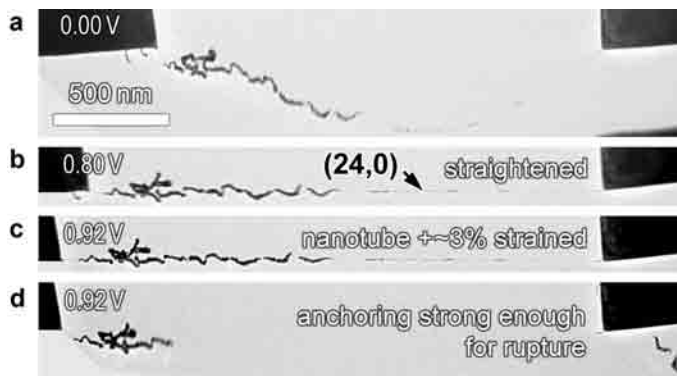
- Overview** SWNTs were grown on poly-Si supports and optionally clamped by patterned metal evaporation. Electrically driven micro actuators displaced one of the poly-Si support tips to induce strain on the nanotube (Section 3.4). The micro actuators were operated inside a TEM to investigate the clamping conditions of suspended nanotubes.

#### 5.3.1 TEM imaging of mechanical contacts

- Slippage** Slippage of SWNTs grown on oxidised poly-Si tips was often observed upon actuation. Initial slack was removed with increasing tip displacement. The straightened nanotube was pulled further. After moving the actuated tips back to the undisplaced state, the slack increased which has to be attributed to slippage instead of straining.
- Pd Contacts** By shadow masking, Pd was evaporated onto the poly-Si supports after nanotube growth (Section 3.2). Figure 5.5 shows a TEM image series at different actuator displacements of Device #m3s. The nanotube started slipping at a strain of ~5%, deduced by measuring the distances between the edge of the poly-Si tip and metal markers (Pd beads) formed on the nanotube by shadow masking. At 0.9 V actuator bias, resulting in a displacement of 0.38  $\mu\text{m}$  in plane, which corresponds to an elongation in tube direction of 19% (initial slack), the nanotube slipped off the anchor. Thereafter, vibration of the single-clamped nanotube was observed. Electron diffraction confirmed that the carbon nanotube consisted of



**Figure 5.5:** TEM images of in situ tensile loading of nanotube Device #m3s. (a) Nanotube suspended between an actuated poly-Si tip (left) and a fixed tip (right). (b) The nanotube was straightened. (c) Measuring the distance between the anchor and the Pd markers yielded a strain of ~4% at  $V_{\text{act}} = 0.5$  V. (d) At larger displacements, slippage was detected (arrow). Pd had been evaporated from the top at 30° tilted rotation. (e) Enabled by the non-spherical shape of the Pd marker beads, rotation around the nanotube axis was observed. (f) At an actuator voltage of 0.9 V, the nanotube became single-clamped and vibrated. Adapted and reprinted from [2]. © IEEE, 2011.



**Figure 5.6:** A (24,0) SWCNT of chiral angle  $0^\circ$  and a diameter of 1.88 nm was strained until failure (Device #m4s). The increase in strain from the straightened position at an actuator voltage of 0.80 V to 0.92 V was  $\sim 3\%$ . In the last panel, the SWCNT was ruptured as clearly seen from the displaced bead positions. The chirality of (24,0) was extracted from a electron diffraction pattern. The bottom left corners of the rotated TEM images are coloured grey for clarity. Adapted and reprinted from [2]. © IEEE, 2011.

two shells. The intensity profile line along the equatorial line of the diffraction pattern showed modulation in peak intensities which is a characteristic feature of double-walled carbon nanotubes [310]. Upon reducing the tip displacement, the single-clamped DWNT reattached to the tip. Repeated detachment and reattachment resulted in slightly varying attachment points.

Discussion

In contrast to previous work [201] where gold spheres were produced by global Au deposition and subsequent coagulation by heating, the Pd beads can be located intentionally at the end section of the nanotube, leaving the middle section undisturbed. Additionally, detection of rotation of the nanotube around its axis was enabled by non-spherical bead shapes. This indicates that nanotubes can exhibit torsional deformation after direct growth which can cause torsion-induced bandgap changes. The clamping forces for the nanotube attached to the sidewall and the bottom of the poly-Si tip (Pd evaporation from the top) were too weak to rupture the nanotube, rather slippage occurred.

### Rupturing

Rupturing  
(24,0)

Figure 5.6 shows a strained SWCNT where the clamping was strong enough to allow breaking the nanotube (Device #m4s). After initial slack was removed by pulling the nanotube into a straight position using the actuator, a diffraction pattern was recorded. The chirality was determined to be (24,0). The corresponding diameter of 1.88 nm matches with the bright field TEM image  $1.8 \pm 0.2$  nm. Between  $V_{\text{act}} = 0.80$  V and 0.92 V an increase in strain of  $\sim 3\%$  is extracted between the Pd markers on the nanotube. The mechanical clamping was strong enough to allow rupturing the nanotube. Pd beads clearly showed that the nanotube was ruptured rather than detached from the oxidised poly-Si surface coated with Pd.

Discussion

The actuator can provide sufficient displacement to rupture nanotubes even if

they had slack initially. A slight out of plane movement was observed which may be caused by geometrical asymmetry in the anchors and consequently in heat dissipation. The motion response to voltage steps is immediate. For larger actuation currents, image drift is induced due to thermal expansion. After large voltage steps, a settling time of approximately 30 s was required before sharp images could be taken (see drift in Figure 5.6b). If initial slack is present nanotubes can be straightened. Thus, the prerequisite for electron diffraction of having straight nanotubes can be met (bending corrupts the periodicity of the structure).

### Conclusions on straining

Carbon nanotubes were strained via thermomechanical micro actuators inside a transmission electron microscope, where Pd beads were used to identify the strain regime. Tensile loading of a chirality-assigned SWNT and of an individual DWNT was demonstrated by TEM-compatible micro actuators.

Slippage was typically observed for nanotubes on oxidised poly-Si. Shadow masking enabled deposition of markers on the nanotube for detection of strain and rotation. Mechanical clamping was improved by metallisation, but for nanotubes which landed on the sidewalls, clamping was not always sufficient for application of the force needed to induce mechanical breakage of the nanotube.

Summary

Conclusion

## 5.4 Electromechanical response of MEMS-embedded CNFETs

Electrically interfaced nanotubes were integrated in tensile stages by fork transfer and clamping was optionally aimed to be improved by surface-selective ALD or by patterned Pd evaporation. Electromechanical responses of hysteresis-free CNFETs were demonstrated [306] which will be important for exploiting gauge factor tuning [26] in nanotube-based electromechanical transducers.

Overview

### 5.4.1 Piezoresistive response of CNFET fabricated by transfer

Figure 5.7a shows the strain-dependend electron transport measurement of transistor #t11m fabricated by nanotube transfer onto Pd-coated electrodes.  $I_{ds}$  decreased for increasing strain. The response was repeatable as demonstrated by the three subsequent sets of three dual sweeps recorded at increasing actuator voltages  $V_{act}$  of 0 V, 0.5 V, and 0.7 V.

Electromechanical Response

The chirality of the CNFET was assigned by electron diffraction. The SWNT is most likely a (24,20) semiconducting nanotube.

Electron Diffraction

The class  $p = 1$  predicts a decrease in  $I_{ds}$  upon tensile strain. This matches to the observed decrease in current. The chiral angle  $\theta$  of 27.0° is close to 30°. Consequently, the model of bandgap modulation [311] predicts a relatively small change in bandgap of +15.2 meV/% strain. The experimentally obtained  $dE/dc$  of +42 meV/% exceeded the predicted value, but is still small.

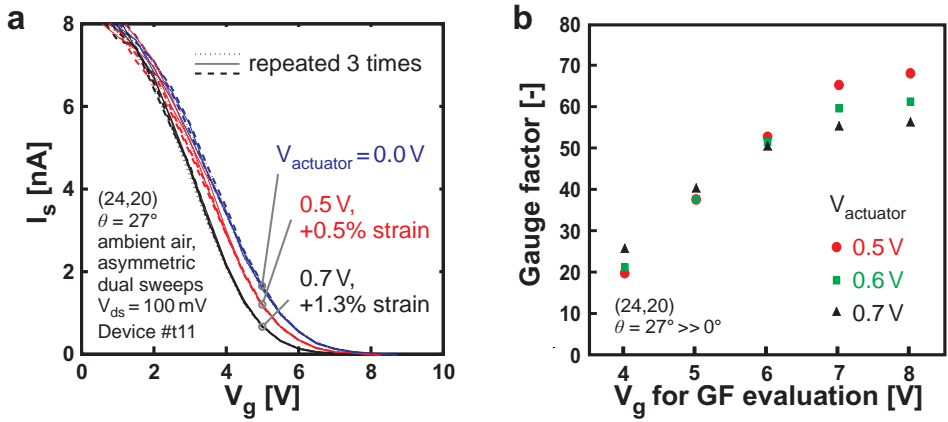
Model Comparison

Displacement was calibrated using the planar motion analyzer. The displacement output was  $u(V_{act}) = 79.956 \cdot V_{act}^2 - 18.924 \cdot V_{act} + 1.016$  [nm].

PMA

For Device #t1 (presented earlier in Figures 4.14 to 4.17), mechanical actuation using the electrically heated thermomechanical actuator resulted in small

Actuation



**Figure 5.7:** (a) Electromechanical response of a suspended CNFET of chirality (24,20) to uniaxial tensile strain applied by a micro actuator (Device #t11m). (b) Extraction of gauge factor (GF) for different gate voltages [306].

changes of  $I_{ds}$ , but they were not reproducible. Possibly slippage occurred.

Conclusion

Mechanically induced changes in the transistor transfer characteristics was observed for some of the as-transferred devices, but not for all of them. Clamping has to be improved.

#### 5.4.2 Piezoresistive response of CNFET encapsulated by $Al_2O_3$

Encapsulation

The electron transport measurement under different displacements of the micro actuator for Device #t12 showed inconsistent responses. Possibly, slippage occurred for the as-transferred nanotube. Figure 5.8 shows the electron transport measurement after encapsulation of the contact areas by atomic-layer-deposited  $Al_2O_3$  (Section 3.6). Repeatable straining was achieved, however, only for small strain ranges.

For Devices #t6 and #t7 the electrical responses were lost during or after ALD.

Conclusion

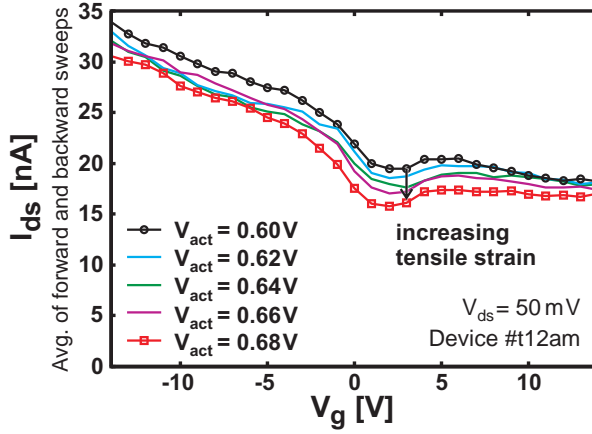
Zero-level encapsulation by ALD  $Al_2O_3$  improved exemplarily the enforcement of mechanical contacts of a tensile loaded CNFET. However, slippage seemed to occur at increased  $V_{act}$ .

#### 5.4.3 Piezoresistive response of CNFET with top-metallisation

Transfer &  
Shadow  
Masking

The mechanical clamping of suspended nanotubes placed by transfer was improved by additional metal deposition patterned by shadow masking. The inset of Figure 5.9a shows the actuated source electrode of CNFET #t14sm. First, the nanotubes were transferred onto the Pd-coated electrodes. Then, an on-chip shadow mask was shielding the nanotubes during the second deposition of Pd<sup>1</sup>.

<sup>1</sup> The nanotube-to-gate distance was reduced to 2.25  $\mu m$  by placing the Poly2 electrodes onto Poly1. By executing the dimple etch in the region of the electrodes, the topside of the electrodes was 5.5  $\mu m$  above the substrate. Placing a 0.5  $\mu m$ -thick Poly0 spacer at the initial position of the mask, in addition to the upwards-bending of the mask induced during the first Pd evaporation, enabled sliding of the mask in close proximity above of the electrodes.



**Figure 5.8:** Electromechanical response of Device #t12am after encapsulation by 40 nm ALD  $\text{Al}_2\text{O}_3$ . The forward and backward sweeps were averaged for each actuator driving voltage  $V_{\text{act}}$ .

Thus, the nanotubes were sandwiched between the Pd deposited before transfer and the Pd evaporated onto the nanotubes patterned by shadow masking.

The electrode displacement- $V_{\text{act}}$  relationship of Device #t14sm is plotted in Figure 5.9a. For the straight nanotube section with an angular misalignment of  $9^\circ$  and suspended length of  $2.9 \mu\text{m}$ , the strain was extracted to be  $\varepsilon = 8.919 \cdot 10^{-3} \cdot V_{\text{act}}^2 - 6.881 \cdot 10^{-5} \cdot V_{\text{act}} - 2.738 \cdot 10^{-4}$ .

Figure 5.9b shows the transistor characteristics at varying strain levels. The p-type transistor showed increased conductance with increasing strain. Conduction in the n-branch appeared at strains larger than 3%. The strain was increased up to 4.6%. The  $I_{\text{ds}}-V_{\text{g}}$  curves for decreasing levels of strain matched those obtained for increasing strain.

Figure 5.9c shows TEM images of the two straight nanotubes spanning across the electrodes. Electron diffraction (Figure 5.9d) revealed that both CNTs are double-walled and have the same chirality of  $(16,5)@(20,12)$ .

Both walls are of class  $p = -1$ . The expected decrease in bandgap is in agreement with the observed increase in current upon strain. As shown by Liu *et al.* [234], the outer wall is dominating the electrical properties of DWNTs. Here, the outer  $(20,12)$ -wall has the smaller bandgap anyhow ( $E_{g, \text{outer}, \sigma=0} = 350 \text{ mV}$ ). The predicted change in bandgap for the outer wall with  $\theta_{\text{outer}} = 21.8^\circ$  is  $-40.2 \text{ mV}/\% \text{ strain}$ .

Enhancement of thermally activated transport or enhanced electron-phonon scattering due to thermal crosstalk of the actuator can not be ruled out. However, the observation of both classes  $p = +1$  and  $p = -1$  indicates that the bandgap is indeed strain-modulated.

Pre-straining of the nanotubes during placement is likely ( $\varepsilon > 0$  for  $V_{\text{act}} = 0$ ) and is currently under investigation [274].

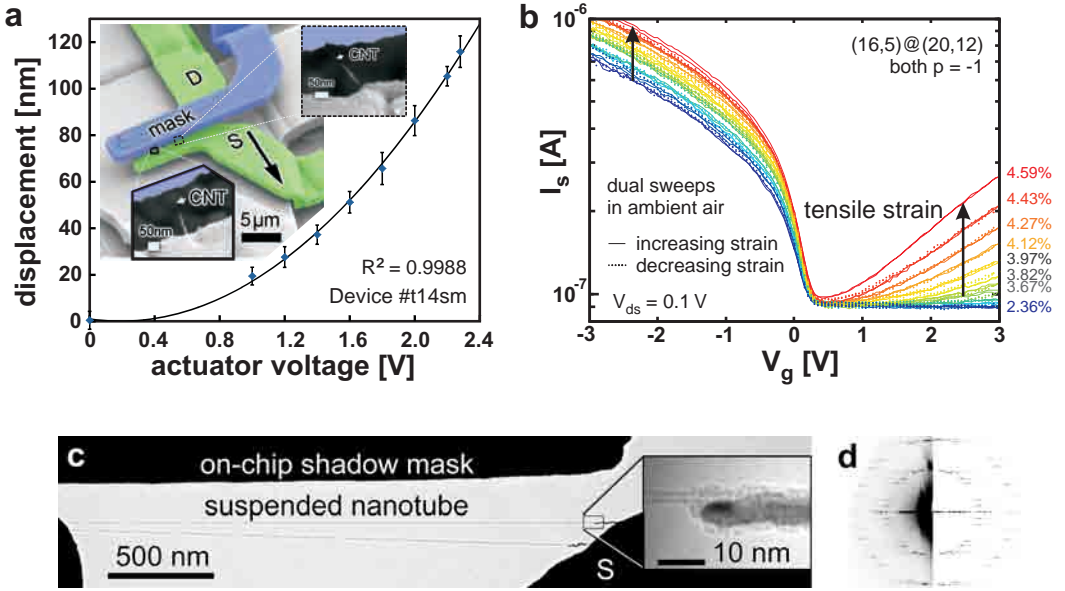
PMA

 Electromechanical  
Response

TEM &amp; ED

 Structural  
Prediction

Discussion



**Figure 5.9:** (a) Deduction of displacement to actuation-voltage relation using the planar motion analyser operating at ambient air. Insets show SEM images of Device #t14sm fabricated by transfer and additionally clamped by shadow masking. (b) Electromechanical response of CNFET #t14sm consisting of two DWNTs of chirality  $(16,5)@(20,12)$ . The dual sweeps of  $V_g$  are plotted as lines for increasing strain, and as dotted lines for decreasing strain. The strain level is indicated for the DWNT which is nearly perpendicular to the electrodes. For the second DWNT segment, the strain is reduced by 28% due to inclination. (c) Corresponding TEM image in side view showing the straight DWNTs. In addition to stigmation, the image of the inset is blurred by vibrations. The apparent wall width is larger than 0.8 nm which is exceeding the anticipated width of a SWNT. (d) The electron diffraction patterns (one of them given on the left, simulation on the right) revealed that both DWNTs have the same chirality of  $(16,5)@(20,12)$  [306].

## Conclusion

Electromechanical responses of ultraclean, MEMS-embedded CNFETs were recorded. The orientation and location control of the fabrication approach by fork transfer was combined with the resist-free lithography provided by on-chip shadow masking. Additional clamping by metal evaporation improved the mechanical clamping conditions of transferred nanotubes. This way, piezoresistive characterization of chirality-assigned, ultraclean, hysteresis-free carbon nanotube transistors was achieved. Preliminary comparisons with the theoretical model of bandgap change confirmed the influence of the class  $p$  on the sign of the current modulation.



# 6 Conclusion and Outlook

## 6.1 Summary and Conclusions

Suspended single-walled carbon nanotubes were embedded in microelectromechanical tensile actuators allowing in situ TEM experiments [2, 5].

MEMS & TEM

Electrical contacts to suspended SWNTs in microfabricated structures were fabricated by two processes. Both approaches avoid any wet-chemistry after nanotube growth and simultaneously prevent the contacts from exposure to the harsh nanotube synthesis conditions.

Contamination-free & Low-Temperature

Combining localised direct growth of suspended SWNTs with resist-free stencil lithography avoids exposure of the contact material to high temperatures and the nanotubes are neither affected by resist residuals, or damaged by cleaning processes nor contaminated by surfactants. Compared to approaches for nanotube integration in MEMS, incorporating supporting oxide bridges [43], release etching is circumvented which eliminates another potential source of contamination [69] and device loss. An on-chip shadow mask is guided by a movable slider and is placed atop the suspended part of the as-grown nanotube.

Shadow Masking

The nano-tapered Pd contacts are self-aligned to the suspended pristine SWNTs [101]. The subthreshold swing (230 mV/dec) was remarkably good for the large air gap between the metallised bottom gate and the nanotube suspended between microstructures at an elevation of 3  $\mu\text{m}$  above the gate.

Needle-like & Self-aligned

In the transfer approach, the contact metal is deposited on a die which is not exposed at any time to the high-temperature growth. The nanotubes are grown on a separate die. In a dry direct transfer, the nanotube suspended between the arms of a fork-like growth support is placed onto electrodes of the receiving die. Current-feedback is used to trigger successful nanotube placement during light microscopy observation. Hence, carbonaceous contamination is avoided which would typically occur during manipulation under electron-beam observation. Carbonaceous contamination induced during SEM was shown to deteriorate the transistor gate response which indicates the importance of avoiding electron-beam exposure during nanotube transfer.

Transfer

Orientation and location control is improved compared to the direct growth employed in the approach of shadow masking. The risk of the occurrence of short-circuiting nanotubes due to misorientation or due to incomplete catalyst lift-off is overcome. Moreover, number control is facilitated as the adjustment of the nanotube area-density is outsourced on series of fork-like growth substrates. Placement can be repeated until at least one nanotube is integrated which increases device yield. The possibility is opened up to select a specific nanotube for integration. Wire bonding can be completed before nanotube integration and

Orientation & Location

Number

Selection

Packaging

therewith losses of suspended nanotubes during wire bonding are excluded.

**MEMS** Integration of SWNTs by transfer allows pre-characterisation of the MEMS device concerning displacement-output. The absence of any leakage current between source, drain and gate can be verified before nanotube integration. Thus, the measured source-drain current can be entirely attributed to the nanotube.

**No Hysteresis** For both fabrication approaches, the carbon nanotube field-effect transistors showed hysteresis-free gate responses even at slow gate sweep rates at humid ambient conditions. We suggest that metal-coverage of all oxide surfaces eliminates dynamic gate screening typically caused by charge injection/trapping in the surrounding of the nanotube channel (bulk and surface defects) [28, 31, 87, 193]. Furthermore, the high-quality nanotube material and the residual-free and gentle processing is expected to contribute to the absence of gate hysteresis [29, 33]. We induced dramatic hysteretic effects by covering the nanotube with low-quality aluminium oxide. This demonstrates the use of the previously hysteresis-free CNFETs as a test-bench for investigation of origins of hysteresis [104].

**Zero-Level Encapsulation** CNFETs with encapsulated contacts were obtained by surface-selective atomic-layer-deposition of  $\text{Al}_2\text{O}_3$  and showed nearly hysteresis-free operation (Section 4.8). The extracted hysteresis widths were  $0.018 \pm 0.023$  V and  $0.028 \pm 0.028$  V.

**Chirality-assigned CNFETs** By combining these clean fabrication process flows with electron diffraction in the tilted-view TEM inspection [103], chirality was assigned to hysteresis-free, MEMS-embedded CNFETs [2].

**In situ Straining** Pd beads formed on the suspended part of CNTs were used to identify the strain regime (straight/strained/slipping) inside a TEM and even to detect axial rotation of carbon nanotubes integrated in MEMS. Tensile loading of an individual chirality-assigned SWNT and of an individual DWNT was demonstrated by TEM-compatible micro actuators, which will be helpful in deepening the understanding of nanotubes for electromechanical devices.

**Clamping** As revealed by in situ TEM tensile tests, only very few of the unclamped and only some of the partially metal-clamped nanotubes were sufficiently attached to take up large mechanical strain before slippage occurred. The random growth direction during direct synthesis often leads to unfavourable nanotube attachment on the sidewall of the actuated tip rather than on the topside. This impairs clamping. The nanotube transfer on the other hand ensures nanotube placement on the topside of the electrodes. However, mechanical anchoring is inferior as clamping by a top metallisation is missing [201]. Encapsulation by ALD indicated strengthening of mechanical clamping (Device #t12am, Section 5.4). Including a shadow mask in addition to the receiving electrodes for nanotube transfer enabled to combine transfer and shadow masking (Device #t14sm 5.4.3). Pd evaporated after transfer aims at improved mechanical clamping. Strain up to  $\sim 4.6\%$  was withstood. The combination of transfer and shadow masking enables sandwiching a well-oriented nanotube between two metal layers. Proper mechanical clamping enabled electromechanical characterisation of clean, hysteresis-free, TEM-accessible, chirality-assigned nanotubes in the large strain regime.

**Electro-mechanical & TEM**

## 6.2 Outlook

Designs optimised for radiofrequency signal transduction may enable nanoelectromechanical resonator applications. The blunt contact geometry obtained by transfer and the unique capability to alter the contacts of the very same device using shadow masking (Section 4.5.4) may offer a versatile test bench to investigate quality factors and anchor losses.

Resonators

Following the route of functionalising the suspended nanotube to induce ALD nucleation [185], high-quality dielectrics for circular wrap-around gates might be achieved to boost the gate coupling in mechanically static devices.

Circular Gates

Whether the fabrication process schemes of transfer and shadow masking will reach large scale fabrication may be questioned. However, the expectation is that these clean integration methods will enable further exploration of nanotube electromechanical properties in well-defined configurations with minimized process-related disturbances. Progress in wafer-scale stencil masking as well as in automation of assembly at the micro/nano scale is foreseeable. Coupled with advances in the synthesis of few-chirality material and fast mapping, the transfer approach may develop impact beyond its application for demonstrator devices.

Scalability

Major competing materials for future large-scale transistor applications are graphene nanoribbons, germanium-silicium heterostructures, advanced silicon-based transistors with deterministically placed dopant atoms, diamond with nitrogen-vacancies, and molybdenum disulfide.

Concurrence

In the field of displacement and force measurements, strong competitors are emerging optomechanical systems and Si-based nanostructures. However, carbon nanotubes can withstand exceptionally large strain up to 13% [20] which make them very promising for transducer operation in the large-strain regime – which cannot be entered by brittle semiconductors which typically break at strain levels <1%. In gyroscopes whose readout relies on piezoresistive strain gauges made of Si nanowires [312], the high gauge factors of certain nanotubes could outperform Si.

Opportunities

Creep and mechanical hysteresis within the nanotube are expected to be abundant and long-term stability was shown for substrate-bound nanotubes in pressure sensors [26]. However, for the large strain regime in suspended device configuration, the contacts have to be examined carefully considering long-term operation.

Stability

Incorporation of highly compliant bearings (nanotubes perpendicular to the displacement direction) might enable substantial size reduction of proof masses in nanotube-based piezoresistive accelerometers. However, better control over chirality and cost-effective integration will be the key to exploit the superior material properties and the extreme aspect ratio of single-walled carbon nanotubes in electromechanical devices.

Control  
Costs



# A Appendix

## A.1 Safety considerations

Currently, there is no consensus concerning the characterization of carbon nanotube toxicity [313]. If inhaled nanotubes are potentially a high risk, possibly depending on morphology, size, catalyst remainders, and functionalization [313].

### Unloading LPCVD reactor

Although the here employed Fe catalyst nanoparticles are placed on the surface of the die and are not intentionally airborne as in other CNT synthesis approaches, care was taken while handling samples. Filter masks (X-plore 2100 FMP3D/P100, Dräger) and goggles were worn during loading and unloading of the 8 inch quartz furnace for CNT synthesis (LPCVD, PEO-603-PLC-300C, at FIRST). Additionally, a separate compartment of the cleanroom was built around the LPCVD system. An air filter system was included and a pressure gradient between the rest of the lab and the compartment was established. After completion in 2009, the LPCVD operator had no longer to distribute filter masks to all other persons in the adjacent rooms. For impressions, be referred to Figure A.1. The dedicated filter system was installed not only because of the SWNTs, but larger amounts of MWNTs were grown from  $C_2H_2$  in the same system. Silicon nanowires were grown too in the same furnace. A dedicated carrier wafer and avoiding Au catalysts at the outer areas of the die aimed to prevent the spread of nanomaterials during handling.

### Sample handling

CNTs can transfer within a sample as observed during contact mode AFM imaging and observed after cleaving of chips in solution. At scratches on CNT-coated surfaces, the tubes are missing. One SWNT clearly labelled to have undergone an ALD process by having attached some  $Al_2O_3$  beads was found on another die which was never subjected to ALD. The observation of the possibility of unintended die to die migration of SWNT and of multi-walled CNTs indicates the importance of avoiding impinging CNT chips with tweezers. A probably reasonable option is to coat the CNTs by a continuous layer of ALD, as we introduced in the ALD-assisted photolithography [42] and to limit the area of CNT growth by patterned catalyst deposition.

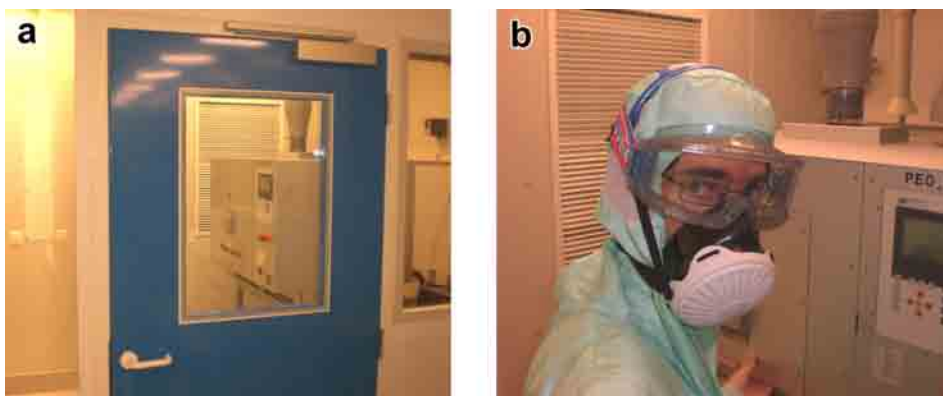
## A.2 Experimental procedure for electron diffraction at FEI CM12

The recording of electron diffraction patterns of nanotubes is based on the work of J. Meyer *et al.* [97] and was established with the help of Fabian Gramm (EMEZ). As the procedure is not comprised in the general introductions to the CM12, a description is given here. Permission and schooling are provided by EMEZ.

The carrier box of imaging plates is stored inside the exsiccator. Before loading the box, the emission and the high voltage must be turned off. The plate chamber is vented and the box is loaded using gloves. The chamber is evacuated and the vacuum has to recover for at least 20 min. Thereafter, liquid nitrogen is filled into the cold trap. The sample holder is plasma-cleaned (B.2.2) for 30 min. The

Loading

Pre-settings



**Figure A.1:** Photographs of the low-pressure chemical vapour deposition system (LPCVD, PEO-603-PLC-300C, ATV Technologie GmbH) in FIRST used for SWNT synthesis and Si nanowire growth. (a) Separate cleanroom compartment with slight underpressure and dedicated air filter system. (b) Filter mask and goggles were worn during loading and unloading of the LPCVD furnace for CNT synthesis.

acceleration voltage is set to 100 kV and the 'TEM low dose mode' is selected. Emission is turned on. The smallest condenser aperture is inserted (10  $\mu\text{m}$ ). The condenser aperture is mechanically aligned while wobbling the illumination. The illumination is set such as to fill the screen. The sample is inserted into the holder. For samples mounted in tilted-view (3.5.2), the edge of interest is oriented along the holder axis. The holder is loaded into the microscope. The eucentric height is mechanically adjusted by minimizing the image shift while alternating the tilt angle. „Auto focus“ is pressed to reset the lenses. In ideal case, the eucentric height is exactly in focus. Else, a slight image shift is preferred over detuning the focus from the auto focus position, because the microscope was aligned for the „Auto focus“ lens settings. If the sample is to be accessed in tilted-view (3.5.2) the sample tilt is adjusted to enable access to the tip pair of interest.

Eucentric  
Height

Tilt, Shift

The gun tilt (alignment) is adjusted for maximum brightness of a small-area beam in low SA magnification. At spot size 9, the beam spot is centred using Beam shift X,Y. Then, after changing to spot size 3, the beam is re-centred using the X,Y gun shift (alignment).

Pivot Points

The Pivot points of the beam deflection coils are aligned.

Diffraction

Astigmatism

The diffraction pattern astigmatism has to be corrected by making use of the crossover image of the diffraction lens. A bright-field TEM image is to be obtained in the SA magnification. The sample and the objective aperture are removed from the beam path. The spot size is set to number 4. To correct the diffraction astigmatism, the beam is projected on the fluorescent screen at maximised illuminated area (low intensity of illumination). This is done by turning the illumination knob to expand the beam, resulting in a low area dose. After verifying that the fluorescent screen is closed to shield the CCD camera from overexposure, the button „D“ is pressed. This enters the diffraction mode which projects the backfocal plane onto the screen. The camera length to be used is set (680 mm) using the magnification knob. Defocussing yields a circular beam shape with a highlighted rim: the diffraction crossover image. The stigmation button is pushed and the 'DIFF astigmatism' is selected. The values are noted

and are reset after the session as changes can induce large image shifts in the low magnification mode. Using the multifunction knobs, the stigmator is adjusted to obtain a three-fold symmetrical image in the centre of the circle. Then, the projection lens is set to imaging mode by pressing again the „D“ button which deactivates the diffraction mode.

The illuminated area is shrunk to the centre of the fluorescent screen at a magnification of 66 kX. By correcting the condenser astigmatism, the shape of the illuminated area is adjusted to remain circular while wobbling the illumination intensity. The spot size is set to 11 and the condenser astigmatism is again adjusted carefully. The spot size is changed to 4 or 7 to increase the intensity.

Condenser  
Astigmatism

Magnification is reduced and illumination is adapted. The sample is moved into the illuminated area and the region of interest (ROI) is placed to the centre of the screen. Strong defocussing can help to locate the nanotubes. A Si tip apex, or a similar feature at the height of the nanotube, is focussed and objective astigmatism is corrected. The nanotube end sections are imaged at high resolution (340 kX or higher). As the centre part of the suspended nanotube is typically vibrating, high resolution is only achievable at the clamped ends. The difference in focus for the two nanotube end sections is an indication whether the nanotube is aligned with the focal plane. The mid-section of a straight, suspended nanotube is moved to the centre of the screen. The spot size is decreased to the smallest available spot size 11. The magnification is set to 66 kX. The illuminated area is adjusted to yield a circle filling the field of view of the CCD camera at 66 kX magnification. Larger size of illuminated area results typically in sharper diffraction patterns. A CCD image can be used to verify that the nanotube is crossing the illuminated area (low dose, hence ~5 s recording time). Beam shift X,Y can be used to centre the illuminated area on the nanotube.

ROI

Selected Area

The fluorescent screen is put in place to shield the CCD camera. The diffraction mode is activated and a camera length of 680 mm is selected (corresponding to 770 mm as soon as screen is flipped up). The zero-beam is focussed. To use the CCD camera for a immediate check of the diffraction pattern, the beam stop must be inserted to protect the CCD from damage. The zero-order beam can be shifted using the multifunction knobs. After ensuring that the zero-beam is fully blocked, quick test patterns can be recorded on the CCD camera using exposure times of 20 s. For better contrast, exposure times longer than 180 s are required. Imaging plates offer superior dynamic range and high resolution. Up to 36 imaging plates can be loaded per box. To record the diffraction pattern on the imaging plate, the detector mode is set to 'TV'. The TEM camera setting is chosen to be 'manual', exposure time 300 s. The objective aperture is removed. The CCD cameras are retracted. The fluorescent screen is removed. The viewing glass is covered. The controller switch is toggled down to 'neg.'. The image plate is exposed by pressing „Exposure“. After deactivating the diffraction mode, toggle up the controller switch, and inserting the camera, a CCD image can verify that beam shift and sample drift was acceptable.

Diffraction  
Pattern

CCD

Imaging Plate

The imaging plates are unloaded – analogously to loading. Wearing gloves is mandatory. The box is opened without exposure to light and the plates are loaded into the scanner (Micron DITABIS, Settings: highsens, 100% laser intensity, 120 000 gain, resolution 15  $\mu\text{m}$ , binning factor 1, blacklevel correction activated, standard 16 bit). The files are loaded as full image and are exported as .tiff for analysis using Gatan's Digital Micrograph<sup>TM</sup>. The imaging plates are erased by 20 min exposure to UV light.

Readout

Run sheet - shadow masking					
Module	Stage	Parameter		Shadow masking	ID
Dicing	Dicing	program No.		44	1
		feed rate [mm/s]		2	
		wafer thickness [μm]		650	
		cutting depth [μm]		690	
	Photo-resist removal (PolyMUMPs)	acetone rinse	time [min], temp. [°C]	dip 3 s, 22 °C	2
		acetone	time [min], temp. [°C]	10 min, 22 °C	3
		isopropanol	time [min], temp. [°C]	5 min, 22 °C	4
Sacrificial layer etch	Wetting	DI water rinse	time [min]	>1 min	5
	Etching	HF	concentration	40%	6
			time [min], temp. [°C]	3 - 5 min, 22 °C	
	Rinse	DI water	time [min]	10	7
	Drying	DI:IPA = 1:1	time [min], temp. [°C]	3 min, 22 °C	8
		IPA	time [min], temp. [°C]	3 min, 22 °C	9
		N2 stream	time [s]	~2s	10
	Bake	hotplate	time [min], temp. [°C] support	>5 min, start at 65 °C, heat to 120 °C microscope slide	11
Growth barrier layer	Oxidation	Material		silicon oxide on poly-silicon	12
		Bunsen burner	time [min], temp. [°C]	15 min, >600 °C, on ceramic plate	
		thickness [nm]		>~8 nm	
E-beam lithography	Resist spin coating	resist		PMMA/MAA pure	13
		spinner sequence		500rpm, 3s, 5s; 4000rpm, 5s, 45s	
	Soft bake	temperature [°C]		150	14
		time [s]		70	
	Resist spin coating 2	resist		PMMA/MAA pure	15
		spinner sequence		500rpm, 3s, 5s; 4000rpm, 5s, 45s	
	Soft bake	temperature [°C]		150	16
		time [s]		70	
	Resist spin coating 3	resist		PMMA/MAA pure	17
		spinner sequence		500rpm, 3s, 5s; 4000rpm, 5s, 45s	
	Soft bake	temperature [°C]		150	18
		time [s]		70	
	Exposure	E-beam writer	acceleration voltage [kV]	30	19
			aperture [μm]	30	
			dose [μC/cm²]	420	
			current [nA]	~0.34	
	Development	developer, concentration		MIBK:IPA 1:3	20
		developing time [s]		70	
		developing stop bath		IPA pure	21
		time [s]		60	
	Drying	N2 stream	time [s]	~2 s	22
Patterned catalyst adsorption	Iron particle size	target particle height after oxidation [nm]		~3-4	
	Iron particle density	target nanotube density [1μm²]		~3	
	Preconditioning	Plasma cleaning	time [min], power [W]	(3 min, 250 W)	23
		MES buffer 50 mM		1 min	24
		DI-water		1 min	
		N2 stream		~5 s	
	Protein absorption	stock solution diluted in MES pH4, 50 mM		ferritin stock solution: MES ~1:50-300	25
	Rinse in DI water	time [min], temp. [°C]		3, RT	
		temperature [°C]		RT	26
		time [min]		1	
	Drying	N2 stream	time [s]	~5 s	27
	Lift-off	Acetone	time [s], temp. [°C]	10 s, RT	28
		Acetone	time [s], temp. [°C]	10 s, RT	29
		Acetone	time [s], temp. [°C]	30 s, RT	30
		Acetone	time [min], temp. [°C]	10 min, 50 °C	31
		IPA	time [min], temp. [°C]	5 min, 50 °C	32
		N2 stream	time [s]	~4 s, gently	33
	Drying	hotplate	time [min], temp. [°C]	1, ~120 °C	34
		support		~2 s	
	Ferritin oxidation, calcination	ambient air, Bunsen burner temp. [°C]		>600 °C	35
		time [min]		1 min	



Shadow masking, continued				
Module	Stage	Parameter		Shadow masking
Subdicing	Resist spin coating	resist		PMMA/MAA pure
		spinner sequence		500rpm, 3s, 5s; 3000rpm, 5s, 45s
	Soft bake	temperature [°C]		150
		time [s]		70
	Resist spin coating	resist		PMMA/MAA pure
		spinner sequence		500rpm, 3s, 5s; 3000rpm, 5s, 45s
	Soft bake	temperature [°C]		150
		time [s]		70
	Dicing	program No., same parameters as in ID 1		44
		acetone rinse	temp. [°C]	dip 10 s, 22 °C
	Resist removal	acetone	time [min], temp. [°C]	15 min, 50 °C
		isopropanol	time [min], temp. [°C]	5 min, 50 °C
	Drying	N2 stream	time [s]	~4s, gently
		hotplate	time [min], temp. [°C]	>5 min, start at 65 °C, heat to 120 °C
		support		microscope slide
		temperature [°C]		850
SWNT growth	Growth	H2	H2 reduction [s], [slm]	31 s, 3 slm
			H2 growth [s], [slm]	58 s, 0.2 slm
		CH4	carbon source [s], [slm]	34 s, 1 slm
			Growth time [min]	12 min
Metal patterning	Mask placement	Micromanipulator, light microscope		move shadow mask with AFM tip
	Metal evaporation	element		Pd
		thick. [nm], sample tilt [°], sample rotation		120 nm, 30°, 5 rpm
Passivation	ALD	Al2O3	temp [°C]	110 - 300, better 300
			thickness [nm]	40
			selective nucleation: clean, defect-free, individual nanotube	
Wire bonding	wedge-wedge wire bonding	Devotek, silver paste, aluminium wire	on package, US-power	130
			US-time	55 ms
			on die, US-power	125
			US-time	50 ms

Steps 47-50 after nanotube growth are free of wet-chemistry.

Run sheet - Fork transfer						
Die	Module	Stage	Parameter		Value	ID
growth die device die	Dicing	Dicing	program No.		44	1
			feed rate [mm/s]		2	
			wafer thickness [µm]		650	
			cutting depth [µm]		690	
		Photo-resist removal (PolyMUMPs)	acetone rinse	time [min], temp. [°C]	dip 3s, 22 °C	2
			acetone	time [min], temp. [°C]	10 min, 22 °C	3
		isopropanol	time [min], temp. [°C]	5 min, 22 °C	4	
growth die device die	Sacrificial layer etch	Weting	DI water rinse	time [min]	>1 min	5
		Etching	HF	concentration	40%	6
				time [min], temp. [°C]	3 - 5 min, 22 °C	
		Rinse	DI water	time [min]	10	7
		Drying	DI:IPA = 1:1	time [min], temp. [°C]	3 min, 22°C	8
			IPA	time [min], temp. [°C]	3 min, 22°C	9
		Bake	N2 stream	time [s]	~2s	10
			hotplate	time [min], temp. [°C]	>5 min, start at 65°, heat to 120°	11
		support	microscope slide			
growth	Growth barrier layer	Oxidation	Material		silicon oxide on poly-silicon	12
			Bunsen burner	time [min], temp. [°C]	15 min, >600°C, on ceramic plate	
			thickness [nm]		>~8 nm	
	E-beam lithography	none				
growth die	Catalyst adsorption	Iron particle size	target particle height after oxidation [nm]		~3-4	13
		Iron particle density	target nanotube density [1µm²]		~2	
		Protein absorption	stock solution diluted in MES pH4, 50 mM		ferritin stock solution:MES ~1:100-800	14
		Rinse in DI water	time [min], temp. [°C]		3, RT	
			temperature [°C]		RT	
		Drying	time [min]		1	15
			time [s]		~5 s	
		Ferritin oxidation, calcination	N2 stream		time [s]	~5 s
	ambient air, Bunsen burner		temp. [°C]	>600°C	16	
			time [min]	1 min		
g	Sliding	Fork movement	Micromanipulator, light microscope		move fork beyond die edge by AFM tip	17
growth die	SWNT growth	Growth	temperature [°C]		850	18
			H2	H2 reduction [s], [slm]	31 s, 3 slm	
				H2 growth [s], [slm]	58 s, 0.2 slm	
			CH4	carbon source [s], [slm]	34 s, 1 slm	
			Growth time [min]		12 min	
device	Sliding*	ALD	Micromanipulator, light microscope		move mask slider a little	19
	Barrier*		Al2O3	Diffusion barrier	25 nm, 300 °C	20
	Metal patterning	Intrinsic shadowing	undercuts in poly-Si		anchored to silicon nitride	21
		Metal evaporation	element		Pd	
			thick. [nm], sample tilt [°], sample rotation			120 nm, 30°, 5 rpm
device	Die & Wire bonding**	wedge-wedge wire bonding	Delvotek, silver paste, aluminium wire	package: power, weight	90, 1	22
				US-time	40 ms	
				on die: power, weight	100, 4	
				US-time	45 ms	
growth die device die	Transfer	Current monitoring	Keithley 2400	voltage, current [V], [A]	0.2, 0	23
		Nanotube transfer	Light microscope	Burleigh piezo actuator	manual placement, until current ~1-100 nA	
		Annealing	Keithley 2400	N2 stream, voltage sweep [V]	0.2 to ~2 to -2 to 0.2, until current increases suddenly	24
		Fork withdrawal	Keithley 2400	voltage, current [V], [A]	0.2, >0	25
device	Passivation	ALD	Al2O3	temp [°C]	110 - 300, better 300	26
				thickness [nm]	40	
				selective nucleation: needs clean, defect-free+individual nanotube		

All steps 19-26 after SWNT growth are wet-chemistry free and electron beam observation is avoided.

Wire bonding is completed before nanotube integration.

\*optional for designs with additional shadow masks (moved to final position after step 25, followed by evaporation of 80 nm Pd at 10° tilt)

\*\*Die and wire bonding: details

The receiving die (device die) for transfer were placed on top of two 500-µm-thick spacer die which were die bonded into a ceramic package (PLCC32) using conductive epoxy glue. The bonding parameters for the ultrasonic wire bonder Delvotek FEK 5425 were:

Speed 3, Z working height 2000

1st bond on package: S search height 2820, ultrasonic-power 90, time 40, bond weight 1, TD step 3, Loop speed 1, reverse 10, loop height 750; move farer than needed, lower needle position, return towards pad position.

2nd bond: D destination height 2400, US-power 100, time 45, bond weight 4, TD step 2.

# B Theory and methods:

## Carbon nanotube properties and characterisation

This chapter introduces concepts to represent the molecular structure of single-walled carbon nanotubes. Theories predicting the electronic properties of SWNTs are summarised. In the second section, experimental methods are described to probe the structural, electronic and optical properties of nanotubes. Experimental instrumentation utilised in this Thesis is presented. Parts of this chapter are based on the following references where more detailed derivations can be found [47, 88, 99, 219].

### B.1 Carbon nanotube properties

The structure of single-walled carbon nanotubes and their mechanical properties are described. Subsequently, the electronic behaviour is discussed.

#### B.1.1 Structural description

Single-walled carbon nanotubes (SWNTs) are molecular tubes whose walls consist of a single layer of carbon atoms. Figure B.1 shows ball-stick models of SWNTs. The C atoms of the tube wall are arranged as a hexagonal honeycomb lattice. Instead of being a flat two-dimensional sheet as in graphene (1-atom-thin graphite), the 1-atom-thin carbon sheet is wrapped up into a seamless tube.

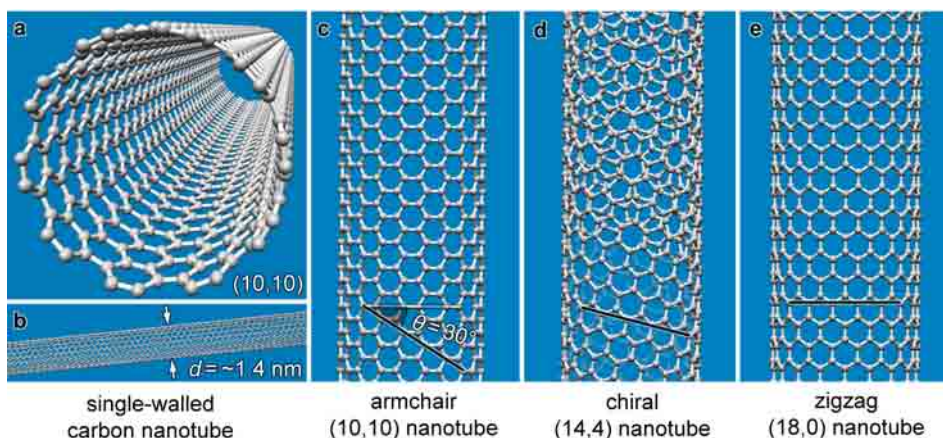
In contrast to single-walled carbon nanotubes whose walls consist of a single layer, a multi-walled carbon nanotube (MWNT) has several carbon layers arranged as concentrically stacked tubes. Describing a SWNT can start from describing its wall as if it would be unrolled into a planar graphene sheet. The covalent carbon-carbon bond length  $a_{C-C}$  of the honeycomb graphene lattice is approximately 0.142 nm, as illustrated in Figure B.2a. Elemental carbon has four valence electrons, which occupy the 2s, 2p<sub>x</sub>, 2p<sub>y</sub> and 2p<sub>z</sub> orbitals. The orbitals represent the distribution of the electron around the nucleus of the atom. Orbitals of neighbouring atoms can interact and form mixed orbitals, known as hybridisation. In planar graphene, the 2p<sub>x</sub> and 2p<sub>y</sub> orbitals hybridise with the 2s orbital into three sp<sub>2</sub> orbitals. Resulting bonds are called  $\sigma$ -bonds. All three  $\sigma$ -bonds are arranged in the same plane and point in 0°, 120° and 240° direction. The strong  $\sigma$ -bonds are the origin of the superior mechanical strength of graphene and carbon nanotubes. The remaining 2p<sub>z</sub> electrons are only weakly bound to the nucleus and form  $\pi$ -bonds out of plane. These  $\pi$  orbitals govern the electrical transport properties. As shown in Figure B.2b and following [99] pp.33, the honeycomb crystal lattice is not a fundamental lattice: To describe the periodicity of the atom lattice and its bonds, more than just one atom has to be taken into account because the surrounding of atom A is geometrically different from the surrounding of atom B. The crystal lattice is converted into a fundamental direct lattice (Bravais lattice) by grouping atom A and atom B together. Repeating this instance

SWNTs

MWNT

Graphene Sheet

Direct Lattice

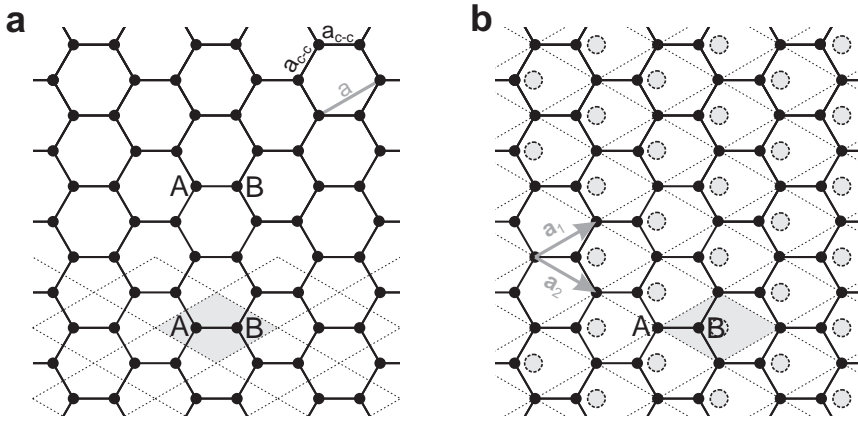


**Figure B.1:** Model of three different SWNTs. The balls represent carbon atoms and the sticks indicate bonds. (a-c) Armchair-type nanotube of chiral indices (10,10) with a diameter  $d = 1.356$  nm and a chiral angle  $\theta = 30^\circ$ . Perspective views of short segments. Typical lengths would range from microns up to centimetres. (d) Chiral (14,4) nanotube,  $d = 1.282$  nm,  $\theta = 12.2^\circ$ . In the lower part of the image, atoms of the nanotube backside are shaded for clarity. (e) Zigzag-type (18,0) nanotube,  $d = 1.409$  nm,  $\theta = 0^\circ$ . Figures were calculated using Nanotube Modeler™, JCrystalSoft, [www.jcrystal.com](http://www.jcrystal.com).

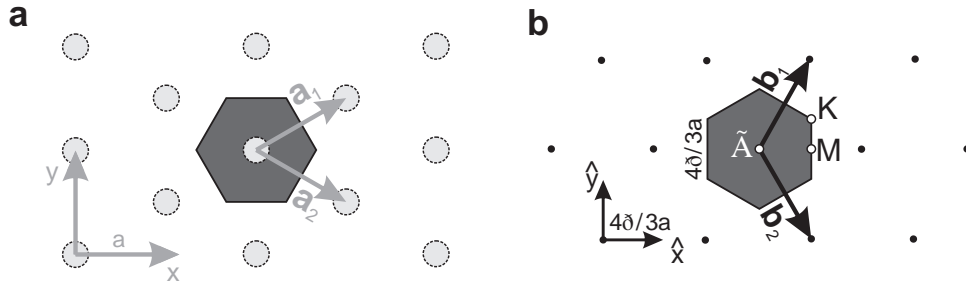
consisting of A and B forms a fundamental lattice where the surrounding looks exactly the same for every unit. This instance is called basis of the Bravais lattice. The real honeycomb lattice is mapped using a basis of two atoms.

A primitive unit cell with a special boundary around a single Bravais lattice point is called Wigner-Seitz cell and is depicted in Figure B.3a. The speciality is that the boundary is there, where it is exactly as close to the Bravais lattice point in the middle of the cell as to any of the other surrounding Bravais lattice points. Fourier analysis is a concept for periodical systems. Applying the direct Fourier transform to the direct lattice leads to the so-called reciprocal lattice. Figure B.3b shows the reciprocal lattice of graphene. The reciprocal lattice is hexagonal as well, but it is rotated by  $90^\circ$  with respect to the direct lattice. A Wigner-Seitz primitive cell can also be defined for the reciprocal lattice and is called the first Brillouin zone. Three locations of the Brillouin zone exhibit high symmetry: The centre is called  $\Gamma$ -point. The six corners are referred to as K-points. The middle of each side is called M-point.

The diameter of a SWNT can range from about 0.4 nm [14] to at least 5 nm [99] p.73. The diameter alone is not enough to describe the structure of a SWNT. The only structural restriction in the conceptual rolling-up of a tube from a graphene sheet is that the carbon atom sites have to coincide as a seamless joint. Figure B.4 shows an illustration of the conceptual un-rolling of nanotubes into graphene stripes. The stripes, or ribbons, can not only vary in width but also in angular orientation. A ribbon whose future circumference  $C_h$  is oriented along the A-B direction (here horizontally) forms a so-called armchair nanotube. A different lattice orientation can be constructed from ribbons rotated with respect to the armchair ribbons. Rotating a ribbon by  $30^\circ$  away from the armchair orientation results in a nanotube with a zigzag pattern along the circumference, giving rise to



**Figure B.2:** (a) Schematic representation of the hexagonal graphene lattice. The  $\sigma$ -bonds are in plane and drawn as lines, the  $\pi$ -bonds would be out of plane. The bond length  $a_{C-C}$  between neighbouring carbon atoms is 0.142 nm. The graphene lattice constant  $a$  is 0.246 nm. (b) The Bravais lattice is mapping the real honeycomb lattice. The basis of the Bravais lattice incorporates two atoms (atoms A and B). The centre point of the Bravais lattice is highlighted by a dashed circle. In contrast to the real lattice, the Bravais lattice is a fundamental lattice where the surrounding is the same for every lattice point. In a, another option for choosing a Bravais lattice is shown.



**Figure B.3:** (a) The fundamental hexagonal lattice of graphene in real space. The Wigner-Seitz primitive cell is marked as grey hexagon. The primitive vectors of the direct lattice are  $\vec{a}_1$  and  $\vec{a}_2$ .  $\vec{a}_{1,2} = \left( \sqrt{3}a/2, \pm a/2 \right)$  (b) Reciprocal lattice of graphene. The first Brillouin zone is given as grey hexagon. The high symmetry points are marked with  $\Gamma$ , K and M. The primitive vectors of the reciprocal lattice are  $\vec{b}_1$  and  $\vec{b}_2$  and have units of  $\text{nm}^{-1}$ .  $\vec{b}_{1,2} = \left( 2\pi/(\sqrt{3}a), \pm 2\pi/a \right)$ . Partially based on [99].

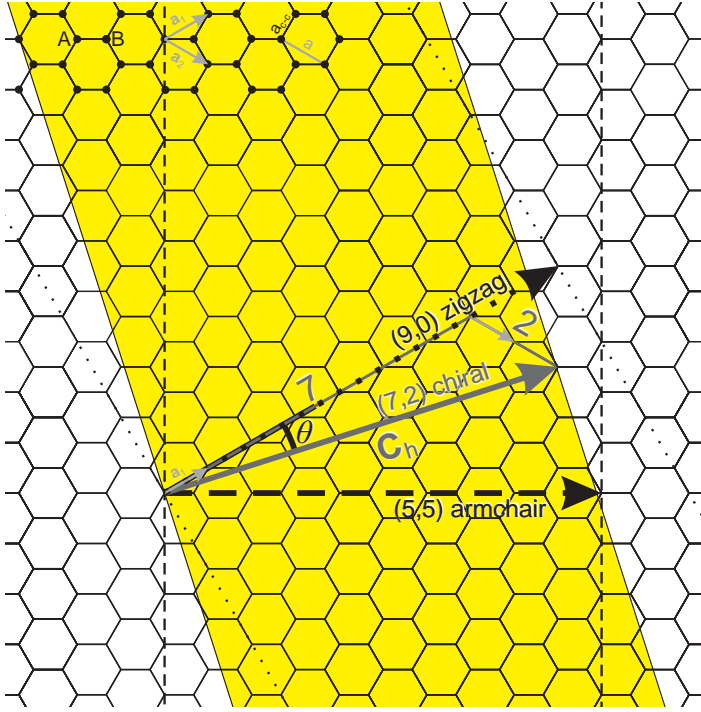
Chiral Angle

the label zigzag nanotube. Intermediated pattern orientations can be described by the chiral angle. The chiral angle  $\theta$  is the angle between the circumferential direction and the zigzag direction of the primitive lattice vector  $\vec{a}_1$ . Together, the two attributes, diameter and chiral angle, fully describe the structure of an ideal SWNT.

Chiral Vector

The former circumference of the un-rolled nanotube can be represented by using the vectors  $\vec{a}_1 = (\sqrt{3}a/2, a/2)$  and  $\vec{a}_2 = (\sqrt{3}a/2, -a/2)$  as a basis, and is called chiral vector, wrapping or folding vector:

$$\vec{C}_h = n\vec{a}_1 + m\vec{a}_2 \quad (\text{B.1})$$



**Figure B.4:** Schematic illustration of the conceptual description of nanotubes based on planar graphene ribbons. Conceptually, the circumference  $C_h = |\vec{C}_h|$  of a nanotube corresponds to the chiral vector  $\vec{C}_h$  drawn in the plane of a graphene sheet. (dashed lines) A ribbon with horizontally oriented circumference leads to an armchair nanotube. (dotted lines) Chiral vectors rotated by  $30^\circ$  with respect to the A-B direction lead to zigzag-type nanotubes. The deviation from the zigzag-direction is the chiral angle  $\theta$ . (shaded ribbon) Ribbon from which a (2,7) nanotube can be rolled up conceptually.

Chiral Indices

The indices  $n$  and  $m$  must be positive integers to allow seamless tubes. Instead of using  $d$  and  $\theta$ , the structure of a nanotube can be described by the chiral indices  $(n,m)$ , also called wrapping index. For most considerations, the indices  $n$  and  $m$  are typically re-arranged such that the first integer is larger than the second one  $(i_1, i_2)$  with  $0 \leq i_2 \leq i_1$ . This neglects the handedness [52] of a nanotube: a (7,2)

nanotube and a (2,7) nanotube have basically the same pattern but moving along the zigzag direction closest to the circumferential direction is yielding a right or a left-turning helix. This simplification is equal to restricting the values of the chiral angle  $\theta$  to  $0^\circ - 30^\circ$  instead of  $0^\circ - 60^\circ$  and is not affecting electronic considerations due to symmetry, unless torsional deformations are treated. In the context of nanotubes, the chiral indices  $(n, m)$  are often called chirality. Armchair nanotubes have a chirality of  $(n, m=n)$ . All  $(n, 0)$  nanotubes are of zigzag type. Armchair and zigzag nanotubes are achiral: they are perfectly superimposable with their mirror images. All other chiral angles result in chiral nanotubes.

Chirality

Chiral vs.  
Achiral

The diameter of a nanotube can be calculated from the chiral indices  $(n, m)$ :

$(n, m) \Rightarrow d$

$$d = \frac{|\vec{C}_h|}{\pi} = \frac{a \sqrt{n^2 + nm + m^2}}{\pi} \quad (\text{B.2})$$

Different combinations of  $n$  and  $m$  can result in the same diameter. Hence, dissimilar SWNTs can exist for equivalent diameters as discussed in Section C.1 about chirality control.

The chiral angle  $\theta$  is calculated from the chiral indices as following:

$(n, m) \Rightarrow \theta$

$$\cos \theta = \frac{\vec{C}_h \cdot \vec{a}_1}{|\vec{C}_h| |\vec{a}_1|} = \frac{2n + m}{2\sqrt{n^2 + nm + m^2}} \quad (\text{B.3})$$

The primitive unit cell of a SWNT is defined by the area spanned by the translation vector  $\vec{T}$  and the chiral vector  $\vec{C}_h$ . The translation vector  $\vec{T}$  is the shortest lattice vector along the nanotube axis (perpendicular to  $\vec{C}_h$ ).  $\vec{T}$  is  $((2m + n)/g_{gcd}, -(2n + m)/g_{gcd})$ , where  $g_{gcd}$  is the greatest common divisor of  $2m + n$  and  $2n + m$ . The unit cell of armchair and zigzag nanotubes consist of  $N = 2n$  hexagons, or  $4n$  carbon atoms respectively. For chiral nanotubes, the number  $N$  of hexagons per unit cell can be substantially larger:

$$N = \frac{2(n^2 + nm + m^2)}{g_{gcd}} \quad (\text{B.4})$$

Consequently, the computational effort in simulations is often much larger for chiral nanotubes than for the highly symmetric zigzag or armchair nanotubes.

### B.1.2 Mechanical properties

The mechanical strength of carbon nanotubes is based on the strong  $\sigma$ -bonds of the hexagonal lattice.

The Young's modulus of carbon nanotubes is around 1 TPa [18, 19] which is extraordinarily high. Despite this high stiffness under tensile strain, nanotubes can undergo large elastic deformations without brittle fracture.

Young's  
Modulus  
Elasticity

From a point of view of structural mechanics, a planar sheet or ribbon tends to bulge and buckle, which renders planar structures inferior to hollow profiles like frames or tubes.

Shape

When surpassing a critical tensile strain of about 5%, SWNT were modelled to release strain energy by defect formation [314]. But as indicated by simulation, defect formation requires high activation energies. Perfect nanotube lattices are therefore expected to stay kinetically stable even for strains substantially larger than 5% [315]. Ropes of suspended nanotubes were measured to elastically strain in some cases slightly more than 5% [18, 316].

Breaking  
Strain

Strain up to  $13.7 \pm 0.3\%$  was endured without any evidence of defect formation for ultralong SWNTs [20].

Maximum Stress	The ultimate tensile strength of the nanotubes was extracted to be 99 GPa [20]. The extracted strength-to-weight ratio of $\sim 74\,000\text{ kN}\cdot\text{m/kg}$ is by 30 times larger than for Kevlar® and by 117 times larger than for steel [20].
Chirality Dependence	According to simulation, the Young's modulus (1.0 TPa) and the maximum tensile strength ( $\sim 100\text{ GPa}$ ) are only weakly dependent on chirality [19]. Softening was suggested for nanotubes with small diameters [317]. The critical tensile strain for breaking is predicted to depend on the chiral angle, favouring zigzag nanotubes over armchair [318].
Compression	Under compression, nanotubes kink rather than suffer brittle fracture [319].

### Interfacial forces

Friction	The friction force between a nanotube and a $\text{SiO}_2$ substrate is as small as about $10\text{ pN/nm}$ [309]. Therefore, slippage of nanotubes can be an issue as long as they are not clamped. For bundles of nanotubes, applied displacement can lead to debundling instead of straining [320].
----------	--

### B.1.3 Electronic properties

The small dimensions and the tubular shape of carbon nanotubes results in unique electrical transport properties. The diversity in chirality contributes to a rich range of electronic properties. Electronic band structures are reviewed starting from graphene. Subsequently, effects caused by the curvature of a tube wall are included. Parts of this Chapter follow the explanations given by Park *et al.* [88] pp.1 and by F. Léonard [47] pp.3.

### Band structure of graphene

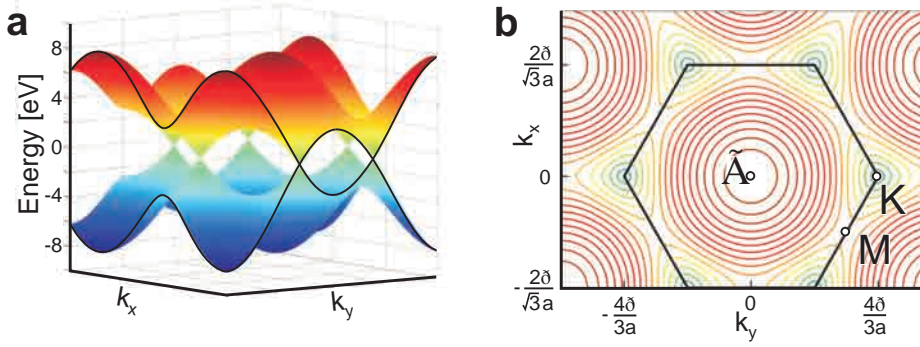
As a SWNT can be considered as a wrapped-up graphene ribbon, examining the electronic band structure of graphene is the starting point for understanding band structures of nanotubes. Electrical transport in carbon nanomaterial is dominated by charge carriers, may it be negatively charged electrons or positive holes (a missing negative charge). The delocalised states of the  $\pi$  orbitals are close to the Fermi level and govern the electrical properties.

Tight-Binding Approximation NNTB	The electronic band structure of a planar hexagonal carbon lattice can be calculated using the tight-binding approximations [321]. The nearest-neighbour approximation takes into account only interactions between the three atoms of type B next to the atom of type A (see Figure B.2 ). Compared with ab initio calculations, the nearest-neighbour tight binding (NNTB) approximation for the $\pi$ bands is in good agreement for low energies. Those energies close to the Fermi level are the relevant ones for electrical transport. The band structure of the $\pi$ orbitals of graphene can be calculated via the Schrödinger equation. The energy $E$ of $\pi$ orbital electrons can be found using linear combinations of Bloch functions for the total wave function, while neglecting the overlap of $2p_z$ wave functions. The following analytical expression for the $\pi$ bands describes the energy dispersion of graphene [88] p.4, [99] p.61:
Energy Dispersion in Graphene	

$$E = E_0 \mp \gamma_0 \sqrt{1 + 4 \cos\left(\frac{\sqrt{3}k_x a}{2}\right) \cos\left(\frac{k_y a}{2}\right) + 4 \cos^2\left(\frac{k_y a}{2}\right)} \quad (\text{B.5})$$

The negative sign corresponds to valence bands of bonding  $\pi$  orbitals, where the mobile charges are holes. The positive sign denotes conduction bands of anti-





**Figure B.5:** (a) Energy dispersion of graphene as 3D surface plot showing zero band gap at the K-points according to Equation B.5. (b) Contour plot of the energy dispersion with highlighted first Brillouin zone and symmetry points.

bonding  $\pi^*$  orbitals, where the mobile charges are electrons.  $E_0$  is the reference potential, which is for graphene the Fermi energy  $E_F$  and can be set to 0 eV. The carbon–carbon interactions are described by  $\gamma_0$  which can be regarded as a fitting parameter.  $\gamma_0$  is called hopping integral, transfer energy, tight-binding overlap integral or nearest neighbour overlap energy. It can be estimated as transfer integral between the nearest neighbours and the commonly used values for  $\gamma_0$  range from 2.5 eV to 3.3 eV [99]. The momentum vector  $\vec{k}$  of the first Brillouin zone is described by its components  $k_x$  and  $k_y$ . The graphene lattice constant  $a$  is equal to  $\sqrt{3} a_{C-C} = 0.246$  nm, and is also called Bravais lattice constant. Figure B.5a shows the energy dispersion of graphene in reciprocal space as a 3D plot. The highest energy states of the valence band occur at the six K-points where they meet the lowest energy states of the conduction band. The dispersion near each K-point has a conical shape. The linear approximation of the dispersion is called Dirac cone.

Density of states (DOS) is a concept that describes the ability of a material to host up to a certain number of particles  $D(E)$  at a specific energy  $E$ . The DOS represents the number of states available for particles of certain energy. The states can be occupied by wave-like particles or entities, such as electrons or holes, photons, phonons, or excitons [99] p.103. The density of mobile charge carriers available in a solid material is linked to the DOS and can be calculated based on the energy dispersion. A conductor possesses mobile charge carriers, while an insulator does not. At the Fermi level, the DOS vanishes for graphene. Therefore graphene is not truly metallic, but a zero bandgap semiconductor [88, 115]

### Band structure of SWNTs

As the wall of a SWNT consists of a wrapped-up graphene sheet, the electronic properties can be expected to be partially similar to ones of graphene. The rolling imposes additional boundary conditions compared to an infinitely large graphene layer. As it will be shown, the Brillouin zone of a SWNT consists of line cuts of the Brillouin zone of graphene. Two wave vectors are associated with an infinitely long SWNT. The wave vector  $\vec{k}_{||}$  parallel to the nanotube axis is continuous if the SWNT is assumed to be infinitely long. The length of  $\vec{k}_{||}$  is  $2\pi/|\vec{T}|$ . The

 $\gamma_0$  $\vec{k}$ 

DOS

Overview

Wave Vectors

Periodic  
Boundary

wave vector  $\vec{k}_\perp$  perpendicularly to the nanotube axis points along the circumference.  $\vec{k}_\perp$  has to satisfy a periodic boundary condition because the wave function in circumferential direction must be repetitive for each full revolution ( $2\pi$ ):

$$\vec{k}_\perp \cdot \vec{C}_h = \pi d k_\perp = 2\pi q \quad (\text{B.6})$$

The diameter of the nanotube is denoted again with  $d$  and  $q$  is an integer. Owing to this periodic boundary condition, the allowed values of  $k_\perp$  are not continuous but become quantised and can only be of those discrete lengths which fulfil Equation B.6.

Zone-Folding

Using the so-called zone-folding scheme, the band structures of SWNTs are obtained from the energy dispersion of graphene while obeying additionally the periodic boundary conditions for  $\vec{k}_\perp$ . As illustrated in Figure B.6, the regularly-spaced allowed  $k_\perp$  states intersect with the energy dispersion of graphene. At the allowed  $k_\perp$  states, the 1-dimensional subbands of SWNTs are obtained as cross-sectional line cuts of the two-dimensional energy dispersion of graphene. The band structure relevant for electrical transport in a SWNT is obtained by those cross-sections near the K-points – where the Dirac cone approximation is applicable. Figure B.6a,b and c,d show single cutting planes representing allowed  $k_\perp$  states for a metallic and a semiconducting nanotube using the cone approximation. Certain combinations of  $(n,m)$  result in line cuts of allowed states exactly through a K-point. For those cross-sections of the Dirac cone through a K-point, the one-dimensional energy dispersion exhibits a meeting point of valence and conduction band. Those  $(n,m)$  SWNTs behave metallic.

Metallic

If the periodic boundary condition of  $k_\perp$  prohibits line cuts through a K-point, the nanotube band structure has a parabolic line shape. An energy bandgap is opening between the valence and the conduction band. Thus, chiralities without allowed cross-sections through one of the six K-points exhibit a bandgap and can behave semiconducting.

Semiconducting

After introducing the zone-folding generally, the Brillouin zones for specific SWNT-types are summarised. For zigzag nanotubes,  $(n,0)$ , the periodic boundary condition (Equation B.6) can be simplified by inserting the diameter  $d = na/\pi$  (Equation B.2) to  $\pi d k_\perp = na k_\perp = 2\pi q$ . To have an allowed  $k_\perp$  that hits a K-point at the coordinates  $(0, 4\pi/3a)$ , the condition  $2n = 3q$  has to be fulfilled. Only for values  $n$  being a multiple of three, a matching integer  $q$  can be found. Consequently, a line cut through a K-point occurs and those zigzag nanotubes behave metallic. For other cases where  $n$  is not a multiple of three, the K-points are missed by  $2/3d$  [88] p.8. The energy bandgap  $E_g$  can then be estimated by approximating the slope of the Dirac cone by  $\sqrt{3}a\gamma_0/2$ . Illustratively, the height gained is measured while moving along the slope of the cone for a horizontal distance of  $2/3d$ . A factor of 2 is taken as both conduction and valence bands are separating:

Zigzag

$$E_g = 2 \times \left( \frac{\partial E}{\partial k} \right) \times \frac{2}{3d} = \frac{2a\gamma_0}{\sqrt{3}d} \approx \frac{0.77}{d} eV \quad \text{with diameter } d \text{ of units [nm]} \quad (\text{B.7})$$

Chiral

Although the bandgap-diameter relation was derived for semiconducting zigzag nanotubes, the bandgaps of semiconducting chiral nanotubes can be estimated equally accurate, as indicated by comparison with NNTB simulations [99] p. 95. The bandgap of semiconducting nanotubes is inversely proportional to the

diameter and is in the range of 0.2–1.9 eV.

For arbitrary chiralities  $(n,m)$  the allowed cross-sections cut through K-points only if the condition  $(n - m)/3 = q$  with integer  $q$  can be fulfilled. If the difference between the chiral indices is not a multiple of three ( $(n - m) = 3q + p$  with  $p \in \{-1,1\}$ ) the nanotube is semiconducting.

The indices  $(n,m=n)$  of armchair nanotubes always fulfil the following condition  $(n - m)/3 = q = 0$ . Therefore, armchair nanotubes are expected to behave metallic.

Armchair

So far, the tubular shape of nanotubes was considered to impose nothing more than periodic boundary conditions. But the curvature of the wall also changes the previously perfectly orthogonal orientation between the  $\pi$  orbitals and the  $\sigma$  orbitals. Especially for small diameter nanotubes, the curvature induces a mixing of the orbitals. Due to this hybridisation, the transfer integral  $\gamma_0$  becomes different for the three bonds of a C atom with its neighbours ( $\gamma_0 \Rightarrow \{\gamma_1, \gamma_2, \gamma_3\}$ ). The effect of  $\pi$ - $\sigma$  hybridisation is predicted to open a small bandgap in all metallic nanotubes with  $n \neq m$ . This curvature-induced bandgap is proportional to  $1/d^2$  and is approximately 0.04 eV for a 1 nm-diameter nanotube [47, 88, 115, 322]. Kleiner *et al.* presented a unified analytic expression for bandgap opening due to curvature (and deformation). The bandgap induced by symmetry breaking because of curvature is [323]:

Curvature Effects

 $E_g$  curvature

$$E_{g \text{ curvature}} = \left| \frac{\gamma_0 a^2}{4d^2} \cos 3\theta \right| \quad (\text{B.8})$$

Only the armchair nanotubes ( $\theta = 30^\circ$ ) have completely vanishing bandgaps and are truly metallic. Those nanotubes which were expected to be metallic as they fulfill  $(n - m)/3 = q$  while neglecting curvature effects, have small bandgaps induced by curvature effects. The size of the bandgap does depend on diameter and chiral angle. The nanotubes with curvature-induced bandgap are called quasi-metallic, primary metallic or small bandgap semiconducting (SGS) nanotubes.

The different SWNTs are categorised as following.

Summary of Types

Achiral SWNTs:

- armchair nanotubes,  $(n,n)$ ,  $\theta = 30^\circ$   
metallic
- zigzag nanotubes,  $(n,0)$ ,  $\theta = 0^\circ$   
quasi-metallic if  $n$  is a multiple of 3, else semiconducting

Chiral SWNTs:

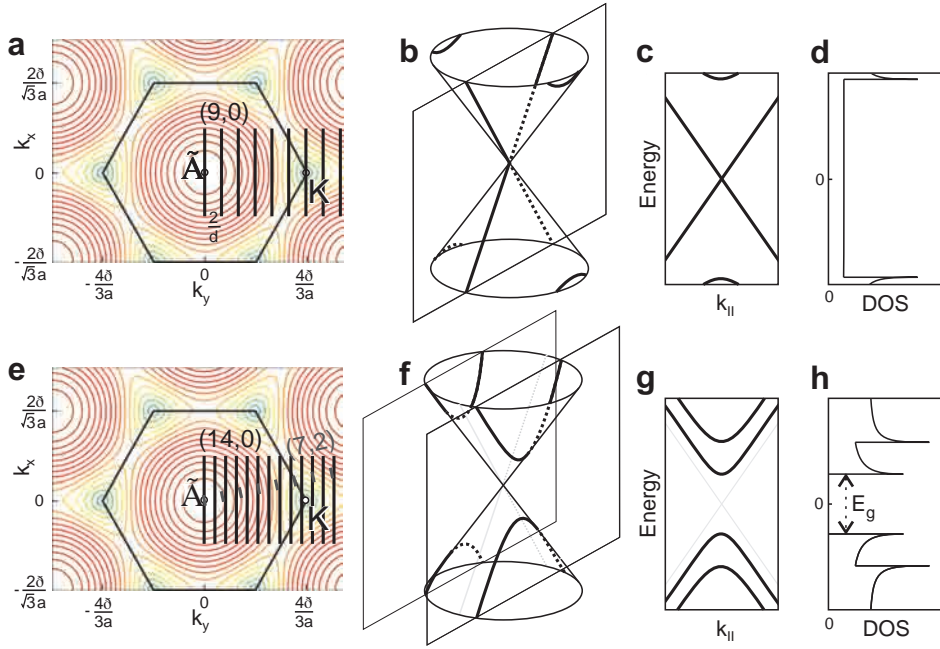
- chiral nanotubes  $(n,m \neq n \neq 0)$ ,  $0^\circ \leq \theta \leq 30^\circ$   
quasi-metallic if  $n-m$  is a multiple of 3, else semiconducting

For the electronic behaviour of semiconducting and quasi-metallic nanotubes, the diameter is the most important feature. The diameter prescribes the bandgap by  $\approx 0.77 \text{ eV}/d[\text{nm}]$  for semiconducting and by  $\approx 0.04 \text{ eV}/d[\text{nm}]^2 \cdot \cos 3\theta$  (Equation B.8) for quasi-metallic nanotubes.

The density of states per carbon atom of SWNTs can be obtained as [47] p.15:

DOS in SWNTs

$$D(E) = \frac{2a}{\pi^2 d \gamma_0} \sum_i \frac{|E|}{\sqrt{E^2 - E_i^2}} \quad (\text{B.9})$$



**Figure B.6:** Zone folding in nanotubes. Contour plots of planar graphene in reciprocal space and the additional restrictions imposed by periodic boundary conditions of tubular SWNTs. (a) Zone-folding for a quasi-metallic (9,0) nanotube. The cutting planes of the periodic boundary condition hit the K-point. (b) Schematic illustration of the Dirac cone and the allowed  $k_{\perp}$  states, forming the 1-dimensional subbands of the SWNT by cross-sectional line cuts with the two-dimensional energy dispersion of graphene. (c) Band diagram. (d) Sketch of the density of states. (e-h) Zone-folding for a semiconducting (14,0) nanotube. The cutting lines miss the K-point and a bandgap  $E_g$  occurs. The planes are spaced by  $2/d$ , are of length  $4\pi/T$  and show  $\theta$ -dependent orientation (see (7,2) with  $\theta = 12.2^\circ$ ). Partially based on work by Helbling [219] and Minot *et al.* [91].

where  $E_i = |3i + 1|a\gamma_0/d$  is the energy at the bottom of the  $i^{th}$  subband for semiconducting nanotubes, and  $E_i = |3i|a\gamma_0/d$  for metallic nanotubes. As typical for quasi-one-dimensional structures, the density of states increases dramatically as the energy  $E$  approaches  $\pm E_i$ . These peaks are called van Hove singularities (VHS). For (quasi-)metallic nanotubes, the subband with  $i = 1$  contributes a non-zero DOS at the Fermi level, as shown in Figure B.6d. For semiconducting nanotubes, as sketched in Figure B.6h,  $D(E_F)$  is zero in the bandgap  $E_g$  ranging from  $-E_1$  to  $E_1$  (electron/hole symmetry).

At equilibrium conditions, foremost the first subband contributes to the carrier density in SWNTs. As a consequence of the van Hove singularity at the band edge, the density of intrinsic carriers is large. The intrinsic carrier density of semiconducting nanotubes is larger than the intrinsic carrier density in bulk semiconductors [47] p18. This accounts in parts for the high current densities found in nanotube devices [99] p. 122.

The bandgap is only weakly dependent on temperature [47] p.20.

Doping of nanotubes can be achieved by many ways. Among them are electro-

Carriers in  
SWNTs

Temperature  
Doping

statically gating, charge transfer from adsorbates or from the substrate, insertion of atoms into the inside of nanotubes, and substitution of carbon atoms by boron or nitride. The doping fraction (electrons/atom) at which the Fermi level reaches the band edge can be approximated at room temperature by  $f^* \approx 10^{-3}/r^{3/2}$  [47] p.19. Substitution by replacing a lattice atom with another element severely degrades the carrier mobility. Instead, doping by charge transfer from adsorbed molecules avoids lattice displacements. Charge injection from adsorbates can also be employed as sensing mechanism [23, 298].

#### B.1.4 Electrical transport

The conductance in systems with low density of defects can be described by using the electron transmission probability according to Landauer. The ideal transmission probability is 1 for each channel. For small bias values  $V_{ds}$ , corresponding to energies within the first subbands, two subbands (double degeneracy) are available as channels (modes). The ideal conductance of a metallic nanotube treated as ballistic system is twice the quantum conductance  $G_0 = 2e^2/h$  [47] p.31. The ideal total current is then [219] p. 17:

Landauer

$$I_{ds} = 2G_0 V_{ds} = \frac{4e^2}{h} V_{ds} \quad (\text{B.10})$$

where  $e$  is the electron charge and  $h$  the Planck's constant.

As summarised by F. Léonard [47] p.32, for armchair nanotubes, only one of the modes is coupling well to metal contacts and hence a maximum conductance of  $2e^2/h$  is expected. For zigzag nanotubes, both modes couple well and the current carrying capacity is doubled.

Metallic nanotubes can maintain near perfect conductance even in non-ideal surroundings. Scattering sources such as disorder, defects, surface interactions and phonons are only weakly affecting conductance because of the following reasons [47] pp.33: (i) Large Fermi velocity and relatively weak electron-phonon interactions lead to long mean free paths (~microns) for scattering with acoustic phonons. (ii) Nanotubes have crystalline, well-defined surfaces – in contrast to disordered Si/SiO<sub>2</sub> interfaces. (iii) Any potential which is long-ranged relatively to the graphene lattice constant  $a$  cannot efficiently couple to the subbands. (iv) Localization lengths because of weak disorder are long.

Scattering

At low bias, electrons have only enough energy to interact with acoustic phonons. At high bias, the electrons possess sufficient energy to interact also with optical phonons. In contrast to long mean free paths for scattering with acoustic phonons, the mean free path for scattering with optical phonons is short (~10 to 50 nm) [47] pp.40. Therefore, the current magnitude at high bias can be strongly affected by electron-phonon scattering [324]. The current through a metallic nanotube substantially longer than the mean free path is saturating at ~25  $\mu\text{A}$ , because high-energy electrons are reflected by phonon emission [47] p.41.

High Bias

#### Electrical transport in semiconducting nanotubes

Nanotubes can behave as ballistic conductors [9]. The system resistance of nanotube devices is often governed by the contact resistances of the metal/nanotube interfaces. The charge carriers face barriers at the interfaces which have to be overcome by either tunnelling through the barrier, thermionic emission over the barrier or electron-hole recombination [325]. Compared to traditional microfabricated planar contacts of metals to semiconductors, contacts to nanotube are of even smaller dimensions. Upon connecting the semiconductor to a metal, a

Barriers

Fermi Level  
Pinning

metal/semiconductor interface is built. According to boundary conditions of the Schrödinger equation, electronic states appear in the semiconductor bandgap at the interface. These metal-induced gap states (MIGS) decay exponentially with distance to the interface. The Fermi levels of a metal and a semiconductor are different in general. The formation of an interface leads to a charge accumulated near the interface. The charge in the semiconductor is balanced by charge of opposite sign and magnitude in the metal. For planar contacts, the electric potential of the dipole sheet bends the bands in the semiconductor until the charge neutrality level is aligned with the Fermi level of the metal [47]. Assuming the neutrality level at the interface to be in the middle of the semiconductor bandgap, the metal Fermi level will lie at the middle of the semiconductor bandgap. For transport across the interface, charge carriers will face a barrier height equal to half of the bandgap. For metal/nanotube contacts, the charge distribution is more localized due to the small contact area. For a nanotube end-bonded to a metal plane, any shift in potential near the interface will decay more quickly than in planar interfaces. Potential shifts fade within few nanometres [326]. Consequently, the barrier due to Fermi level pinning is very thin and charge carriers can efficiently tunnel through the barrier [47] p.60. Also for side-contacted nanotubes, the additional barrier due to Fermi level pinning is expected to be small and is of minor importance. But for planar metal/semiconductor interfaces, the barriers due to Fermi level pinning are comparatively large, on the order of microns [47] p.59.

Schottky  
Barrier

The so-called Schottky barrier  $\phi_{b0}$  at the metal/nanotube interface can be described for electrons as the difference between the work function of the metal  $\Phi_m$  and the electron affinity of the nanotube  $\chi$ . As a simple model, the barrier height for holes  $\Delta_0$  can be deduced from the relation  $E_g = \phi_{b0} + \Delta_0$ . The nanotube midgap is approximately 4.5 eV below the vacuum level [327]. For bulk semiconductors, the Fermi level pinning renders the Schottky barrier nearly independent of  $\Phi_m$ . But quasi-one-dimensional contacts to SWNTs allow the barriers to be tuned by choosing an appropriate material ( $\Phi_m$ ). For large metal work functions the Schottky barriers can diminish for holes. The metal is contacting the conduction band and an ohmic contact is expected.  $\Phi_m$  is ~5.5 eV for Au and ~5.2 eV for Pd. In the simple model, ohmic contact formation by Pd can be assumed for nanotube bandgaps up to 1.2 eV (twice the difference between  $\Phi_m$  and the nanotube midgap of 4.5 eV). Sufficiently small metal work functions can yield ohmic contacts by lowering the Schottky barriers for electrons. As the Schottky barrier height depends on the metal used, p-type transistors (hole current at negative gate voltages) can be formed using large work function metals. Transistors with n-type characteristic (electron current at positive gate voltages) can be obtained using small work function metals [328]. More detailed explanations were given by Léonard and Talin [325], or by Helbling [219] pp.19.

Contact  
materials

Ab initio studies indicate that titanium (Ti) yields better contacts to nanotubes than Au or Al [329, 330]. However, Ti is prone to oxidise at ambient conditions. Indicated by theory and supported experimentally, the best contact material for ohmic contacts appears to be Pd [9, 331, 332]. Pd-contacted SWNT devices showed increasing conductance at lower temperature as scattering with acoustic phonons is reduced. The increased conductance indicates the absence of Schottky barriers [9]. In case Schottky barriers are present, the decrease in temperature reduces the thermionic emission across the barrier and resistance increases. Also with rhodium (Rh), near-ohmic contacts were achieved [78]. Cr/Au contacts can show Schottky barriers (5 nm Cr), which can be eliminated after annealing, sug-

gestively caused by Au penetrating the Cr layer [333].

### Diameter dependent contact properties

Experimentally, the nanotube diameter was observed to influence the Schottky barrier height in side-contacted nanotubes [78, 334]. Owing to the small dimensions of the nanotube, only a small region can be depleted [47] pp.61. This results in partial band re-alignment. Schottky barriers arise at Pd/nanotube contacts for nanotube diameters smaller than 1.4 nm, foremost because of the large band gaps at small diameters [47, 78]. Ohmic contacts to small-diameter nanotubes can be achieved with large metal work function metals at low temperature, or with a large contact capacitance. Because of the latter, contact geometries where the metal is wrapped around the nanotube are advantageous [47] p.67.

Diameter  
Influence  
Semiconducting  
Nanotubes  
Small  $d$

Contacts to metallic nanotubes are also influenced by the nanotube diameter, although a Schottky barrier is not to be expected. As for semiconducting SWNTs, the conductance deteriorates for small diameters. To describe this observation, diameter-dependant tunnelling barriers are proposed to exist between the metal and the (metallic) nanotube [78]. The tunnelling barriers are diameter-dependent as the surface properties and the chemical reactivity are curvature-dependent [88] p.69.

Metallic  
Nanotubes  
Tunnelling  
Barrier

### B.1.5 Carbon nanotube field-effect transistors

The conductance of the nanotube serving as transistor channel can be modulated by a gate. In the back gate configuration, the gate is below the nanotube and is separated by an insulating layer. Alternatively to a back gate, a top gate can be placed on top of the nanotube, again separated by an insulating layer. Combining both, allows to electrostatically dope the contact regions of the nanotube by the back gate while modulating the channel conductance by the top gate [99] p.193.

Gate  
Configuration

The strong electrostatic coupling of the source and drain electrode at short channel length deteriorates the gate coupling. An ideal gate configuration would be a tubular gate wrapped around the nanotubes. Needle-like contact were identified to shield gate potentials the least [183]. To maximise the gate coupling, the distance to the channel has to be as small as possible. The gate dielectric layer (the layer separating the gate from the channel) need a minimum thickness as otherwise the tunnelling gate leakage current increases unacceptably. The gate coupling can be increased by using gate dielectrics with high relative permittivities ( $\epsilon_{\text{SiO}_2} = 3.9$ ,  $\epsilon_{\text{HfO}_2, \text{ZrO}_2} = 15\text{--}25$ ) [88] p.70.

Gate Coupling

### Subthreshold swing and threshold voltage

The subthreshold swing  $S$  in units of mV/dec is a device performance figure concerning transistor switching.  $S$  represents the change in  $V_g$  needed to obtain a change of one decade in  $I_{\text{ds}}$ . The smaller the subthreshold swing is the better (less change in  $V_g$  needed for switching, less capacitive gate currents).

Subthreshold  
Swing

The threshold voltage of a field-effect transistor is the gate voltage at which the amount of induced carriers is sufficient to form a conducting channel [99] p.209. As pointed out by Mattmann [298] p.95, there are numerous strategies how to extract  $V_{\text{th}}$ . In silicon-based FETs, the threshold voltage is the minimum gate voltage which is sufficient to induce an inversion layer. Because of the lack of carrier inversion in intrinsic semiconductors, the threshold voltage  $V_{\text{thsteep}}$  for CNFETs is often defined as the gate voltage for which the slope of  $I_{\text{ds}}$  is steepest (maximum of the transconductance gradient) [99] p.209. Another common convention is utilised here which follows Helbling [219] and Mattmann [298]. The

$V_{\text{th}}$

threshold voltage  $V_{th}$  is extracted by fitting a linear line at the point of steepest slope of  $I_{ds}$ , followed by extrapolating the line to zero  $I_{ds}$  and taking the corresponding  $V_g$  as threshold voltage.

CNFETs Charge transport in carbon nanotube field-effect transistors (CNFETs) can be modelled in a ballistic or in a diffusive regime depending on the number of scattering sites. In each regime, the contacts can be treated either as ohmic contacts or as Schottky-barrier contacts.

MOSFET Instead of being operated as a conventional transistor, such as a metal-oxide-semiconductor field-effect transistor, CNFETs are often dominated by the Schottky barriers. For Schottky-barrier transistors the modulation of the barrier width is governing the current. Band-to-band tunnelling is an effect not observed in conventional transistors which face a limit for the subthreshold swing at 60 mV/dec. Tunnel transistors may not be subject to this limitation [335].

BTBT The conductance  $G$  of a channel-controlled CNFET can be represented by [88] p.35, [336]:

$$G(V_g) = \frac{4e^2}{h} \frac{\ell_{mfp}}{L} \frac{(\Delta V_g/u)^2}{1 + (\Delta V_g/u)^2} \quad \text{with } \Delta V_g = |V_g - V_{th}| \quad (\text{B.11})$$

where  $u = 8e/3\pi d C_g$  with gate capacitance  $C_g$  per unit length, device channel length  $L$  and mean free path at high energies  $\ell_{mfp}$ .  $V_{th}$  is the threshold voltage of the transistor. More detailed models, especially for Schottky-barrier-dominated CNFETs, are described in the following references [99] pp.119, pp.107, [219] pp.15.

### Transistor polarity

Polarity In case that the majority charge carriers are electrons, the CNFET is called n-type and a large  $I_{ds}$  is observed for positive  $V_g$ . If the majority charge carriers are holes the current increases for negative  $V_g$  and the transistor is p-type. Ambipolar transistors show large currents for both, for electrons as majority carriers at positive  $V_g$  and for holes as majority carriers at negative  $V_g$ . Pd reduces its work function upon exposure to  $H_2$  [88] p.67, which was shown to reduce conductivity at the p-branch by a factor of 2 at 0.5%  $H_2$ , and 7 at 50%  $H_2$  respectively [9]. Exposure of Pd contacts to  $H_2$  decreased the hole current and increased the electron current. This change from p-type towards n-type behaviour is explained by the reduced work function and supports the absence of strong Fermi level pinning [9].

### B.1.6 Electromechanical properties

Bandgap  
Modulation

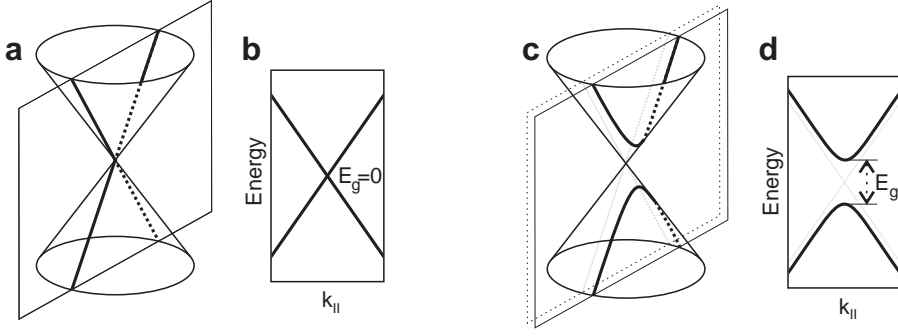
Mechanical deformation can change the electronic transport properties of carbon nanotubes. Mechanical strains alter bond lengths and bond angles which influence the coupling between  $\sigma$  and  $\pi$  orbitals [47]. As it will be summarised in this section, the bandgaps can be modulated – depending on chirality and type of strain [24, 322, 337]. Sensitivity of the electronic transport characteristics to mechanical stimuli is not only of fundamental interest, piezoresistive effects can be exploited in nano-electromechanical systems (NEMS).

### Bandgap change upon axial and torsional strain

Strain

For axial strain, a nanotube can again be treated first as unrolled graphene ribbon. Elastic deformation along the ribbon axis results in axial strain  $\varepsilon$ . Uniform axial strain is related to the undeformed length  $\ell_0$  and the deformed length  $\ell$  as  $\varepsilon = (\ell - \ell_0)/\ell_0$ . Perpendicular to the axial strain, transverse strain is induced and contracts the sheet by a factor of  $(1 - \varepsilon \nu)$ , where  $\nu$  is the Poisson's ratio.





**Figure B.7:** Sketch of the band structure of a quasi-metallic  $(n,0)$  SWNT using the Dirac cone linearization. (a,b) Without strain. (c,d) With axial tensile strain. For semiconducting nanotubes, the band gap increase for  $p = 1$ , or decrease for  $p = -1$ , provided the strain is smaller than the critical strain. Based on work of Minot *et al.* [91].

Strain will deform the unit cell and change the bond lengths. Consequently, the transfer integral  $\gamma_0$  of unstrained graphene will split into three  $\gamma_{1,2,3}$ . Using the unstrained bond length  $a_{C-C}$  and the strained bond length  $a_i$ , the transfer integrals become [338]:

$$\gamma_i = \gamma_0 \left( \frac{a_{C-C}}{a_i} \right)^2 \quad (B.12)$$

As presented by Yang and Han [311], or described in book style [219] pp. 29 [47] pp.146, the changes in the transfer integrals influence the energy dispersion. The energy dispersion of the deformed graphene (conceptually unrolled nanotube) will still show crossings at the K-points. But the positions of the K-points shift. The allowed  $k_{\perp}$  states of the periodic boundary condition for a nanotube will also shift, because the diameter shrinks under strain to  $(1 - \epsilon\nu)d$  [88] p.26. For semiconducting zigzag nanotubes  $(n,0)$  with  $n = 3q \pm 1$ , the shift of the nearest allowed  $k_{\perp}$  states away from the K-point is:

$$\Delta k_{\perp} = \frac{1}{a} \sqrt{3} (1 + \nu) \epsilon \pm \frac{2}{3d} \quad (B.13)$$

Figure B.7 schematically illustrates the effect of strain on the bandgap of a quasi-metallic nanotube [91], [88] p.27.

The bandgap change under small mechanical strains for nanotubes of different chiralities was derived by Yang and Han using the Hückel tight-binding approximation [311] and shows dependence on the chiral angle  $\theta$ :

Yang Han  
Model

$$\Delta E_g(\epsilon, \zeta) = \underbrace{\text{sgn}(2p+1)}_{+/-} 3\gamma_0 \left[ \underbrace{(1+\nu) \cos 3\theta \cdot \epsilon}_{\propto \text{axial strain}} + \underbrace{\sin 3\theta \cdot \zeta}_{\propto \text{torsion}} \right] \quad (B.14)$$

where  $p \in \{-1, 0, 1\}$  obeys  $n - m = 3q + p$  and defines the sign of the bandgap change.  $\gamma_0$  is again the hopping integral,  $\nu$  is the Poisson's ratio, and  $\theta$  is the chiral angle.  $\epsilon$  is elastic axial strain and  $\zeta$  is torsion.

The bandgap of zigzag nanotubes ( $\theta = 0^\circ$ ) is sensitive to uniaxial tensile strain, but remains unchanged under torsion.

Zigzag

Armchair The bandgap of armchair nanotubes ( $\theta = 30^\circ$ ) is insensitive to uniaxial tensile strain, but torsion is inducing a bandgap.

Chiral For chiral nanotubes, small chiral angles pronounce the bandgap modulation by tensile strain. Large chiral angles pronounce the modulation by torsion.

Simplified for pure axial strain, the absolute change in bandgap for a semiconducting SWNT is predicted to be approximately  $\cos(3\theta) \cdot 97 \text{ meV}/\%$ .

Large Strain The Yang Han model is only valid for small strains, limited because of the following reason. In the zone-folding picture of semiconducting SWNTs, the distance of the nearest cutting line to a K-point is changed in size oppositely than the distance of the second nearest cutting line to the same K-point. In other words, be  $p = +1$  then the two van Hove singularities of the first pair move farer from each other upon increasing strain – the bandgap increases. But the two van

Critical Strain Hove singularities of the second pair are moving closer. At a critical strain, both subbands will reach the same size of energy gap. At higher strains, the second subband with decreasing bandgap will become the dominant one. Although the energy gap of the formerly first subband is still increasing, the bandgap of the nanotube will change from increasing to decreasing. At following critical strains the bandgap change alternates from increasing to decreasing [311], which is not covered by Equation B.14: Decreasing bandgaps start to increase as soon as the cutting line passes the K-point (zero bandgap).

$$\begin{aligned} \text{for } p = 1 \quad \epsilon_{crit1YH} &= \frac{a_{C-C}}{3d(1+\nu)\cos3\theta} \approx \frac{0.039}{d_{[nm]}\cos3\theta} \\ \text{for } p = 0 \quad \epsilon_{crit0YH} &= 3 \cdot \epsilon_{crit1YH} \\ \text{for } p = -1 \quad \epsilon_{crit-1YH} &= 2 \cdot \epsilon_{crit1YH} \end{aligned} \quad (\text{B.15})$$

Influence of Bandgap on Contacts As pointed out by Yang and Han [311], the change in K-point not only changes the intrinsic electronic properties of the nanotube. The contact resistances may also be affected.

ab initio Guo *et al.* [339] presented ab initio density-functional calculations which confirmed the characteristics of the Yang Han model. The maximum bandgap modulation rates with strain were calculated to be  $\pm 140 \text{ meV}/\%$  which is larger than the prediction of  $\pm 97 \text{ meV}/\%$  by Yang and Han [311]. More recent work treated lattice relaxation and bandgap change for zigzag nanotubes ab initio. The maximum bandgap change rates with tensile strain were calculated to be  $\pm 115 \text{ meV}/\%$  with an uncertainty of  $\pm 10 \text{ meV}/\%$  [219, 340].

### Small bandgap semiconducting nanotubes under deformation

SGS The bandgap modulation upon strain for SGS-SWNTs was seen in simulations by Yang and Han but was not covered by their analytical model [311]. Kleiner *et al.* [323] expressed the bandgap modulation for SGS-SWNTs in dependence of chiral angle  $\theta$  and diameter  $d$ :

$$E_g = \left| \left( \frac{\gamma_0 a^2}{4d^2} - \frac{ab\sqrt{3}}{2} \epsilon \right) \cos 3\theta - \frac{ab\sqrt{3}}{2} \zeta \sin 3\theta \right| \quad (\text{B.16})$$

The first fraction is the intrinsic curvature effect (Equation B.8),  $\epsilon$  is the uniaxial strain along the tube axis,  $\zeta$  is the torsional strain (twist), and  $b$  is the linear change of the transfer integral  $\gamma_0$  upon a change of the bond length ( $b \approx 35 \text{ eV/nm}$ ). The largest change in bandgap is predicted for zigzag nanotubes of large diameters. For all SGS-SWNTs under increasing tensile strain (and

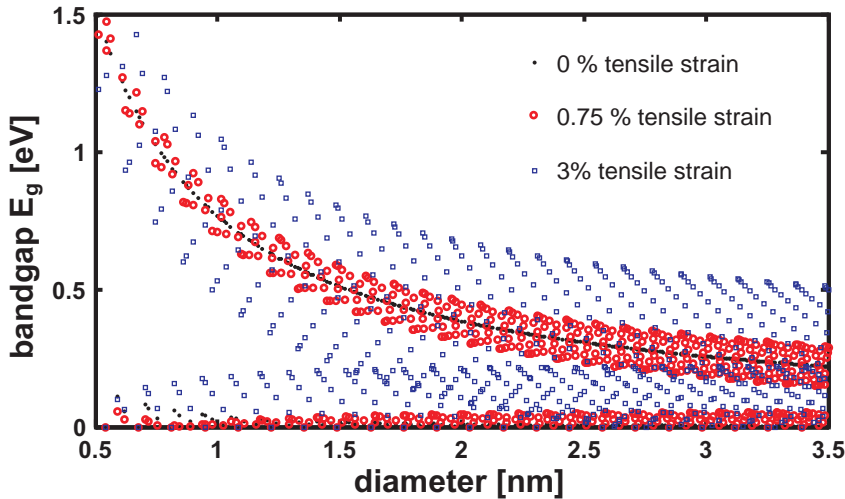
zero torsion), the initial bandgap caused by curvature is predicted to decrease first. The critical strain for SGS-nanotubes, where the decreasing bandgap is fully closed and will start to open up again at larger strain values, is:

Critical Strain  
SGS

$$\varepsilon_{crit\ Kleiner} = \frac{\sqrt{3}\gamma_0 a}{6b} \frac{1}{d^2} \approx \frac{0.55}{d^2} \quad (B.17)$$

Figure B.8 shows the bandgap changes for SWNTs, combined for both the Yang Han model [311] and the Kleiner model [323]. The latter covers the SGS-SWNTs, whose changes are not included in the Yang Han model. Bandgaps are plotted as dots for the unstrained state. The bandgaps at strains of 0.75% and 3% are plotted as circles and as squares, respectively. For many semiconducting nanotubes with large diameter and closing bandgaps ( $p = -1$ ), the critical strain at  $E_g = 0$  is reached within 3% of strain. SGS-nanotubes also first close their bandgap. However, their initial bandgaps are relatively small. Most suited for piezoresistive applications are large-diameter SGS-nanotubes [219], also because their initial bandgap is closed already at small strains and thereafter increases monotonically for a large range of strain. For semiconducting nanotubes increasing bandgaps are preferred in case of a large system resistance, because the gauge factor deteriorates less pronouncedly than for decreasing bandgaps. Large diameters offer smaller initial bandgaps which enables a large relative change in bandgap.

Bandgap  
Modulation  
upon Strain



**Figure B.8:** The bandgap in SWNTs is modulated upon pure uniaxial tensile strain according to Yang and Han [311] and Kleiner *et al.* [323]. Bandgaps are calculated for zero tensile strain (dots), for 0.75% tensile strain (open circles) and for 3% tensile strain (open squares).

### Bending

Surface-bound nanotubes are often bended during growth and kept in place by van der Waals interactions with the substrate surface [77, 199]. For dielectrophoretically deposited nanotubes or devices undergoing release etching, bending around metal contacts can be expected. For small bending curvatures, the nanotube can buckle. The conductance is not much affected unless the bending

radius is smaller than 20 nm [47] p.137. Yang and Han [311] mentioned that in pure bending the bond stretching and compression is cancelled along the circumference. Positions of K-point and VHS are invariant. The VHS intensity is increased at the elongated bonds and decreased at the compressed bonds [311]. A bend-induced bandgap opening for quasi-metallic nanotubes was calculated for a bending radius  $R_b$  [341]:

$$E_g = c(\theta) \cdot \left( \frac{r}{R_b} \right)^2 eV \quad (\text{B.18})$$

where  $c(\theta)$  is a factor of value 0 to 0.42 depending on the chiral angle  $\theta$ . The radius of the nanotube  $r$  is  $d/2$ . Taking a  $d = 2$  nm nanotube, a bend radius as small as 20 nm is needed to result in a bandgap of 1 meV.

Intrinsic  
Curvature

By transmission electron diffraction, a C-C bond stretching was observed for the inner wall relative to the outer wall of a 0.7-nm-diameter double-walled carbon nanotube [342].

### Radial deformation

Uniform

Bandgap changes upon uniform radial expansion or compression of SWNT has been modelled [343, 344]. Upon radial compression, a bandgap can open up in armchair nanotubes [344] and in metallic zigzag nanotubes [343]. Deformations caused by van der Waals interactions with the substrate [199] or by mechanical loads from external probes [213, 345, 346] can cause a non-uniform change of the cross-section and influence conductivity [345]. Radial deformation of bundled SWNTs was also deduced from electron diffraction pattern [232, 347]. Perfectly line-symmetrically squashed armchair SWNTs do not show a bandgap. But by changes in symmetry, substantial bandgaps can be induced on the order of hundreds of milli-electronvolts. Non-regular oscillations of the bandgap were simulated [47, 344]. For large compression, the bandgaps vanish, as summarised by F. Léonard [47] pp.152. The predicted oscillations are indicating that radial squeezing might be difficult to be exploited for transducers.

Non-uniform

### Piezoresistivity: Electrical transport under strain

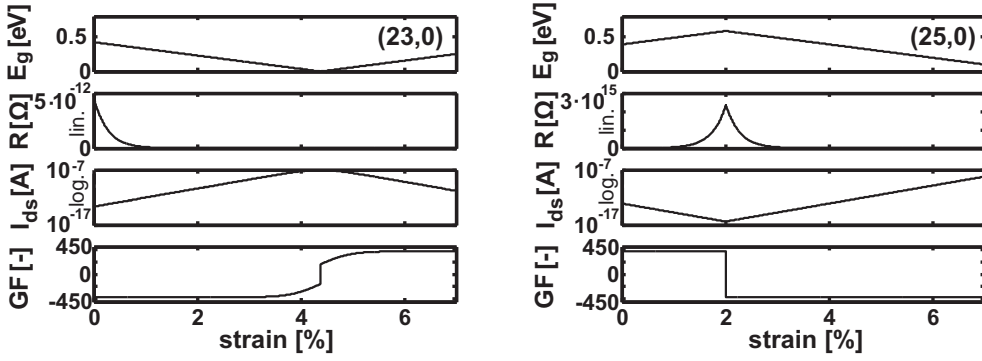
Background

To exploit nanotubes as strain-sensing transducers, the bandgap change has to be measured. As discussed by T. Helbling [219] pp.35., the bandgap change can be assessed by optical or electrical means. Optical methods, such as Raman spectroscopy or Rayleigh scattering [167, 348], are typically expensive and not suitable for miniaturised systems. The same applies for spectroscopy measurements based on scanning tunnelling microscopy. In contrast, electrical readout is less costly and can be implemented on smaller system dimensions. The strain-induced bandgap change influences the resistance, enabling piezoresistive readout schemes. The resistance  $R$  can be extracted from the measured current  $I_{ds}$  and the applied bias  $V_{ds}$  using Ohm's law:  $R = V_{ds}/I_{ds}$ . Analytical models [25, 91, 218] can be used to predict the resistance change at the transistor off-state owing to a bandgap change. Based on the model of thermally activated transport at low bias, the resistance at the off-state in dependence of  $E_g$  is [91]:

Electrical  
Readout

$$R = R_c + \frac{h}{8e^2 |\mathcal{T}|} \left[ 1 + \exp \left( \frac{E_g(\epsilon, \xi)}{k_B T} \right) \right] \quad (\text{B.19})$$

where  $R_c$  is the contact resistance,  $\epsilon$  and  $\xi$  are axial and torsional strains,  $k_B$  is the Boltzmann constant,  $T$  is the temperature and  $\mathcal{T}$  is the transmission function



**Figure B.9:** Piezoresistive effect in SWNTs plotted according the Yang and Han [311]. Bandgap  $E_g$ , resistance  $R$  in linear scale, current  $I_{ds}$  in semi-logarithmic scale, and gauge factor in dependence of uniform axial tensile strain. (left) Zigzag (23,0) nanotube with  $p = -1$ . (right) Zigzag (25,0) nanotube with  $p = 1$ .

of a quantum channel.

For a piezoresistive sensor element, sensitivity is described by the gauge factor (GF). The gauge factor is the relative change in electrical resistance per strain:

Gauge Factor

$$GF = \frac{\Delta R}{R} \frac{1}{\epsilon} \quad (B.20)$$

This definition is the differential gauge factor, associated with an infinitesimal change in resistance from an arbitrary initial resistance (at a specific  $\epsilon$ ). The GF can vary with the strain level and represents a local GF at a specific level of strain. The engineering gauge factor has to consider finite changes in strains to allow measurement of finite resistance changes:  $GF_e = [R(\epsilon_2) - R(\epsilon_1)]R^{-1}\epsilon^{-1}$ . An exponentially increasing GF is obtained only if the resistance change is considered for large strains with respect to the resistance in the undeformed state. Figure B.9 shows the differential GF for a zigzag nanotube calculated using the thermally activated transport given in Equation B.19. The maximum GF exceed the GFs of metal strain gauges ( $\sim 2$  for thin films to  $\sim 4$ ) and of doped Si ( $\sim -120$  to  $+200$ ). Nanotubes of small chiral angle yield larger bandgap modulation. The nanotube class  $p = -1$  result in decreasing gaps and increased currents. The GF of nanotubes of class  $p = 1$  is less affected by contact resistances. For sensor operation in a large strain range, the critical strain has to be considered because a non-monotonous current change renders the sensor output ambiguous. Suitable nanotubes for displacement sensing in a large strain regime are SGS-nanotubes which show increasing bandgaps after a small amount of prestraining.

Temperature-induced resistance changes can crosstalk with strain. Bias has to be adapted according to the device resistance to limit the effect of self-heating. Creep can be pronounced at elevated temperatures in metallic strain gauges.

Temperature

According to Yoon and Guo [349], the conductance change in a CNFET is affected most at the current off-state. They predict an increase in current by a factor of 10 for 1% of strain in a (17,0) Schottky-barrier CNFET. For a (16,0) nanotube ( $p = 1$ ), the bandgap enlarges with strain and results in a smaller current at the off-state. The on-current is also decreasing, but with a smaller magnitude. Hence,

CNFET  
Performance  
Tuning

strain is predicted to be a mean to tune the  $I_{ON}/I_{OFF}$  ratio.

Fermi Level  
Pinning

Guo *et al.* [339] attributed small modulation in conductance of strained nanotubes to the pinning of the Fermi level near the valence or near the conduction band. The substantial gap opening due to strain does not necessarily need to be fully represented in a conductance change, unless a local perturbation is applied such as electrostatic gating or additional mechanical deformation induced by a local probe.

### Summary on electromechanical properties

Summary

Nanotubes show a pronounced and divers bandgap dependence on strain and torsion. Armchair nanotubes remain metallic under axial strain as the mirror symmetry is preserved. Torsion is inducing a bandgap opening. In zigzag nanotubes, the bandgaps change upon uniaxial strain, while torsion is not affecting the bandgap. For increasing strain, a reversal of the change in bandgap can occur. An increasing bandgap starts to decrease from a crossover point on: At a critical strain, the increasing gap of the lowest subband becomes larger than the decreasing gap of the second lowest subband. For larger strain ranges, the number of chiralities with monotonous current change decreases.

## B.2 Characterisation techniques for carbon nanotubes

Overview

Techniques for the characterisation of nanotubes are presented based on scanning probes, electron beams, optical excitation and electrical transport. From high-resolution images and electron diffraction pattern, the chiral indices ( $n,m$ ) can be directly deduced. Assignment of indices by spectroscopic techniques is indirect, as modelling of vibrational and electronic properties are required [70] p.37.

### B.2.1 Transmission electron microscopy (TEM)

TEM

In transmission electron microscopy [350, 351] an electron beam is passed through the specimen and projected on a screen for image formation, as illustrated in Figure B.11a. Changing the current of the electromagnetic lenses adjusts the magnification obtained on the screen. The fundamental advantage of electron microscopy compared to optical microscopy is the reduced wavelength of electrons compared to photons in the range of visible light. As large mean free paths of the electrons are needed, the beam path has to be evacuated. The sample has to be electron transparent and therefore needs to be thin. For typical electron beam energies of 100–300 keV a reasonable sample thickness is smaller than 100 nm, depending on the atomic mass and atomic packing density of the sample. Carbon has the atomic number 6 and a standard atomic weight of 12.01. This results in a relatively small scattering cross-section with high-energy electron beams. To obtain the contrast of a phase object, the microscope must be slightly defocused. The nanotube walls show more contrast at small underfocus,  $\sim 1.2$  Scherzer defocus. The nanotube side walls appear as dark lines accompanied by bright lines farther away from the nanotube axis [70] p.55.

Wavelength

Sample  
Requirements

Atomic Mass  
Contrast

Phase Contrast

Aberrations

Deviations from ideal lens properties are called aberrations and deteriorate image resolution.

Astigmatism

Astigmatism aberration is an off-axis effect which distorts the beam yielding elliptical shapes in underfocus and  $90^\circ$ -rotated elliptical shapes in overfocus, caused by different focal depths for ray paths passing the lens with different rotational orientation.

Coma

Coma is an aberration causing off-axis shifts between the focal points of beam paths at the centre part of the lens and the outer part of the lens.

Spherical aberration is an on-axis lens imperfection causing different focal points for the beam paths at the centre of the lens than for the beam paths at the outer part of the lens. In light optical systems, aspherical lens shapes can compensate spherical aberration. In electromagnetic lens systems, multi-pole lenses (Cs-corrector) are used to minimise spherical aberration [352],[351] p. 229.

Spherical  
Aberration

Chromatic aberration is a lens imperfection causing different focal points for rays of different energy. In light optical systems, chromatic aberration can be compensated by including concave lenses in addition to the convex lens (achromatic lens). In electron lens systems, the effect of chromatic aberration is minimised by narrowing the energy distribution of the beam (cold field-emitter, monochromator).

Chromatic  
Aberration

Diameters measured from a TEM bright-field image as the distance of the two dark lines was reported to be generally smaller than the real nanotube diameter and to depend on nanotube alignment with respect to the incident beam (inclination angle  $\tau$ ) [353]. The discrepancy in apparent and real diameter was found to be typically less than 10% for nanotubes larger than 1 nm.

Diameter from  
Imaging

Recent double-aberration-corrected TEM images (JEOL-2200FS TEM/STEM, 80 kV) proved accurate measurement of the SWNT diameter, well matching the theoretical diameter calculated from indices assigned by electron diffraction [354]. Aberration-corrected TEM [351, 352] at 80 kV enables atomic-resolution TEM imaging of SWNTs [355, 356], including visualisation of defects [357, 358] and can enable measurement of chiral indices [84, 356, 357, 359].

Aberration  
Correction

Atoms of the top and bottom surfaces of the nanotube are most susceptible to be ballistically ejected by an incident electron. For energies larger than 139 keV, all atoms can be knocked out [291]. Small-diameter nanotubes can suffer damage at 80 keV [292].

Knock-on  
Damage

Increased contrast is achieved for lower beam energies, as the atomic scattering factor scales with electron wavelength [291]. Aberration-corrected low-voltage TEM at 20 kV improves contrast for carbon materials and enhances stability of beam-sensitive objects such as fullerenes [360].

Low Voltage

Differential pumping systems enable increased pressures around the sample. Environmental TEM demonstrated the observation of dynamic effects during SWNT growth [125].

Environmental  
TEM

### Experimental: TEM imaging – CM12

For this study, TEM images were recorded on an FEI CM12 microscope at the Electron Microscopy Facility of ETH Zurich (EMEZ). The acceleration voltage of the CM12, shown in Figure B.10, can be tuned from 120 kV to 60 kV and hence provides operation below the knock-on damage threshold of 87 kV for carbon nanotubes [291]. The electron gun is equipped with a tungsten filament. Liquid nitrogen cooling of Cu fingers is available to enhance the vacuum conditions around the sample.

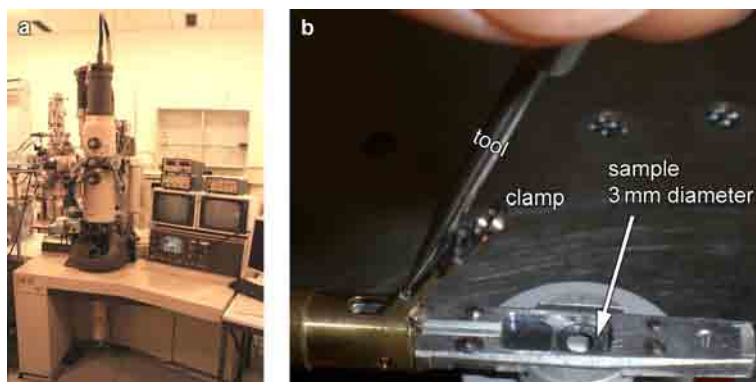
CM 12

### Sample Holders

Due to preferably small spacings between the pole pieces of the electromagnetic lenses above and below the specimen, the space for specimen holders is restricted to typically less than 6 mm. The CM12 is equipped with a double-tilt holder where a hexring is clamping the sample of maximum size of 3 mm in diameter. A single-tilt holder is shown in Figure B.10 b. Chip sizes slightly larger than 5 mm  $\times$  3 mm can be loaded, however their top surface is touched by the clamping ring with inner diameter of 2.3 mm.

Space

Standard  
Holders



**Figure B.10:** (a) TEM microscope CM12. (b) Single-tilt holder with half-way withdrawn clamping ring.

A special sample holder with electrical feedthroughs<sup>1</sup> connecting to printed circuit boards (PCBs) was used to deliver power to wirebonded MEMS actuators.

### B.2.2 Electron diffraction

Transmission electron diffraction is based on TEM and capable of measuring the chirality of carbon nanotubes [6, 94, 95, 97, 98, 114, 236, 296, 361, 362].

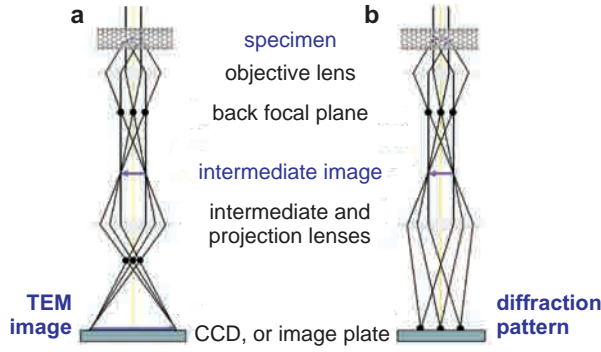
High-energy electrons have wavelengths shorter than the spacing between atoms ( $\lambda_{100\text{ keV}} = 3.7\text{ pm} = 0.0037\text{ nm}$ ). The atomic lattice of a thin crystal acts as a diffraction grating for a parallel electron beam. Depending on the periodicity of the crystal lattice, some of the electrons are scattered in specific directions. Electrons scattered in a certain direction will pass through the same point of the back focal plane, as illustrated in Figure B.11. Unscattered electrons pass straight through the sample and form an intense spot at the centre of the back focal plane. In TEM imaging mode, the electrons of these spots propagate, interfere, and form an image on the detector screen. In electron diffraction mode, the spots of the back focal plane are recorded, as sketched in Figure B.11b. Technically, the projection lens is weakened such as to record the diffraction spots instead of the image (the image would be formed far behind the detector). The detector screen records the diffraction pattern: the physical Fourier transform of the image.

To obtain the crystal features of a nanoscale area, a parallel electron beam is formed by Köhler illumination [97] and is illuminating a small part of the sample by making use of a small condenser aperture. Alternatively, an aperture for selected area electron diffraction (SAED) can constrict the area which contributes to the diffraction pattern.

For graphene oriented perpendicularly to the penetrating electron beam ( $\tau = 0^\circ$ ), the diffraction pattern yields a hexagonal array of spots [363], as sketched in Figure B.12a. Highlighted in Figure B.12b, the innermost diffraction spots, closest to the unscattered zero beam, are arranged as a hexagon. They result from the 0.213 nm atomic lattice spacing shown in Figure B.12d. Using the Miller-Bravais indices ( $hkil$ ), the innermost hexagon is labelled with (0-110). The second smallest hexagon with indices (1-210) originates from the 0.123 nm spacing [363],

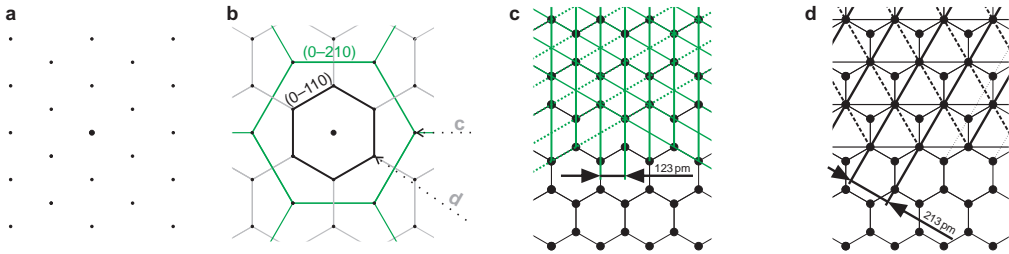
<sup>1</sup> The holder is owned by Prof. D. Poulidakos, Laboratory of Thermodynamics in Emerging Technologies (LTNT) at ETH Zürich and was designed by Nicole Bieri and Mr. Dörfler.





**Figure B.11:** Schematic illustration of the beam path in TEM electron diffraction. (a) Simplified TEM imaging mode. The image is projected onto the detector screen. (b) Simplified TEM diffraction mode. The projection lens is weakened and the back focal plane is projected onto the detector. Adapted from EMEZ. © EMEZ - ETH Zurich, 2008.

shown in Figure B.12c. The diffraction pattern corresponds to reciprocal space. Hence, a narrower pitch of the real crystal lattice spacing leads to a more extended pitch of the diffraction spots.



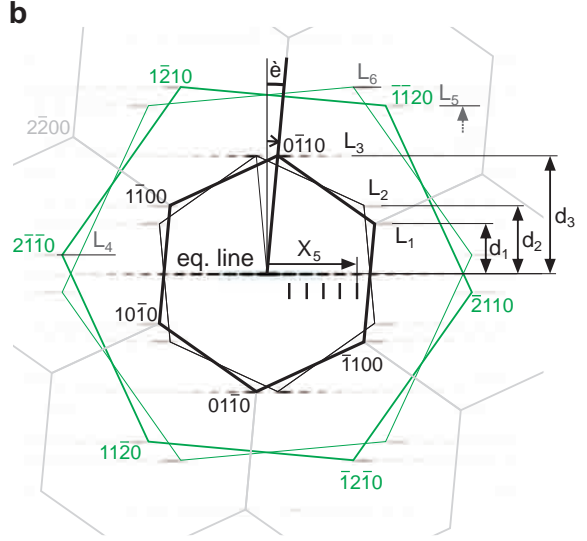
**Figure B.12:** (a) Sketch of the diffraction pattern of graphene. A planar graphene sheet oriented perpendicularly to a parallel beam of penetrating electrons scatters some electrons in characteristic angular directions. The obtained diffraction pattern shows a hexagonal array of intensity spots. (b) The (0-110) diffraction spots arranged as hexagon closest to the unscattered zero beam (indicated as larger dot) originate from the 213 pm lattice spacing shown in (d). (c) Real graphene lattice with highlighted spacing of 0.123 nm which gives rise to the (0-210) diffraction spots forming the larger second-order hexagons. (d) 213 pm spacing of the real graphene lattice causing the zero-order.

The diffraction patterns of SWNTs are unique for each chirality ( $n,m$ ) [6]. Figure B.13a shows the simulated diffraction pattern of a (18,2) nanotube. The FORTRAN code of the DIFFRACT simulation was provided by courtesy of Ph. Lambin *et al.* [95]. Again, a SWNT can be described starting with graphene and then including curvature effects. The electron beam penetrates the wall of the nanotube twice, first at the top while entering the nanotube and then at the bottom while leaving the nanotube. Neglecting curvature and multiple scattering, both graphene sheets of the top and the bottom wall contribute each a

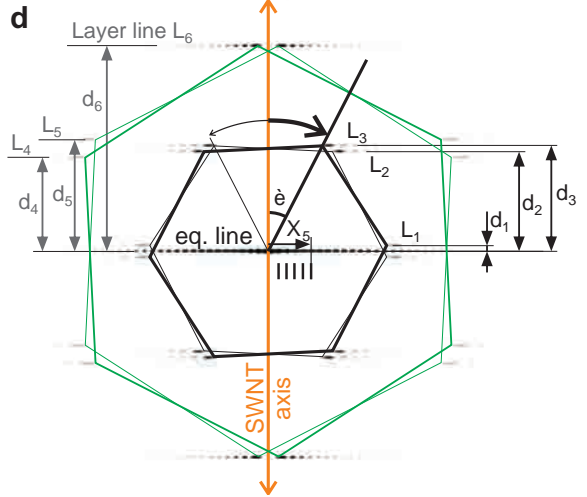
SWNTs

Rotation	hexagonal spot pattern. For chiral angles $>0^\circ$ , the two graphene sheets are rotated with respect to each other and consequently their diffraction spots rotate around the central zero beam in reciprocal space. Figure B.13b shows a small rotation
Curvature	$[\theta = 5.21^\circ]$ , and B.13d a large rotation $[\theta = 27.16^\circ]$ . Owing to curvature and small diameter of the nanotube, the diffraction spots are elongated perpendicularly to the nanotube axis [361]. The primary graphene reflections (0-110) lead to three pairs of layer lines, labelled with $L_1$ , $L_2$ , and $L_3$ . Each horizontal layer line passes through two elongated spots: through the clockwise rotated graphene reflections and through the counter-clockwise rotated reflections. The layer lines $L_4$ , $L_5$ , and $L_6$ correspond to the (0-210) graphene reflections (second-order hexagons). The intensity along the layer lines is governed by Bessel functions [361]. The layer line pairs are symmetric to the equatorial line.
Walls → Equatorial Line	The central spot is accompanied by the equatorial line of high intensity. The equatorial line is oriented perpendicularly to the nanotube axis and its intensity is modulated by the square of a zero-order Bessel function. The electron wave is scattered strongest at the outermost part of the nanotube where the walls are nearly parallel to the electron beam. As a qualitative analogy, the equatorial line is the far-field of a double slit interference pattern [296].
Rotation Angle $\approx \theta$	The chiral angle can be estimated as rotation angle measured between the first scattering intensity maximum of layer line $L_3$ and the axial direction (here vertical). Cylindrical correction factors have to account for the discrepancy between the apparent rotation angle and the true chiral angle. Correction factors are largest for small $n$ [364].
Theory	Simulation theory of diffraction patterns by the path summation approach or by calculating the Fourier transform of projected atomic potentials were described by Meyer [70] pp.40. The 3-dimensional Fourier transform of a nanotube exhibits a set of discs oriented perpendicularly to the nanotube axis. For orthogonal incidence of the beam on the nanotube, a planar section through the discs approximates the Ewald sphere. The inclination angle $\tau$ is the deviation from orthogonal orientation of the nanotube axis with respect to the incident electron beam. The approximately planar section is tilted if $\tau \neq 0^\circ$ . Consequently, the layer lines shift away from the equatorial line and change their intensity distribution [70] p.59.
Inclination Angle	
Equatorial Line $\Rightarrow d$	The intensity periodicity of the equatorial line is related to the diameter $d$ . The intensity distribution along the equatorial line is dominated by the square of the zero-order Bessel function $J_0(\pi d R)$ . $R$ is the reciprocal vector along the equatorial line. The diameter $d$ can be extracted from the following expression, as described by Liu <i>et al.</i> [96]:
	$d = \frac{X_j}{\pi R_j} \quad (\text{B.21})$ <p>where <math>X_j</math> is the unit-less value for which the square of the Bessel function <math>J_0(x)</math> reaches its <math>j</math>-th maximum. The fifth maximum is reached at <math>X_5 = 16.4706</math>. <math>R_j</math> is half the distance between the <math>j</math>-th peak maxima (<math>X_{j,exp}</math>) measured from the experimental diffraction pattern in units of <math>\text{nm}^{-1}</math>. If the first maxima were oversaturating the detector, the ratio <math>X_j/X_{j-1}</math> can be used to identify the peak number <math>j</math> [365]. The equatorial line is affected only very little by nanotube inclination <math>\tau</math> (slight curvature at extreme inclination).</p>
DWNT	A double-walled nanotube shows an additional intensity modulation of the equatorial line [310], and in general two sets of layer lines. The mean diameter

**a** (18,2)  $d = 1.494 \text{ nm}$ ,  $\hat{e} = 5.21^\circ$



**c** (25,21)  $d = 3.123 \text{ nm}$ ,  $\hat{e} = 27.16^\circ$



**Figure B.13:** (a) Simulated electron diffraction pattern of an (18,2) nanotube with a diameter of 1.494 nm and a chiral angle of  $5.21^\circ$ . (b) The equatorial line shows intensity intervals related to the nanotube diameter (Equation B.21). The distance of the layer lines  $L_{1..6}$  from the equatorial line are called layer line spacings  $d_{1..6}$  and are related to the chiral angle  $\theta$ . Ratios of  $d_{1..6}$  provide a route to extract the chiral angle (Equations B.22, B.24). The apparent rotation angle can deviate from the true  $\theta$  due to cylindrical effects for small  $n$  [364]. (c) Simulated pattern of a (25,21) nanotube with [3.123 nm,  $27.16^\circ$ ] (d) The equatorial line is perpendicular to the nanotube axis. The patterns are simulated for perpendicular incidence of the beam on the nanotube ( $\tau = 0^\circ$ ). Code for diffraction simulation was provided by Ph. Lambin [95] and implemented for MATLAB<sup>®</sup> by C. Roman.

is labelled  $d_m$  and the interlayer distance is labelled  $c$ . The intensity is approximated by the product of the squared zero-order Bessel function  $|J_0(2\pi d_m X)|^2$  and the modulation related to the interlayer distance  $|\cos(2\pi c X)|^2$  [310].

**Bundles** For bundles of SWNTs, the spot positions of the equatorial line are depending on the stacking distances of the nanotubes within the bundle and can have complex intensity distributions [347, 366]. Multiple SWNTs show multiple sets of layer lines, unless the same  $\theta$  occurs several times.

### Layer line spacing ratios

**Layer Line Spacings  $\Rightarrow \theta$**  The layer line spacings can be used to extract accurately the chiral angle  $\theta$  [364]. The layer line spacing  $d_i$  corresponds to the layer line  $L_i$ , as indicated in Figure B.13b,d. The spacings  $d_{1,2,3}$  of the principal layer lines, with  $d_1 \leq d_2 \leq d_3$ , can be measured and inserted in the following ratios considering either all three spacings  $d_{1,2,3}$  or the larger spacings  $d_2$  and  $d_3$  only [365]:

$$\theta = \text{atan} \left( \frac{d_2 - d_1}{\sqrt{3} d_3} \right) = \text{atan} \left( \frac{2d_2 - d_3}{\sqrt{3} d_3} \right) \quad (\text{B.22})$$

**Independence on Inclination** Inclination of the nanotube axis ( $\tau \neq 0$ ) does not affect the relative layer line spacings.

The relative spacings are also independent of diffraction astigmatism or of the scale, set by the camera length. The chiral angle can be accurately measured with a precision of up to  $0.1^\circ$  [70] p.57. An error calculation can be found in work of Liu *et al.* [96].

**Layer Line Spacings  $\Rightarrow m/n$**  The ratio  $m/n$  can be obtained from the layer line spacings. It is independent of the inclination angle  $\tau$  of the nanotube with respect to perpendicular orientation to the electron beam [287, 296, 362]:

$$\frac{m}{n} = \frac{2d_2 - d_3}{2d_3 - d_2} = \frac{d_3 - 2d_1}{d_1 + d_3} = 1 - \frac{3d_1}{d_5} = \frac{3d_3}{d_5} - 2 = \frac{2d_6 - 3d_3}{3d_3 - d_6} \quad (\text{B.23})$$

### Intrinsic layer line spacings

**Measure  $\tau$**  Jiang *et al.* introduced the so-called intrinsic layer line spacings to rule out ambiguities resulting from nanotube inclination  $\tau$  which affects the apparent chiral angle. Moreover, the inclination angle  $\tau$  is extracted. The intrinsic spacings  $D_i$  are defined as layer line spacing  $d_i$  multiplied with the nanotube diameter  $d$ :  $D_i = d \cdot d_i$ . From experimental diffraction patterns,  $D_i$  is obtained by measuring  $d_i$  and the regular distance  $\delta$  between intensity peak minima of the equatorial line, as:

$$D_i = \frac{d_i}{\delta} \quad (\text{B.24})$$

Since  $D_i$  is unit-less (pixel/pixel), calibration of the diffraction pattern is not needed, respectively included by the measurement of the interval  $\delta$ .

Each intrinsic layer line spacing has a geometrical relation to  $n$  and  $m$ . Evaluating any set of two of those relations results in a pair of equations for  $n$  and  $m$ .

For the experimentally most pronounced layer lines, the equations are [296]:

$$D_2, D_3 \Rightarrow n = \frac{\pi}{\sqrt{3}} \cdot (2D_3 - D_2), \quad m = \frac{\pi}{\sqrt{3}} \cdot (2D_2 - D_3) \quad (\text{B.25})$$

$$D_3, D_6 \Rightarrow n = \frac{\pi}{\sqrt{3}} \cdot (3D_3 - D_6), \quad m = \frac{\pi}{\sqrt{3}} \cdot (2D_6 - 3D_3) \quad (\text{B.26})$$

$$D_3, D_4 \Rightarrow n = \frac{\pi}{2\sqrt{3}} \cdot (3D_3 - D_4), \quad m = \frac{\pi}{\sqrt{3}} \cdot D_4 \quad (\text{B.27})$$

$$D_2, D_5 \Rightarrow n = \frac{\pi}{\sqrt{3}} \cdot D_5, \quad m = \frac{\pi}{2\sqrt{3}} \cdot (3D_2 - D_5) \quad (\text{B.28})$$

For non-perpendicular orientation of the nanotube ( $\tau \neq 0$ ) the values deduced from the experiment  $n_{exp}$  and  $m_{exp}$  will deviate from the real values of  $n$  and  $m$  by the inclination-effect errors  $\epsilon_n$  and  $\epsilon_m$ :

$$n_{exp} = n \cdot \frac{1}{\cos\tau} = n + \epsilon_n, \quad m_{exp} = m \cdot \frac{1}{\cos\tau} = m + \epsilon_m \quad (\text{B.29})$$

As the error  $\epsilon_{n,m}$  increases with increasing chiral indices, it is more robust to evaluate first  $m$ , as  $m \leq n$ . Afterwards,  $n$  can also be deduced from the  $m/n$  ratio given by Equation B.23 [296]. The maximal tolerated inclination angle  $\tau_{max}$  can be estimated by  $\tau_{max} = \arccos[m/(m + 0.9)]$ . The procedure is reliable for  $\tau < 20^\circ$  if  $m \leq 15$ . Cross-checking with the diameter measurement after calibration is recommended.

To calibrate the pattern for deduction of the diameter, the tilt angle can be calculated after  $n$  and  $m$  were assigned (possibly tentatively yet):

$$\cos\tau = \frac{n}{n_{exp}} = \frac{m}{m_{exp}} = \frac{D_3}{D_{3,exp}} = \frac{2n + m}{\sqrt{3} \pi \cdot D_{3,exp}} = \frac{D_6}{D_{6,exp}} = \frac{\sqrt{3}(n + m)}{\pi \cdot D_{6,exp}} \quad (\text{B.30})$$

By considering the inclination angle  $\tau$ , the absolute calibration of the diffraction pattern can be obtained by calculating the scale for a layer line spacings [296]. For instance for  $d_3$ , based on the graphene lattice constant  $a$ :

$$d_3 = \frac{2\sqrt{3}}{3a} \cdot \frac{\cos\theta}{\cos\tau} \quad (\text{B.31})$$

The diameter in units of nanometres is then obtained from:

Intrinsically-calibrated  $d$

$$d = \frac{1}{\delta_{[nm^{-1}]}} = \frac{1}{\delta_{[pixel]} \cdot \frac{d_{3[nm^{-1}]}}{d_{3[pixel]}}} = \frac{d_{3[pixel]}}{\delta_{[pixel]}} \cdot \frac{3a}{2\sqrt{3}} \cdot \frac{\cos\tau}{\cos\theta} \left( = \frac{D_{3,exp}}{d_{3[nm^{-1}]}} \right) \quad (\text{B.32})$$

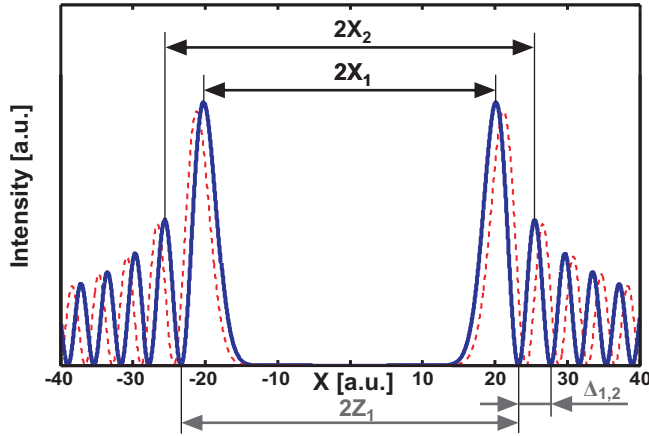
Based on the intrinsic layer line spacings, an index assignment strategy for double-walled carbon nanotubes was presented by Liu *et al.* [234].

DWNTs

### Layer line intensity profiles

The intensity profiles along the layer lines are Bessel functions whose order are related to the chiral indices  $n$  and  $m$ . The scattering amplitude is a summation of Bessel functions of different order according to the selection rule [362]. One order of Bessel function dominates the intensity distribution of a certain layer line.

Layer Line Intensity  
 $\Rightarrow n; m$



**Figure B.14:** Layer line profiles along  $L_3$  and  $L_2$  can be approximated by the Bessel function of orders  $n$  and  $m$  according to the chiral indices. The Bessel function orders are extracted from the ratio  $X_2/X_1$  as proposed by Liu *et al.* [287], or from the ratios  $2Z_1/\Delta_{1,2}$  and  $2X_1/\Delta_{1,2}$  as proposed by Jiang *et al.* [368]. Solid line is for  $n = 18$ , dashed line is for  $n = 19$ .

The intensity of the layer line  $L_3$  is a Bessel function  $J_n(x)$  of order  $n$ , where  $x$  is the coordinate along the layer line in reciprocal space. As shown in Figure B.14, the distance between the first intensity peaks is  $2 \cdot X_1$ . The distance between the second largest intensity peaks is  $2 \cdot X_2$ . The ratio of  $X_2/X_1$  is depending on the order of the Bessel function. Hence, the chiral index  $n$  can be found by extracting  $X_2/X_1$ . Analogously, the intensity peak position ratio of the middle layer line  $L_2$  is related to by a Bessel function  $J_m(x)$  of order  $m$  [287]. For  $n = 1$  the ratio is 2.892, and approaches 1 for increasing  $n$ . For large  $n$ , the difference between the ratio for  $n$  and  $n + 1$  becomes small. Fitting the full Bessel function can be more accurate as more intensity peaks can be considered. To match the experimental intensity of the peaks and not only their position, a radial damping factor is required [367]. In contrast to the layer line spacing ratios, the layer line intensity profiles are sensitive to the inclination angle  $\tau$ : position and intensity distribution change [368]. Therefore, non-perpendicular incidence of the beam with respect to the nanotube axis has to be avoided. Layer lines with wider spaced intensity peaks (higher order Bessel functions) are less distorted by inclination than those corresponding to a small chiral index [368]. The intensity layer line profiles are especially helpful for analysis of DWNTs, as the equatorial line is not involved [368].

An improved readout scheme was presented by Jiang *et al.* [368]. Instead of taking  $X_2/X_1$ , the distance  $2 \cdot X_1$  between the first pair of intensity peaks is normalised by the interval between the first and the second intensity minima  $\Delta_{1,2}$ . A second value is extracted by normalising the distance between the first pair of intensity minima. Both values are related to the Bessel function order corresponding to  $n$  for  $L_3$  and to  $m$  for  $L_2$ .

More detailed derivation of diffraction theory can be found in [70, 95, 97]. Independently of this Section, recent reviews on chirality determination methods were provided by Allen *et al.* [98] and Zhao *et al.* [236].

**Experimental: Electron diffraction – CM12**

Electron diffraction pattern were recorded at 80 kV or 100 kV using the FEI CM12 at EMEZ. At an acceleration voltage of 100 kV the contrast is slightly improved. Although the knock-on damage threshold of 87 kV is exceeded, loss of nanotubes did not occur at low intensities used for diffraction. A 100 to 300 nm long segment of a straight [70] p.56, suspended SWNT was illuminated. The diffraction patterns were recorded on imaging plates during 300 s at a camera length set to 770 mm. Imaging plates allow diffraction measurements at high dynamic range. Unlike for CCD cameras where overexposure must be prevented, a beam stop for the bright zero-order beam is not required. Data readout at 16-bit,  $5744 \times 5066$  pixel was performed at high gain of the scanner. The empty sample holder was cleaned for 20 min in plasma (25% O<sub>2</sub> + 75% Ar) (Fischione Instruments, plasma cleaner Model 1020). Plasma ashing is crucial to minimise carbonaceous deposition [233] during long exposure times. Detailed description of how to record diffraction pattern can be found in Appendix A.2.

TEM Electron Diffraction

Imaging Plates

**B.2.3 Scanning electron microscopy (SEM)**

A scanning electron microscope [369] scans a focussed electron beam along the specimen surface. Caused by the impinging beam, secondary and backscattered electrons are emitted from the specimen. Collecting these electrons by a detector allows assigning intensity to each pixel of the scanned area. Besides material contrast due to material-dependent backscattering and charging effects, the topography of the sample contributes to the contrast. Secondary electrons can more numerous escape at edges of the specimen. Resolution in SEM is limited by the range from which electrons are ejected – which is larger than the beam size. The lower the acceleration voltage and the larger the atomic mass of the sample, the smaller the interaction volume becomes from where secondary electrons are ejected. Surface-bound nanotubes appear bright and broad at low acceleration voltages owing to electron-beam-induced charges accumulating on the SWNTs [277].

SEM

Resolution

Apparent Diameter

Major advantages of SEM over TEM are the relaxed sample requirements. As no projection lens is needed below the specimen, the chamber and the specimen can be relatively large. The sample can be thick as electron transparency is not needed.

Sample Requirements

**Experimental: SEM - Ultra55**

Field-emission scanning electron microscopy images were recorded at the Zeiss ULTRA 55 or ULTRA plus at FIRST, or at the NVision40 crossbeam SEM/FIB at EMEZ. All instruments are equipped with a GEMINI® columns. Typical operation voltages were 1.2 kV on substrates and 2.4 to 5 kV for suspended CNTs. For images with inclined sample orientation, the depth of focus was increased by using 10 kV and the lens settings of the high current mode.

**B.2.4 Scanning transmission electron microscopy (STEM)**

In a scanning transmission electron microscope [351], the focussed electron beam is scanned along the specimen and the penetrating electrons are collected for image formation. In a simplified view, an STEM can be described as an SEM operated in transmissive mode. The ray path starts at the electron gun, followed by the condenser lens and objective lens and the sample stage. A coil deflects the beam to scan the area of interest and defines magnification. Opposed to TEM, a projection lens is not needed as the intensity is collected pixel by pixel.

STEM

**Imaging Modes** STEM images can be recorded in bright-field or in dark-field mode, namely as phase contrast image (TE) or as Z-contrast image (ZC). The TE detector is a circular detector centred to the beam axis. The ZC detector has the shape of a concentric ring and is hence recording only the electrons which were deflected by interaction with the specimen. Owing to the scanning type of image formation, secondary electron images (SE image) can be collected by the use of an Everhart-Thornley detector.

**Chemical Mapping** At 80 kV, energy-filtered elemental maps were recorded of SWNTs revealing elemental distribution of C and Fe [354].

**Diffraction** Nanodiffraction pattern can be recorded by widening the beam in STEM.

**Tomography** The contact geometry between Pd clusters and a suspended SWNT was reconstructed by annular dark-field electron tomography and revealed deformation of the nanotube [187].

### Experimental: Spherical-aberration-corrected STEM – Hitachi HD-2700

**Cs-corrected STEM HD-2700** The Hitachi STEM HD-2700 located at EMEZ is equipped with a Cs-corrector using a hexapole transfer lens design from CEOS. The dedicated STEM, designed for 200 kV, can also be operated at 120 kV and is equipped with the option for 80 kV. The gun is a cold field emitter. The measured pressure in the specimen

**Sample Holder** chamber can reach  $10^{-5}$  Pa. The lateral sample movement is  $\pm 1$  mm and the height movement is  $\pm 0.4$  mm. A specimen tilt of  $\pm 18^\circ$  is applicable for the high resolution lens (changes according to sample position). A dedicated MEMS sample holder was purchased from Gatan to accommodate MEMS dies wire bonded to PCBs.

**Diffraction** Although nanodiffraction is available for 200 kV, diffraction is not available for 80 kV nor for 120 kV. As a beam stop for the zero-order beam is missing, long exposure times would be prohibited by the sensitivity of the CCD camera anyways.

**Dedicated STEM** The HD-2700 is an STEM dedicated to analysis. Combined STEM/TEM imaging is not available as the projection lens required for TEM imaging is not incorporated.

### B.2.5 Raman spectroscopy and related optical techniques

**Phonons Basic Principle** Phonons are quantised vibrations of the atomic lattice. The atoms are connected by springs, allowing for vibrations. Impacting optical photons can induce phonons. In a Raman scattering event, a photon is firstly exciting an electron from the valence band into the conduction band. Secondly, the excited electron is emitting a phonon and thereafter relaxes to the valence band while emitting a photon of lower frequency (Stokes process). On the other hand, excited electrons can absorb phonons and emit an optical photon of higher energy (Anti-Stokes process). Higher order and multiple phonon scattering events are also possible [370]. In Raman spectroscopy, the specimen is excited by a monochromatic laser beam and the spectral intensity distribution of the backscattered (or transmitted) light is analysed. In nanotubes, there are transverse, longitudinal, twist, and radial phonon modes [370, 371]

**RBM  $\omega_{RBM}(d)$**  The radial mode is a synchronous expansion/contraction of all atoms with respect to the nanotube axis and is called radial breathing mode (RBM). The phonon frequency of the RBM  $\omega_{RBM}$  is related to the nanotube diameter  $d$ . Theoretical models predict for individual, pristine SWNTs a relation of  $\omega_{RBM} = C_1/d$  [371]. Interaction effects arising from dispersion in surfactant-stabilized solution, nanotube bundling, or substrate adhesion are assumed to require a second fitting parameter  $C_2$ :  $\omega_{RBM} = C_1/d + C_2$ . The nanotube diameter  $d$  is obtained from the



experimental relation to the RBM frequency:

$$d = \frac{C_1}{\omega_{RBM} - C_2} [\text{nm}] \quad (\text{B.33})$$

The experimentally determined values for  $C_1$  and  $C_2$  vary significantly [276, 290]. Table B.1 lists the parameters determined for different nanotube conditions.

**Table B.1:** Experimental parameters  $C_1$  and  $C_2$  for the diameter-RBM relation determined for different nanotube conditions.

Nanotube conditions	Reference	$C_1$ nm]	$C_2$ [rel. cm <sup>-1</sup> ]
		[rel. cm <sup>-1</sup> .	
Surfactant-surrounded in water suspension	Bachilo <i>et al.</i> [289]	223.5	12
Surfactant-surrounded in water suspension	Alvarez <i>et al.</i> [372]	232	6.5
High-density mats	Robertson <i>et al.</i> [373]	220.4±0.7	7.4±0.7
As-grown SWNTs in contact with a Si/SiO <sub>2</sub> substrate	Jorio <i>et al.</i> [374]	248	0
Dry, suspended by a resist-based process & wet etching <sup>a</sup>	Meyer <i>et al.</i> [290]	204	27
As-grown, ultralong, large- diameter SWNTs <sup>a</sup>	Liu <i>et al.</i> [15]	228±1	0 <sup>b</sup>

<sup>a</sup> Relation was determined on individual SWNTs characterised by electron diffraction

<sup>b</sup>  $C_2$  equals zero which matches the theoretical prediction for pristine SWNTs

In cases where potential chirality candidates are spread far enough, the chirality ( $n,m$ ) can be assigned based on the RBM position and comparison to the resonance modes calculated by tight-binding models [288, 373]. Chirality assignment based on RBM is not completely unambiguous [92, 93].

Tentative  
Chirality  
Assignment

The shape of the G mode and a redshift in the transition energy can indicate bundling of nanotubes [93]. The diameter of nanotubes measured in a bundle are underestimated [93].

Bundles

Radial breathing-like modes are also present in MWNTs [375].

MWNTs

The G mode of metallic nanotubes is split in a sharp component at about 1590 rel. cm<sup>-1</sup> (transvers-optical TO, high-frequency mode G<sup>+</sup>) and in a broad component at a lower frequency (longitudinal-optical LO mode, G<sup>-</sup>) of Breit-Wigner-Fano shape [93]. The G<sup>-</sup> mode is diameter-dependent [93, 376] and can be used to determine the chirality [377].

Metallic

The G mode of semiconducting nanotubes consists of two sharp components of Lorentzian line shapes. Opposite to metallic nanotubes, the higher frequency mode corresponds to the LO mode and the lower frequency component corresponds to TO [93].

Semiconducting

In double-walled carbon nanotubes, the G' mode appears as a doublet structure, but is often difficult to be resolved due to peak broadening [378]

DWNTs

The D mode at ~1350 rel. cm<sup>-1</sup> is induced by disorder such as lattice defects.

D mode

### Experimental: Raman spectroscopy – CRM200

Equipment

A confocal Raman microscope CRM200 (WiTec Wissenschaftliche Instrumente und Technologie GmbH, Ulm) [212, 276, 379] was operated at an excitation laser wavelength  $\lambda$  of 532.3 nm or 632.8 nm. A single-mode optical fibre supporting only a single transversal mode guides the laser light towards the sample. The spectra were recorded in a backscattering geometry. An objective of 100 $\times$  magnification with a numerical aperture (NA) of 0.8 (or alternatively 0.9) and a multi-mode fibre acting as a pinhole of 100  $\mu\text{m}$  in diameter (or 50  $\mu\text{m}$  optionally) established confocal conditions. While the excitation is polarised, the reflected light is collected independent of polarisation. An edge filter attenuates the elastic Rayleigh component and cuts off Raman peaks of shifts smaller than  $\sim 50 \text{ rel. cm}^{-1}$ . The collected light is split at the grating (600, 1200 or 1800 grooves/mm) and is converted A 1024 pixel charge coupled spectrometer, cooled to  $-54^\circ\text{C}$  and is converted into 16-bit data.

Laser-induced  
Heating

As the laser is focused to a spot size of  $\sim 400 \text{ nm}$  in diameter, the power density can be high. Laser power exceeding 2 mW at  $\lambda = 532.3 \text{ nm}$  was found to shift the phonon frequencies of nanotubes suspended between poly-Si supports [379, 380].

### Optical microscopy, photoluminescence excitation and Rayleigh scattering

Optical  
Microscopy

Suspended SWNTs can be located using an optical microscope if the nanotubes are coated by metal [19], for instance by 30 nm Au [151].

Photo-  
luminescence

The photoluminescence excitation technique (PLE) is typically applied to characterise SWNTs dispersed in solutions. Intensity maps are constructed by recording photoluminescence spectra for a range of excitation energies. Characteristic PLE peaks can be used to identify the occurrence of specific chiralities in the ensemble. PLE, also known as fluorescence spectroscopy, is limited to semiconducting nanotubes and only diameters smaller than  $\sim 2 \text{ nm}$  can be detected [88, 289].

Rayleigh  
Scattering

In contrast to Raman spectroscopy where matching the electronic resonance is a prerequisite (a single wavelength can or cannot hit the resonance of a given chirality), Rayleigh scattering [167, 348, 381] provides data for every chirality, as the excitation is done by white light of a broad energy range. The electric polarizability is probed and the band structure represented as intensity versus energy [382]. Bandgap changes upon strain were observed [167].

### B.2.6 Scanning tunnelling microscopy (STM) and spectroscopy

STM

Scanning tunnelling microscopy scans the sample surface by a sharp conductive tip [383]. The tunnelling current between tip and surface is maintained constant by adjusting the height position. From the height, topography is reconstructed, line by line. Alternatively the height is kept constant and the current is taken as value to be mapped.

STS

The atomic structure of nanotube can be resolved by STM and scanning tunnelling spectroscopy (STS) can extract the DOS [384, 385].

From the atomic resolution STM images, the chirality can be determined. For characterising functional nanotube devices, the major drawback of STM is the requirement of conductive sample surfaces. Electrical devices inherently require isolating areas. By scanning parallel to the nanotube axis, atomic-resolution images on a 0.1- $\mu\text{m}$ -short suspended nanotube segment were demonstrated [386].

### B.2.7 Atomic force microscopy (AFM)

Basic Principle

An atomic force microscope scans a sharp mechanical tip across the sample surface. The tip is attached to a single-clamped cantilever which serves as force

sensor. A closed loop control is usually adjusting the height position of the base of the clamped cantilever to maintain the forces between sample and tip constant. Recording the height information allows to deduce a topographical image. The resolution in vertical direction can reach sub-Å. But the lateral resolution is limited by the finite tip size (convolution of the sample topography with the tip shape). Depending on the sharpness of the tip, the set-points of the control loop must be adjusted to enter the repulsive force regime. Otherwise the height measurements can be strongly misleading. For large pressures, the extracted height of nanotubes can be smaller due to radial deformation [346].

Artefacts

AFM imaging (MFP 3-D, Asylum Research; Dimension 3100, Veeco) was employed to measure catalyst particle heights in tapping mode in the repulsive regime (phase  $< 90^\circ$ ).

Equipment

### B.2.8 Electrical transport measurements

A computerised 'Semiconductor Characterization System' from Keithley (Model 4200-SCS) was employed to measure the suspended nanotube transistors. The software 'Keithley Interactive Test Environment' (KITE) was running the DC 4200-SCS semiconductor parameter analyzer. Linear dual voltage sweeps from 0 V to the maximum voltage and back to 0 V in reverse direction were applied having the integration time set to Normal unless mentioned differently. Gate, source and drain currents and bias voltages were measured separately. The bond pads of the devices fabricated by shadow masking (Section 3.2.3) were connected at a Karl Süss PM8 probestation using Au-coated tungsten needles. Devices fabricated by transfer (Section 3.3.1) were interfaced by Al-wire bonds for the connection to the Au bond pads of a ceramic package. The pins of the package socket were soldered to a printed circuit board connected by Cu wires to BNC plugs. Keithley 2400 SourceMeters were utilised at the Raman setup, TEM and the micromanipulator. Four SourceMeters controlled by a LabVIEW™ interface were used for electromechanical measurements. The pulsed gate measurement setup of Helbling *et al.* [219, 298] was used for noise measurements.

Electrical

# C Towards chirality control during synthesis

**Chirality** This chapter debates about the quest of control over chirality for carbon nanotubes and for graphene nanoribbons. Spectroscopic characterisation of chirality-pure graphene nanoribbons is presented and the precursor-based synthesis performed by J. Cai *et al.* [105] achieving atomical precision is discussed. Parts of this Chapter were published in Nature by J. Cai, R. Fasel, K. Müllen *et al.* [105].

## C.1 State-of-the-art in chirality control for SWNTs

**Chirality Control** Chirality control is the ability to obtain the identical chirality for all SWNTs during growth. Full control also includes the fabrication of a specific chirality (B.1.1).  
**Motivation** As the electrical and the piezoresistive properties depend sensitively on the chiral indices, defining the chirality of SWNTs for devices is a long sought goal.

### C.1.1 Catalyst control

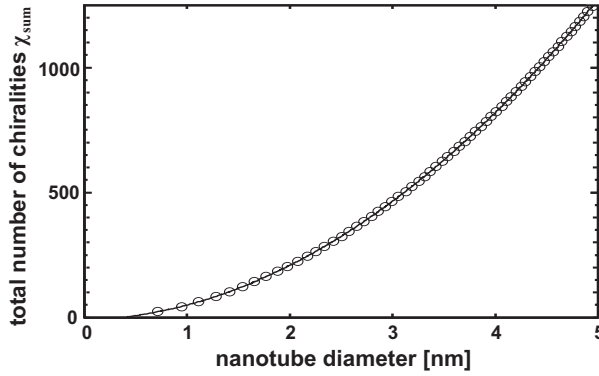
**Diameter Distribution** The size of the catalyst nanoparticle defines to a certain extent the diameter of SWNTs [77, 387].

**Ferritin** The protein cage ferritin (see Section 3.2.3) can be used to deposit metallic catalyst nanoparticles [260, 387]. Partially loaded ferritin yielded a diameter distribution of  $1.5 \pm 0.4$  nm [388]. L. Durrer achieved a narrow diameter distribution of  $1.9 \text{ nm} \pm 0.27 \text{ nm}$  by sorting ferritin according to their mass-loading using sedimentation velocity centrifugation in a density gradient [77, 263]. The distribution is in the larger diameter range suitable for ohmic contacts (see B.1.4). It is in general more challenging to obtain narrow distributions for larger diameters, as the lower boundary for energetically stable diameters ( $\sim 0.4$  nm) is not efficiently cutting-off the diameter distribution.

**Substrate** Ultimate diameter control is not only a subject of defining monodispersed catalyst particle sizes. Even for identical nanoclusters, a nanotube diameter standard deviation of 0.18 nm around a mean diameter of 1.0 nm was observed on SiO<sub>2</sub> [389]. The particle-substrate interaction can influence the size and activity of the catalyst, as by roughness, or by partial diffusion of Fe catalysts into SiO<sub>2</sub> [390], [77] p.88. Aggregation during the catalyst reduction and size-enhanced evaporation can change the catalyst during the pre-treatment and the heating phase [88] p.53.

### Number of chiralities

**Diameter Distribution** Theoretically, for a diameter distribution, the expected number of obtained chiralities does not only depend on the width of the distribution but also on the mean diameter. In the diameter range from 0.4 nm to 1 nm 48 different chiralities exist. Shifting the diameter range to larger values increased the possible number of different chiralities. In the range from 1 nm to 1.6 nm 83 chiralities exist. In Figure C.1, the total numbers of possible chiralities up to a certain diameter are plotted. The total number of chiralities  $\chi_{sum}$  follows a  $2^{nd}$  order polynomial function and



**Figure C.1:** Plot of the total number of possible chiralities counted up to a certain diameter. Every twentieth count is highlighted by a circle. The ten chiralities below 0.4 nm are not considered as they are assumed to be energetically unstable. The exactly counted number of chiralities plotted in this Figure can be approximated by  $\approx 51 \text{ nm}^{-2} \cdot d^2$ .

can be approximated by  $\chi_{sum} \approx 51 \text{ nm}^{-2} \cdot d^2$ , where  $d$  denotes the diameter in [nm] up to which the chiralities are counted.

From 1.6 nm to 2.2 nm, already 118 distinct chiralities occur. Among these 118 chiralities, 18 doublets and one triplet occur where for the very same diameter two, respectively three, chiralities with different chiral angles  $\theta$  exist. Already for a diameter as small as 0.5480 nm, two distinct chiral angles can occur:  $21.8^\circ$  and  $0^\circ$  for the chiral indices (5,3) and (7,0).

Same  $d$ ,  
Different  $\theta$

Even ideal diameter control cannot produce any arbitrary chirality with 100% yield. To obtain a small number of chiralities at finite diameter distribution, small mean diameters are reducing the possible number of chiralities. Moreover, for small diameters, the deviation in diameter is naturally reduced as the distribution becomes asymmetric as nanotubes with  $d < 0.4 \text{ nm}$  are not occurring. For larger diameter nanotubes, being beneficial for ohmic contact formation, the narrow diameter distribution achieved by Durrer *et al.* [263] ( $1.9 \text{ nm} \pm 0.27 \text{ nm}$ ) corresponds to an ensemble of 109 different chiralities within  $1-\sigma$  standard deviation.

Discussion

### Chirality-selective growth

Chirality seems to be influenced during the nucleation phase [130, 391]. Growth conditions adjusted by plasma yielded preferentially semiconducting nanotubes [392]. CVD growth using bimetallic CoPt catalysts, yielded narrow chirality distribution according to Raman spectroscopy and PLE intensity ratio interpretation [393]. SWNT growth rates were observed to increase with chiral angles [92]. Kinetic control may be envisioned.

Preferential  
Growth  
Plasma  
Bimetal  
Kinetics

Despite progress in reducing diameter distribution and in chirality-preferred growth, chirality control by direct growth is still not achieved yet.

Discussion

### Chirality separation

Motivated by the difficulty to obtain small numbers of chiralities during growth, nanotube separation techniques have been introduced to extract the nanotubes of desired properties or even chirality [394].

Aim

Metallic nanotubes can be removed by large electrical currents, while the semiconducting nanotubes are held in the OFF-state [395].

Electrical  
Breakdown

**Dielectrophoresis** Dielectrophoresis proved to deposit metallic nanotubes more efficiently than semiconducting nanotubes [169]. Commercially available raw material for nanotube suspensions often incorporates substantial amount of amorphous carbon. As suggested by T. Helbling, B. Burg *et al.* dispersed SWNTs into solution directly from the substrates by short ultrasonic pulses [82]. Burg *et al.* confirmed an enrichment of metallic SWNTs when using higher frequencies for dielectrophoresis [106]. Depleting the solution from metallic nanotubes as a pre-treatment might allow subsequently for higher yield of semiconducting nanotubes.

**Chirality Sorting** Nanotubes dispersed in solution were separated by (iterative) density gradient ultracentrifugation [396]. Single surfactant multicolumn gel chromatography allowed enrichment of some chiralities by overloading the gel with nanotubes. **Centrifugation** The separation order is found to be similar to the C–C bond curvature. The degree of bending of the C–C bonds seems to influence the interaction with the gel. **Chromatography** However, according to Kataura, it is very difficult to remove surfactants completely and separation works only for diameters up to 1.2 nm [397]. Moreover, the length of separation-treated SWNTs is typically shorter than 1.5  $\mu\text{m}$ .

**Characterisation** Discrepancies between the ratio of semiconducting to metallic nanotubes were found between characterisation using optical absorption spectra and ED [356].

### C.1.2 Chirality amplification by regrowth

**Regrowth** Smalley *et al.* introduced the re-activated growth of nanotubes with the vision of amplification of a specific chirality [398]. A parental nanotube is cut and equipped with a new catalyst particle. The subsequent growth is aimed to extend the nanotube while maintaining its chirality.

**Amplification** End-functionalised nanotubes were coupled to catalyst precursors to bypass the nucleation phase, resulting in increased growth yield compared to non-seeded catalysts [399].

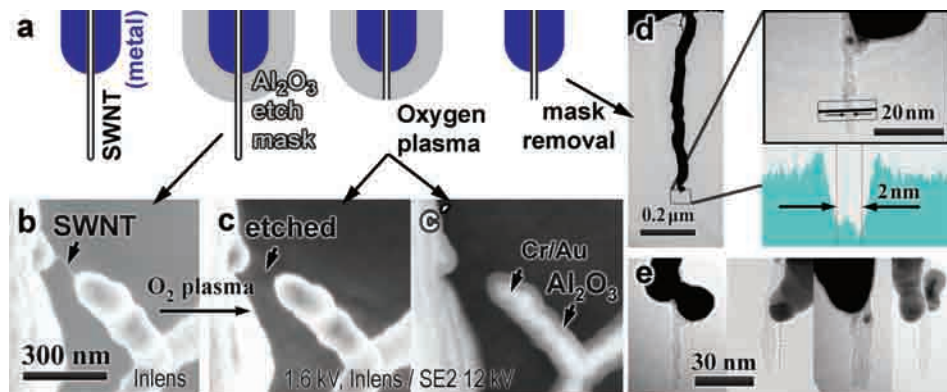
**Elongating Open Ends** Elongation of parental nanotubes was demonstrated even without the use of metal catalysts [400]. Nanotubes were cut by electron beam lithography and oxygen plasma ion etching. After a pre-treatment in flowing Ar/H<sub>2</sub> at 700 °C to remove -COOH and -OH groups from the opened nanotube ends, the temperature was raised above 945 °C to induce noncatalytic decomposition of CH<sub>4</sub>. To increase yield, C<sub>2</sub>H<sub>4</sub> was added and a quartz substrate was used. In an open-end growth mechanism, the nanotubes gained up to 4.6  $\mu\text{m}$  in length [400].

## C.2 Opening ends of CNTs at defined lengths

**Open Ends** Open-ended nanotubes are a prerequisite for chirality amplification for both approaches, with new catalyst particles docked onto existing nanotubes [399] or by catalyst-free regrowth [400].

**Cutting Mask** Selective nucleation of atomic-layer-deposited Al<sub>2</sub>O<sub>3</sub> (3.6) was applied as an etching mask for cutting SWNTs by oxygen plasma. Figure C.2 shows the removal of the uncoated nanotube section and the TEM images obtained after removal of the etch mask by HF followed by supercritical point drying.

**Conculsion Outlook** Nanotubes accessible by TEM can be cut which might be used for the study of regrowth. The length of the shortened nanotubes depends on the thickness of the ALD layer. Control over the nanotube length is important for the use as tip in scanning probe microscopy, as individual SWNT needs to be short enough (~10 nm) to provide sufficient bending stiffness.



**Figure C.2:** Nanotubes cut by plasma ashing. The section supposed to remain after the etching step is protected by  $\text{Al}_2\text{O}_3$  applied by surface-selective atomic layer deposition. (a) Illustration depicting a closed-capped SWNT protruding from a metal support, followed by surface-selective nucleation of an etching mask by ALD, after cutting the nanotube by oxygen plasma, and after removal of the etch mask by HF. (b) SEM image of a (doubly-clamped) nanotube partially covered by ALD  $\text{Al}_2\text{O}_3$  grown surface-selectively on the metal (chipping). (c) SEM image after etching by oxygen plasma, and (c') same but with imaging settings revealing material contrast. (d,e) TEM images of shortened and opened nanotubes after removing the  $\text{Al}_2\text{O}_3$  protection layer by HF etching. The sample was dried by supercritical point drying. Close-up shows the nanotube protruding from the metal coated section which served as ALD nucleation site. The intensity profile was taken along the black line (80 pixel average).

### C.3 Electrophoretically mediated ferritin adsorption

Local placement of the charged ferritin proteins on the opened ends of SWNTs was investigated by K. Truckses [401]. Similar to an approach of [402], we employed electrostatic forces to attract the dispersed ferritin onto a target area. Adsorption of ferritin (0.5 mM MES, pH 6-7) on  $\text{SiO}_2/\text{Si}$  surfaces was induced by backgate potentials, while at zero electrode potentials adsorption was suppressed. Despite trials to adjust the Debye length, pH, potentials, and distance from the counter electrode, localized adsorption of ferritin was not achieved [401]. In contrast to the work by Yoshii *et al.*, where the charged areas had diameters of 32 nm, the SWNTs acting as electrodes have an even smaller area. Moreover, the applicable electrode potentials in aqueous solution are limited by electrolysis of water.

Catalyst

### C.4 Chirality control for graphene nanoribbons

To evade the difficulties faced in controlling the chirality of carbon nanotubes with high precision, in large amounts and at unimpaired cleanliness and structural intactness, one may intend to switch from tubes to graphene nanoribbons. GNRs are indeed very appealing carbon nanostructures as bandgaps can be induced by narrow ribbon widths, and hence nanoribbons overcome the lack of an intrinsic bandgap in extended graphene sheets. While the two-dimensional graphene [7] behaves semi-metallic, edge effects and quantum confinement [403] in narrow nanoribbons are predicted to induce semiconducting behaviour. The bandgap in edged graphene is predicted to depend on the width and on the crys-

GNRs

Bandgap

tallographic orientation, the chirality, of the GNR [404]. An interesting range of band gaps of 1–3 eV is expected for ribbon widths of 2–1 nm [403].

FET	Experimental evidence of the approximately inverse scaling of the energy gap with respect to width was obtained for lithographically patterned graphene nanoribbons [17]. Field-effect transistor operation was demonstrated for sub-10 nm
Edge Roughness	narrow two-layer GNRs [190]. Structured by electron beam lithography, resist is covering a part of the graphene and the unprotected graphene parts are etched to obtain ribbons. The nanometre-rough edges are considered to be the cause why the expected transport dependence on crystallographic direction was not observed yet [17]. Wang <i>et al.</i> [84] pointed out that defects in lithographically fabricated ribbons dominate transport characteristics at low-temperature.
Defects	Defects can be of many different types, including vacancies, interstitials, heptagon-pentagon pairs (5-7) and pentagon-octagon-pentagon defects (5-8-5).

### Synthesis of graphene nanoribbons

Etching	Graphene nanoribbons can be obtained from lithographically patterned graphene flakes obtained from mechanical exfoliation of graphite [7] or by chemical vapour deposition, or from chemical and sonochemical methods.
Unzipping CNTs	An alternative approach to fabricate GNRs, is unzipping of carbon nanotubes along their axis. The intrinsic quantum-confined bandgaps and the high conductivities observed suggest that defect-induced deviations which are hardly controllable can be minimized by more well-defined fabrication techniques. However, for the route via nanotubes, the chirality of the nanoribbon is still prescribed by the chirality of the nanotube to be unzipped. In contrast, lithographically etched GNRs can be cut at defined cutting directions with respect to the parental graphene sheet. According to simulation, the crystallographic orientation of the ribbon will not only influence the intrinsic electronic transport properties, it is also predicted to govern the extent of influence of disorder, such as oxygen edge adsorbates or structural protrusions [405].
Substrate Disorder	In addition to edge-induced transport gaps, transport can be hindered by disorder potential fluctuations originating from charged impurities in the substrate [406].
Geometric Steps	Suspending the ribbons [407] can reduce the substrate-induced disorder. Armchair and zigzag ribbons <sup>1</sup> are the only chiralities of GNRs with atomically smooth edges. Assuming perfect etching capabilities, even a minute deviation in the cutting direction of 0.1° would result in a first atomic nook at the edge after every 70 nm. Currently available lithographic patterning or unzipping are struggling in controlling the shape of GNR with atomic precision. To investigate the intrinsic properties of GNRs and allow for production of chirality-pure material of uniform width in large amounts alternative fabrication concepts are needed. The task of controlling chirality in ribbons is indeed not tremendously simplified compared to nanotubes.
Width Control	In a bottom-up approach, GNRs were grown at facets of SiC [191].
Chemical Route	A technique based on chemical crosslinking of precursor monomers was demonstrated by Cai <i>et al.</i> to enable precise nanoribbons [105]. GNRs with well controlled widths, various shapes and atomically precise edges were produced.

<sup>1</sup> Armchair and zigzag is used controversially in literature. Here we denote with armchair and zigzag the edge orientation, rather than the ribbon cross-section.



### C.4.1 Characterisation of atomically precise graphene nanoribbons

In 2010, Jinming Cai *et al.* [105] presented in Nature<sup>1</sup> graphene nanoribbons synthesised by surface-assisted coupling of precursor monomers. A schematic illustration of the atomically precise bottom-up synthesis is given in Figure C.3a. 10,10'-dibromo-9,9'-bianthryl precursor monomers [408] are deposited onto an atomically-flat solid surface by thermal sublimation in an ultrahigh-vacuum setup. Dehalogenation of the monomer precursors yields bi-radicals induced by heating the substrate to 200 °C during monomer deposition. While diffusing on the surface, the bi-radical monomers link at their free radical sites and well-defined linear chains are formed. Upon heating to 400 °C, surface-assisted cyclo-dehydrogenation establishes a fully aromatic systems: In addition to the central C–C link at the former halogen site, the hydrogen atoms of benzene rings of opposing anthracene units are expelled and C–C bonds are established. Thus, a GNR of perfectly defined edge shape and with full hydrogen-termination is formed. According to a specific chemical functionality pattern, the radical addition reaction can be employed to form a multitude of atomically precise ribbon structures. J. Cai *et al.* synthesised GNRs.

Precise GNRs

Polymer Chain

Versatility

The linear polymer chain formed by intermolecular colligation through radical addition are given as STM image in Figure C.3b. The colour-coded height image reveals that the single-bonded chain shows vertical protrusions that appear alternately on both sides of the chain axis. The periodicity of 0.86 nm is in excellent agreement with the periodicity of the bianthryl core of 0.85 nm ( $6 \cdot a_{C-C}$ ). Steric hindrance between the hydrogen atoms of adjacent anthracene units rotates the relatively stiff anthracene units around the single  $\sigma$ -bonds connecting them. Thus, the opposite tilts of adjacent anthracene units result in the periodic height changes. This deviation from planarity explains the large apparent height of the single-linked chains of about 0.4 nm. Due to convolution with the finite size of the scanning probe tip, the width of the polymer is recorded to be 1.5 nm, which is much larger than expected from the structural model (1.0 nm). STM simulations, shown as an overlay in the right side of Figure C.3b, perfectly reproduce the apparent height and width of the chain if accounting for the finite tip radius.

Non-planar Chain

The fully aromatic system is obtained by annealing the sample in a second step at 400 °C. Intramolecular cyclo-dehydrogenation of the polymer chain adds two C–C bonds between the previously single-bonded anthracene units and hence forms an N=7 armchair ribbon. Flat ribbons are recorded in the STM image shown in Figure C.3c-d. The apparent height is reduced to 0.18 nm. STM simulations, given as an overlay in Figure C.3d, are confirming that the reaction products are atomically precise N = 7 GNRs with fully hydrogen-terminated armchair edges.

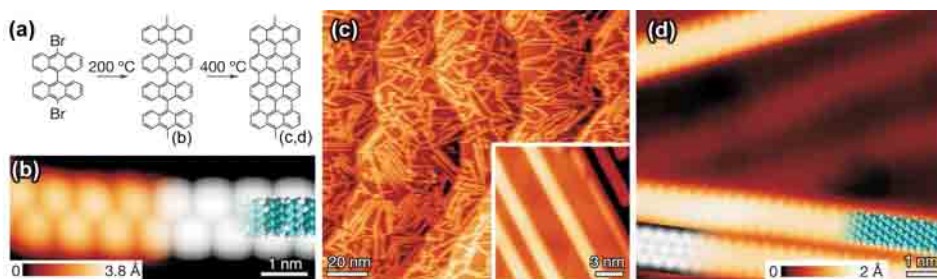
Flat Ribbon

### Raman spectroscopy of atomically precise graphene nanoribbons

The Raman spectrum of a densely packed layer of N = 7 armchair GNRs grown on a 200 nm thick Au(111) film on a mica substrate is shown in Figure C.4. The confocal Raman microscope CRM200 was operated at an excitation laser wavelength of 532.3 nm. Raman spectra were recorded at 2 mW laser power using the 100X

N = 7

<sup>1</sup> „Ownership of copyright in original research articles remains with the Authors, and provided that, when reproducing the contribution or extracts from it, the Authors acknowledge first and reference publication in the Journal, the Authors retain the [...] non-exclusive rights [...] to reproduce the contribution in whole or in part in any printed volume (book or thesis) of which they are the author(s) [...] and to reuse figures or tables created by them.“ Available at <http://www.nature.com/reprints/permission-requests.html>, October 5, 2011



**Figure C.3:** Synthesis of straight GNRs from bianthryl monomers on Au(111). (a) Reaction scheme from 10,10'-dibromo-9,9'-bianthryl precursor monomers to straight  $N=7$  GNRs. (b) Scanning tunnelling microscopy (STM) image recorded after surface-assisted C–C coupling at 200 °C but before final cyclo-dehydrogenation, showing a non-planar polyanthrylene chain (left, temperature  $T=5$  K, tip voltage  $U_t=1.9$  V, tip current  $I_t=0.08$  nA), and (right) DFT-based simulation of the STM image with partially overlaid ball-and-stick model of the linear polymer. (c) Larger-scale STM image after cyclo-dehydrogenation at 400 °C, showing straight and planar  $N=7$  GNRs (300 K,  $-3$  V, 0.03 nA; inset: 35 K,  $-1.5$  V, 0.5 nA). (d) High-resolution STM image with partly overlaid ball-and-stick model (bottom right) of the ribbon (5 K,  $-0.1$  V, 0.2 nA). At the bottom left, a DFT-based STM simulation of the  $N=7$  ribbon is shown. Images were recorded/simulated by the Main-Authors, not by Muoth. Adapted from J. Cai *et al.* [105], Nature 2010, and reprinted with Authors rights. © Macmillan Publishers Limited, 2010.

objective of 0.8 NA and having the integration time set to 30 s. A well-developed Raman signature was found to be evenly distributed over the sample (spot size  $\sim 400$  nm). A D-peak appeared, as expected due to the finite width and low symmetry of the ribbons.

RBLM As a width-specific feature, the experimental spectrum exhibits a radial-breathing-like mode (RBLM) [409] peak at  $396 \pm 1$  rel.  $\text{cm}^{-1}$ . The full mean half width is  $\sim 25$  rel.  $\text{cm}^{-1}$ .

Figure C.4c shows Raman spectra for the  $N=7$  GNRs, for a larger Raman shift range and for two laser lines, at 532.3 nm as before and at 632.8 nm. The RBLM peak at 396 rel.  $\text{cm}^{-1}$  was also detected using excitation at 632.8 nm, although at smaller intensity. These spectra were recorded 2.5 years after the samples were prepared, which indicates the stability of  $N=7$  GNRs in ambient conditions.

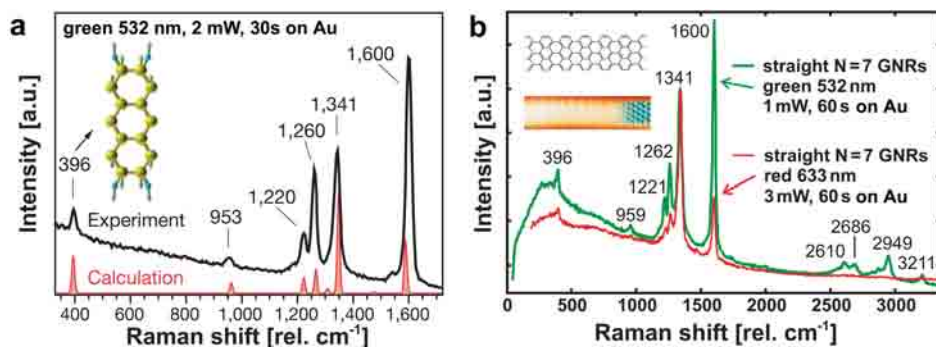
Comparison  
with Theory

The position of the RBLM is in good agreement with the theoretical value of 394 rel.  $\text{cm}^{-1}$  calculated by S. Blankenburg and A. P. Seitsonen [105]. The closest alternatives would be  $N=6$  and  $N=8$  GNRs which have radial-breathing-like mode frequencies about 50 rel.  $\text{cm}^{-1}$  higher and lower, respectively. This implies that the radial-breathing-like mode is indeed a sensitive probe of GNR width.

Vandescuren *et al.* calculated the peak position to be at 378 rel.  $\text{cm}^{-1}$  using the second-generation reactive empirical bond order potential [409]. Using a zonefolding approximation, Gillen *et al.* [410] calculated the radial-breathing-like mode (1-TA) to occur at 430.2 rel.  $\text{cm}^{-1}$  for  $N=7$  armchair GNRs. Ab initio calculations predict 385.1 rel.  $\text{cm}^{-1}$  respectively.

3-TA

The third transvers-acoustic overtone (3-TA) was calculated to occur at about 940 rel.  $\text{cm}^{-1}$  and the longitudinal-optical fundamental mode (0-LO) at



**Figure C.4:** Raman spectrum of straight  $N=7$  GNRs recorded at an excitation wavelength of 532.3 nm. The peak at 396  $\text{rel. cm}^{-1}$  is characteristic for the 0.74 nm width of  $N=7$  ribbons. The inset shows the atomic displacements related to the radial-breathing-like mode (RBLM) at 396  $\text{rel. cm}^{-1}$ . Spectra were taken by Muoth, samples were not fabricated by Muoth. Adapted from J. Cai *et al.* [105], Nature 2010, and reprinted with Authors rights. © Macmillan Publishers Limited, 2010.

1600  $\text{rel. cm}^{-1}$  [410], both in good agreement with the experimental spectra.

As the ribbons are ascertained by STM to be of  $N=7$  armchair type, the second-order response approach can be verified to match best the experimental position of the RBLM. The Raman investigations are in agreement with the STM images and further attest to the uniform width of the ribbons. We demonstrated one of the first Raman characterisations of high-quality GNRs. In early 2010, at the IWEPM in Kirchberg, it was debated whether at all the RBLM of Au-supported GNR would be detectable. Thus, we contribute valuable insights not only the confirmation of the molecular structure of the GNR, but also to fundamental questions and experimental validation of theoretical predictions of few-Å-thin, nanometre-wide and atomically precise graphene nanoribbons.

### Chevron-type nanoribbons

Figure C.5 shows STM images of GNRs synthesised by Cai *et al.* using another monomer precursor, 6,11-dibromo-1,2,3,4-tetraphenyltriphenylene.

Figure C.5c shows the Raman spectrum of chevron-type GNRs. A peak with at least two components at 1270  $\text{rel. cm}^{-1}$  and 1320  $\text{rel. cm}^{-1}$ , and peaks at 1540  $\text{rel. cm}^{-1}$  and 1600  $\text{rel. cm}^{-1}$  were observed. An RBLM was not detected – not at 532.3 nm neither at 632.8 nm. This could be due to the periodic changes in width ( $N=6 / N=9$ ) or due to excitation outside of the resonance window.

### Orientation and length

The preferred growth direction of the GNRs is given by the herringbone reconstruction of the Au(111) substrate. This substrate-controlled growth direction seems to limit the ribbon length. The length histogram drops significantly above 30 nm, which corresponds to the typical length of the straight segments of the herringbone reconstruction of the Au(111) sample used [105]. For nanostructure integration, the currently achieved length distribution imposes challenges for electrode dimensions and limits the contact length, which was shown to be relevant for nanotube contacts [149].

Interlinking of ribbons is enabled via junction monomers. Threefold symmet-

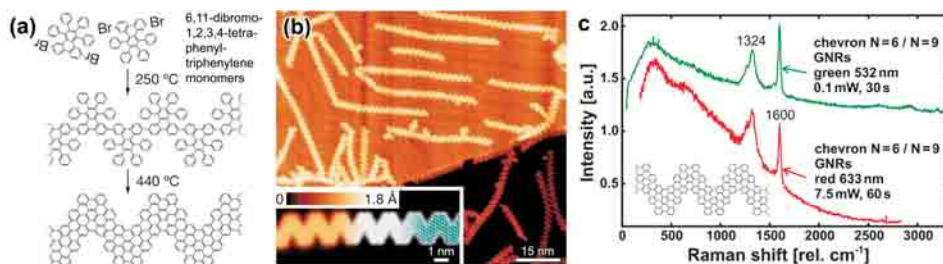
Discussion

Raman

Discussion

Orientation  
Length

Junction  
monomers

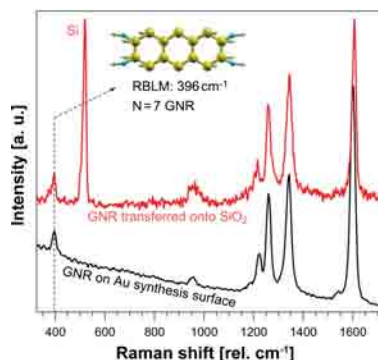


**Figure C.5:** Chevron-type  $N=6 / N=9$  nanoribbons synthesised from tetraphenyltriphenylene monomers. (a) Chemical reaction scheme from 6,11-dibromo-1,2,3,4-tetraphenyltriphenylene monomers to chains via C–C linking and dehalogenation to fully-linked, periodically meandering GNRs. (b) STM image of chevron-type GNRs fabricated on Au(111) ( $T=35\text{ K}$ ,  $U_t=-2\text{ V}$ ,  $I_t=0.02\text{ nA}$ ). The inset shows a close-up STM image ( $T=77\text{ K}$ ,  $U_t=-2\text{ V}$ ,  $I_t=0.5\text{ nA}$ ) and a DFT simulation of the STM image, partly overlaid by the molecular model of the GNR (carbon is printed in grey, hydrogen is white). (c) Raman spectra of chevron-type GNRs recorded 2.5 years after sample preparation (532.3 nm, 0.1 mW, 30 s and 632.8 nm, 7.5 mW, 60 s, intensity compressed by factor 5 and shifted for better visibility). Images were not recorded/simulated by Muoth. Spectrum was taken by Muoth, samples were not fabricated by Muoth. Adapted from J. Cai *et al.* [105], Nature 2010, and reprinted with Authors rights. © Macmillan Publishers Limited, 2010.

rical GNR junctions can be formed [105]. Specifically designed heteromolecular coupling holds promise for the growth of chemically doped GNRs and may enable regularly oriented nanoribbon arrays.

### Towards electronic devices

Substrate	The well-defined and clean substrates Au(111) or Ag(111) surfaces suitable for the bottom-up synthesis provide an ideal substrate for STM investigations of the intrinsic properties of the GNRs. And as demonstrated, the substrates are suited for Raman spectroscopy despite the intense background from the metal. But the major hurdle for device fabrication is the conductivity of the metallic substrates. Electronic devices prohibit the use of a short-circuiting substrate. Alternative substrate materials able to promote the chemical steps might be sought in the direction of aluminium or copper, and their oxides, which were found to be interesting for CMOS-compatible nanowire synthesis [411]. An alternative might be offered by the adaptation of transfer methods. For the publication of Cai <i>et al.</i> [105], Muoth contributed preliminary results using a simple chip-to-chip pressing method indicating that GNRs can be successfully transferred from gold films onto an insulating $\text{SiO}_2$ substrate. As a rudimentary demonstration of GNR transfer onto substrates suitable for prototype device implementation, we have performed first preliminary experiments on the transfer of GNRs from metal substrates onto $\text{SiO}_2/\text{Si}$ samples. Figure C.6 shows the confocal Raman spectrum of straight $N=7$ armchair GNRs grown on an Au(111)/mica substrate and subsequently transferred onto $\text{SiO}_2/\text{Si}$ by simple repeated mechanical pressing of the two die against each other. Besides the silicon peak at $520\text{ rel. cm}^{-1}$ , the spectrum is virtually identical to the one of the original GNR/Au(111)/mica sample. This demonstrates that the GNRs have been transferred from the Au(111) sur-
Electronic Integration	
Transfer	



**Figure C.6:** Preliminary results on transfer of GNRs onto an insulating substrate suitable for device integration. Raman spectra of N=7 armchair GNRs grown on Au(111)/mica (lower spectra) and subsequently transferred onto an oxidized silicon wafer surface (spectra is upshifted in intensity for better visibility). Spectra were recorded by Muoth. Adapted from [408], Nature 2010, and reprinted with Authors rights. © Macmillan Publishers Limited, 2010.

face to the SiO<sub>2</sub>/Si wafer surface suitable for electronic device integration. However, the spatial distribution of occurrence of Raman signals from GNR became sparsely. The drastically reduced background intensity at the spots of GNR signal after transfer is attributed to the absence of gold, which is a prerequisite for integration of the semiconducting material.

The Raman signals obtained were large in intensity. Li *et al.* [412] (supplementary information) measuring GNR of undefined widths resulting from sonication by surface enhance Raman scattering at 785 nm, a rather weak but broad peak at about 1590 rel. cm<sup>-1</sup> was found. The absence of any RBM over large areas was taken as confirmation of the absence of nanotubes, obviously no RBLM was detected neither.

Comparison

### Conclusion and Outlook

The chemical route to synthesise GNRs achieves surpassing precision down to the single atom level. Linking precursor monomers into linear polyphenylenes and subsequent cyclo-dehydrogenation allows designing the topology, width and edge periphery of the nanoribbon products by choosing the structure of the precursor monomers. Thus, possibly a wide range of different graphene nanoribbons can be fabricated. The N=7 armchair GNRs exhibit homogeneous structural properties, as shown by STM and confirmed by Raman spectroscopy. A shortcoming is the currently limited length which is possibly related to the reduced diffusivity of larger assemblies. The major challenge is, that the substrates allowing for dehalogenation and interlinking of the monomers are metals – currently. Conducting substrates are unsuitable for fabrication of devices based on electronic transduction. A transfer onto non-conductive surfaces (as demonstrated in a primitive scheme), alternative surface materials, surfaces to be oxidised, or thin metal coatings to be etched in later steps might be viable concepts to exploit these GNRs in electronic devices. The demonstrated use of junction monomers encourages the vision of well-ordered arrays of nanoribbons as bottom-up assembled channel-material for top down patterned electrodes.

Precision

Length

Synthesis  
Surface

Outlook

# D Symbols and abbreviations

## List of Symbols

Symbol	Unit	Description
$a$	nm	Graphene lattice constant = $\sqrt{3} a_{C-C}$ ( $\approx 0.246$ nm)
$a_{C-C}$	nm	Carbon-carbon bond length ( $\approx 0.142$ nm)
$\alpha$	$^\circ$	Primary tilt angle of the TEM sample holder
$\vec{a}_1, \vec{a}_2$	nm	Primitive vectors of the direct graphene lattice
$\beta$	$^\circ$	Secondary tilt angle of the TEM sample holder
$\vec{b}_1, \vec{b}_2$	$\text{nm}^{-1}$	Primitive vectors of the reciprocal lattice
$c$	nm	Interlayer distance
$C_1$	$\text{rel. cm}^{-1} \text{ nm}$	First parameter of the RBM–diameter relation $\omega_{RBM} = C_1/d + C_2$
$C_2$	$\text{rel. cm}^{-1}$	Second parameter of the RBM–diameter relation (environmental influence)
$\vec{C}_h$	nm	Chiral vector of a nanotube
$C_h$	nm	Circumference of a nanotube
$\chi$	eV	Electron affinity of a nanotube
$C_g$	F	Gate capacitance
$d$	nm	Diameter of a nanotube
$d_{1,2,3,4,5,6}$	$\text{nm}^{-1}$	Layer line spacings: distances of layer lines $L_{1,2,3,4,5,6}$ from the equatorial line, $d_1 \leq d_2 \leq d_3$ and $d_4 \leq d_5 \leq d_6$
$D_{1,2,3,4,5,6}$	–	Intrinsic layer line spacings, $D_i = d_i / \delta$
$D(E)$	$\text{cm}^{-1}$	Density of states, 1-dimensional
$\delta$	$\text{nm}^{-1}$	Interval between intensity peak minima of the equatorial line
$\Delta_{1,2}$	$\text{nm}^{-1}$	Interval between the first two minima of a layer line intensity profile
$e$	C	Electron charge ( $1.602 \cdot 10^{-19}$ C)
$E$	eV	Energy
$E$	GPa	Young's modulus
$E_0$	eV	Reference potential
$E_F$	eV	Fermi energy
$E_g$	eV	Energy bandgap
$\varepsilon$	–	Strain
$\epsilon$	–	Relative permittivity, dielectric constant

$\epsilon_0$	F/m	Vacuum permittivity, electric permittivity constant ( $8.85418781\dots \cdot 10^{-12}$ F/m)
$\epsilon_n, \epsilon_m$	–	Error of deduced experimental chiral indices due to tilt-effect
$F$	N	Force
$g$	m	Mask-to-substrate gap
$G$	$\Omega^{-1}$	Conductance
$G_0$	$\Omega^{-1}$	Quantum conductance
$\gamma_0$	eV	Transfer integral, also: hopping integral, transfer energy, nearest neighbour overlap energy ( $\approx 2.5$ to $3.3$ eV, here $2.7$ eV)
$\gamma_i$	eV	Transfer integrals of the strained graphene lattice
$g_{gcd}$	-	Greatest common divisor of $2m + n$ and $2n + m$
$h$	m	Material source to stencil mask distance
$h$	Js	Planck's constant ( $6.62 \cdot 10^{-34}$ Js)
$I_g$	A	Gate leakage current
$I_{ds}$	A	Source-drain current
$I_t$	A	Tip current setpoint in scanning tunnelling microscopy
$J_n(x)$	–	Bessel function of order $n$ . Corresponds to intensity in diffraction pattern.
$k_B$	J/K	Boltzmann constant, $k_B = 1.380649 \cdot 10^{-23}$ J/K = $8.617332 \cdot 10^{-5}$ eV/K
$k$	N/m	Stiffness
$\ell$	m	Undeformed length
$\ell_0$	m	Deformed length
$\ell_{mfp}$	nm	Mean free path at high energies
$\lambda$	nm	Laser wavelength
$L$	nm	Channel length
$m$	–	Second chiral index
$m_{exp}$	–	Experimentally deduced $m$
$n$	–	First chiral index
$n_{exp}$	–	Experimentally deduced $n$
$N$	–	Number of hexagons per unit cell
NA	–	Numerical Aperture
$\nu$	–	Poisson's ratio
$\Phi_m$	eV	Metal work function
$\phi_{b0}$	eV	Schottky barrier
$p$	–	Integer $p = \{-1, 0, 1\}$ , satisfying $n - m = 3q + p$ with integer $q$ , used to predict metallicity and sign of bandgap change upon strain
$r$	m	Distance of mask aperture from flux centre

$\Delta r$	m	Lateral shift of deposited material
$R$	$\Omega$	Resistance
$R_b$	nm	Bending radius
$R_c$	$\Omega$	Contact resistance
$s$	m	Width of material source
$S$	mV/dec	Subthreshold swing, minimum change required in $V_g$ to induce one decade of change in $I_{ds}$
$T$	K or $^{\circ}\text{C}$	Temperature, in Kelvin unless labelled with Celsius
$\vec{T}$		Translation vector
$t$	m	Stencil mask thickness
$t_g$	nm	Gate oxide thickness
$\tau$	$^{\circ}$	Inclination angle of nanotube axis with respect to incident electron beam
$\theta$	$^{\circ}$	Chiral angle
$\mathcal{T}$	–	Transmission function of a quantum channel
$u(V_{\text{act}})$	nm	Displacement of tip due to actuation voltage $V_{\text{act}}$
$V_{\text{act}}$	V	Actuation voltage
$V_{\text{ds}}$	V	Source-drain voltage
$V_g$	V	Gate voltage
$U_t$	V	Tip voltage setpoint in scanning tunnelling microscopy
$V_{\text{th}}$	V	Threshold voltage of a transistor
$V_{\text{th,forward}}$	V	Threshold voltage for increasing $V_g$
$V_{\text{th,backward}}$	V	Threshold voltage for decreasing $V_g$
$\omega_{\text{RBM}}$	rel. $\text{cm}^{-1}$	Phonon frequency of the radial breathing mode
$\Delta w$	m	Blurring extension of deposited material
$w$	m	Size of mask aperture
$x$	$\text{m}^{-1}$	Coordinate along a layer line of a diffraction pattern
$X_1$	$\text{m}^{-1}$	First peak position of Bessel function (layer line intensity profile)
$X_2$	$\text{m}^{-1}$	Second peak position of Bessel function
$X_5$	$\text{m}^{-1}$	Fifth peak position of Bessel function
$\zeta_5$	–	Torsional strain



## Abbreviations

Symbol	Description
ALD	Atomic layer deposition
CNFET	Carbon nanotube field-effect transistor
CNT	Carbon nanotube
CCVD	Catalysed chemical vapour deposition
CVD	Chemical vapour deposition
CMOS	Complementary metal oxide semiconductor
D	Drain electrode
DFT	Density function theory
DIC	Differential interference contrast
DOS	Density of states
DWNT	Double-walled carbon nanotube
e-beam	Electron beam
EBID	Electron-beam induced deposition
EBL	Electron beam lithography
ED	Electron diffraction
EDX	Energy-dispersive X-ray spectroscopy, or EDAX, EDS
EELS	Electron energy loss spectroscopy
ESD	Electrostatic discharge
FEM	Finite element method
FFT	Fast Fourier transform
FIB	Focused ion beam
G	Gate electrode
GF	Gauge factor
GNR	Graphene nanoribbon
HF	Hydrofluoric acid
ICP	Inductively coupled plasma
ITO	Indium tin oxide
KOH	Potassium hydroxide
L <sub>1</sub>	Layer line closest to equatorial line
L <sub>2</sub>	Middle layer line of (0-110)
L <sub>3</sub>	Topmost layer line of (0-110)
L <sub>4,5,6</sub>	Closest, middle and topmost layer lines of (0-210)
LO	Longitudinal-optical mode
MBE	Molecular beam epitaxy
MEMS	Microelectromechanical systems
MIBK	Methyl isobutyl ketone
MOSFET	Metal-oxide-semiconductor field-effect transistor
MWNT	Multi-walled carbon nanotube
MIGS	Metal-induced gap states

Symbol	Description
NEMS	Nanoelectromechanical systems
NNTB	Nearest-neighbour tight binding
PCB	Printed circuit board
Pd	Palladium
PLD	Pulsed laser deposition
PDMS	Poly(dimethylsiloxane)
PLE	Photoluminescence excitation
PMMA	Poly(methyl methacrylate)
P(MMA/MAA)	Copolymer methylmethacrylate/methylacrylic acid
PolyMUMPs	Poly-Si Multi-User MEMS Processes; MUMPs® are commercial wafer-scale multi-project services from MEMSCAP
poly-Si	Polycrystalline silicon
Poly0	Lowest Poly-Si layer of PolyMUMPs (0.5 µm thick)
Poly1	Middle Poly-Si layer of PolyMUMPs (1.5 µm thick)
Poly2	Upper Poly-Si layer of PolyMUMPs (2 µm thick)
PVD	Physical vapour deposition
RBM	Radial breathing mode
RIE	Reactive ion etching
ROI	Region of interest
S	Source electrode
SE	Secondary electrons
SEM	Scanning electron microscopy
SGS	Small bandgap semiconducting
SNR	Signal-to-noise ratio
STEM	Scanning transmission electron microscopy
STM	Scanning tunnelling microscopy
SWNT	Single-walled carbon nanotube
TA	Transvers-acoustic mode
TE	Bright-field phase contrast imaging mode
TEM	Transmission electron microscopy
VHS	van Hove singularity
ZC	Dark-field Z-contrast imaging mode (intensity proportional to $Z^2$ , with atomic number $Z$ )
#ed1	Device No., electron diffraction only
#s1	Device No., CNFET fabricated by shadow masking
#t1	Device No., CNFET fabricated by transfer
#m1	Device No., mechanical loading only
#[t1]s	Device No., additional clamping by shadow masking
#[.1]a	Device No., additional encapsulation by ALD $\text{Al}_2\text{O}_3$
#[.1..]m	Device No., electromechanical measurements

# Bibliography

- [1] M. Muoth, S.-W. Lee, K. Chikkadi, M. Mattmann, T. Helbling, A. Intlekofer, and C. Hierold, "Encapsulation of electrical contacts for suspended single-walled carbon nanotubes by atomic layer deposition," *Physica Status Solidi B*, vol. 247, no. 11-12, pp. 2997-3001, 2010.
- [2] M. Muoth, S.-W. Lee, and C. Hierold, "Platform for strainable, TEM-compatible, MEMS-embedded carbon nanotube transistors," in *IEEE MEMS, Cancun, Mexico*, 2011, pp. 83-86.
- [3] M. Muoth, C. Kiran, Y. Liu, and C. Hierold, "Suspended CNT-FET piezoresistive strain gauges: Chirality assignment and quantitative analysis," in *IEEE MEMS 2013*. IEEE, 2013, pp. 496-499.
- [4] J. Carter, A. Cowen, B. H., R. Mahadevan, M. Stonefield, and S. Wilcenski, "PolyMUMPs design handbook - a MUMPs® process, revision 11.0," *MEMSCAP Inc.*, vol. 11, pp. PolyMUMPs, Reference Material, PolyMUMPs Design Rules, 2005.
- [5] M. Muoth, J. Grimm, and C. Hierold, "Confocal Raman spectroscopy on carbon nanotubes uniaxially loaded by micro actuators," in *XXVth International Winterschool on Electronic Properties of Novel Materials and Molecular Nanostructures*, 26 February - 5 March, Kirchberg, Austria, 2011.
- [6] S. Iijima and T. Ichihashi, "Single-shell carbon nanotubes of 1-nm diameter," *Nature*, vol. 363, no. 6430, pp. 603-605, 1993.
- [7] K. S. Novoselov, A. K. Geim, S. V. Morozov, D. Jiang, Y. Zhang, S. V. Dubonos, I. V. Grigorieva, and A. A. Firsov, "Electric field effect in atomically thin carbon films," *Science*, vol. 306, no. 5696, pp. 666-669, 2004.
- [8] T. Durkop, S. A. Getty, E. Cobas, and M. S. Fuhrer, "Extraordinary mobility in semiconducting carbon nanotubes," *Nano Letters*, vol. 4, no. 1, pp. 35-39, 2004.
- [9] A. Javey, J. Guo, Q. Wang, M. Lundstrom, and H. J. Dai, "Ballistic carbon nanotube field-effect transistors," *Nature*, vol. 424, no. 6949, pp. 654-657, 2003.
- [10] D. Mann, A. Javey, J. Kong, Q. Wang, and H. Dai, "Ballistic transport in metallic nanotubes with reliable pd ohmic contacts," *Nano Letters*, vol. 3, no. 11, pp. 1541-1544, 2003.
- [11] L. E. Hueso, J. M. Pruneda, V. Ferrari, G. Burnell, J. P. Valdes-Herrera, B. D. Simons, P. B. Littlewood, E. Artacho, A. Fert, and N. D. Mathur, "Transformation of spin information into large electrical signals using carbon nanotubes," *Nature*, vol. 445, no. 7126, pp. 410-413, 2007.
- [12] A. Fert, "Challenges and emerging directions in spintronics," in *IEEE 25th Int. Conference on Micro Electro Mechanical Systems (MEMS)*, pp. 1-2, Jan 29 - Feb 2, 2012.
- [13] M. Dresselhaus, G. Dresselhaus, and P. Avouris, *Carbon nanotubes: synthesis, structure, properties, and applications*, ser. Topics in applied physics. Berlin: Springer, 2001, vol. 80.
- [14] N. Wang, Z. K. Tang, G. D. Li, and J. S. Chen, "Materials science: Single-walled 4 Å carbon nanotube arrays," *Nature*, vol. 408, no. 6808, pp. 50-51, 2000.
- [15] C.-H. Liu, C.-C. Wu, and Z. Zhong, "A fully tunable single-walled carbon nanotube diode," *Nano Letters*, vol. 11, no. 4, pp. 1782-1785, 2011.
- [16] X. Wang, Q. Li, J. Xie, Z. Jin, J. Wang, Y. Li, K. Jiang, and S. Fan, "Fabrication of ultralong and electrically uniform single-walled carbon nanotubes on clean substrates," *Nano Letters*, vol. 9, no. 9, pp. 3137-3141, 2009.
- [17] M. Y. Han, B. Özyilmaz, Y. Zhang, and P. Kim, "Energy band-gap engineering of graphene nanoribbons," *Physical Review Letters*, vol. 98, no. 20, p. 206805, 2007.
- [18] M. F. Yu, O. Lourie, M. J. Dyer, K. Moloni, T. F. Kelly, and R. S. Ruoff, "Strength and breaking mechanism of multiwalled carbon nanotubes under tensile load," *Science*, vol. 287, no. 5453, pp. 637-640, 2000.
- [19] Y. Wu, M. Huang, F. Wang, X. M. H. Huang, S. Rosenblatt, L. Huang, H. Yan, S. P. O'Brien, J. Hone, and T. F. Heinz, "Determination of the young's modulus of structurally defined carbon nanotubes," *Nano Letters*, vol. 8, no. 12, pp. 4158-4161, 2008.
- [20] C.-C. Chang, I. K. Hsu, M. Aykol, W.-H. Hung, C.-C. Chen, and S. B. Cronin, "A new lower limit for the ultimate breaking strain of carbon nanotubes," *ACS Nano*, vol. 4, no. 9, pp. 5095-5100, 2010.
- [21] C. Rutherglen, D. Jain, and P. Burke, "Nanotube electronics for radiofrequency applications," *Nature Nanotechnology*, vol. 4, no. 12, pp. 811-819, 2009.

- [22] N. R. Franklin, Q. Wang, T. W. Tomblor, A. Javey, M. Shim, and H. J. Dai, "Integration of suspended carbon nanotube arrays into electronic devices and electromechanical systems," *Applied Physics Letters*, vol. 81, no. 5, pp. 913–915, 2002.
- [23] J. Kong, N. R. Franklin, C. Zhou, M. G. Chapline, S. Peng, K. Cho, and H. Dai, "Nanotube molecular wires as chemical sensors," *Science*, vol. 287, no. 5453, pp. 622–625, 2000.
- [24] L. Yang, M. P. Anantram, J. Han, and J. P. Lu, "Band-gap change of carbon nanotubes: Effect of small uniaxial and torsional strain," *Physical Review B*, vol. 60, no. 19, pp. 13 874–13 878, 1999.
- [25] C. Stampfer, T. Helbling, D. Oberfell, B. Schoberle, M. K. Tripp, A. Jungen, S. Roth, V. M. Bright, and C. Hierold, "Fabrication of single-walled carbon-nanotube-based pressure sensors," *Nano Letters*, vol. 6, pp. 233–237, 2006.
- [26] T. Helbling, C. Roman, L. Durrer, C. Stampfer, and C. Hierold, "Gauge factor tuning, long-term stability, and miniaturization of nanoelectromechanical carbon-nanotube sensors," *IEEE Transactions on Electron Devices*, vol. 58, no. 11, pp. 4053–4060, 2011.
- [27] N. Harjee, A. Haemmerli, D. Goldhaber-Gordon, B. L. Pruitt, and Ieee, "Coaxial tip piezoresistive scanning probes with sub-nanometer vertical displacement resolution," in *2010 IEEE Sensors*, ser. IEEE Sensors, 2010, pp. 1962–1966.
- [28] W. Kim, A. Javey, O. Vermesh, O. Wang, Y. M. Li, and H. J. Dai, "Hysteresis caused by water molecules in carbon nanotube field-effect transistors," *Nano Letters*, vol. 3, no. 2, pp. 193–198, 2003.
- [29] H. Shimauchi, Y. Ohno, S. Kishimoto, and T. Mizutani, "Suppression of hysteresis in carbon nanotube field-effect transistors: Effect of contamination induced by device fabrication process," *Japanese Journal of Applied Physics Part 1*, vol. 45, no. 6B, pp. 5501–5503, 2006.
- [30] Y. Dan, Y. Lu, N. J. Kybert, Z. Luo, and A. T. C. Johnson, "Intrinsic response of graphene vapor sensors," *Nano Letters*, vol. 9, no. 4, pp. 1472–1475, 2009.
- [31] A. Vijayaraghavan, S. Kar, C. Soldano, S. Talapatra, O. Nalamasu, and P. M. Ajayan, "Charge-injection-induced dynamic screening and origin of hysteresis in field-modulated transport in single-wall carbon nanotubes," *Applied Physics Letters*, vol. 89, no. 16, p. 162108, 2006.
- [32] M. Rinkio, A. Johansson, M. Y. Zavodchikova, J. J. Toppari, A. G. Nasibulin, E. I. Kauppinen, and P. Torma, "High-yield of memory elements from carbon nanotube field-effect transistors with atomic layer deposited gate dielectric," *New Journal of Physics*, vol. 10, p. 103019, 2008.
- [33] V. K. Sangwan, V. W. Ballarotto, M. S. Fuhrer, and E. D. Williams, "Facile fabrication of suspended as-grown carbon nanotube devices," *Applied Physics Letters*, vol. 93, no. 11, p. 113112, 2008.
- [34] H. Cao, Q. Wang, D. W. Wang, and H. J. Dai, "Suspended carbon nanotube quantum wires with two gates," *Small*, vol. 1, no. 1, pp. 138–141, 2005.
- [35] L. Roschier, R. Tarkiainen, M. Ahlskog, M. Paalanen, and P. Hakonen, "Manufacture of single electron transistors using AFM manipulation on multiwalled carbon nanotubes," *Microelectronic Engineering*, vol. 61-2, pp. 687–691, 2002.
- [36] Y. M. Lin, J. C. Tsang, M. Freitag, and P. Avouris, "Impact of oxide substrate on electrical and optical properties of carbon nanotube devices," *Nanotechnology*, vol. 18, pp. 295 202–8, 2007.
- [37] J. Appenzeller, Y.-M. Lin, J. Knoch, Z. Chen, and P. Avouris, "1/f noise in carbon nanotube devices - on the impact of contacts and device geometry," *IEEE Transactions on Nanotechnology*, vol. 6, no. 3, pp. 368–373, 2007.
- [38] V. Sazonova, Y. Yaish, H. Ustunel, D. Roundy, T. A. Arias, and P. L. McEuen, "A tunable carbon nanotube electromechanical oscillator," *Nature*, vol. 431, no. 7006, pp. 284–287, 2004.
- [39] C. C. Wu and Z. Zhong, "Capacitive spring softening in single-walled carbon nanotube nanoelectromechanical resonators," *Nano Letters*, vol. 11, no. 4, pp. 1448–1451, 2011.
- [40] E. A. Laird, F. Pei, W. Tang, G. A. Steele, and L. P. Kouwenhoven, "A high quality factor carbon nanotube mechanical resonator at 39 GHz," *Nano Letters*, vol. 12, no. 1, pp. 193–197, 2012.
- [41] H. Y. Chiu, P. Hung, H. W. C. Postma, and M. Bockrath, "Atomic-scale mass sensing using carbon nanotube resonators," *Nano Letters*, vol. 8, no. 12, pp. 4342–4346, 2008.
- [42] S.-W. Lee, M. Muoth, C. Roman, H. Chandralhalim, and C. Hierold, "Characterization of suspended carbon nanotubes integrated in MEMS structures," in *CabTuRes, Posters 2011*, available: <http://www.nano-tera.ch/projects/37.php> 21 April 2012, 2011.
- [43] S.-W. Lee, M. Muoth, L. Durrer, C. Roman, and C. Hierold, "Integration of clamped-clamped suspended single-walled carbon nanotubes into SOI MEMS," in *IEEE Int. Conference on Nano/Micro Engineered and Molecular Systems (NEMS)*, 2011, pp. 37–40.
- [44] H. Chandralhalim, C. Roman, and C. Hierold, "Analytic modeling and piezoresistive detection

- theory of acoustic resonances in carbon nanotubes," in *IEEE Nano 2010*. 10th International Conference on Nanotechnology, Seoul, Korea, Aug 17-20, 2010.
- [45] X. L. Wei, Q. Chen, S. Y. Xu, L. M. Peng, and J. M. Zuo, "Beam to string transition of vibrating carbon nanotubes under axial tension," *Advanced Functional Materials*, vol. 19, no. 11, pp. 1753–1758, 2009.
  - [46] S. O. Koswatta, V. Perebeinos, M. S. Lundstrom, and P. Avouris, "Computational study of exciton generation in suspended carbon nanotube transistors," *Nano Letters*, vol. 8, no. 6, pp. 1596–1601, 2008.
  - [47] F. Léonard, *The physics of carbon nanotube devices*. Norwich, NY, USA: William Andrew Inc., 2009.
  - [48] S. Q. Ren, M. Bernardi, R. R. Lunt, V. Bulovic, J. C. Grossman, and S. Gradecak, "Toward efficient carbon nanotube/p3ht solar cells: Active layer morphology, electrical, and optical properties," *Nano Letters*, vol. 11, no. 12, pp. 5316–5321, 2011.
  - [49] F. Fornasiero, H. G. Park, J. K. Holt, M. Stadermann, C. P. Grigoropoulos, A. Noy, and O. Bakajin, "Ion exclusion by sub-2-nm carbon nanotube pores," *Proceedings of the National Academy of Sciences*, vol. 105, no. 45, pp. 17 250–17 255, 2008.
  - [50] J. Nygard and D. H. Cobden, "Quantum dots in suspended single-wall carbon nanotubes," *Applied Physics Letters*, vol. 79, no. 25, pp. 4216–4218, 2001.
  - [51] A. M. Fennimore, T. D. Yuzvinsky, W. Q. Han, M. S. Fuhrer, J. Cumings, and A. Zettl, "Rotational actuators based on carbon nanotubes," *Nature*, vol. 424, no. 6947, pp. 408–410, 2003.
  - [52] J. C. Meyer, M. Paillet, and S. Roth, "Single-molecule torsional pendulum," *Science*, vol. 309, no. 5740, pp. 1539–1541, 2005.
  - [53] C. Stampfer, A. Jungen, R. Linderman, D. Obergfell, S. Roth, and C. Hierold, "Nano-electromechanical displacement sensing based on single-walled carbon nanotubes," *Nano Letters*, vol. 6, no. 7, pp. 1449–1453, 2006.
  - [54] T. Helbling, C. Hierold, L. Durrer, C. Roman, R. Pohle, and M. Fleischer, "Suspended and non-suspended carbon nanotube transistors for  $\text{NO}_2$  sensing - a qualitative comparison," *Physica Status Solidi B*, vol. 245, no. 10, pp. 2326–2330, 2008.
  - [55] D. S. Macintyre, O. Ignatova, S. Thoms, and I. G. Thayne, "Resist residues and transistor gate fabrication," *Journal of Vacuum Science & Technology B*, vol. 27, no. 6, pp. 2597–2601, 2009.
  - [56] T. Kim, S. Kim, E. Olson, and J.-M. Zuo, "In situ measurements and transmission electron microscopy of carbon nanotube field-effect transistors," *Ultramicroscopy*, vol. 108, no. 7, pp. 613–618, 2008.
  - [57] S. K. Kim, Y. Xuan, P. D. Ye, S. Mohammadi, J. H. Back, and M. Shim, "Atomic layer deposited  $\text{Al}_2\text{O}_3$  for gate dielectric and passivation layer of single-walled carbon nanotube transistors," *Applied Physics Letters*, vol. 90, no. 16, pp. 163 108–163 108–3, 2007.
  - [58] S.-W. Lee, M. Muoth, T. Helbling, M. Mattmann, and C. Hierold, "Ald-assisted metal lift-off for contamination-free contact areas to carbon nanotubes," in *36th international conference on Micro and Nano Engineering (MNE)*, Genova, Italy, 2010.
  - [59] R. Frielinghaus, K. Goss, S. Trelenkamp, L. Houben, C. M. Schneider, and C. Meyer, "Comprehensive characterization of an individual carbon nanotube transport device," *Physica Status Solidi B*, vol. 248, no. 11, pp. 2660–2663, 2011.
  - [60] S. Yae, M. Tashiro, M. Abe, N. Fukumuro, and H. Matsuda, "High catalytic activity of palladium for metal-enhanced HF etching of silicon," *Journal of the Electrochemical Society*, vol. 157, no. 2, pp. D90–D93, 2010.
  - [61] K. R. Williams, K. Gupta, and M. Wasilik, "Etch rates for micromachining processing - part ii," *Journal of Microelectromechanical Systems*, vol. 12, no. 6, pp. 761–778, 2003.
  - [62] A. Jungen, C. Stampfer, J. Hoetzel, C. Hierold, and Ieee, "Novel process flow for the integration of carbon nanotubes into MEMS," in *13th International Conference on Solid-State Sensors, Actuators and Microsystems*, Seoul, South Korea, Jun 05-09, ser. Transducers '05, Digest of Technical Papers, Vols 1 and 2, 2005, pp. 105–108.
  - [63] A. Jungen, C. Stampfer, J. Hoetzel, V. M. Bright, and C. Hierold, "Process integration of carbon nanotubes into microelectromechanical systems," *Sensors and Actuators a-Physical*, vol. 130, pp. 588–594, 2006.
  - [64] A. B. Kaul, E. W. Wong, L. Epp, and B. D. Hunt, "Electromechanical carbon nanotube switches for high-frequency applications," *Nano Letters*, vol. 6, no. 5, pp. 942–947, 2006.
  - [65] B. Peng, M. Locascio, P. Zapol, S. Li, S. L. Mielke, G. C. Schatz, and H. D. Espinosa, "Measurements of near-ultimate strength for multiwalled carbon nanotubes and irradiation-induced crosslinking improvements," *Nat Nano*, vol. 3, no. 10, pp. 626–631, 2008.

- [66] R. M. Langford, T. X. Wang, M. Thornton, A. Heidelberg, J. G. Sheridan, W. Blau, and R. Leahy, "Comparison of different methods to contact to nanowires," *Journal of Vacuum Science & Technology B: Microelectronics and Nanometer Structures*, vol. 24, no. 5, pp. 2306–2311, 2006.
- [67] P. Jaroenapibal, Y. Jung, S. Evoy, and D. E. Luzzi, "Electromechanical properties of individual single-walled carbon nanotubes grown on focused-ion-beam patterned substrates," *Ultramicroscopy*, vol. 109, no. 2, pp. 167–171, 2009.
- [68] K. Molhave, D. N. Madsen, S. Dohn, and P. Boggild, "Constructing, connecting and soldering nanostructures by environmental electron beam deposition," *Nanotechnology*, vol. 15, no. 8, pp. 1047–1053, 2004.
- [69] J. C. Meyer, D. Obergfell, S. Roth, S. H. Yang, and S. F. Yang, "Transmission electron microscopy and transistor characteristics of the same carbon nanotube," *Applied Physics Letters*, vol. 85, no. 14, pp. 2911–2913, 2004.
- [70] J. C. Meyer, "Structure and properties of carbon nanotubes," Dissertation, Eberhard-Karls-Universität, Fakultät für Mathematik und Physik, Tübingen, Germany, 2006.
- [71] D. Mann, Y. K. Kato, A. Kinkhabwala, E. Pop, J. Cao, X. R. Wang, L. Zhang, Q. Wang, J. Guo, and H. J. Dai, "Electrically driven thermal light emission from individual single-walled carbon nanotubes," *Nature Nanotechnology*, vol. 2, no. 1, pp. 33–38, 2007.
- [72] G. A. Karp, A. Ya'akovovitz, M. David-Pur, Z. Ioffe, O. Cheshnovsky, S. Krylov, and Y. Hanein, "Integration of suspended carbon nanotubes into micro-fabricated devices," *J. of Micromechanics and Microengineering*, vol. 19, no. 8, p. 085021, 2009.
- [73] A. W. Bushmaker, "Raman spectroscopy and electrical transport in suspended carbon nanotube field effect transistors under applied bias and gate voltages," Ph.D. dissertation, USC University of Southern California, USA, 2010.
- [74] H. Miyashita, T. Ono, and M. Esashi, "Nanomechanical structures with an integrated carbon nanotube," in *Transducers'03, Jun 08-12, 2003 Boston, MA, USA*, 2003, pp. 182–185.
- [75] A. Intlekofer, *Direct growth of suspended single-walled carbon nanotubes across conductive electrodes*, bachelor Thesis, ETH Zurich, D-MAVT, Micro and Nanosystems, Zurich, Switzerland, 2010.
- [76] S. Park, S. Park, H.-M. So, E.-K. Jeon, D.-W. Park, J.-J. Kim, B. S. Kim, K.-j. Kong, H. Chang, and J.-O. Lee, "Computer-aided design and growth of single-walled carbon nanotubes on 4Å in. wafers for electronic device applications," *Carbon*, vol. 48, no. 8, pp. 2218–2224, 2010.
- [77] L. Durrer, "Controlled single-walled carbon nanotube growth for sensing applications," Dissertation, Diss. ETH No. 18947, D-MAVT, ETH Zurich, Zurich, Switzerland, Der Andere Verlag, Tönning, Lübeck und Marburg, 2010.
- [78] T. Kim, J. M. Zuo, E. A. Olson, and I. Petrov, "Imaging suspended carbon nanotubes in field-effect transistors configured with microfabricated slits for transmission electron microscopy," *Applied Physics Letters*, vol. 87, no. 17, p. 173108, 2005.
- [79] G. Steele, personal communication, XXIVth IWEPNM, Kirchberg, Austria, March, 2010.
- [80] A. Vijayaraghavan, S. Blatt, D. Weissenberger, M. Oron-Carl, F. Hennrich, D. Gerthsen, H. Hahn, and R. Krupke, "Ultra-large-scale directed assembly of single-walled carbon nanotube devices," *Nano Letters*, vol. 7, no. 6, pp. 1556–1560, 2007.
- [81] A. M. I. J. Cao, S. T. Bartsch, "Large-scale assembly of tunable resonant-body carbon nanotube transistors without hysteresis," *submitted*, 2012.
- [82] B. R. Burg, J. Schneider, M. Muoth, L. Durrer, T. Helbling, N. C. Schirmer, T. Schwamb, C. Hierold, and D. Poulikakos, "Aqueous dispersion and dielectrophoretic assembly of individual surface-synthesized single-walled carbon nanotubes," *Langmuir*, vol. 25, no. 14, pp. 7778–7782, 2009.
- [83] M. Liebau, E. Unger, G. S. Duesberg, A. P. Graham, R. Seidel, F. Kreupl, and W. Hoenlein, "Contact improvement of carbon nanotubes via electroless nickel deposition," *Applied Physics a-Materials Science & Processing*, vol. 77, no. 6, pp. 731–734, 2003.
- [84] H. Wang, L. Jun, F. Schäffel, M. H. Rummeli, G. A. D. Briggs, and J. H. Warner, "Carbon nanotube nanoelectronic devices compatible with transmission electron microscopy," *Nanotechnology*, vol. 22, no. 24, p. 245305, 2011.
- [85] B. R. Burg, T. Helbling, C. Hierold, and D. Poulikakos, "Piezoresistive pressure sensors with parallel integration of individual single-walled carbon nanotubes," *Journal of Applied Physics*, vol. 109, no. 6, p. 064310, 2011.
- [86] I. Radu, Y. Hanein, and D. H. Cobden, "Oriented growth of single-wall carbon nanotubes using alumina patterns," *Nanotechnology*, vol. 15, no. 5, pp. 473–476, 2004.
- [87] S. H. Jin, A. E. Islam, T.-i. Kim, J.-h. Kim, M. A. Alam, and J. A. Rogers, "Sources of hysteresis in carbon nanotube field-effect transistors and their elimination via methylsiloxane encapsulation," *Applied Physics Letters*, vol. 87, no. 17, p. 173108, 2005.

- sulants and optimized growth procedures," *Advanced Functional Materials*, vol. n. a., p. doi: 10.1002/adfm.201102814, 2012.
- [88] A. Javey, *Carbon nanotube electronics*, J. Javey, Ali Kong, Ed. Springer, New York, USA, 2009.
- [89] T. Helbling, C. Hierold, C. Roman, L. Durrer, M. Mattmann, and V. M. Bright, "Long term investigations of carbon nanotube transistors encapsulated by atomic-layer-deposited  $\text{Al}_2\text{O}_3$  for sensor applications," *Nanotechnology*, vol. 20, no. 43, p. 434010, 2009.
- [90] S. A. McGill, S. G. Rao, P. Manandhar, P. Xiong, and S. Hong, "High-performance, hysteresis-free carbon nanotube field-effect transistors via directed assembly," *Applied Physics Letters*, vol. 89, no. 16, p. 163123, 2006.
- [91] E. D. Minot, Y. Yaish, V. Sazonova, J. Y. Park, M. Brink, and P. L. McEuen, "Tuning carbon nanotube band gaps with strain," *Physical Review Letters*, vol. 90, no. 15, pp. 156401–4, 2003.
- [92] R. Rao, D. Liptak, T. Cherukuri, B. I. Yakobson, and B. Maruyama, "In situ evidence for chirality-dependent growth rates of individual carbon nanotubes," *Nature Materials*, vol. 11, no. 3, pp. 213–216, 2012.
- [93] T. Michel, M. Paillet, D. Nakabayashi, M. Picher, V. Jourdain, J. C. Meyer, A. A. Zahab, and J. L. Sauvajol, "Indexing of individual single-walled carbon nanotubes from raman spectroscopy," *Physical Review B*, vol. 80, no. 24, p. 245416, 2009.
- [94] L. C. Qin, "Electron diffraction from cylindrical nanotubes," *Journal of Materials Research*, vol. 9, no. 9, pp. 2450–2456, 1994.
- [95] P. Lambin and A. A. Lucas, "Quantitative theory of diffraction by carbon nanotubes," *Physical Review B*, vol. 56, no. 7, pp. 3571–3574, 1997.
- [96] Z. J. Liu, Q. Zhang, and L. C. Qin, "Determination and mapping of diameter and helicity for single-walled carbon nanotubes using nanobeam electron diffraction," *Physical Review B*, vol. 71, no. 24, pp. 245413–6, 2005.
- [97] J. C. Meyer, M. Paillet, G. S. Duesberg, and S. Roth, "Electron diffraction analysis of individual single-walled carbon nanotubes," *Ultramicroscopy*, vol. 106, no. 3, pp. 176–190, 2006.
- [98] C. S. Allen, C. Zhang, G. Burnell, A. P. Brown, J. Robertson, and B. J. Hickey, "A review of methods for the accurate determination of the chiral indices of carbon nanotubes from electron diffraction patterns," *Carbon*, vol. 49, no. 15, pp. 4961–4971, 2011.
- [99] H.-S. P. Wong and D. Akinwande, *Carbon nanotube and graphene device physics*. Cambridge University Press, Cambridge, 2011.
- [100] N. Sarkar, C. Baur, E. Stach, Z. Jandric, R. Stallcup, M. Ellis, G. Skidmore, J. Liu, and G. K. Fedder, "Modular MEMS experimental platform for transmission electron microscopy," in *IEEE International Conference on Micro Electro Mechanical Systems (MEMS 2006) Jan 22-26, Istanbul, Turkey*. IEEE, 2006, pp. 146–149.
- [101] M. Muoth, T. Helbling, L. Durrer, S. W. Lee, C. Roman, and C. Hierold, "Hysteresis-free operation of suspended carbon nanotube transistors," *Nature Nanotechnology*, vol. 5, no. 8, pp. 589–592, 2010.
- [102] M. Muoth and C. Hierold, "Transfer of carbon nanotubes onto microactuators for hysteresis-free transistors at low thermal budget," in *IEEE MEMS 2012, Paris, France, Jan 29 - Feb 2*, 2012.
- [103] M. Muoth, F. Gramm, K. Asaka, L. Durrer, T. Helbling, C. Roman, S. W. Lee, and C. Hierold, "Chirality assignment to carbon nanotubes integrated in MEMS by tilted-view transmission electron microscopy," *Sensors and Actuators B: Chemical*, vol. 154, pp. 155–159, 2011.
- [104] M. Muoth, V. Döring, and C. Hierold, "Gate hysteresis originating from atomic layer deposition of  $\text{Al}_2\text{O}_3$  onto suspended carbon nanotube field-effect transistors," *Physica Status Solidi B*, vol. 248, no. 11, pp. 2664–2667, 2011.
- [105] J. Cai, P. Ruffieux, R. Jaafar, M. Bieri, T. Braun, S. Blankenburg, M. Muoth, A. P. Seitsonen, M. Saleh, X. Feng, K. Mullen, and R. Fasel, "Atomically precise bottom-up fabrication of graphene nanoribbons," *Nature*, vol. 466, no. 7305, pp. 470–473, 2010.
- [106] B. R. Burg, J. Schneider, V. Bianco, N. C. Schirmer, and D. Poulikakos, "Selective parallel integration of individual metallic single-walled carbon nanotubes from heterogeneous solutions," *Langmuir*, vol. 26, no. 13, pp. 10419–10424, 2010.
- [107] M. Reibold, P. Paufler, A. A. Levin, W. Kochmann, N. Patzke, and D. C. Meyer, "Materials: Carbon nanotubes in an ancient damascus sabre," *Nature*, vol. 444, no. 7117, pp. 286–286, 2006, 10.1038/444286a.
- [108] L. V. Radushkevich and V. M. Lukyanovich, "O strukture ugleroda, obrazujucesja pri termiceskom razlozenii oksidi ugleroda na zeleznom kontakte [on the structure of carbon formed by the thermal dissoziation of carbon monoxide at the contact with iron]," *Zum. Fizic. Chim.*, vol. 26, pp. 88–95, 1952.

- [109] W. Davis, R. J. Slawson, and G. R. Rigby, "An unusual form of carbon," *Nature*, vol. 171, pp. 756–756, 1953.
- [110] M. Hillert and N. Lange, "The structure of graphite filaments," *Zeitschrift für Kristallographie*, vol. III, pp. 24–34, 1958.
- [111] R. Bacon, "Growth, structure, and properties of graphite whiskers," *Journal of Applied Physics*, vol. 31, no. 2, pp. 283–290, 1960.
- [112] A. Oberlin, M. Endo, and T. Koyama, "Filamentous growth of carbon through benzene decomposition," *Journal of Crystal Growth*, vol. 32, no. 3, pp. 335–349, 1976.
- [113] H. W. Kroto, J. R. Heath, S. C. O'Brien, R. F. Curl, and R. E. Smalley, "C<sub>60</sub>: Buckminsterfullerene," *Nature*, vol. 318, no. 6042, pp. 162–163, 1985.
- [114] S. Iijima, "Helical microtubules of graphitic carbon," *Nature*, vol. 354, no. 6348, pp. 56–58, 1991.
- [115] R. Saito, M. Fujita, G. Dresselhaus, and M. S. Dresselhaus, "Electronic structure of graphene tubules based on C<sub>60</sub>," *Physical Review B*, vol. 46, no. 3, pp. 1804–1811, 1992.
- [116] N. Hamada, S. Sawada, and A. Oshiyama, "New one-dimensional conductors: Graphitic microtubules," *Physical Review Letters*, vol. 68, no. 10, pp. 1579–1581, 1992.
- [117] Y. Chai, T. Guo, C. Jin, R. E. Haufler, L. P. F. Chibante, J. Fure, L. Wang, J. M. Alford, and R. E. Smalley, "Fullerenes with metals inside," *The Journal of Physical Chemistry*, vol. 95, no. 20, pp. 7564–7568, 1991.
- [118] D. S. Bethune, C. H. Klang, M. S. de Vries, G. Gorman, R. Savoy, J. Vazquez, and R. Beyers, "Cobalt-catalysed growth of carbon nanotubes with single-atomic-layer walls," *Nature*, vol. 363, no. 6430, pp. 605–607, 1993.
- [119] S. J. Tans, A. R. M. Verschueren, and C. Dekker, "Room-temperature transistor based on a single carbon nanotube," *Nature*, vol. 393, no. 6680, pp. 49–52, 1998.
- [120] R. Martel, T. Schmidt, H. R. Shea, T. Hertel, and P. Avouris, "Single- and multi-wall carbon nanotube field-effect transistors," *Applied Physics Letters*, vol. 73, no. 17, pp. 2447–2449, 1998.
- [121] K. S. Novoselov, A. K. Geim, S. V. Morozov, D. Jiang, M. I. Katsnelson, I. V. Grigorieva, S. V. Dubonos, and A. A. Firsov, "Two-dimensional gas of massless dirac fermions in graphene," *Nature*, vol. 438, no. 7065, pp. 197–200, 2005.
- [122] P. J. F. Harris, *Carbon nanotube science: synthesis, properties and applications*. Cambridge University Press, Cambridge, 2009.
- [123] G. D. Nessim, "Properties, synthesis, and growth mechanisms of carbon nanotubes with special focus on thermal chemical vapor deposition," *Nanoscale*, vol. 2, no. 8, pp. 1306–1323, 2010.
- [124] A. Thess, R. Lee, P. Nikolaev, H. J. Dai, P. Petit, J. Robert, C. H. Xu, Y. H. Lee, S. G. Kim, A. G. Rinzler, D. T. Colbert, G. E. Scuseria, D. Tomanek, J. E. Fischer, and R. E. Smalley, "Crystalline ropes of metallic carbon nanotubes," *Science*, vol. 273, no. 5274, pp. 483–487, 1996.
- [125] S. Hofmann, R. Sharma, C. Ducati, G. Du, C. Mattevi, C. Cepek, M. Cantoro, S. Pisana, A. Parvez, F. Cervantes-Sodi, A. C. Ferrari, R. Dunin-Borkowski, S. Lizzit, L. Petaccia, A. Goldoni, and J. Robertson, "In situ observations of catalyst dynamics during surface-bound carbon nanotube nucleation," *Nano Letters*, vol. 7, no. 3, pp. 602–608, 2007.
- [126] A. Jungen, C. Stampfer, L. Durrer, T. Helbling, and C. Hierold, "Amorphous carbon contamination monitoring and process optimization for single-walled carbon nanotube integration," *Nanotechnology*, vol. 18, no. 7, p. 075603, 2007.
- [127] C. Lu and J. Liu, "Controlling the diameter of carbon nanotubes in chemical vapor deposition method by carbon feeding," *Journal of Physical Chemistry B*, vol. 110, no. 41, pp. 20 254–20 257, 2006.
- [128] M. Cantoro, S. Hofmann, S. Pisana, V. Scardaci, A. Parvez, C. Ducati, A. C. Ferrari, A. M. Blackburn, K. Y. Wang, and J. Robertson, "Catalytic chemical vapor deposition of single-wall carbon nanotubes at low temperatures," *Nano Letters*, vol. 6, no. 6, pp. 1107–1112, 2006.
- [129] Z. Ghorannevis, T. Kato, T. Kaneko, and R. Hatakeyama, "Narrow-chirality distributed single-walled carbon nanotube growth from nonmagnetic catalyst," *Journal of the American Chemical Society*, vol. 132, no. 28, pp. 9570–9572, 2010.
- [130] W.-H. Chiang, M. Sakr, X. P. A. Gao, and R. M. Sankaran, "Nanoengineering ni(x)fe(1-x) catalysts for gas-phase, selective synthesis of semiconducting single-walled carbon nanotubes," *ACS Nano*, vol. 3, no. 12, pp. 4023–4032, 2009.
- [131] L. C. Qin, D. Zhou, A. R. Krauss, and D. M. Gruen, "Growing carbon nanotubes by microwave plasma-enhanced chemical vapor deposition," *Applied Physics Letters*, vol. 72, no. 26, pp. 3437–3439, 1998.
- [132] S. Hofmann, C. Ducati, J. Robertson, and B. Kleinsorge, "Low-temperature growth of carbon



- nanotubes by plasma-enhanced chemical vapor deposition," *Applied Physics Letters*, vol. 83, no. 1, pp. 135–137, 2003.
- [133] T. Kato, G. H. Jeong, T. Hirata, R. Hatakeyama, K. Tohji, and K. Motomiya, "Single-walled carbon nanotubes produced by plasma-enhanced chemical vapor deposition," *Chemical Physics Letters*, vol. 381, no. 3-4, pp. 422–426, 2003.
- [134] K. Hata, "Water-assisted highly efficient synthesis of impurity-free single-walled carbon nanotubes," *Science*, vol. 306, pp. 1362–1364, 2004.
- [135] J. Kong, H. T. Soh, A. M. Cassell, C. F. Quate, and H. J. Dai, "Synthesis of individual single-walled carbon nanotubes on patterned silicon wafers," *Nature*, vol. 395, no. 6705, pp. 878–881, 1998.
- [136] H. Park, A. Afzali, S.-J. Han, G. S. Tulevski, A. D. Franklin, J. Tersoff, J. B. Hannon, and W. Haensch, "High-density integration of carbon nanotubes via chemical self-assembly," *Nature Nanotechnology*, vol. advance online publication, p. 10.1038/nnano.2012.189, 2012.
- [137] A. M. Cassell, N. R. Franklin, T. W. Tomblor, E. M. Chan, J. Han, and H. J. Dai, "Directed growth of free-standing single-walled carbon nanotubes," *Journal of the American Chemical Society*, vol. 121, no. 34, pp. 7975–7976, 1999.
- [138] A. Jungen, S. Hofmann, J. C. Meyer, C. Stampfer, S. Roth, J. Robertson, and C. Hierold, "Synthesis of individual single-walled carbon nanotube bridges controlled by support microstructuring," *Journal of Micromechanics and Microengineering*, vol. 17, no. 3, pp. 603–608, 2007.
- [139] Y. G. Zhang, A. L. Chang, J. Cao, Q. Wang, W. Kim, Y. M. Li, N. Morris, E. Yenilmez, J. Kong, and H. J. Dai, "Electric-field-directed growth of aligned single-walled carbon nanotubes," *Applied Physics Letters*, vol. 79, no. 19, pp. 3155–3157, 2001.
- [140] Z. Jin, H. B. Chu, J. Y. Wang, J. X. Hong, W. C. Tan, and Y. Li, "Ultralow feeding gas flow guiding growth of large-scale horizontally aligned single-walled carbon nanotube arrays," *Nano Letters*, vol. 7, no. 7, pp. 2073–2079, 2007.
- [141] A. Reina, M. Hofmann, D. Zhu, and J. Kong, "Growth mechanism of long and horizontally aligned carbon nanotubes by chemical vapor deposition," *The Journal of Physical Chemistry C*, vol. 111, no. 20, pp. 7292–7297, 2007.
- [142] S. J. Kang, C. Kocabas, H. S. Kim, O. Cao, M. A. Meitl, D. Y. Khang, and J. A. Rogers, "Printed multilayer superstructures of aligned single-walled carbon nanotubes for electronic applications," *Nano Letters*, vol. 7, no. 11, pp. 3343–3348, 2007.
- [143] S. Esconjauregui, M. Fouquet, B. C. Bayer, C. Ducati, R. Smajda, S. Hofmann, and J. Robertson, "Growth of ultrahigh density vertically aligned carbon nanotube forests for interconnects," *ACS Nano*, vol. 4, no. 12, pp. 7431–7436, 2010.
- [144] L. Durrer, T. Helbling, C. Zenger, A. Jungen, C. Stampfer, and C. Hierold, "SWNT growth by cvd on ferritin-based iron catalyst nanoparticles towards cnt sensors," *Sensors and Actuators B-Chemical*, vol. 132, no. 2, pp. 485–490, 2008.
- [145] K. A. Williams, P. T. M. Veenhuizen, la Torre B. G., R. Eritja, and C. Dekker, "Nanotechnology: carbon nanotubes with DNA recognition," *Nature*, vol. 420, p. 761, 2002.
- [146] D. N. Madsen, K. Mølhave, R. Mateiu, A. M. Rasmussen, M. Brorson, C. J. H. Jacobsen, and P. Boggild, "Soldering of nanotubes onto microelectrodes," *Nano Letters*, vol. 3, no. 1, pp. 47–49, 2003.
- [147] C. S. Allen, M. D. Elkin, G. Burnell, B. J. Hickey, C. Zhang, S. Hofmann, and J. Robertson, "Transport measurements on carbon nanotubes structurally characterized by electron diffraction," *Physical Review B*, vol. 84, no. 11, pp. 115 444–5, 2011.
- [148] L. Y. Jiao, X. J. Xian, Z. Y. Wu, J. Zhang, and Z. F. Liu, "Selective positioning and integration of individual single-walled carbon nanotubes," *Nano Letters*, vol. 9, no. 1, pp. 205–209, 2009.
- [149] A. D. Franklin and Z. Chen, "Length scaling of carbon nanotube transistors," *Nature Nanotechnology*, vol. 5, no. 12, pp. 858–862, 2010.
- [150] J. Svensson, N. Lindahl, H. Yun, M. Seo, D. Midtvedt, Y. Tarakanov, N. Lindvall, O. Nerushev, J. Kinaret, S. Lee, and E. E. B. Campbell, "Carbon nanotube field effect transistors with suspended graphene gates," *Nano Letters*, vol. 11, no. 9, pp. 3569–3575, 2011.
- [151] X. M. H. Huang, R. Caldwell, L. M. Huang, S. C. Jun, M. Y. Huang, M. Y. Sfeir, S. P. O'Brien, and J. Hone, "Controlled placement of individual carbon nanotubes," *Nano Letters*, vol. 5, no. 7, pp. 1515–1518, 2005.
- [152] Z. R. Abrams, Z. Ioffe, A. Tsukernik, O. Cheshnovsky, and Y. Hanein, "A complete scheme for creating predefined networks of individual carbon nanotubes," *Nano Letters*, vol. 7, no. 9, pp. 2666–2671, 2007.
- [153] F. Pei, E. A. Laird, G. A. Steele, and L. P. Kouwenhoven, "Valley-spin blockade and spin reson-

- ance in carbon nanotubes," *Nature Nanotechnology*, vol. 7, no. 10, pp. 630–634, 2012.
- [154] C. C. Wu, C. H. Liu, and Z. Zhong, "One-step direct transfer of pristine single-walled carbon nanotubes for functional nanoelectronics," *Nano Letters*, vol. 10, no. 3, pp. 1032–1036, 2010.
  - [155] N. K. Chang, C. C. Su, and S. H. Chang, "Fabrication of single-walled carbon nanotube flexible strain sensors with high sensitivity," *Applied Physics Letters*, vol. 92, no. 6, p. 063501, 2008.
  - [156] Y. A. Kasumov, A. Shailos, I. Khodos, V. T. Volkov, V. I. Levashov, V. N. Matveev, S. Gueron, M. Kobylko, M. Kociak, H. Bouchiat, V. Agache, A. S. Rollier, L. Buchailot, A. M. Bonnot, and A. Y. Kasumov, "CVD growth of carbon nanotubes at very low pressure of acetylene," *Applied Physics a-Materials Science & Processing*, vol. 88, no. 4, pp. 687–691, 2007.
  - [157] Y. X. Zhou and A. T. Johnson, "Simple fabrication of molecular circuits by shadow mask evaporation," *Nano Letters*, vol. 3, no. 10, pp. 1371–1374, 2003.
  - [158] W. Bao, G. Liu, Z. Zhao, H. Zhang, D. Yan, A. Deshpande, B. J. LeRoy, and C. N. Lau, "Lithography-free fabrication of high quality substrate-supported and freestanding graphene devices," *Nano Research*, vol. 3, no. 2, pp. 98–102, 2010.
  - [159] M. Y. Timmermans, K. Grigoras, A. G. Nasibulin, V. Hurskainen, S. Franssila, V. Ermolov, and E. I. Kauppinen, "Lithography-free fabrication of carbon nanotube network transistors," *Nanotechnology*, vol. 22, no. 6, p. 065303, 2011.
  - [160] T. Banks, personal communication, Raith Seminar, Düsseldorf, March 3, 2009.
  - [161] D. Bischoff, "Residues - towards better contacts - resist tests," in *EBL Workshop, ETH Zurich*, November 15, 2011.
  - [162] N. Tombros, A. Veligura, J. Junesch, J. J. van den Berg, P. J. Zomer, M. Wojtaszek, I. J. V. Marun, H. T. Jonkman, and B. J. van Wees, "Large yield production of high mobility freely suspended graphene electronic devices on a polydimethylglutarimide based organic polymer," *Journal of Applied Physics*, vol. 109, no. 9, pp. 093702–5, 2011.
  - [163] J. Chan, D. Kidd, B. Burke, L. Harriott, and K. Williams, "Noise analysis of carbon nanotube field effect transistors irradiated by electron beam," *Journal of Vacuum Science & Technology B*, vol. 28, no. 6, pp. C6P66–C6P69, 2010.
  - [164] C. O. Girit and A. Zettl, "Soldering to a single atomic layer," *Applied Physics Letters*, vol. 91, no. 19, p. 193512, 2007.
  - [165] T. Schwamb, B. R. Burg, N. C. Schirmer, and D. Poulikakos, "On the effect of the electrical contact resistance in nanodevices," *Applied Physics Letters*, vol. 92, no. 24, p. 243106, 2008.
  - [166] Y. X. Zhou, A. Gaur, S. H. Hur, C. Kocabas, M. A. Meitl, M. Shim, and J. A. Rogers, "p-channel, n-channel thin film transistors and p-n diodes based on single wall carbon nanotube networks," *Nano Letters*, vol. 4, no. 10, pp. 2031–2035, 2004.
  - [167] M. Huang, Y. Wu, B. Chandra, H. Yan, Y. Shan, T. F. Heinz, and J. Hone, "Direct measurement of strain-induced changes in the band structure of carbon nanotubes," *Physical Review Letters*, vol. 100, no. 13, pp. 136803–4, 2008.
  - [168] H. Wang, J. Luo, A. Robertson, Y. Ito, W. Yan, V. Lang, M. Zaka, F. Schäffel, M. H. Rummeli, G. A. D. Briggs, and J. H. Warner, "High-performance field effect transistors from solution processed carbon nanotubes," *ACS Nano*, vol. 4, no. 11, pp. 6659–6664, 2010.
  - [169] R. Krupke, F. Hennrich, H. v. Löhneysen, and M. M. Kappes, "Separation of metallic from semiconducting single-walled carbon nanotubes," *Science*, vol. 301, no. 5631, pp. 344–347, 2003.
  - [170] E. Frackowiak, "Carbon materials for supercapacitor application," *Physical Chemistry Chemical Physics*, vol. 9, no. 15, pp. 1774–1785, 2007.
  - [171] W. A. DeHeer, A. Chatelain, and D. Ugarte, "A carbon nanotube field-emission electron source," *Science*, vol. 270, no. 5239, pp. 1179–1180, 1995.
  - [172] K. Jensen, K. Kim, and A. Zettl, "An atomic-resolution nanomechanical mass sensor," *Nature Nanotechnology*, vol. 3, no. 9, pp. 533–537, 2008.
  - [173] H. J. Dai, J. H. Hafner, A. G. Rinzler, D. T. Colbert, and R. E. Smalley, "Nanotubes as nanoprobe in scanning probe microscopy," *Nature*, vol. 384, no. 6605, pp. 147–150, 1996.
  - [174] C. W. Zhou, J. Kong, E. Yenilmez, and H. J. Dai, "Modulated chemical doping of individual carbon nanotubes," *Science*, vol. 290, no. 5496, pp. 1552–1555, 2000.
  - [175] M. S. Fuhrer, J. Nygard, L. Shih, M. Forero, Y. G. Yoon, M. S. C. Mazzoni, H. J. Choi, J. Ihm, S. G. Louie, A. Zettl, and P. L. McEuen, "Crossed nanotube junctions," *Science*, vol. 288, no. 5465, pp. 494–497, 2000.
  - [176] Z. Yao, H. W. C. Postma, L. Balents, and C. Dekker, "Carbon nanotube intramolecular junctions," *Nature*, vol. 402, no. 6759, pp. 273–276, 1999.

- [177] J. Cao, W. A. Vitale, and A. M. Ionescu, "Self-assembled nano-electro-mechanical tri-state carbon nanotube switches for reconfigurable integrated circuits," *2012 IEEE MEMS*, 2012.
- [178] J. Choi, J.-I. Lee, Y. Eun, M.-O. Kim, and J. Kim, "Aligned carbon nanotube arrays for degradation-resistant, intimate contact in micromechanical devices," *Advanced Materials*, vol. 23, no. 19, p. 2231, 2011.
- [179] *A 22nm high performance and low-power CMOS technology featuring fully-depleted tri-gate transistors, self-aligned contacts and high density MIM capacitors*, 12-14 June 2012.
- [180] Y. M. Lin, J. Appenzeller, Z. H. Chen, Z. G. Chen, H. M. Cheng, and P. Avouris, "High-performance dual-gate carbon nanotube fets with 40-nm gate length," *IEEE Electron Device Letters*, vol. 26, no. 11, pp. 823–825, 2005.
- [181] A. D. Franklin, M. Luisier, S.-J. Han, G. Tulevski, C. M. Breslin, L. Gignac, M. S. Lundstrom, and W. Haensch, "Sub-10 nm carbon nanotube transistor," *Nano Letters*, vol. 12, no. 2, pp. 758–762, 2012.
- [182] H. R. Byon and H. C. Choi, "Network single-walled carbon nanotube-field effect transistors (SWNTFETs) with increased Schottky contact area for highly sensitive biosensor applications," *Journal of the American Chemical Society*, vol. 128, no. 7, pp. 2188–2189, 2006.
- [183] S. Heinze, J. Tersoff, R. Martel, V. Derycke, J. Appenzeller, and P. Avouris, "Carbon nanotubes as schottky barrier transistors," *Physical Review Letters*, vol. 89, no. 10, p. 106801, 2002.
- [184] J. Cao, Q. Wang, and H. J. Dai, "Electromechanical properties of metallic, quasimetallic, and semiconducting carbon nanotubes under stretching," *Physical Review Letters*, vol. 90, no. 15, pp. 157 601–1–4, 2003.
- [185] Y. R. Lu, S. Bangsaruntip, X. R. Wang, L. Zhang, Y. Nishi, and H. J. Dai, "DNA functionalization of carbon nanotubes for ultrathin atomic layer deposition of high kappa dielectrics for nanotube transistors with 60 mV/decade switching," *Journal of the American Chemical Society*, vol. 128, no. 11, pp. 3518–3519, 2006.
- [186] Y. Zhang and H. J. Dai, "Formation of metal nanowires on suspended single-walled carbon nanotubes," *Applied Physics Letters*, vol. 77, no. 19, pp. 3015–3017, 2000.
- [187] J. J. Cha, M. Weyland, J. F. Briere, I. P. Daykov, T. A. Arias, and D. A. Muller, "Three-dimensional imaging of carbon nanotubes deformed by metal islands," *Nano Letters*, vol. 7, no. 12, pp. 3770–3773, 2007.
- [188] B. R. Burg, personal communication, ETH Zurich, LTNT, 2010.
- [189] A. Javey, J. Guo, D. B. Farmer, Q. Wang, E. Yenilmez, R. G. Gordon, M. Lundstrom, and H. J. Dai, "Self-aligned ballistic molecular transistors and electrically parallel nanotube arrays," *Nano Letters*, vol. 4, no. 7, pp. 1319–1322, 2004.
- [190] X. Wang, Y. Ouyang, X. Li, H. Wang, J. Guo, and H. Dai, "Room-temperature all-semiconducting sub-10-nm graphene nanoribbon field-effect transistors," *Physical Review Letters*, vol. 100, no. 20, p. 206803, 2008.
- [191] M. Sprinkle, M. Ruan, Y. Hu, J. Hankinson, M. Rubio Roy, B. Zhang, X. Wu, C. Berger, and W. A. de Heer, "Scalable templated growth of graphene nanoribbons on sic," *Nature Nanotechnology*, vol. 5, no. 10, pp. 727–731, 2010.
- [192] A. Robert-Peillard and S. V. Rotkin, "Modeling hysteresis phenomena in nanotube field-effect transistors," *IEEE ASSP Magazine Transactions on Nanotechnology*, vol. 4, no. 2, pp. 284–288, 2005.
- [193] A. D. Franklin, G. S. Tulevski, S.-J. Han, D. Shahrjerdi, Q. Cao, H.-Y. Chen, H. S. P. Wong, and W. Haensch, "Variability in carbon nanotube transistors: Improving device-to-device consistency," *ACS Nano*, vol. 6, no. 2, pp. 1109–1115, 2012.
- [194] K. Bradley, J. Cumings, A. Star, J. C. P. Gabriel, and G. Gruner, "Influence of mobile ions on nanotube based FET devices," *Nano Letters*, vol. 3, no. 5, pp. 639–641, 2003.
- [195] G. P. Siddons, D. Merchin, J. H. Back, J. K. Jeong, and M. Shim, "Highly efficient gating and doping of carbon nanotubes with polymer electrolytes," *Nano Letters*, vol. 4, no. 5, pp. 927–931, 2004.
- [196] M. Lin, J. P. Y. Tan, C. Boothroyd, K. P. Loh, E. S. Tok, and Y. L. Foo, "Direct observation of single-walled carbon nanotube growth at the atomistic scale," *Nano Letters*, vol. 6, no. 3, pp. 449–452, 2006.
- [197] M. Mattmann, D. Bechstein, C. Roman, K. Chikkadi, and C. Hierold, "Reduction of gate hysteresis above ambient temperature via ambipolar pulsed gate sweeps in carbon nanotube field effect transistors for sensor applications," *Applied Physics Letters*, vol. 97, no. 15, p. 153103, 2010.
- [198] D. Estrada, S. Dutta, A. Liao, and E. Pop, "Reduction of hysteresis for carbon nanotube mobility measurements using pulsed characterization," *Nanotechnology*, vol. 21, no. 8, p. 085702, 2010.

- [199] T. Hertel, R. E. Walkup, and P. Avouris, "Deformation of carbon nanotubes by surface van der Waals forces," *Physical Review B*, vol. 58, no. 20, pp. 13 870–13 873, 1998.
- [200] H. Maki, T. Sato, and K. Ishibashi, "Direct observation of the deformation and the band gap change from an individual single-walled carbon nanotube under uniaxial strain," *Nano Letters*, vol. 7, no. 4, pp. 890–895, 2007.
- [201] B. Gao, L. Jiang, X. Ling, J. Zhang, and Z. Liu, "Chirality-dependent Raman frequency variation of single-walled carbon nanotubes under uniaxial strain," *The Journal of Physical Chemistry C*, vol. 112, no. 51, pp. 20 123–20 125, 2008.
- [202] M. A. Haque, H. D. Espinosa, and H. J. Lee, "MEMS for in situ testing-handling, actuation, loading, and displacement measurements," *Mrs Bulletin*, vol. 35, no. 5, pp. 375–381, 2010.
- [203] B. Pant, B. L. Allen, T. Zhu, K. Gall, and O. N. Pierron, "A versatile microelectromechanical system for nanomechanical testing," *Applied Physics Letters*, vol. 98, no. 5, pp. 053 506–3, 2011.
- [204] H. D. Espinosa, Y. Zhu, and N. Moldovan, "Design and operation of a MEMS-based material testing system for nanomechanical characterization," *Journal of Microelectromechanical Systems*, vol. 16, no. 5, pp. 1219–1231, 2007.
- [205] Y. Zhu and H. D. Espinosa, "An electromechanical material testing system for in situ electron microscopy and applications," *Proceedings of the National Academy of Sciences of the United States of America*, vol. 102, no. 41, pp. 14 503–14 508, 2005.
- [206] D. Zhang, J. M. Breguet, R. Clavel, V. Sivakov, S. Christiansen, and J. Michler, "In situ electron microscopy mechanical testing of silicon nanowires using electrostatically actuated tensile stages," *Journal of Microelectromechanical Systems*, vol. 19, no. 3, pp. 663–74, 2010.
- [207] Y. Zhang, X. Y. Liu, C. H. Ru, Y. L. Zhang, L. X. Dong, and Y. Sun, "Piezoresistivity characterization of synthetic silicon nanowires using a MEMS device," *Journal of Microelectromechanical Systems*, vol. 20, no. 4, pp. 959–967, 2011.
- [208] J. J. Brown, A. I. Baca, K. A. Bertness, D. A. Dikin, R. S. Ruoff, and V. M. Bright, "Tensile measurement of single crystal gallium nitride nanowires on MEMS test stages," *Sensors and Actuators a-Physical*, vol. 166, no. 2, pp. 177–186, 2011.
- [209] A. B. Hartman, P. Rice, D. S. Finch, G. D. Skidmore, and V. M. Bright, *Force-deflection characterization of individual carbon nanotubes attached to MEMS devices*, ser. IEEE Micro Electro Mechanical Systems Workshop. New York: IEEE, 2004, pp. 426–429.
- [210] S. W. Lee, G.-H. Jeong, and E. E. B. Campbell, "In situ Raman measurements of suspended individual single-walled carbon nanotubes under strain," *Nano Letters*, vol. 7, no. 9, pp. 2590–2595, 2007.
- [211] A. Jungen, L. Durrer, C. Stampfer, and C. Hierold, "Nanoscale straining of individual carbon nanotubes by micromachined transducers," in *Transducers '07 & Eurosensors XXI. 10-14 June, Lyon, France, 2007*. IEEE, 2007, pp. 1561–1564.
- [212] A. Jungen, "Direct integration by synthesis and properties of single-walled carbon nanotubes," Dissertation, Diss. ETH No. 17089, D-MAVT, ETH Zurich, Zurich, Switzerland, Der Andere Verlag, Tönning, Lübeck und Marburg, 2007.
- [213] S. Paulson, M. R. Falvo, N. Snider, A. Helser, T. Hudson, A. Seeger, R. M. Taylor, R. Superfine, and S. Washburn, "In situ resistance measurements of strained carbon nanotubes," *Applied Physics Letters*, vol. 75, no. 19, pp. 2936–2938, 1999.
- [214] S. B. Cronin, A. K. Swan, M. S. Unlu, B. B. Goldberg, M. S. Dresselhaus, and M. Tinkham, "Resonant Raman spectroscopy of individual metallic and semiconducting single-wall carbon nanotubes under uniaxial strain," *Physical Review B (Condensed Matter and Materials Physics)*, vol. 72, no. 3, pp. 35 425–1–8, 2005.
- [215] T. W. Tomblar, C. W. Zhou, L. Alexseyev, J. Kong, H. J. Dai, L. Lei, C. S. Jayanthi, M. J. Tang, and S. Y. Wu, "Reversible electromechanical characteristics of carbon nanotubes under local-probe manipulation," *Nature*, vol. 405, no. 6788, pp. 769–772, 2000.
- [216] A. Maiti, A. Svizhenko, and M. P. Anantram, "Electronic transport through carbon nanotubes: Effects of structural deformation and tube chirality," *Physical Review Letters*, vol. 88, no. 12, p. 126805, 2002.
- [217] T. Cohen-Karni, L. Segev, O. Srur-Lavi, S. R. Cohen, and E. Joselevich, "Torsional electromechanical quantum oscillations in carbon nanotubes," *Nature Nanotechnology*, vol. 1, no. 1, pp. 36–41, 2006.
- [218] R. J. Grow, Q. Wang, J. Cao, D. W. Wang, and H. J. Dai, "Piezoresistance of carbon nanotubes on deformable thin-film membranes," *Applied Physics Letters*, vol. 86, no. 9, p. 3, 2005.
- [219] T. Helbling, "Carbon nanotube field effect transistors as electromechanical transducers," Dissertation, Diss. ETH No. 18823, D-MAVT, ETH Zurich, Zurich, Switzerland, Der Andere Verlag,

- Tønning, Lübeck und Marburg, 2010.
- [220] V. T. Dau, T. Yamada, D. V. Dao, B. T. Tung, K. Hata, and S. Sugiyama, "Integrated cnts thin film for MEMS mechanical sensors," *Microelectronics Journal*, vol. 41, no. 12, pp. 860–864, 2010.
  - [221] C. C. Hsu, R. M. Chao, C. W. Liu, and Y. L. Steven, "Evaluation of the gauge factor for single-walled carbon nanonets on the flexible plastic substrates by nano-transfer-printing," *J. Micromechanics and Microengineering*, vol. 21, no. 7, p. 075012, 2011.
  - [222] L. Dongil, H. Hyun Pyo, L. Myung Jin, P. Chan Won, and M. Nam Ki, "A prototype high sensitivity load cell using single walled carbon nanotube strain gauges," *Sensors and Actuators: A*, vol. 180, pp. 120–126, 2012.
  - [223] Z. Fu-Zhong, Z. Zhao-Ying, Y. Xing, T. Yi-Ke, and W. Ying, "Investigation on strain-sensing suspended single-walled carbon nanotube arrays," *IEEE Transactions on Nanotechnology*, vol. 10, no. 4, pp. 694–698, 2011.
  - [224] C. C. Su, T. Liu, N. K. Chang, B. R. Wang, and S. H. Chang, "Two dimensional carbon nanotube based strain sensor," *Sensors and Actuators A: Physical*, vol. 176, no. 0, pp. 124–129, 2012.
  - [225] T. Yamada, Y. Hayamizu, Y. Yamamoto, Y. Yomogida, A. Izadi-Najafabadi, D. N. Futaba, and K. Hata, "A stretchable carbon nanotube strain sensor for human-motion detection," *Nature Nanotechnology*, vol. 6, no. 5, pp. 296–301, 2011.
  - [226] D. J. Lipomi, M. Vosgueritchian, B. C. K. Tee, S. L. Hellstrom, J. A. Lee, C. H. Fox, and Z. Bao, "Skin-like pressure and strain sensors based on transparent elastic films of carbon nanotubes," *Nature Nanotechnology*, vol. 6, no. 12, pp. 788–792, 2011.
  - [227] H. Zhao, Y. Zhang, P. D. Bradford, Q. Zhou, Q. Jia, F.-G. Yuan, and Y. Zhu, "Carbon nanotube yarn strain sensors," *Nanotechnology*, vol. 21, no. 30, p. 305502, 2010.
  - [228] A. Ya'akobovitz, S. Krylov, and Y. Hanein, "A mems nano-extensometer with integrated de-amplification mechanism," *Microsystem Technologies-Micro-and Nanosystems-Information Storage and Processing Systems*, vol. 17, no. 3, pp. 337–345, 2011.
  - [229] T. Helbling, C. Roman, and C. Hierold, "Signal-to-noise ratio in carbon nanotube electromechanical piezoresistive sensors," *Nano Letters*, vol. 10, no. 9, pp. 3350–3354, 2010.
  - [230] M. A. Cullinan and M. L. Culpepper, "Carbon nanotubes as piezoresistive microelectromechanical sensors: Theory and experiment," *Physical Review B*, vol. 82, p. 115428, 2010.
  - [231] B. Chandra, R. Caldwell, M. Huang, L. M. Huang, M. Y. Sfeir, S. P. O'Brien, T. F. Heinz, and J. Hone, "Electrical transport measurements of nanotubes with known (n, m) indices," *Physica Status Solidi B*, vol. 243, no. 13, pp. 3359–3364, 2006.
  - [232] T. Kim, G. Kim, W. I. Choi, Y.-K. Kwon, and J.-M. Zuo, "Electrical transport in small bundles of single-walled carbon nanotubes: Intertube interaction and effects of tube deformation," *Applied Physics Letters*, vol. 96, no. 17, p. 173107, 2010.
  - [233] R. F. Egerton, P. Li, and M. Malac, "Radiation damage in the TEM and SEM," *Micron*, vol. 35, no. 6, pp. 399–409, 2004.
  - [234] K. Liu, W. Wang, Z. Xu, X. Bai, E. Wang, Y. Yao, J. Zhang, and Z. Liu, "Chirality-dependent transport properties of double-walled nanotubes measured in situ on their field-effect transistors," *Journal of the American Chemical Society*, vol. 131, no. 1, pp. 62–63, 2009.
  - [235] D. Golberg, P. Costa, M. S. Wang, X. L. Wei, D. M. Tang, Z. Xu, Y. Huang, U. K. Gautam, B. D. Liu, H. B. Zeng, N. Kawamoto, C. Y. Zhi, M. Mitome, and Y. Bando, "Nanomaterial engineering and property studies in a transmission electron microscope," *Advanced Materials*, vol. 24, no. 2, pp. 177–194, 2012.
  - [236] J. Zhao and J. Zhu, "Electron microscopy and in situ testing of mechanical deformation of carbon nanotubes," *Micron*, vol. 42, no. 7, pp. 663–79, 2011.
  - [237] S. Schürle, M. K. Tiwari, K. Shou, D. Poulidakos, and B. J. Nelson, "Fabricating devices with dielectrophoretically assembled, suspended single walled carbon nanotubes for improved nanoelectronic device characterization," *Microelectronic Engineering*, vol. 88, no. 8, pp. 2740–2743, 2011.
  - [238] M. Kociak, K. Suenaga, K. Hirahara, Y. Saito, T. Nakahira, and S. Iijima, "Linking chiral indices and transport properties of double-walled carbon nanotubes," *Physical Review Letters*, vol. 89, no. 15, pp. 155501–1–4, 2002.
  - [239] Y. Lu, C. Peng, Y. Ganesan, J. Y. Huang, and J. Lou, "Quantitative in situ TEM tensile testing of an individual nickel nanowire," *Nanotechnology*, vol. 22, no. 35, p. 355702, 2011.
  - [240] M. A. Haque and M. T. A. Saif, "Application of mems force sensors for in situ mechanical characterization of nano-scale thin films in SEM and TEM," *Sensors and Actuators A: Physical*, vol. 97-98, pp. 239–245, 2002.

- [241] Y. Choi and A. Ural, "Micromachined silicon grids for direct TEM and Raman characterization of CVD grown carbon nanotubes," *Proceedings of the SPIE - The International Society for Optical Engineering*, vol. 6464, pp. 6464A 1–5, 2007.
- [242] D. Takagi, Y. Homma, and Y. Kobayashi, "Selective growth of individual single-walled carbon nanotubes suspended between pillar structures," *Physica E: Low-dimensional Systems and Nanostructures*, vol. 24, no. 1–2, pp. 1–5, 2004.
- [243] S. Gray and W. P.K., "Production of fine patterns by evaporation," *RCA Review*, vol. 20, pp. 413–425, 1959.
- [244] J. Arcamone, A. Sanchez-Amores, J. Montserrat, M. A. F. van den Boogaart, J. Brugger, and F. Perez-Murano, "Dry etching for the correction of gap-induced blurring and improved pattern resolution in nanostencil lithography," *Journal of Micro-Nanolithography MEMS and MOEMS*, vol. 6, no. 1, p. 013005, 2007.
- [245] K. Sidler, G. Villanueva, O. Vazquez-Mena, and J. Brugger, "Minimized blurring in stencil lithography using a compliant membrane," in *Solid-State Sensors, Actuators and Microsystems Conference, 2009. Transducers, 2009*, pp. 1612–1615.
- [246] O. Vazquez-Mena, L. G. Villanueva, V. Savu, K. Sidler, P. Langlet, and J. Brugger, "Analysis of the blurring in stencil lithography," *Nanotechnology*, vol. 20, no. 41, p. 415303, 2009.
- [247] J. Köhler, M. Albrecht, C. R. Musil, and E. Bucher, "Direct growth of nanostructures by deposition through an  $\text{Si}_3\text{N}_4$  shadow mask," *Physica E*, vol. 4, no. 3, pp. 196–200, 1999.
- [248] M. van den Boogaart, "Stencil lithography: An ancient technique for advanced micro and nanopatterning," Ph.D. dissertation, Thesis No. 3598, EPFL Lausanne, Switzerland, 2006.
- [249] O. Vazquez-Mena, K. Sidler, V. Savu, P. Chan Woo, L. Guillermo Villanueva, and J. Brugger, "Reliable and improved nanoscale stencil lithography by membrane stabilization, blurring, and clogging corrections," *Nanotechnology, IEEE Transactions on*, vol. 10, no. 2, pp. 352–357, 2011.
- [250] M. Lishchynska, V. Bourenkov, M. A. F. van den Boogaart, L. Doeswijk, J. Brugger, and J. C. Greer, "Predicting mask distortion, clogging and pattern transfer for stencil lithography," *Microelectronic Engineering*, vol. 84, no. 1, pp. 42–53, 2007.
- [251] J. Arcamone, M. A. F. van den Boogaart, F. Serra-Graells, J. Fraxedas, J. Brugger, and F. Perez-Murano, "Full-wafer fabrication by nanostencil lithography of micro/nanomechanical mass sensors monolithically integrated with cmos," *Nanotechnology*, vol. 19, no. 30, p. 305302, 2008.
- [252] A. Cowen, G. Hames, M. DeMaul, S. Wilcenski, and B. H., "SOIMUMPs design handbook - a MUMPs® process, rev. 8.0," *MEMSCAP Inc.*, vol. 8, pp. SOIMUMPs, Reference Material, SOIMUMPs Design Rules, 2011.
- [253] J. Brugger, C. Andreoli, M. Despont, U. Drechsler, H. Rothuizen, and P. Vettiger, "Self-aligned 3D shadow mask technique for patterning deeply recessed surfaces of micro-electromechanical systems devices," *Sensors and Actuators a-Physical*, vol. 76, no. 1–3, pp. 329–334, 1999.
- [254] J. Brugger, J. W. Berenschot, S. Kuiper, W. Nijdam, B. Otter, and M. Elwenspoek, "Resistless patterning of sub-micron structures by evaporation through nanostencils," *Microelectronic Engineering*, vol. 53, no. 1–4, pp. 403–405, 2000.
- [255] G. J. Burger, E. J. T. Smulders, J. W. Berenschot, T. S. J. Lammerink, J. H. J. Fluitman, and S. Imai, "High-resolution shadow-mask patterning in deep holes and its application to an electrical wafer feed-through," *Sensors and Actuators a-Physical*, vol. 54, no. 1–3, pp. 669–673, 1996.
- [256] J. Köhler, J. hler, M. Albrecht, C. R. Musil, and E. Bucher, "Direct growth of nanostructures by deposition through an  $\text{Si}_3\text{N}_4$  shadow mask," *Physica E: Low-dimensional Systems and Nanostructures*, vol. 4, no. 3, pp. 196–200, 1999.
- [257] C. W. Park, O. V. Mena, M. A. F. van den Boogaart, and J. Brugger, "Reverse transfer of nanostencil patterns using intermediate sacrificial layer and lift-off process," *Journal of Vacuum Science & Technology B*, vol. 24, no. 6, pp. 2772–5, 2006.
- [258] Y. Homma, Y. Kobayashi, T. Ogino, D. Takagi, R. Ito, Y. J. Jung, and P. M. Ajayan, "Role of transition metal catalysts in single-walled carbon nanotube growth in chemical vapor deposition," *Journal of Physical Chemistry B*, vol. 107, no. 44, pp. 12 161–12 164, 2003.
- [259] J. M. Simmons, B. M. Nichols, M. S. Marcus, O. M. Castellini, R. J. Hamers, and M. A. Eriksson, "Critical oxide thickness for efficient single-walled carbon nanotube growth on silicon using thin  $\text{SiO}_2$  diffusion barriers," *Small*, vol. 2, no. 7, pp. 902–909, 2006.
- [260] Y. Li, W. Kim, Y. Zhang, M. Rolandi, D. Wang, and H. Dai, "Growth of single-walled carbon nanotubes from discrete catalytic nanoparticles of various sizes," *The Journal of Physical Chemistry B*, vol. 105, no. 46, pp. 11 424–11 431, 2001.
- [261] D. M. Lawson, P. J. Artymiuk, S. J. Yewdall, J. M. A. Smith, J. C. Livingstone, A. Treffry, A. Luzzago, S. Levi, P. Arosio, G. Cesareni, C. D. Thomas, W. V. Shaw, and P. M. Harrison,

- "Solving the structure of human h ferritin by genetically engineering intermolecular crystal contacts," *Nature*, vol. 349, no. 6309, pp. 541–544, 1991.
- [262] K. Chikkadi, M. Mattmann, M. Muoth, L. Durrer, and C. Hierold, "The role of pH in the density control of ferritin-based catalyst nanoparticles towards scalable single-walled carbon nanotube growth," *Microelectronic Engineering*, vol. 88, no. 8, pp. 2478–2480, 2011.
- [263] L. Durrer, J. Greenwald, T. Helbling, M. Muoth, R. Riek, and C. Hierold, "Narrowing SWNT diameter distribution using size-separated ferritin-based Fe catalysts," *Nanotechnology*, vol. 20, no. 35, pp. 355 601–355 607, 2009.
- [264] A. Jungen, C. Stampfer, L. Durrer, T. Helbling, and C. Hierold, "A method for enhanced analysis of specific as-grown carbon nanotubes," *Physica Status Solidi B*, vol. 243, no. 13, pp. 3138–3141, 2006.
- [265] N. R. Franklin and H. J. Dai, "An enhanced CVD approach to extensive nanotube networks with directionality," *Advanced Materials*, vol. 12, no. 12, pp. 890–894, 2000.
- [266] Y. Homma, Y. Kobayashi, T. Ogino, and T. Yamashita, "Growth of suspended carbon nanotube networks on 100-nm-scale silicon pillars," *Applied Physics Letters*, vol. 81, no. 12, pp. 2261–2263, 2002.
- [267] Y. Homma, D. Takagi, and Y. Kobayashi, "Suspended architecture formation process of single-walled carbon nanotubes," *Applied Physics Letters*, vol. 88, no. 2, p. 023115, 2006.
- [268] S. Pisana, A. Jungen, C. Zhang, A. M. Blackburn, R. Sharma, F. Cervantes-Sodi, C. Stampfer, C. Ducati, A. C. Ferrari, C. Hierold, J. Robertson, and S. Hofmann, "Flying and crawling modes during surface-bound single wall carbon nanotube growth," *Journal of Physical Chemistry C*, vol. 111, pp. 17 249–17 253, 2007.
- [269] A. Jungen, L. Durrer, C. Stampfer, C. Roman, and C. Hierold, "Progress in carbon nanotube based nanoelectromechanical systems synthesis," *Physica Status Solidi B*, vol. 244, pp. 4323–4326, 2007.
- [270] A. Witvrouw, "Cmos-mems integration today and tomorrow," *Scripta Materialia*, vol. 59, no. 9, pp. 945–949, 2008.
- [271] H. Takeuchi, A. Wung, X. Sun, R. T. Howe, and T. J. King, "Thermal budget limits of quarter-micrometer foundry CMOS for post-processing mems devices," *IEEE Transactions on Electron Devices*, vol. 52, no. 9, pp. 2081–2086, 2005.
- [272] Y. C. Tseng, P. Q. Xuan, A. Javey, R. Malloy, Q. Wang, J. Bokor, and H. J. Dai, "Monolithic integration of carbon nanotube devices with silicon mos technology," *Nano Letters*, vol. 4, no. 1, pp. 123–127, 2004.
- [273] Z. R. Abrams and Y. Hanein, "Tube-tube and tube-surface interactions in straight suspended carbon nanotube structures," *Journal of Physical Chemistry B*, vol. 110, no. 43, pp. 21 419–21 423, 2006.
- [274] A. Kemelbay, *Raman shifts in suspended carbon nanotube FETs strained by microactuators*, semester Thesis, supervisors: M. Muoth, Prof. C. Hierold, ETH Zurich, D-MAVT, Micro and Nanosystems, Zurich, Switzerland, 2012.
- [275] A. Jungen, C. Meder, M. Tonteling, C. Stampfer, R. Linderman, and C. Hierold, "A MEMS actuator for integrated carbon nanotube strain sensing," in *4th IEEE Conference on Sensors Oct 31 - Nov 03, Irvine, CA, 2005*, pp. 93–96.
- [276] S.-A. Pohl, "Characterisation of single-walled carbon nanotubes by Raman spectroscopy and AFM - correlative study of single-walled carbon nanotube diameter determination and monitoring defects induced by metallization processes," Master's thesis, ETH Zurich, D-MAVT, Micro and Nanosystems, Zurich, Switzerland, 2008.
- [277] Y. Homma, D. Takagi, S. Suzuki, K.-i. Kanzaki, and Y. Kobayashi, "Electron-microscopic imaging of single-walled carbon nanotubes grown on silicon and silicon oxide substrates," *Journal of Electron Microscopy*, vol. 54, no. suppl 1, pp. i3–i7, 2005.
- [278] C.-H. Weng, C.-K. Wu, C.-H. Tsai, and K.-C. Leou, "Electromechanical analysis of single-walled carbon nanotubes suspended across carbon nanofiber templates using scanning electron microscopy," *Carbon*, vol. 47, no. 11, pp. 2655–2661, 2009.
- [279] M. Mattmann, T. Helbling, L. Durrer, C. Roman, C. Hierold, R. Pohle, and M. Fleischer, "Sub-ppm NO<sub>2</sub> detection by Al<sub>2</sub>O<sub>3</sub> contact passivated carbon nanotube field effect transistors," *Applied Physics Letters*, vol. 94, no. 18, pp. 183 502–3, 2009.
- [280] M. D. Groner, S. M. George, R. S. McLean, and P. F. Garcia, "Gas diffusion barriers on polymers using Al<sub>2</sub>O<sub>3</sub> atomic layer deposition," *Applied Physics Letters*, vol. 88, no. 5, p. 051907, 2006.
- [281] M. D. Groner, F. H. Fabreguette, J. W. Elam, and S. M. George, "Low-temperature Al<sub>2</sub>O<sub>3</sub> atomic layer deposition," *Chemistry of Materials*, vol. 16, no. 4, pp. 639–645, 2004.

- [282] D. B. Farmer and R. G. Gordon, "ALD of high-kappa dielectrics on suspended functionalized SWNTs," *Electrochemical and Solid State Letters*, vol. 8, no. 4, pp. G89–G91, 2005.
- [283] C. F. Herrmann, F. H. Fabreguette, D. S. Finch, R. Geiss, and S. M. George, "Multilayer and functional coatings on carbon nanotubes using atomic layer deposition," *Applied Physics Letters*, vol. 87, no. 12, p. 123110, 2005.
- [284] A. Javey, H. Kim, M. Brink, Q. Wang, A. Ural, J. Guo, P. McIntyre, P. McEuen, M. Lundstrom, and H. J. Dai, "High-kappa dielectrics for advanced carbon-nanotube transistors and logic gates," *Nature Materials*, vol. 1, no. 4, pp. 241–246, 2002.
- [285] M. Muoth, T. Helbling, L. Durrer, S. W. Lee, C. Roman, and C. Hierold, "Supplementary information to: Hysteresis-free operation of suspended carbon nanotube transistors," *Nature Nanotechnology*, vol. 5, no. 8, pp. 589–592, 2010.
- [286] M. Muoth, F. Gramm, K. Asaka, L. Durrer, T. Helbling, C. Roman, S. W. Lee, and C. Hierold, "Tilted-view transmission electron microscopy-access for chirality assignment to carbon nanotubes integrated in MEMS," *Procedia Chemistry*, vol. 1, no. 1, pp. 601–604, 2009.
- [287] Z. J. Liu and L. C. Qin, "A direct method to determine the chiral indices of carbon nanotubes," *Chemical Physics Letters*, vol. 408, no. 1-3, pp. 75–79, 2005.
- [288] A. Jungen, V. N. Popov, C. Stampfer, L. Durrer, S. Stoll, and C. Hierold, "Raman intensity mapping of single-walled carbon nanotubes," *Physical Review B*, vol. 75, no. 4, p. 041405(R), 2007.
- [289] S. M. Bachilo, M. S. Strano, C. Kittrell, R. H. Hauge, R. E. Smalley, and R. B. Weisman, "Structure-assigned optical spectra of single-walled carbon nanotubes," *Science*, vol. 298, no. 5602, pp. 2361–2366, 2002.
- [290] J. C. Meyer, M. Paillet, T. Michel, A. Moréac, A. Neumann, G. S. Duesberg, S. Roth, and J.-L. Sauvajol, "Raman modes of index-identified freestanding single-walled carbon nanotubes," *Physical Review Letters*, vol. 95, no. 21, p. 217401, 2005.
- [291] B. W. Smith and D. E. Luzzi, "Electron irradiation effects in single wall carbon nanotubes," *Journal of Applied Physics*, vol. 90, no. 7, pp. 3509–3515, 2001.
- [292] J. H. Warner, F. Schäffel, G. Zhong, M. H. Rummeli, B. Büchner, J. Robertson, and G. A. D. Briggs, "Investigating the diameter-dependent stability of single-walled carbon nanotubes," *ACS Nano*, vol. 3, no. 6, pp. 1557–1563, 2009.
- [293] A. Maiti and A. Ricca, "Metal-nanotube interactions - binding energies and wetting properties," *Chemical Physics Letters*, vol. 395, no. 1-3, pp. 7–11, 2004.
- [294] F. E. Jones, A. A. Talin, F. Leonard, P. M. Dentinger, and W. M. Clift, "Effect of electrode material on transport and chemical sensing characteristics of metal/carbon nanotube contacts," *Journal of Electronic Materials*, vol. 35, no. 8, pp. 1641–1646, 2006.
- [295] L. F. Dong, S. Youkey, J. Bush, J. Jiao, V. M. Dubin, and R. V. Chebiam, "Effects of local joule heating on the reduction of contact resistance between carbon nanotubes and metal electrodes," *Journal of Applied Physics*, vol. 101, p. 024320, 2007.
- [296] H. Jiang, A. G. Nasibulin, D. P. Brown, and E. I. Kauppinen, "Unambiguous atomic structural determination of single-walled carbon nanotubes by electron diffraction," *Carbon*, vol. 45, no. 3, pp. 662–667, 2007.
- [297] E. Pop, D. Mann, J. Cao, Q. Wang, K. Goodson, and H. J. Dai, "Negative differential conductance and hot phonons in suspended nanotube molecular wires," *Physical Review Letters*, vol. 95, no. 15, p. 155505, 2005.
- [298] M. P. P. Mattmann, "Carbon nanotube field effect transistors with Al<sub>2</sub>O<sub>3</sub> passivated metal contacts as NO<sub>2</sub> gas sensors," Dissertation for the degree of Doctor of Sciences, Diss. ETH No. 19724, D-MAVT, ETH Zurich, Zurich, Switzerland, Der Andere Verlag, Tönning, Lübeck und Marburg, 2011.
- [299] K. Chikkadi, M. Muoth, and C. Hierold, "Hysteresis-free, suspended pristine carbon nanotube gas sensors," in *Transducers 2013, accepted*, 2013.
- [300] X. Deng, T. Herranz, C. Weis, H. Bluhm, and M. Salmeron, "Adsorption of water on Cu<sub>2</sub>O and Al<sub>2</sub>O<sub>3</sub> thin films," *Journal of Physical Chemistry C*, vol. 112, no. 26, pp. 9668–9672, 2008.
- [301] S. Kar, A. Vijayaraghavan, C. Soldano, S. Talapatra, R. Vajtai, O. Nalamasu, and P. M. Ajayan, "Quantitative analysis of hysteresis in carbon nanotube field-effect devices," *Applied Physics Letters*, vol. 89, no. 13, pp. 132118–3, 2006.
- [302] M. S. Fuhrer, B. M. Kim, T. Durkop, and T. Brintlinger, "High-mobility nanotube transistor memory," *Nano Letters*, vol. 2, no. 7, pp. 755–759, 2002.
- [303] M. D. Groner, J. W. Elam, F. H. Fabreguette, and S. M. George, "Electrical characterization of thin Al<sub>2</sub>O<sub>3</sub> films grown by atomic layer deposition on silicon and various metal substrates,"



- Thin Solid Films*, vol. 413, no. 1-2, pp. 186–197, 2002.
- [304] K. Chikkadi, M. Politou, M. Cagin, O. Kurapova, M. Döbeli, and C. Hierold, “Investigations on passivation layers for carbon nanotube transistors for sensing applications,” in *IEEE NEMS, Kyoto, Japan, March 6*, 2012.
  - [305] V. Derycke, R. Martel, J. Appenzeller, and P. Avouris, “Controlling doping and carrier injection in carbon nanotube transistors,” *Applied Physics Letters*, vol. 80, no. 15, pp. 2773–2775, 2002.
  - [306] M. Muoth, C. K., L. Y., and H. C., “Suspended CNT-FET piezoresistive strain gauges: Chirality assignment and quantitative analysis,” *IEEE MEMS 2013, Taipei*, vol. 1, pp. 496–499, 2013.
  - [307] J. Grimm, *Raman spectroscopy on strained single-walled carbon nanotubes*, semester Thesis, supervisors: K. Ensslin, M. Muoth, C. Hierold, ETH Zurich, D-MAVT, Micro and Nanosystems, Zurich, Switzerland, 2010.
  - [308] G. Wu, J. Zhou, and J. M. Dong, “Raman modes of the deformed single-wall carbon nanotubes,” *Physical Review B*, vol. 72, no. 11, p. 115411, 2005.
  - [309] H. Son, G. G. Samsonidze, J. Kong, Y. Zhang, X. Duan, J. Zhang, Z. Liu, and M. S. Dresselhaus, “Strain and friction induced by van der Waals interaction in individual single walled carbon nanotubes,” *Applied Physics Letters*, vol. 90, no. 25, p. 253113, 2007.
  - [310] K. Hirahara, M. Kociak, S. Bandow, T. Nakahira, K. Itoh, Y. Saito, and S. Iijima, “Chirality correlation in double-wall carbon nanotubes as studied by electron diffraction,” *Physical Review B*, vol. 73, no. 19, p. 195420, 2006.
  - [311] L. Yang and J. Han, “Electronic structure of deformed carbon nanotubes,” *Physical Review Letters*, vol. 85, no. 1, pp. 154–157, 2000.
  - [312] A. Walther, M. Savoye, G. Jourdan, P. Renaux, F. Souchon, P. Robert, C. Le Blanc, N. Delorme, O. Gigan, and C. Lejoste, “3-axis gyroscope with si nanogage piezo-resistive detection,” in *IEEE MEMS 2012, Paris Jan 29 - Feb 2*, 2012.
  - [313] C. Buzea, I. I. Pacheco, and K. Robbie, “Nanomaterials and nanoparticles: Sources and toxicity,” *Biointerphases*, vol. 2, no. 4, pp. MR17–MR71, 2007.
  - [314] M. B. Nardelli, B. I. Yakobson, and J. Bernholc, “Mechanism of strain release in carbon nanotubes,” *Physical Review B*, vol. 57, no. 8, pp. R4277–R4280, 1998.
  - [315] Q. Z. Zhao, M. B. Nardelli, and J. Bernholc, “Ultimate strength of carbon nanotubes: A theoretical study,” *Physical Review B*, vol. 65, no. 14, p. 144105, 2002.
  - [316] D. A. Walters, L. M. Ericson, M. J. Casavant, J. Liu, D. T. Colbert, K. A. Smith, and R. E. Smalley, “Elastic strain of freely suspended single-wall carbon nanotube ropes,” *Applied Physics Letters*, vol. 74, no. 25, pp. 3803–3805, 1999.
  - [317] D. H. Robertson, D. W. Brenner, and J. W. Mintmire, “Energetics of nanoscale graphitic tubules,” *Physical Review B*, vol. 45, no. 21, pp. 12 592–12 595, 1992.
  - [318] H. Mori, Y. Hirai, S. Ogata, S. Akita, and Y. Nakayama, “Chirality dependence of mechanical properties of single-walled carbon nanotubes under axial tensile strain,” *Japanese Journal of Applied Physics Part 2*, vol. 44, no. 42-45, pp. L1307–L1309, 2005.
  - [319] S. Iijima, C. Brabec, A. Maiti, and J. Bernholc, “Structural flexibility of carbon nanotubes,” *The Journal of Chemical Physics*, vol. 104, no. 5, pp. 2089–2092, 1996.
  - [320] R. Kumar and S. B. Cronin, “Raman scattering of carbon nanotube bundles under axial strain and strain-induced debundling,” *Physical Review B*, vol. 75, no. 15, p. 155421, 2007.
  - [321] P. R. Wallace, “The band theory of graphite,” *Physical Review*, vol. 71, no. 9, pp. 622–634, 1947.
  - [322] C. L. Kane and E. J. Mele, “Size, shape, and low energy electronic structure of carbon nanotubes,” *Physical Review Letters*, vol. 78, no. 10, pp. 1932–1935, 1997.
  - [323] A. Kleiner and S. Eggert, “Band gaps of primary metallic carbon nanotubes,” *Physical Review B*, vol. 63, no. 7, p. 073408, 2001.
  - [324] Z. Yao, C. L. Kane, and C. Dekker, “High-field electrical transport in single-wall carbon nanotubes,” *Physical Review Letters*, vol. 84, no. 13, pp. 2941–2944, 2000.
  - [325] F. Leonard and A. A. Talin, “Electrical contacts to one- and two-dimensional nanomaterials,” *Nature Nanotechnology*, vol. 6, no. 12, pp. 773–783, 2011.
  - [326] F. Leonard and J. Tersoff, “Role of fermi-level pinning in nanotube Schottky diodes,” *Physical Review Letters*, vol. 84, no. 20, pp. 4693–4696, 2000.
  - [327] S. Suzuki, C. Bower, Y. Watanabe, and O. Zhou, “Work functions and valence band states of pristine and cs-intercalated single-walled carbon nanotube bundles,” *Applied Physics Letters*, vol. 76, no. 26, pp. 4007–4009, 2000.
  - [328] Y. Nosho, Y. Ohno, S. Kishimoto, and T. Mizutani, “Relation between conduction property

- and work function of contact metal in carbon nanotube field-effect transistors," *Nanotechnology*, vol. 17, no. 14, pp. 3412–3415, 2006.
- [329] C.-K. Yang, J. Zhao, and J. P. Lu, "Binding energies and electronic structures of adsorbed titanium chains on carbon nanotubes," *Physical Review B*, vol. 66, no. 4, p. 041403, 2002.
- [330] J. J. Palacios, A. J. Pérez-Jiménez, E. Louis, E. SanFabian, and J. A. Vergés, "First-principles phase-coherent transport in metallic nanotubes with realistic contacts," *Physical Review Letters*, vol. 90, no. 10, p. 106801, 2003.
- [331] N. Nemec, D. Tomanek, and G. Cuniberti, "Contact dependence of carrier injection in carbon nanotubes: An ab initio study," *Physical Review Letters*, vol. 96, no. 7, p. 076802, 2006.
- [332] V. Vitale, A. Curioni, and W. Andreoni, "Metal-carbon nanotube contacts: The link between schottky barrier and chemical bonding," *Journal of the American Chemical Society*, vol. 130, no. 18, pp. 5848–5849, 2008.
- [333] Y. Yaish, J. Y. Park, S. Rosenblatt, V. Sazonova, M. Brink, and P. L. McEuen, "Electrical nanoprobing of semiconducting carbon nanotubes using an atomic force microscope," *Physical Review Letters*, vol. 92, no. 4, pp. 046401–4, 2004.
- [334] J. Y. Chen, A. Kutana, C. P. Collier, and K. P. Giapis, "Electrowetting in carbon nanotubes," *Science*, vol. 310, no. 5753, pp. 1480–1483, 2005.
- [335] J. Appenzeller, Y. M. Lin, J. Knoch, Z. H. Chen, and P. Avouris, "Comparing carbon nanotube transistors - the ideal choice: A novel tunneling device design," *Ieee Transactions on Electron Devices*, vol. 52, no. 12, pp. 2568–2576, 2005.
- [336] X. Zhou, J.-Y. Park, S. Huang, J. Liu, and P. L. McEuen, "Band structure, phonon scattering, and the performance limit of single-walled carbon nanotube transistors," *Physical Review Letters*, vol. 95, no. 14, p. 146805, 2005.
- [337] R. Heyd, A. Charlier, and E. McRae, "Uniaxial-stress effects on the electronic properties of carbon nanotubes," *Physical Review B*, vol. 55, no. 11, pp. 6820–6824, 1997.
- [338] W. A. Harrison, *Electronic Structure and the Properties of Solids - The Physics of the Chemical Bond*. San Francisco: Freeman and Company, 1980.
- [339] G. Y. Guo, L. Liu, K. C. Chu, C. S. Jayanthi, and S. Y. Wu, "Electromechanical responses of single-walled carbon nanotubes: Interplay between the strain-induced energy-gap opening and the pinning of the fermi level," *Journal of Applied Physics*, vol. 98, no. 4, p. 4, 2005.
- [340] P. K. Valavala, D. Banyai, M. Seel, and R. Pati, "Self-consistent calculations of strain-induced band gap changes in semiconducting (n,0) carbon nanotubes," *Physical Review B*, vol. 78, no. 23, p. 235430, 2008.
- [341] L. F. Chibotaru, S. A. Bovin, and A. Ceulemans, "Bend-induced insulating gap in carbon nanotubes," *Physical Review B*, vol. 66, no. 16, p. 161401, 2002.
- [342] K. Hirahara, S. Bandow, H. Kataura, M. Kociak, and S. Iijima, "Stretching of carbon-carbon bonds in a 0.7 nm diameter carbon nanotube studied by electron diffraction," *Physical Review B*, vol. 70, no. 20, p. 205422, 2004.
- [343] C. J. Park, Y. H. Kim, and K. J. Chang, "Band-gap modification by radial deformation in carbon nanotubes," *Physical Review B*, vol. 60, no. 15, pp. 10656–10659, 1999.
- [344] H. Mehrez, A. Svizhenko, M. P. Anantram, M. Elstner, and T. Frauenheim, "Analysis of band-gap formation in squashed armchair carbon nanotubes," *Physical Review B*, vol. 71, no. 15, p. 155421, 2005.
- [345] C. Gomez-Navarro, P. J. de Pablo, and J. Gomez-Herrero, "Radial electromechanical properties of carbon nanotubes," *Advanced Materials*, vol. 16, no. 6, pp. 549–552, 2004.
- [346] T. DeBorde, J. C. Joiner, M. R. Leyden, and E. D. Minot, "Identifying individual single-walled and double-walled carbon nanotubes by atomic force microscopy," *Nano Letters*, vol. 8, no. 11, pp. 3568–3571, 2008.
- [347] Y. Y. Jiang, W. Zhou, T. Kim, Y. Huang, and J. M. Zuo, "Measurement of radial deformation of single-wall carbon nanotubes induced by intertube van der Waals forces," *Physical Review B*, vol. 77, no. 15, pp. 153405–1–4, 2008.
- [348] D. Y. Joh, L. H. Herman, S.-Y. Ju, J. Kinder, M. A. Segal, J. N. Johnson, G. K. L. Chan, and J. Park, "On-chip rayleigh imaging and spectroscopy of carbon nanotubes," *Nano Letters*, vol. 11, no. 1, pp. 1–7, 2011.
- [349] Y. Yoon and J. Guo, "Analysis of strain effects in ballistic carbon nanotube FETs," *Ieee Transactions on Electron Devices*, vol. 54, no. 6, pp. 1280–1287, 2007.
- [350] D. B. Williams and C. B. Carter, *Transmission electron microscopy - A textbook for materials science*. Springer, 2009.

- [351] R. Erni, *Aberration-Corrected Imaging in Transmission Electron Microscopy: An Introduction*. London: Imperial College Press, 2010.
- [352] M. Haider, S. Uhlemann, E. Schwan, H. Rose, B. Kabius, and K. Urban, "Electron microscopy image enhanced," *Nature*, vol. 392, no. 6678, pp. 768–769, 1998.
- [353] C. Qin and L. M. Peng, "Measurement accuracy of the diameter of a carbon nanotube from TEM images," *Physical Review B*, vol. 65, no. 15, p. 155431, 2002.
- [354] H. Jiang, J. Ruokolainen, N. Young, T. Oikawa, A. G. Nasibulin, A. Kirkland, and E. I. Kauppinen, "Performance and early applications of a versatile double aberration-corrected JEOL-2200FS FEG TEM/STEM at aalto university," *Micron*, vol. 43, no. 4, pp. 545–550, 2012.
- [355] D. Golberg, Y. Bando, L. Bourgeois, and K. Kurashima, "Atomic resolution of single-walled carbon nanotubes using a field emission high-resolution transmission electron microscope," *Carbon*, vol. 37, no. 11, pp. 1858–1860, 1999.
- [356] Y. Sato, K. Yanagi, Y. Miyata, K. Suenaga, H. Kataura, and S. Iijima, "Chiral-angle distribution for separated single-walled carbon nanotubes," *Nano Letters*, vol. 8, no. 10, pp. 3151–3154, 2008.
- [357] A. Hashimoto, K. Suenaga, A. Gloter, K. Urita, and S. Iijima, "Direct evidence for atomic defects in graphene layers," *Nature*, vol. 430, no. 7002, pp. 870–873, 2004.
- [358] K. Suenaga, H. Wakabayashi, M. Koshino, Y. Sato, K. Urita, and S. Iijima, "Imaging active topological defects in carbon nanotubes," *Nature Nanotechnology*, vol. 2, no. 6, pp. 358–360, 2007.
- [359] R. R. Meyer, S. Friedrichs, A. I. Kirkland, J. Sloan, J. L. Hutchison, and M. L. H. Green, "A composite method for the determination of the chirality of single walled carbon nanotubes," *Journal of Microscopy*, vol. 212, no. 2, pp. 152–157, 2003.
- [360] U. Kaiser, J. Biskupek, J. C. Meyer, J. Leschner, L. Lechner, H. Rose, M. Stoger-Pollach, A. N. Khlobystov, P. Hartel, H. Muller, M. Haider, S. Eyhusen, and G. Benner, "Transmission electron microscopy at 20 kV for imaging and spectroscopy," *Ultramicroscopy*, vol. 111, no. 8, pp. 1239–1246, 2011.
- [361] L.-C. Qin, "Electron diffraction from carbon nanotubes," *Reports on Progress in Physics*, vol. 69, no. 10, p. 2761, 2006.
- [362] Y. X. Qin, M. Hu, H. Y. Li, Z. S. Zhang, and Q. Zou, "Preparation and field emission properties of carbon nanotubes cold cathode using melting ag nano-particles as binder," *Applied Surface Science*, vol. 253, no. 8, pp. 4021–4024, 2007.
- [363] J. C. Meyer, A. K. Geim, M. I. Katsnelson, K. S. Novoselov, T. J. Booth, and S. Roth, "The structure of suspended graphene sheets," *Nature*, vol. 446, no. 7131, pp. 60–63, 2007.
- [364] L. C. Qin, T. Ichihashi, and S. Iijima, "On the measurement of helicity of carbon nanotubes," *Ultramicroscopy*, vol. 67, no. 1-4, pp. 181–189, 1997.
- [365] M. Gao, J. M. Zuo, R. D. Twisten, I. Petrov, L. A. Nagahara, and R. Zhang, "Structure determination of individual single-wall carbon nanotubes by nanoarea electron diffraction," *Applied Physics Letters*, vol. 82, no. 16, pp. 2703–2705, 2003.
- [366] J. F. Colomer, L. Henrard, P. Launois, G. Van Tendeloo, A. A. Lucas, and P. Lambin, "Interpretation of electron diffraction from carbon nanotube bundles presenting precise helicity," *Physical Review B*, vol. 70, no. 7, pp. 075408–5, 2004.
- [367] J.-M. Zuo, T. Kim, A. Celik-Aktas, and J. Tao, "Quantitative structural analysis of individual nanotubes by electron diffraction," *Zeitschrift für Kristallographie*, vol. 222, no. 11, pp. 625–633, 2007.
- [368] H. Jiang, D. P. Brown, A. G. Nasibulin, and E. I. Kauppinen, "Robust bessel-function-based method for determination of the (n,m) indices of single-walled carbon nanotubes by electron diffraction," *Physical Review B*, vol. 74, no. 3, p. 035427, 2006.
- [369] S. L. Flegler, J. W. J. Heckman, and K. L. Klomparens, *Scanning and transmission electron microscopy - An introduction*. New York: Oxford University Press, 1993.
- [370] M. S. Dresselhaus, G. Dresselhaus, R. Saito, and A. Jorio, "Raman spectroscopy of carbon nanotubes," *Physics Reports-Review Section of Physics Letters*, vol. 409, no. 2, pp. 47–99, 2005.
- [371] S. Reich, C. Thomsen, and J. Maultzsch, *Carbon nanotubes : basic concepts and physical properties*. Weinheim: Wiley-VCH, 2004.
- [372] L. Alvarez, A. Righi, T. Guillard, S. Rols, E. Anglaret, D. Laplaze, and J. L. Sauvajol, "Resonant raman study of the structure and electronic properties of single-wall carbon nanotubes," *Chemical Physics Letters*, vol. 316, no. 3-4, pp. 186–190, 2000.
- [373] J. Robertson, G. Zhong, H. Telg, C. Thomsen, J. H. Warner, G. A. D. Briggs, U. Dettlaff-Weglikowska, and S. Roth, "Growth and characterization of high-density mats of single-walled carbon nanotubes for interconnects," *Applied Physics Letters*, vol. 93, no. 16, p. 163111, 2008.

- [374] A. Jorio, R. Saito, J. H. Hafner, C. M. Lieber, M. Hunter, T. McClure, G. Dresselhaus, and M. S. Dresselhaus, "Structural (n,m) determination of isolated single-wall carbon nanotubes by resonant Raman scattering," *Physical Review Letters*, vol. 86, no. 6, p. 1118, 2001.
- [375] C. Spudat, M. Muller, L. Houben, J. Maultzsch, K. Goss, C. Thomsen, C. M. Schneider, and C. Meyer, "Observation of breathing-like modes in an individual multiwalled carbon nanotube," *Nano Letters*, vol. 10, no. 11, pp. 4470–4474, 2010.
- [376] S. Piscanec, M. Lazzeri, J. Robertson, A. C. Ferrari, and F. Mauri, "Optical phonons in carbon nanotubes: Kohn anomalies, peierls distortions, and dynamic effects," *Physical Review B*, vol. 75, no. 3, p. 035427, 2007.
- [377] H. Telg, J. G. Duque, M. Staiger, X. Tu, F. Hennrich, M. M. Kappes, M. Zheng, J. Maultzsch, C. Thomsen, and S. K. Doorn, "Chiral index dependence of the  $G^+$  and  $G^-$  Raman modes in semiconducting carbon nanotubes," *ACS Nano*, vol. 6, no. 1, pp. 904–911, 2012.
- [378] K. Iakoubovskii, N. Minami, T. Ueno, S. Kazaoui, and H. Kataura, "Optical characterization of double-wall carbon nanotubes: Evidence for inner tube shielding," *The Journal of Physical Chemistry C*, vol. 112, no. 30, pp. 11 194–11 198, 2008.
- [379] J. Gauckler, "Temperature-dependent micro-Raman spectroscopy on integrated single-walled carbon nanotubes," Master's thesis, ETH Zurich, D-MAVT, Micro and Nanosystems, Zurich, Switzerland, 2007.
- [380] A. Jungen, J. Gauckler, C. Stampfer, L. Durrer, T. Helbling, and C. Hierold, "Temperature-dependent properties of an individual MEMS-integrated single-walled carbon nanotube," in *21st IEEE MEMS, Technical Digest, Jan 13-17, Tucson, USA*, 2008, pp. 733–736.
- [381] M. Y. Sfeir, F. Wang, L. M. Huang, C. C. Chuang, J. Hone, S. P. O'Brien, T. F. Heinz, and L. E. Brus, "Probing electronic transitions in individual carbon nanotubes by rayleigh scattering," *Science*, vol. 306, no. 5701, pp. 1540–1543, 2004.
- [382] M. Y. Sfeir, T. Beetz, F. Wang, L. M. Huang, X. M. H. Huang, M. Y. Huang, J. Hone, S. O'Brien, J. A. Misewich, T. F. Heinz, L. J. Wu, Y. M. Zhu, and L. E. Brus, "Optical spectroscopy of individual single-walled carbon nanotubes of defined chiral structure," *Science*, vol. 312, no. 5773, pp. 554–556, 2006.
- [383] G. Binnig, H. Rohrer, C. Gerber, and E. Weibel, "Surface studies by scanning tunneling microscopy," *Physical Review Letters*, vol. 49, no. 1, pp. 57–61, 1982.
- [384] J. W. G. Wildöer, L. C. Venema, A. G. Rinzler, R. E. Smalley, and C. Dekker, "Electronic structure of atomically resolved carbon nanotubes," *Nature*, vol. 391, no. 6662, pp. 59–62, 1998.
- [385] T. W. Odom, J. L. Huang, P. Kim, and C. M. Lieber, "Atomic structure and electronic properties of single-walled carbon nanotubes," *Nature*, vol. 391, no. 6662, pp. 62–64, 1998.
- [386] B. J. LeRoy, S. G. Lemay, J. Kong, and C. Dekker, "Electrical generation and absorption of phonons in carbon nanotubes," *Nature*, vol. 432, no. 7015, pp. 371–374, 2004.
- [387] P. Zhang, Y. Huang, P. H. Geubelle, P. A. Klein, and K. C. Hwang, "The elastic modulus of single-wall carbon nanotubes: a continuum analysis incorporating interatomic potentials," *International Journal of Solids and Structures*, vol. 39, no. 13-14, pp. 3893–3906, 2002.
- [388] R. M. Kramer, L. A. Sowards, M. J. Pender, M. O. Stone, and R. R. Naik, "Constrained iron catalysts for single-walled carbon nanotube growth," *Langmuir*, vol. 21, no. 18, pp. 8466–8470, 2005.
- [389] L. An, J. M. Owens, L. E. McNeil, and J. Liu, "Synthesis of nearly uniform single-walled carbon nanotubes using identical metal-containing molecular nanoclusters as catalysts," *Journal of the American Chemical Society*, vol. 124, no. 46, pp. 13 688–13 689, 2002.
- [390] G. H. Jeong, A. Yamazaki, S. Suzuki, Y. Kobayashi, and Y. Homma, "Behavior of catalytic nanoparticles during chemical vapor deposition for carbon nanotube growth," *Chemical Physics Letters*, vol. 422, no. 1-3, pp. 83–88, 2006.
- [391] S. Reich, L. Li, and J. Robertson, "Control the chirality of carbon nanotubes by epitaxial growth," *Chemical Physics Letters*, vol. 421, no. 4-6, pp. 469–472, 2006.
- [392] S. D. Li, Z. Yu, C. Rutherglen, and P. J. Burke, "Electrical properties of 0.4 cm long single-walled carbon nanotubes," *Nano Letters*, vol. 4, no. 10, pp. 2003–2007, 2004.
- [393] B. Liu, W. Ren, S. Li, C. Liu, and H.-M. Cheng, "High temperature selective growth of single-walled carbon nanotubes with a narrow chirality distribution from a CoPt bimetallic catalyst," *Chemical Communications*, vol. 48, no. 18, pp. 2409–2411, 2012.
- [394] C.-H. Liu and H.-L. Zhang, "Chemical approaches towards single-species single-walled carbon nanotubes," *Nanoscale*, vol. 2, no. 10, pp. 1901–1918, 2010.
- [395] P. C. Collins, M. S. Arnold, and P. Avouris, "Engineering carbon nanotubes and nanotube circuits using electrical breakdown," *Science*, vol. 292, no. 5517, pp. 706–709, 2001.

- [396] A. A. Green and M. C. Hersam, "Nearly single-chirality single-walled carbon nanotubes produced via an orthogonal iterative density gradient ultracentrifugation," *Advanced Materials*, vol. 23, no. 19, p. 2185, 2011.
- [397] H. Kataura, "High sensitivity detection of surfactant molecules on swcnts by raman spectroscopy," in *International Winterschool on Electronic Properties of Novel Materials and Molecular Nanostructures*, February 28, 2011.
- [398] R. E. Smalley, Y. B. Li, V. C. Moore, B. K. Price, R. Colorado, H. K. Schmidt, R. H. Hauge, A. R. Barron, and J. M. Tour, "Single wall carbon nanotube amplification: En route to a type-specific growth mechanism," *Journal of the American Chemical Society*, vol. 128, no. 49, pp. 15 824–15 829, 2006.
- [399] D. Ogrin, R. E. Anderson, R. Colorado, B. Maruyama, M. J. Pender, V. C. Moore, S. T. Pheasant, L. McJilton, H. K. Schmidt, R. H. Hauge, W. E. Billups, J. M. Tour, R. E. Smalley, and A. R. Barron, "Amplification of single-walled carbon nanotubes from designed seeds: Separation of nucleation and growth," *Journal of Physical Chemistry C*, vol. 111, no. 48, pp. 17 804–17 806, 2007.
- [400] Y. G. Yao, C. Q. Feng, J. Zhang, and Z. F. Liu, "'cloning' of single-walled carbon nanotubes via open-end growth mechanism," *Nano Letters*, vol. 9, no. 4, pp. 1673–1677, 2009.
- [401] K. Truckses, *Electrostatically mediated ferritin adsorption for nanotube growth*, bachelor Thesis, ETH Zurich, D-MAVT, Micro and Nanosystems, Zurich, Switzerland, 2011.
- [402] S. Yoshii, S. Kumagai, K. Nishio, A. Kadotani, and I. Yamashita, "Electrostatic self-aligned placement of single nanodots by protein supramolecules," *Applied Physics Letters*, vol. 95, no. 13, p. 133702, 2009.
- [403] L. Yang, C.-H. Park, Y.-W. Son, M. L. Cohen, and S. G. Louie, "Quasiparticle energies and band gaps in graphene nanoribbons," *Physical Review Letters*, vol. 99, no. 18, p. 186801, 2007.
- [404] K. Nakada, M. Fujita, G. Dresselhaus, and M. S. Dresselhaus, "Edge state in graphene ribbons: Nanometer size effect and edge shape dependence," *Physical Review B*, vol. 54, no. 24, pp. 17 954–17 961, 1996.
- [405] K. Saloriotta, Y. Hancock, A. Kärkkäinen, L. Kärkkäinen, M. J. Puska, and A.-P. Jauho, "Electron transport in edge-disordered graphene nanoribbons," *Physical Review B*, vol. 83, no. 20, p. 205125, 2011.
- [406] S. Adam, S. Cho, M. S. Fuhrer, and S. Das Sarma, "Density inhomogeneity driven percolation metal-insulator transition and dimensional crossover in graphene nanoribbons," *Physical Review Letters*, vol. 101, no. 4, p. 046404, 2008.
- [407] K. I. Bolotin, K. J. Sikes, Z. Jiang, M. Klima, G. Fudenberg, J. Hone, P. Kim, and H. L. Stormer, "Ultrahigh electron mobility in suspended graphene," *Solid State Communications*, vol. 146, no. 9-10, pp. 351–355, 2008.
- [408] J. Cai, P. Ruffieux, R. Jaafar, M. Bieri, T. Braun, S. Blankenburg, M. Muoth, A. P. Seitsonen, M. Saleh, X. Feng, K. Mullen, and R. Fasel, "Supplementary information to: Atomically precise bottom-up fabrication of graphene nanoribbons," *Nature*, vol. 466, no. 7305, pp. 470–473, 2010.
- [409] M. Vandesuren, P. Hermet, V. Meunier, L. Henrard, and P. Lambin, "Theoretical study of the vibrational edge modes in graphene nanoribbons," *Physical Review B*, vol. 78, no. 19, p. 195401, 2008.
- [410] R. Gillen, M. Mohr, and J. Maultzsch, "Raman-active modes in graphene nanoribbons," *physica status solidi (b)*, vol. 247, no. 11-12, pp. 2941–2944, 2010.
- [411] V. T. Renard, M. Jublot, P. Gergaud, P. Chems, D. Rouchon, A. Chabli, and V. Jousseume, "Catalyst preparation for CMOS-compatible silicon nanowire synthesis," *Nature Nanotechnology*, vol. 4, no. 10, pp. 654–657, 2009.
- [412] X. Li, X. Wang, L. Zhang, S. Lee, and H. Dai, "Chemically derived, ultrasmooth graphene nanoribbon semiconductors," *Science*, vol. 319, no. 5867, pp. 1229–1232, 2008.

# Publications

## Reviewed journal articles

- A1 M. Muoth, V. Döring, and C. Hierold, "Gate hysteresis originating from atomic layer deposition of Al<sub>2</sub>O<sub>3</sub> onto suspended carbon nanotube field-effect transistors," *Physica Status Solidi (b)*, vol. 248, no. 11, pp. 2664–2667, 2011.
- A2 M. Muoth, F. Gramm, K. Asaka, L. Durrer, T. Helbling, C. Roman, S. W. Lee, and C. Hierold, "Chirality assignment to carbon nanotubes integrated in MEMS by tilted-view transmission electron microscopy," *Sensors and Actuators B: Chemical*, vol. 154, pp. 155–159, 2011.
- A3 M. Muoth, S.-W. Lee, K. Chikkadi, M. Mattmann, T. Helbling, A. Intlekofer, and C. Hierold, "Encapsulation of electrical contacts for suspended single-walled carbon nanotubes by atomic layer deposition," *Physica Status Solidi (b)*, vol. 247, no. 11–12, pp. 2997–3001, 2010.
- A4 M. Muoth, T. Helbling, L. Durrer, S. W. Lee, C. Roman, and C. Hierold, "Hysteresis-free operation of suspended carbon nanotube transistors," *Nature Nanotechnology*, vol. 5, pp. 589–592, 2010.  
M. Muoth, T. Helbling, L. Durrer, S.-W. Lee, C. Roman, and C. Hierold, "Supplementary information - Hysteresis-free operation of suspended carbon nanotube transistors," *Supplementary information - Nature Nanotechnology*, available: <http://www.nature.com/nnano/journal/v5/n8/abs/nnano.2010.129.html#supplementary-information>.
- a5 J. Cai, P. Ruffieux, R. Jaafar, M. Bieri, T. Braun, S. Blankenburg, M. Muoth, A. P. Seitsonen, M. Saleh, X. Feng, K. Mullen, and R. Fasel, "Atomically precise bottom-up fabrication of graphene nanoribbons," *Nature*, vol. 466, pp. 470–473, 2010.
- a6 K. Chikkadi, M. Mattmann, M. Muoth, L. Durrer, C. Hierold, "The role of pH in the density control of ferritin-based catalyst nanoparticles towards scalable single-walled carbon nanotube growth," *Microelectronic Engineering*, vol. 88, pp. 2478–2480, 2011.
- a7 B. R. Burg, J. Schneider, M. Muoth, L. Durrer, T. Helbling, N. C. Schirmer, T. Schwamb, C. Hierold, and D. Poulikakos, "Aqueous dispersion and dielectrophoretic assembly of individual surface-synthesized single-walled carbon nanotubes," *Langmuir*, vol. 25, pp. 7778–7782, 2009.
- a8 L. Durrer, J. Greenwald, T. Helbling, M. Muoth, R. Riek, and C. Hierold, "Narrowing SWNT diameter distribution using size-separated ferritin-based Fe catalysts," *Nanotechnology*, vol. 20, pp. 355601–355607, 2009.

## Conference proceedings (reviewed)

- C1 M. Muoth, K. Chikkadi, Y. Liu, and C. Hierold, "Suspended CNT-FET piezoresistive strain gauges: Chirality assignment and quantitative analysis," in *Technical Digest of IEEE MEMS 2013*, Taipei, Taiwan, pp. 496–499, January 20 – 24, 2013. Outstanding Poster Paper Award.
- C2 M. Muoth and C. Hierold, "Transfer of carbon nanotubes onto microactuators for hysteresis-free transistors at low thermal budget," in *Technical Digest of IEEE MEMS 2012*, Paris, France, pp. 1352–1355, January 29 – February 2, 2012.

- C3 M. Muoth, S.-W. Lee, and C. Hierold, "Platform for strainable, TEM-compatible, MEMS-embedded carbon nanotube transistors," in *Technical Digest of IEEE MEMS 2011*, Cancun, Mexico, pp. 83–86, January 23–27, 2011.
- C4 M. Muoth, F. Gramm, K. Asaka, L. Durrer, T. Helbling, C. Roman, S. W. Lee, and C. Hierold, "Tilted-view transmission electron microscopy-access for chirality assignment to carbon nanotubes integrated in MEMS," in *Procedia Chemistry Eurosensors XXIII*, Lausanne, Switzerland, vol. 1, pp. 601–604, 2009.
- c5 J. J. Brown, M. Muoth, C. Hierold, and V. M. Bright, "Carbon nanotube in situ TEM large strain and chiral angle analysis enabled by modular coupon and MEMS test platform system," in *Transducers and Eurosensors 2013*, Barcelona, Spain, accepted, 2013.
- c6 K. Chikkadi, M. Muoth, and C. Hierold, "Hysteresis-free, suspended pristine carbon nanotube gas sensors," in *Transducers and Eurosensors 2013*, Barcelona, Spain, accepted, 2013.

### Conference talks

- T1 M. Muoth and C. Hierold, "Clean integration of suspended carbon nanotubes into microactuators," in *7<sup>th</sup> MRC Graduate Symposium*, ETH Zurich, Zurich, Switzerland, June 7, 2012.
- T2 M. Muoth, S.-W. Lee, and C. Hierold, "Platform for strainable, TEM-compatible, MEMS-embedded carbon nanotube transistors," in *IEEE MEMS 2011*, Cancun, Mexico, January 25, 2011.
- T3 M. Muoth, F. Gramm, K. Asaka, L. Durrer, T. Helbling, C. Roman, S. W. Lee, and C. Hierold, "Tilted-view transmission electron microscopy-access for chirality assignment to carbon nanotubes integrated in MEMS," in *Eurosensors XXIII*, Lausanne, Switzerland, September 7, 2009.

### Invited talks

- I1 M. Muoth, J. Grimm, S.-W. Lee, K. Chikkadi, T. Helbling, L. Durrer, C. Roman, and C. Hierold, "Platform for strainable, TEM-compatible, MEMS-embedded carbon nanotube transistors," *COST Workshop CH-COST MP0901*, EMPA, Dübendorf, Switzerland, April 7, 2011.
- I2 M. Muoth, S.-W. Lee, J. Grimm, K. Chikkadi, M. Mattmann, T. Helbling, L. Durrer, C. Roman, and C. Hierold, "Ultraclean integration of suspended single-walled carbon nanotubes in electromechanical systems," *Seminar talk* at II. Physikalisches Institut – Prof. C. Stampfer, RWTH Aachen, Aachen, Germany, September 22, 2011.

### Miscellaneous talks

- MT1 E. Cagin, M. Muoth, and C. Hierold, "Demonstration von Micro und Nano-systemen - Nehmen Sie Einblick in die Welt der Nanosysteme," in *Maturandentage 2011*, ETH Zurich, Zurich, Switzerland, September 7 and 8, 2011.
- MT2 M. Muoth, "Carbon nanotube integration and suspended CNT transistors," in *Seminar on micro and nanosystems*, Friday talk, ETH Zurich, Zurich, Switzerland, June 4, 2010.
- MT3 M. Muoth, "Electrical integration of suspended single-walled carbon nanotubes – towards nanotransducers based on as-grown SWNTs," in *Seminar on micro and nanosystems*, Friday talk, ETH Zurich, Zurich, Switzerland, October 10, 2008.
- MT4 M. Muoth, "Transmission electron microscopy - comparison of characterization techniques for CNTs," in *Seminar on micro and nanosystems*, Friday talk, ETH Zurich, Zurich, November 16, 2007.

- mt5 S. Schürle, M. K. Tiwari, K. Shou, M. Muoth, S.-W. Lee, B. Nelson, D. Poulikakos, "CabTuRes Project Task 4: Mechanical clamping at contacts," *CabTuRes* annual meetings and general meetings, e.g. 2 July 2010, January 20, 2011, July 13, 2011.
- mt6 S.-W. Lee, M. Muoth, L. Durrer, C. Roman, and C. Hierold, "Integration of clamped-clamped suspended single-walled carbon nanotubes into SOI MEMS," in *IEEE NEMS 2011*, Kaohsiung, Taiwan, 20–23 February, 2011.

## Poster presentations

- P1 M. Muoth and C. Hierold, "Transfer of carbon nanotubes onto microactuators for hysteresis-free transistors at low thermal budget," in *Technical Digest of IEEE MEMS 2012*, Paris, France, pp. 1352–1355, January 29 - February 2, 2012.
- P2 M. Muoth, J. Grimm, and C. Hierold, "Towards Cs-corrected STEM imaging of electrical contacts for suspended carbon nanotubes," in *6<sup>rd</sup> MRC Graduate Symposium*, ETH Zurich, Zurich, Switzerland, June 8, 2011. Poster prize.
- P3 M. Muoth, J. Grimm, and C. Hierold, "Confocal Raman spectroscopy on carbon nanotubes uniaxially loaded by micro actuators," in *XXV<sup>th</sup> International Winterschool on Electronic Properties of Novel Materials and Molecular Nanostructures*, Kirchberg, Austria, February 26 – March 5, 2011.
- P4 M. Muoth, V. Döring (presenting author), and C. Hierold, "Gate hysteresis originating from atomic layer deposition of Al<sub>2</sub>O<sub>3</sub> onto suspended carbon nanotube field-effect transistors," in *XXV<sup>th</sup> International Winterschool on Electronic Properties of Novel Materials and Molecular Nanostructures*, Kirchberg, Austria, Feb 26 – Mar 5, 2011.
- P5 M. Muoth and C. Hierold, "Suspended carbon nanotube transistors," in *Industry Day*, ETH Zurich, Zurich, Switzerland, September 17, 2010.
- P6 M. Muoth and C. Hierold, "Structure determination of quasi-1-dimensional carbon nanotubes by electron diffraction," in *5<sup>th</sup> MRC Graduate Symposium*, ETH Zurich, Zurich, Switzerland, May 10, 2010.
- P7 M. Muoth, K. Chikkadi, M. Mattmann, T. Helbling, C. Hierold, "Encapsulation of electrical contacts for suspended SWNTs by atomic layer deposition," *XXIV<sup>th</sup> International Winterschool on Electronic Properties of Novel Materials and Molecular Nanostructures*, Kirchberg, Austria, March 6–13, 2010.
- P8 M. Muoth, S.-W. Lee, L. Durrer, T. Helbling, R. Grundbacher, and C. Hierold, "Suspended single-walled carbon nanotubes integrated in electromechanical systems," in *4<sup>th</sup> MRC Graduate Symposium*, ETH Zurich, Zurich, Switzerland, June 10, 2009.
- P9 M. Muoth, S.-W. Lee, L. Durrer, T. Helbling, F. Gramm, and C. Hierold, "Electrical contact formation for suspended single-walled carbon nanotubes," in *3<sup>rd</sup> MRC Graduate Symposium*, ETH Zurich, Zurich, Switzerland, May 14, 2008.
- p10 S.-W. Lee, X. Di, M. Muoth, C. Roman, S. Truax, and C. Hierold, "Embedded MEMS actuators for CNT straining tests," in *Annual Meeting of nano-tera.ch*, Zurich, Switzerland, April 26, 2012.
- p11 S.-W. Lee, M. Muoth, C. Roman, H. Chandralalim, C. Hierold, "Characterization of suspended carbon nanotubes integrated in MEMS structures," in *Annual Meeting of nano-tera.ch*, Berne, Switzerland, Mai 12, 2011.
- p12 K. Chikkadi, M. Mattmann, M. Muoth, L. Durrer, C. Hierold, "The role of pH in the density control of ferritin-based catalyst nanoparticles towards scalable single-walled carbon nanotube growth," *36<sup>th</sup> International conference on Micro and Nano Engineering (MNE 2010)*, Genoa, Italy, September 19–22, 2010.
- p13 S.-W. Lee, M. Muoth, T. Helbling, M. Mattmann, C. Hierold, "ALD-assisted metal lift-off for contamination-free contact areas to carbon nanotubes," *36<sup>th</sup> International conference on Micro and Nano Engineering (MNE 2010)*, Genoa, Italy, Sept 19–22, 2010.



- p14 M. Haluska, L. Durrer, T. Helbling, M. Muoth, M. Mattmann, K. Chikkadi, T. Süss, C. Roman, C. Hierold, "Targeted growth of single-walled carbon nanotubes for nano-sensor devices," *NT10, 11<sup>th</sup> International Conference on the Science and Application of Nanotubes*, Montreal, Canada, 2010.
- p15 S.-W. Lee, M. Muoth, C. Roman, H. Chandrahali, and C. Hierold, "Integration of carbon nanotubes into MEMS for tunable resonator applications," in *Industry Day*, ETH Zurich, Zurich, September 17, Switzerland, 2010
- p16 L. Durrer, M. Muoth, M. Mattmann, T. Helbling, K. Chikkadi, T. Süss, M. Haluska (presenting author), C. Hierold, "Targeted growth of single walled carbon nanotubes for applications in nanosensor devices," *XXIV<sup>th</sup> International Winterschool on Electronic Properties of Novel Materials and Molecular Nanostructures*, Kirchberg, Austria, March 6–13, 2010.
- p17 J. Cai, P. Ruffieux, R. Jaafar, M. Bieri, T. Braun, S. Blankenburg, M. Muoth, A. P. Seitsonen, M. Saleh, X. Feng, K. Mullen, and R. Fasel, "Atomically precise bottom-up fabrication of graphene nanoribbons," in *XXIV<sup>th</sup> International Winterschool on Electronic Properties of Novel Materials and Molecular Nanostructures*, Kirchberg, Austria, March 6–13, 2010.
- p18 B. R. Burg, J. Schneider, M. Muoth, L. Durrer, T. Schwamb, N. C. Schirmer, and D. Poulidakos, "Aqueous dispersion and self-limiting assembly of large diameter single-walled carbon nanotubes," in *Materials Research Society (MRS) Fall Meeting*, Boston, MA, U.S.A., December 2008.

#### Public relations and miscellaneous

- M1 R. Waser, J. Lang, "Industrie mit Zukunft," Input-Movie recorded by element p GmbH, in *Swissmem-Industrietag 2011*, Messezentrum Zürich, Zurich, Switzerland, June 29, 2011. Available: [http://www.elementp.ch/video/11011\\_swissmem/swissmem.html](http://www.elementp.ch/video/11011_swissmem/swissmem.html)
- M2 "Kohlenstoff-Nanoröhre als Transistormaterial," P. Rüegg [editor], *ETH Life*, published online July 15, 2010. Available: [http://www.ethlife.ethz.ch/archive\\_articles/100715\\_transistor/](http://www.ethlife.ethz.ch/archive_articles/100715_transistor/)
- M2b "Carbon nanotubes as transistor material," P. Rüegg [editor], *ETH Life*, published online 21 July 2010. Available: [http://www.ethlife.ethz.ch/archive\\_articles/100715\\_transistor\\_EN/index\\_EN](http://www.ethlife.ethz.ch/archive_articles/100715_transistor_EN/index_EN)
- M2c "Carbon nanotubes as transistor material," P. Rüegg [editor], *physorg*, July 21, 2010 [Online]. Available: <http://www.physorg.com/news198948792.html>
- M2d "Durchbruch in der Forschung: Sensoren ohne unerwünschte Gate-Hysterese - Kohlenstoffnanoröhre als Transistormaterial," P. Rüegg [editor], *technica - die Fachzeitschrift für die Maschinen-, Elektro- und Metallindustrie*, August 2010 [Online]. Available: [http://issuu.com/technica/docs/technica\\_august\\_2010](http://issuu.com/technica/docs/technica_august_2010)
- M3 Barbara Simpson [editor] "Heightened Sense Perception but Zero-Power," *ERCIM NEWS*, 87, p. 13, 2011.
- M4 S. Kunz and P. Rüegg. Effiziente Sensoren aus Kohlenstoffnanoröhren. Nanotechnology Center - Eine strategische Partnerschaft in Nanotechnologie von ETH Zürich und IBM Research - Zürich. Europa Forum Luzern, 2010.

### Supervised student's projects

- s1 A. Kemelbay, "Raman characterization of suspended carbon nanotube FETs strained by micro actuators," *Semester thesis*, Supervisors: M. Muoth, C. Hierold, ETH Zurich, Department of Mechanical and Process Engineering (D-MAVT), Micro and Nanosystems, Zurich, Switzerland, autumn semester 2012.
- s2 K. Truckses, "Electrostatically mediated ferritin adsorption for nanotube growth," *Bachelor's thesis*, Supervisors: M. Muoth, C. Hierold, ETH Zurich, D-MAVT, Micro and Nanosystems, Zurich, Switzerland, spring semester 2011.
- s3 J. Grimm, "Raman spectroscopy on strained single-walled carbon nanotubes," *Semester thesis*, Supervisors: M. Muoth, K. Ensslin, C. Hierold, ETH Zurich, D-MAVT, Micro and Nanosystems, Zurich, Switzerland, autumn semester 2010.
- s4 A. Intlekofer, "Aligned SWNT growth," *Semester thesis*, Supervisors: M. Muoth, C. Hierold, ETH Zurich, D-MAVT, Micro and Nanosystems, Zurich, Switzerland, spring semester 2011.
- s5 A. Intlekofer, "Direct growth of suspended single-walled carbon nanotubes across conductive electrodes," *Bachelor's thesis*, Supervisors: M. Muoth, C. Hierold, ETH Zurich, D-MAVT, Micro and Nanosystems, Zurich, Switzerland, spring semester 2010.
- s6 A. Intlekofer, "Carbon nanotube devices," *Studies on Micro and Nanosystems*, Supervisors: M. Muoth, C. Hierold, ETH Zurich, D-MAVT, Micro and Nanosystems, Zurich, Switzerland, autumn semester 2009.
- s7 S.-A. Pohl, "Characterisation of single-walled carbon nanotubes by Raman spectroscopy and AFM - correlative study of single-walled carbon nanotube diameter determination and monitoring defects induced by metallization processes," *Master's thesis*, Supervisors: M. Muoth, C. Hierold, ETH Zurich, D-MAVT, Micro and Nanosystems, Zurich, Switzerland, spring semester 2008.

# Curriculum Vitae

## Personal Details

Name	Matthias Muoth
Birth	January 15, 1982, Zug, Switzerland
Citizenship	Switzerland
Marital Status	Single

## Education

07/2007 – 01/2013	<b>ETH Zurich, Micro and Nanosystems, Switzerland</b> Dissertation: <i>Clean integration of single-walled carbon nanotubes for electromechanical systems</i>
09/2005 – 05/2007	<b>ETH Zurich, Department of Mechanical and Process Engineering</b> Graduation with Master's Degree Willi Studer Award and ETH Zurich medal
10/2002 – 09/2005	<b>ETH Zurich, Department of Mechanical and Process Engineering</b> Graduation with Bachelor's Degree
08/1998 – 06/2002	<b>Kantonsschule Zofingen, AG</b> Graduation with Matura Typus C: mathematics & natural sciences

## Work Experience

07/2012 –	<b>ETH Zurich, Micro and Nanosystems, Switzerland</b> Postdoctoral researcher
07/2007 – 06/2012	<b>ETH Zurich, Micro and Nanosystems, Switzerland</b> Research and teaching assistant
05/2006 – 07/2006	<b>ETH Zurich, Institute for mechanical Systems, Switzerland</b> Exercise co-assistant
07/2005 – 09/2005	<b>Areva T&amp;D AG, Oberentfelden, Switzerland</b> Internship: Mechanical drives for high voltage switches

## Languages

<b>German</b>	mother tongue
<b>English</b>	fluent
<b>French</b>	basic oral communication